Author:
Liu, Chong

Title:
Oxidation and carburisation of 9Cr-1Mo steel in both simulant and in-service AGR coolant gases

Oxidation and carburisation of 9Cr-1Mo steel in both simulant and in-service AGR coolant gases

Chong Liu

A thesis submitted to the University of Bristol in accordance with the requirements for award of the degree of Doctor of Philosophy at the

Interface Analysis Centre, Faculty of Science

October 2018

64922 words

Declaration of authorship

I declare that the work in this dissertation was carried out in accordance with the requirements of the University's Regulations and Code of Practice for Research Degree Programmes and that it has not been submitted for any other academic award. Except where indicated by specific reference in the text, the work is the candidate's own work. Work done in collaboration with, or with the assistance of, others, is indicated as such. Any views expressed in the dissertation are those of the author.

Signed: ……

Date: ……

“Happiness can be found even in the darkest times, when one only remembers to turn on the light.”

Albus Dumbledore, Harry Potter and the Prisoner of Azkaban

Abstract

For many years, commercial 9Cr-1Mo steels have been used for components in the UK advanced gas cooled reactors operated by EDF Energy. The selection of 9Cr-1Mo steel for power plant applications is based on its relatively low cost, resistance to high temperature oxidation and excellent high temperature creep strength. However, degradation occurs in service due to thermal aging and exposure to the CO_2-based coolant gas. Under some circumstances, rapid oxidation can occur, known as "breakaway oxidation". The degradation of the mechanical and corrosion properties has prompted study of the mechanisms of concurrent oxidation and carburisation in a high-temperature CO_2-based atmosphere. Here, experimental finned tube samples with ferritic and martensitic microstructures exposed to simulated in-service environments have been analysed using several techniques to understand the triggers of breakaway oxidation.

Samples were taken of ferritic and martensitic 9Cr-1Mo steels that had been aged in a CO_2-based environment at high temperature, 580-640 °C, in autoclaves and within the simulant AGR environment for various times. Optical and electron microscopy were used to study the form and thickness of the oxide. Energy dispersive X-ray (EDS) analysis was used to determine the distribution of elements and Raman spectroscopy provided oxide type and distribution, as well as strain and the presence of carbon (graphite) within the oxide. X-ray diffraction (XRD) was used to detect the presence of carbides within the metal. Focused ion beam (FIB), in conjunction with XeF_2 gas, was used to image and identify the carbides, including their spatial distribution and area fraction. High-speed atomic force microscopy (HS-AFM) produced high-resolution images of the carbide precipitates. (Scanning) transmission electron microscopy (STEM) was used to identify the carbides and to determine their growth direction with respect to the matrix, as well as the chromium content of the matrix.

Initially a duplex oxide is formed comprising an outer magnetite and inner spinel layer, and the growth of the duplex oxide follows sub-parabolic kinetics in this work. At this stage, an internal oxidation zone (IOZ) is also present between the spinel and the original metal. Raman spectroscopy showed the presence of Cr_2O_3 within the IOZ, and nanocrystalline graphite within the spinel. Attempts were made to measure strain within the oxide and IOZ, although this is difficult due to variations in composition. Carbide precipitates were observed using FIB/XeF_2 imaging and (S)TEM analysis showed these to be $M_{23}C_6$ (coarse and cored coarse carbides), MC (large needles) and M_2C (fined needles), where M can be Fe and/or Cr. Formation of the spinel layer within the oxide and the distribution of carbide precipitates within the metal reduced the Cr content of the ferritic matrix.

After extended exposure at high temperatures, multiple layers of oxide are formed. These multiple layers form when Cr in the matrix falls to approximately 5 wt. %. The IOZ layer disappears, oxidation become more rapid and eventually "laminated" oxide growth occurs. At this stage, oxide forms a fan shape at the fin tips and edges. It is at this stage that the kinetics

of weight gain against time become linear. During this process, the quantity of fine needles M_2C precipitates decreases while large needles increase. Furthermore, coarse carbides $M_{23}C_6$ become “cored” with varying composition between core and shell.

The geometry of the samples is important for achieving breakaway oxidation, since the more complex diffusion paths cause more rapid oxidation at corners and edges compared with planar surfaces. The ferritic and martensitic 9Cr-1Mo steels behave in a similar way, although the lath boundaries in the martensitic material modify the carbide distribution. The moisture content of the gas was found to have little effect below 1200 vppm, but it appeared to accelerate oxidation at this level and above. Observations of oxide thickness at breakaway initiation reveal that breakaway occurs when the Cr level in the metal matrix reduced to a critical level, rather than when the oxide reaches a certain thickness.

Overall, the mechanism of oxidation is acknowledged to be complex, with oxidation and carburisation being interdependent. However, a simple qualitative model is presented showing the progression of oxidation to the stage of breakaway. The data gathered here will be useful for input to and validation of the mathematical models proposed by other workers.

Acknowledgements

I would like to thank many people who have helped me to pass the difficult times and reach this point here. First, I would like to thank my two academic supervisors: Dr. Peter J. Heard and Prof. Peter E. J. Flewitt. Without their encouragement and professional supervision it would have been impossible for me to finish this thesis. I would also like to thank Prof. Tom B Scott for giving me this opportunity to be involved in the Interface Analysis Centre (IAC) and the chance to know something of this fascinating nuclear world. My two industrial supervisors, Dr. Jonathan Pearson and Dr. Aya Shin from EDF Energy, helped me a lot in promoting the staged achievements of my PhD project, improving presentation skills and providing many opportunities to present my work in international conferences.

I would also like to send my thanks especially to Dr. Keith R. Hallam for his help in all aspects in academia and life. He helped me to improve my poor speaking and listening English patiently, and his introduction to British cultures, his help in X-ray diffraction (XRD) analysis, and many other things that are very impressive. To Dr. Peter Martin, thank you for training and help on field emission gun scanning electron microscopy (FEGSEM) and an introduction to traditional British food Marmite source (which is actually horrible according to my taste) and my favourite Sunday Roast. I would also like to thank Dr. Scott Greenwell and Dr. John Day for the help on scanning laser Raman spectroscopy. Many thanks to Dr. Ian Griffiths and Prof. David Cherns for their support on TEM and STEM analysis. Also very much appreciate the help from Dr. Oliver Payton and Dr. Loren Picco on HSAFM analysis. Dr. James Darnbrough and my dear supervisor Dr. Peter Heard, thank you both a lot for training on focused ion beam (FIB) and Dualbeam. Furthermore, many thanks to John Nicholson for technical supports. Dr. Ana Martinez Ubeda (Cariño), Dr. Haris Paraskevoulakos (Μαλάκα), Mr. Gareth Griffiths, Dr. Antonis Banos and Dr. Chris Hutson and his lovely wife Catherine Hutson, many thanks to you all for being friends with me, accompanying me through dark times when I had difficulties in communication, and helping me to improve my English and technical skills, etc.

Outside the university, I would like to thank Huiling Ouyang for great times in Bristol. Thank you Dr. Dong Liu for guiding me into the University of Bristol. Finally, the greatest appreciation to my dearest parents Mr. Jinshu Liu and Ms. Sulian Shi for their patience and endless spiritual encouragement and consideration on all aspects in my life. I could not finish my PhD without them.

Publications

Publications:

C. Liu, P.J. Heard, S.J. Greenwell, P.E.J. Flewitt, A Study of Breakaway Oxidation of 9Cr-1Mo Steel in a Hot CO_2 Atmosphere Using Raman Spectroscopy, Mater. High Temp. 35 (2018) 50-55.

C. Liu, P.J. Heard, O.D. Payton, L. Picco, P.E.J. Flewitt, A comparison of two high spatial resolution imaging techniques for measuring carbide precipitate size in 9Cr-1Mo steel. (In preparation)

C. Liu, P.J. Heard, S.J. Greenwell, P.E.J. Flewitt, The corrosion of 9Cr-1Mo steel exposed to CO_2 dominant simulant AGR coolant gas (part I): mechanism of oxidation. (in preparation)

C. Liu, P.J. Heard, I. Griffiths, D. Cherns, P.E.J. Flewitt, The corrosion of 9Cr-1Mo steel exposed to CO_2 dominant simulant AGR coolant gas (part II): mechanism of carburisation. (In preparation)

C. Liu, P.J. Heard, P.E.J. Flewitt, The evolution of microstructures of oxides and carbides in ferritic 9Cr-1Mo steel following exposure to hot CO_2 dominant simulant AGR coolant gases. (In preparation)

Conferences (papers, posters and presentations):

A. D. Warren, C. Liu, A. El Turke, P. J. Heard and P. E. J. Flewitt. Microstructural factors arising from the carburisation of 9Cr1Mo steel during exposure to hot CO_2 gas. the International Symposium on High-Temperature Oxidation and Corrosion 2018, 21-26 October 2018, Matsue, Shimane Japan. (Conference paper)

C. Liu, P.J. Heard, O.D. Payton, L. Picco, I. Griffiths and P.E.J. Flewitt. An evaluation of the carburised microstructure of ferritic 9Cr-1Mo steel following exposure to hot CO_2 gas. Transactions, SMiRT-24 BEXCO, Busan, Korea - August 20-25, 2017, Division 01-30. (Conference Paper for internal communication)

Hutson, C., Martin, P., Payne, L., Oughton, N., Wyness, K.E., Smith, D., Warren, A.D., Rennie, S.L., Jones, C.P., Banos, A.K., Payton, O.D., Sutcliffe, J.E., Paraskevoulakos, C., Liu, C., Darnbrough, J., Springell, R.S., Hallam, K.R., Stevens, O.A.C., Logan, M., Townes, J., Roberts, L.G.W., Pancost, R.D., Marshall, D., Shaw, H., Gray, A., Liu, D., Hutson, K., Yapp, O., Huntley, S., Adamska, A.M., Smale, R. & Scott, T., 2017, 'The importance and impact of public engagement for the nuclear industry'. in: waste management symposia 2017:

Proceedings of a meeting held 5-9 March 2017, Phoenix, Arizona, USA. Waste Management Symposia, Inc

C. Liu, P. J. Heard, S. J. Greenwell & P. E. J. Flewitt. A study of breakaway oxidation of 9Cr-1Mo steel in a hot CO_2 atmosphere using Raman spectroscopy. (Poster for the 10th International Conference on Microscopy of Oxidation, 3-5 April 2017, Loughborough University, United Kingdom)

C. Liu, P.J. Heard, T.B. Scott, C.M. Younes, P.E.J. Flewitt, J. Pearson and A. Shin. Corrosion of 9Cr-1Mo Steel in CO_2 at High Temperature (Poster for the 57th Corrosion Science Symposium 2016, 5-6 September 2016, Swansea University Bay Campus, United Kingdom).

Acronyms

2D: two dimensions

400 to 800 @ 245: moisture changes from 400 to 800 vppm after 245 hours

ABWR: advanced boiling water reactor

a-C: amorphous carbon

ADF: annular dark field

AFM: atomic force microscopy

AGR: advanced gas-cooled reactor

Å: Angstrom

APR: advanced pressurised water nuclear reactor

at. %: atomic percentage

atm: standard atmosphere (101325 Pa)

BA: breakaway

BCC: body-centred cubic

BF: bright field

BSE: back-scattered electrons

BWR: boiling water reactor

CANDU: Canada deuterium uranium reactor

CDEM: continuous dynode electron multiplier

CDF: centred dark-field

cm: centimetre

°C: degree celsius

DF: dark-field

dia: diameter

EDS: energy dispersive X-ray spectroscopy

EPR: European pressurised reactor

ESBWR: economic simplified boiling water reactor

FCC: face-centred cubic

FIB: focused ion beam

Gen: generation

GFR: gas-cooled fast reactor

h: hour(s)

HCP: hexagonal close-packed

HS-AFM: high speed atomic force microscopy

IEE: insulator enhanced etch

IOZ: internal oxidation zone

J: Joule

K: kelvin

keV: kiloelectronvolt

kHz: kilohertz

LFR: lead-cooled fast reactor

LRS: laser Raman spectroscopy

min: minute(s)

mm: millimetre

MSR: molten-salt reactor

μm: micrometre

mW: milliwatt

N: no

nA: nanoampere

NA: numerical aperture

NC-Graphite: nanocrystalline graphite

nm: nanometre

OM: optical microscopy

pA: picoampere

PE: primary electron

psi: pound per square inch

PWR: pressurised water reactor

R: universal gas constant which is 8.31 J/(mol·K)

s: second(s)

SAD: selected area diffraction

SCWR: supercritical-water-cooled reactor

SDD: silicon drift detector

SE: secondary electrons

SEM: scanning electron microscopy

SFR: sodium-cooled fast reactor

STEM: scanning transmission electron microscopy

TEM: transmission electron microscopy

Temp.: temperature

TTB: time to breakaway

UNGG: uranium natural graphite gas

VHTR: very-high-temperature reactor

vppm: volume parts per million

VVER: Vodo-vodyanoi energetichesky reactor

wt. %: weight percentage

XRD: X-ray diffraction

Y: yes

YAG laser: yttrium aluminium garnet

Symbols

a_C: carbon activity

α: incident angle

β: diffracted angle

C: concentration of carbon

D: diffusion coefficient of carbon in the medium

d: lattice interplanar spacing of the crystal

ΔG_T: standard free energy change

Δj: change in the total angular-momentum quantum number

Δl: change in the orbital angular momentum quantum number

d_{min}: limit resolution

Δn: change in the principal quantum number

D_0: maximal diffusion coefficient (in m^2/s)

E_A: activation energy for diffusion (in J/mol)

G_x: fraction of the total integrated intensity diffracted by a sample of infinite thickness.

h: Planck constant

ΔH and ΔS: enthalpy change and entropy change

hkl: Miller indices for planes

I_0: incident beam intensity

K: constant

k_l: linear rate constant

k_r: parabolic rate constant

K_x: corresponding value to G_x

λ: wavelength of X-rays or light

μ: absorption coefficient

N: positive integer

T: absolute temperature (in K)

T_{aust}: austenitising temperature

T_{temp}: tempering temperature

p: momentum of the particle

t: exposure time

θ: X-ray incidence angle (Bragg angle)

Contents

Chapter 1: Introduction

1.1 Nuclear reactor evolution

Nuclear energy is considered to be a large scale carbon-free source [1]. To achieve electrical power generation from this energy source, six key factors have to be addressed: safety, security and non-proliferation, cost-effectiveness, grid appropriateness, efficiency and the fuel cycle [2]. Nuclear reactors have been categorised into five "generations" based on this: Generation (Gen) I, II, III, III+ and IV, as shown in Figure 1-1 [3].

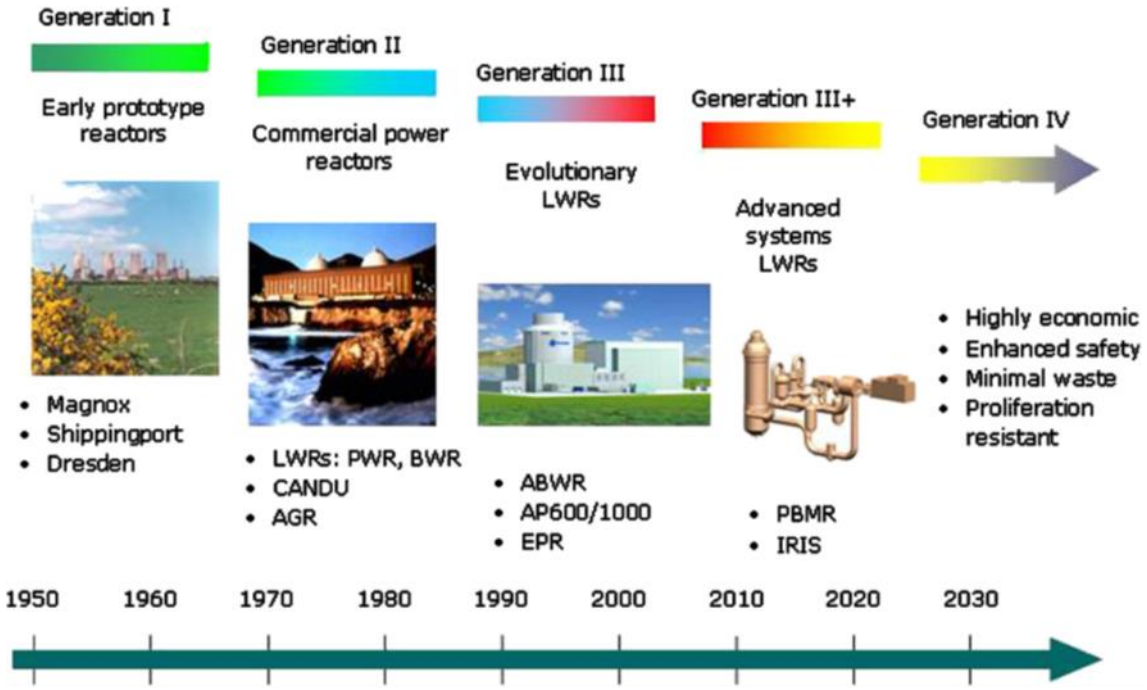

Figure 1-1: Evolution of nuclear power [3].

Gen I reactors refer to the non-commercial power producing reactors in the 1950s and 1960s, which were built as early prototypes for research purposes. Four representative reactors are Shippingport [4], UNGG [5], Fermi 1 [6] and Dresden [7][8]. However, none of these reactors is still operating nowadays [9]. Natural uranium was used as fuel and graphite as moderator for most of these reactors [10][11]. Magnox in the UK [12], which is not a prototype reactor, is also a Gen I reactor.

Gen II refers to early commercial reactors. Five representative reactors established between the mid-1960s and the mid-1990s belonging to Gen II are the Westinghouse designed AP1000 pressurised water reactors (PWR) [13], Canada deuterium uranium reactor (CANDU), boiling water reactors (BWR), Vodo-Vodyanoi energetichesky reactors (VVER) and advanced gas-

cooled reactors (AGR) [2][14]. Furthermore, most present working reactors are Gen II and considered to be safe, reliable and available. In this PhD project, materials used in AGRs in United Kingdom operated by EDF Energy are of concern. The relevant analyses were carried out to investigate materials degradation behaviour caused by oxidation and carburisation processes and are discussed in the following chapters.

Compared with Gen II, the improvement of Gen III reactors focuses on four aspects: fuel technology, thermal efficiency, passive nuclear safety systems and standardised design. Most of them were established during the mid-1990s and 2010 [2]. The existing Gen III reactors include the advanced boiling water reactors (ABWR) [15], and the European pressurised reactors (EPR) which is the third generation of PWR in Europe [16].

Gen III$_+$ reactors have significant improvements in safety and economic considerations compared with Gen III. A few forms of reactors included are: Advanced CANDU Reactor [17], AP1000 [18], Economic Simplified Boiling Water Reactor (ESBWR) [19], APR-1400 [20], VVER-1200 [21], EU-ABWR [22]. Gen III$_+$ reactors perform with higher availability, longer operating time and standardised design [2].

Gen IV currently refers to conceptual reactors under consideration for future use, but not expected to be available until the 2020s or 2030s [23]. There are three thermal reactors using slow or thermal neutrons, and three fast reactors using fast neutrons, with significant advances in sustainability, safety and reliability, economics, proliferation resistance and physical protection [24]. The three thermal reactors are: very-high-temperature reactor (VHTR) [25], molten-salt reactor (MSR) [26] and supercritical-water-cooled reactor (SCWR) [27]. The three fast reactors are: gas-cooled fast reactor (GFR), sodium-cooled fast reactor (SFR), and lead-cooled fast reactor (LFR) [24].

In addition, small modular reactors (SMRs), while outside the traditional nuclear reactor strategy, could offer a more flexible commercial technology, particularly for smaller countries with limited electrical capacity [28][29]. SMRs are considered to be simpler, safer and cheaper compared with traditional power reactors. SMRs are transportable, providing the possibility of use in isolated areas with no infrastructure or power grid facilities [30].

1.2 Advanced gas-cooled reactor

The advanced gas-cooled reactor (AGR) belongs to the Gen II category and continues to operate in the UK [31]. Carbon dioxide gas is used as the main coolant, graphite as the moderator and uranium oxide pellets in stainless steel tubes as the fuel [32]. Figure 1-2 depicts cross-sections of components in the AGR system. The typical reactor shown on the left part of

Figure 1-2a is composed of a reactor core, boilers and gas circulators which are shown in Figure 1-2b [33]. The CO_2 coolant gas is pumped through the reactor channels by gas circulators to reach the top of the pressure vessel, removing the heat produced and reducing the temperature of the core. The gas then flows into the boiler to transfer the heat to water and produce steam via the heat-exchanger tubes in the boiler, and the gas is then cooled when it reaches the bottom of boiler where it is ready for the new cycle. During this process, the cold water at the bottom of boiler eventually turns into steam when it reaches the top of the boiler due to the heat transferred from the coolant gas. The main path of circulation of coolant gas is illustrated in Figure 1-3 [31].

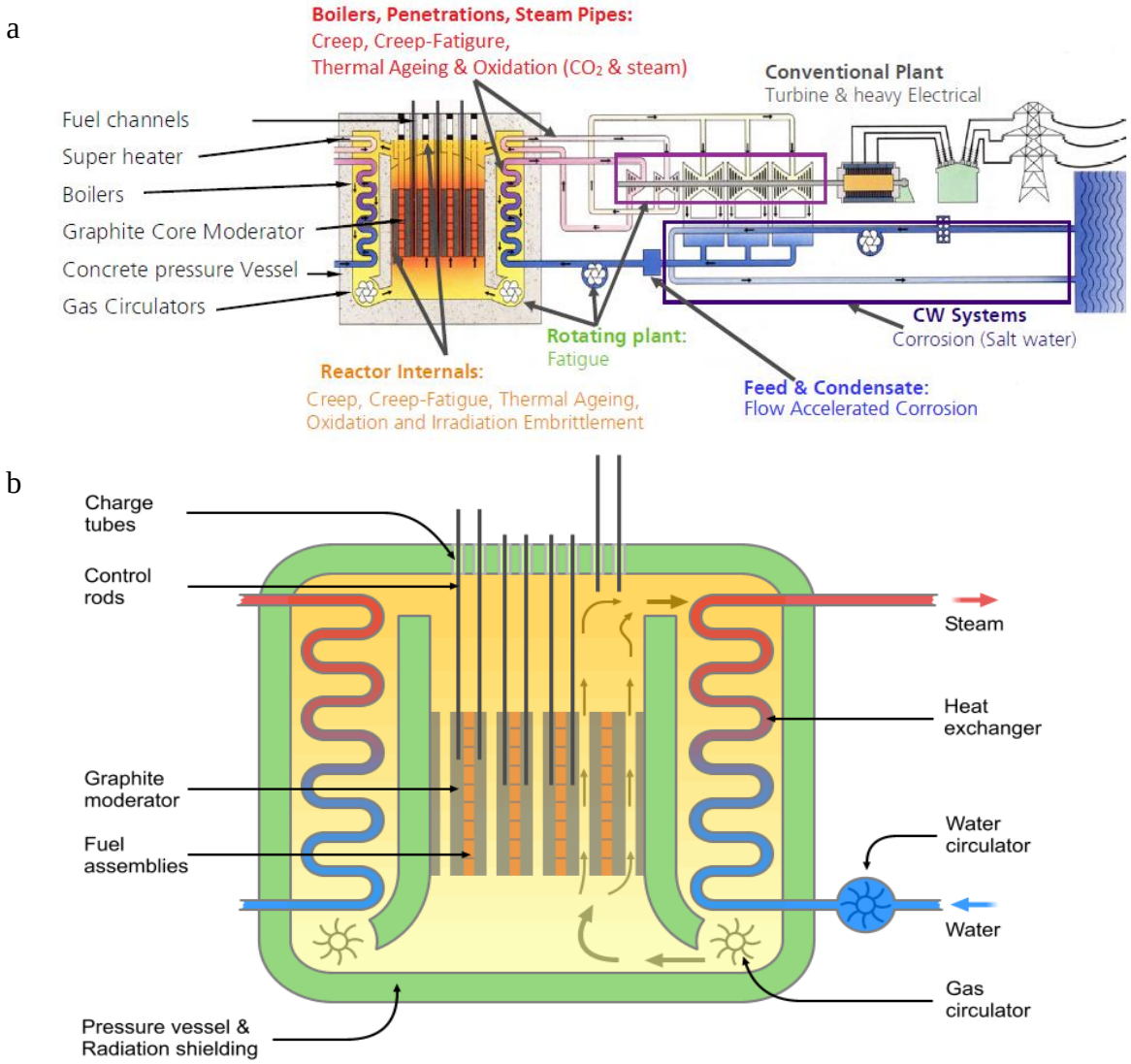

Figure 1-2: (a) cross section of an AGR and (b) details of heat exchanger [33].

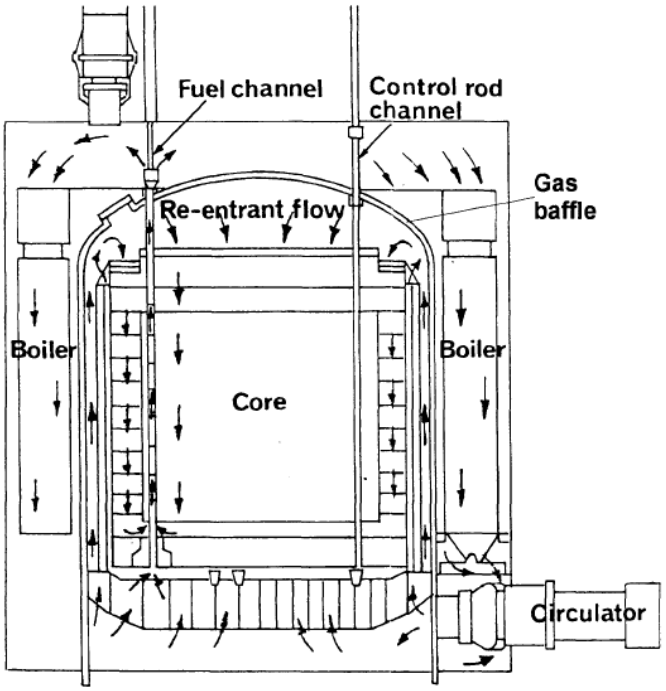

Figure 1-3: Gas flow distribution in the core and vessel [31].

1.3 The selected material for heat-exchangers in AGR

Given the corrosion environment within the primary and secondary water/steam environments in AGRs, material selection is of unique importance. The temperature in AGR boilers ranges from 150 °C at the feed water inlet to above 600 °C on the hot gas inlet. Low carbon steel is used for components in the AGR boiler. 9Cr-1Mo steel, however, for the intermediate temperature region, was selected as the material in the intermediate temperature evaporation zones [1][34]. 316 steel was selected for the superheater and reheater zone with higher temperature [35], as shown in Figure 1-4. 9Cr-1Mo steel has been used for heat exchanger tubing for many years in AGRs [9][36], operated by EDF Energy and its predecessor companies in the UK [31]. The selection of 9Cr-1Mo steel for power plant applications is based on the low cost, low thermal expansion coefficient, excellent resistance to high temperature oxidation, excellent high temperature creep strength and weldability [37][38]. However, changes in the mechanical and corrosion properties occur as a result of thermal aging and exposure to the gas coolant, CO_2 with controlled low levels of CO, H_2, H_2O and CH_4, prompting study of the mechanisms of concurrent oxidation and carburisation in a high-temperature CO_2 atmosphere.

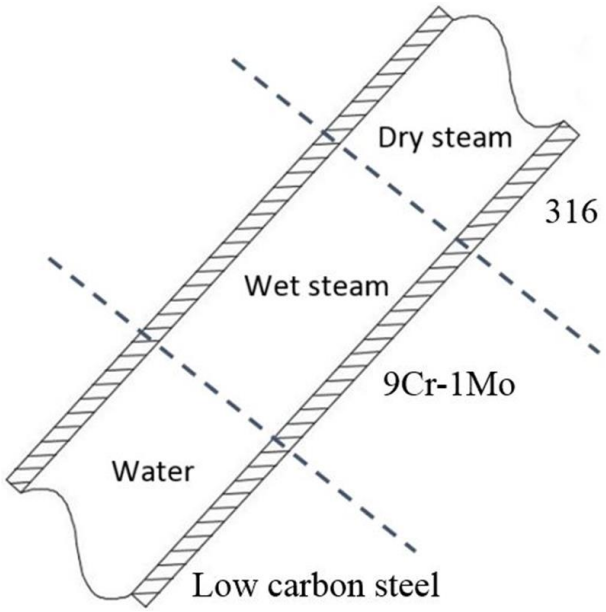

Figure 1-4: Schematic representation of the heat exchanger in an AGR [1]. Finned tube samples were analysed in this thesis.

Recently, consideration of extending the operating life of AGR nuclear plant has revived interest in the durability of 9Cr-1Mo steel [39]. However, the properties of this steel will have changed as a result of thermal aging and exposure to the AGR coolant gas. The overall reaction on outside diameter (OD) of a boiler tube between coolant gas and 9Cr-1Mo steel can be described in two stages:

$$3M + 4CO_2 \rightarrow M_3O_4 + 4CO \qquad 1.1$$

$$4CO \rightarrow 2CO_2 + 2C \downarrow \qquad 1.2$$

where M represents Fe and Cr. Iron diffuses outward resulting in oxidation while C diffuses inward into the metal leading to carburisation, the nature of which may vary from $(Fe,Cr)_3C$ to $(Fe,Cr)_7C_3$ and $(Fe,Cr)_{23}C_6$ [40]. An outer layer of magnetite grows at the gas/oxide interface following the outward diffusion of Fe across the oxide, whilst an inner spinel layer at the oxide/metal interface replaces the space of original metal by the access of molecular oxidant species [40], e.g. CO_2. In most cases, 9Cr-1Mo steel oxidises to form a duplex scale containing magnetite and spinel layers, but a laminated morphology might also be found in some areas of the component, especially where cracks occur. The cracks create paths for CO_2 to gain access to the metal underneath the oxide scale, accelerating oxidation and carburisation. Carbon dioxide reacts with outward diffusing Fe cations; consequently, a new magnetite layer forms.

Chapter 2: Literature review

This chapter introduces the 9Cr-1Mo steel finned tube material studied here. Research has been undertaken on oxidation and carburisation in different environments, studying in particular the microstructure, chemical composition and diffraction patterns obtained from different carbide precipitates. Many of the investigations have sought to understand the trigger of breakaway oxidation. The studies focus on ferritic 9Cr-1Mo steel with relevant mechanics of oxidation and carburisation.

2.1 Background

2.1.1 The microstructure of 9Cr-1Mo steels

As discussed in Chapter 1, 9Cr-1Mo steel was selected for power plant applications based on its many benefits, e.g. low cost, low thermal expansion coefficient, excellent oxidation and corrosion resistance, and excellent high temperature creep strength. Normalising consists of austenitising by annealing above A3 as shown in Figure 2-1, the equilibrium temperature where α-ferrite (BCC) transforms to γ-austenite (FCC), after which it is air cooled. For 9 % Cr steels, martensite (body-centred-tetragonal structure) is produced by rapid cooling [41] while ferrite with fine grains can be produced by sub-critical annealing [42].

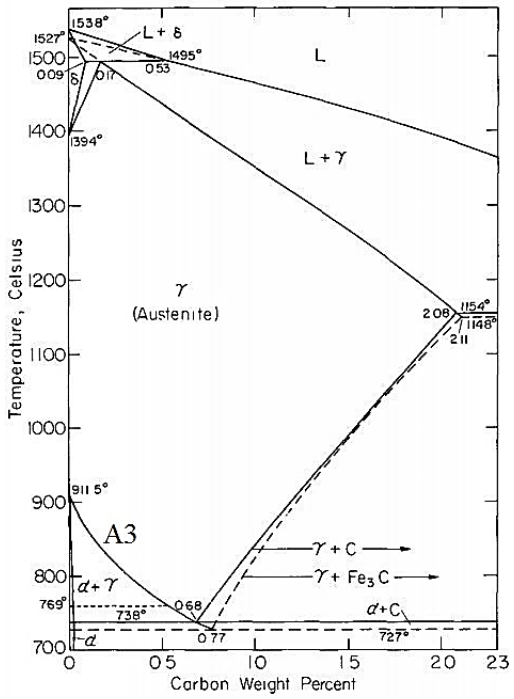

Figure 2-1: Portion of the phase diagram Fe-C, metastable γ-range and system Fe-Fe_3C shown by dashed lines. Curie temperature dotted [43].

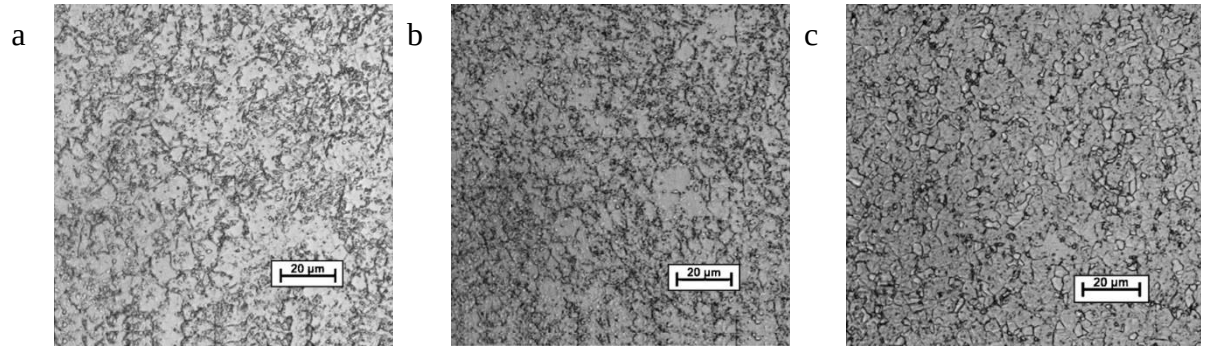

Figure 2-2: Micrographs of cold rolled 9Cr-1Mo steel, recrystallised-annealed at 825 °C for 20 h, furnace cooled (a) 40 %; (b) 80 % cold rolled conditions; and (c) 80 % cold rolled, water quenched [44].

Mungole et al. discussed the recrystalised grain morphology in 9Cr-1Mo steel [44]. The type of microstructure obtained has a direct relationship with the heat treatment. In this case, ferrite formed after being recrystallised-annealed at 825 °C for 20 h followed by furnace cooling exhibited single phase polycrystalline α-ferrite matrix with precipitates embedded in it, as shown in Figure 2-2 [44]. The grain size of steel after annealing ranges from 4 to 6.5 µm, much smaller than that of the virgin sample 15 µm, as discussed in ref [44]. Ferritic 9Cr-1Mo steels have advanced creep resistance and have been used for thick-section components for steam generators operating at temperatures ranging from 550 to 650 °C [45].

Ennis et al [46] showed that ferritic/martensitic 9Cr steels can be hardened by the presence of precipitates embedded in the matrix, which will be discussed later. However, the mean particle diameter increased with the increase of duration time when exposed at 600 and 650 °C in advanced steam power plants.

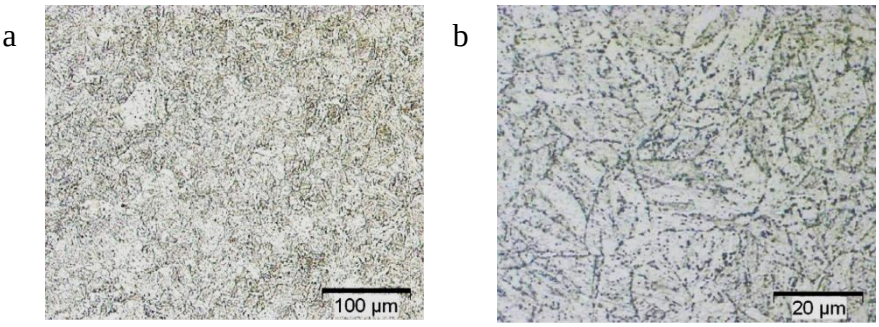

Figure 2-3: Micrographs of G91 showing (a) prior austenitic grains and (b) prior austenitic grain boundaries and lath boundaries [47].

Martensite was formed after normalisation at 1050 °C for 30 min, then air quenching, and tempering for 1 h at 780 °C, as shown in Figure 2-3 where we see prior austenitic grains after heat treatment as well as grain boundaries and lath boundaries formed within grains in a martensitic steel [47]. Martensitic G91 (modified 9Cr-1Mo ASTM Grade 91 [48]) steel has been widely used for conventional energy production industry due to its main advantages compared to austenitic stainless steels: (1) lower thermal expansion, (2) better thermal conductivity, (3) lower material cost and (4) good resistance to stress corrosion [47].

2.1.2 The aging of 9Cr steels and their microstructure

Previous researchers reported that P91 a modified 9Cr-1Mo steel, shows tensile and creep strength properties superior to other ferritic steels [49]. Standard normalising and tempering heat treatments benefit the microstructural stability of 9Cr-1Mo steel. The density of dislocations and the carbide distribution of tempered martensite remain essentially unchanged during subsequent aging at 538 °C for 976 h. However, growth of precipitate and dislocation annihilation occurred under creep conditions at 649 °C, leading to breakaway of the martensite laths and equiaxed substructure [49].

Paul et al. [50] studied the stability of modified 9Cr-1Mo steel aged at high temperatures. They found that the lath structure is retained at certain areas even after long-term aging. However, the growth of coarse precipitates ($M_{23}C_6$, which will be discussed later) and coarsening occurred during aging. Abe et al. found microstructural instability during creep, such as dislocation recovery, carbide agglomeration and the growth of martensite lath sub-grains, resulting in the softening of the examined 9Cr-2W steel [51].

The tungsten alloyed P92 steel (9Cr0.5Mo-1.8W-V-Nb) [52] working at 600 and 650 °C with an initial stress of 120 MPa has been studied by Czyrska-Filemonowicz to underpin the changes of microstructure parameters with respect to exposure time, as shown in Figure 2-4 [52]. It shows that creep was accelerated in the first 1000 h before entering a stable stage, indicating an instability of microstructure in the early stage of creep, and its stability in the following stage.

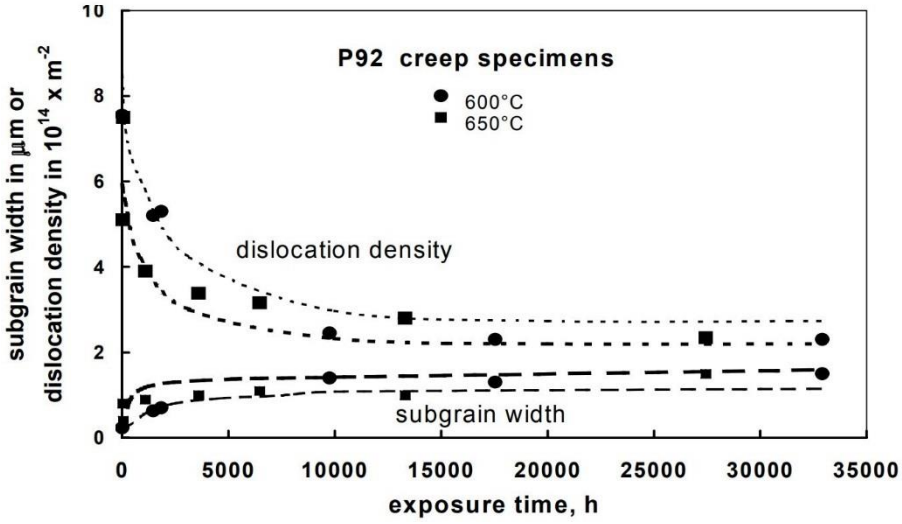

Figure 2-4: Change of subgrain width of martensite laths and dislocation density as a function of exposure time in P92 steel (9Cr0.5Mo-1.8W-V-Nb) creep test at 600 and 650 °C [52].

2.1.3 Role of important alloying elements in 9Cr-1Mo steels

The addition of various alloying elements in steels can be beneficial to physical properties and improve corrosion resistance [53]. Hashimoto et al. have proposed that P, Si, Cr, C, Cu, Ni, Sn, and Mo are beneficial to corrosion resistance while S shows a reverse effect [54]. In this study, Cr, Mo, and Si are the three most important alloying elements and will be discussed separately as follows.

1. Cr: Oxidation resistant alloys usually contain one or more alloying elements to form a stable, slow growing protective oxide on the surface of the metal [55]. The formation of a stable protective oxide layer is the most effective way of controlling oxidation of steel. It hinders the diffusion of iron and reduces the oxidation rate [56]. Chromium is one of the most effective alloying elements to form a stable protective oxide layer [56]. It provides not only oxidation resistance but also affects the hardenability of Fe-Cr steels [57]. Chromium can provide solid solution strengthening, leading to an increase of hardenability of the steel [58]. In ferritic steels which contain Fe, Cr, Mo and C, the Cr is added to provide oxidation resistance [57]. The oxidation behaviour of 9Cr steels depends on the formation of iron and chromium oxides and their mixture due to the insufficiency of Cr for protective chromia (Cr_2O_3) formation [56]. The increase of Cr in the steel to a critical amount of 13 wt. % makes it "stainless", and below this threshold the steel behaves much like iron [59].
2. Mo: In ferritic steels containing Fe, Cr, Mo and C, elevated-temperature strength is provided by a dispersion of Mo_2C. Molybdenum also provides solid-solution strengthening [57]. In steels such as G91, which has a martensitic microstructure containing alloying elements C, N, Nb, V, Cr and Mo, the formation of Cr, Fe, Mo-rich precipitates is promoted, such as Cr_2C and $M_{23}C_6$, in which M contains Fe, Cr and Mo [49]. However, strong carbide-forming elements (e.g. Mo) can also act as a deterrent to particle growth which hinders the coarsening of carbides and improves stability of the microstructure [49].
3. Si: Raman et al. studied the effect of Si on the oxidation of 9Cr-1Mo steel [60]. They found a higher oxidation rate when Si-rich ridges were formed at the grain boundaries and Si depletion occurred in the neighbouring areas, causing lateral growth stresses for spallation at the interface of grain boundary ridges and the adjacent oxide scales. In this study, it was found that fewer Si-rich ridges were formed in the steel with higher Si content at high temperatures, e.g. 500 and 700 °C, giving superior resistance to spallation in the long term. Therefore, a higher Si content gives better oxidation resistance in 9Cr-1Mo steels.

2.2 Oxidation of Fe-Cr steels

The oxidation of steel is a chemical reaction between metal M and oxidant, such as O_2, CO_2, CO, etc. [61]. As discussed in chapter 1, Equations 1.1 and 1.2 represent the processes of oxidation and carburisation of Fe-Cr steel respectively. Under certain conditions, oxidation can proceed rapidly, resulting in a thick oxide composed of multi-layered spinel and magnetite [62].

According to Liu et al. [63], breakaway oxidation of Fe-Cr steel is influenced by sample geometry and commonly occurs at sharp corners or edges. In addition, oxide cracking frequently accompanies breakaway oxidation, but it is unclear whether this is a cause of the breakaway, for example allowing ingress of gas to the oxide/metal interface, or whether it occurs after breakaway initiation due to rapid oxide growth. Figure 2-5a shows a schematic diagram of the oxidation process, while Figure 2-5b shows the stages of oxide growth, including breakaway during exposure at high temperature [40][64]. The curve demonstrates that it follows a parabolic law at the beginning of oxidation, which changes to linear kinetics during the post-breakaway oxidation process. These two processes can be expressed as Equations 2.1 and 2.2 [65]:

$$x^2 = k_r \cdot t \qquad 2.1$$

$$x = k_l \cdot t \qquad 2.2$$

where x is the thickness of oxide; k_r the parabolic rate constant; t the exposure time; and k_l the linear rate constant.

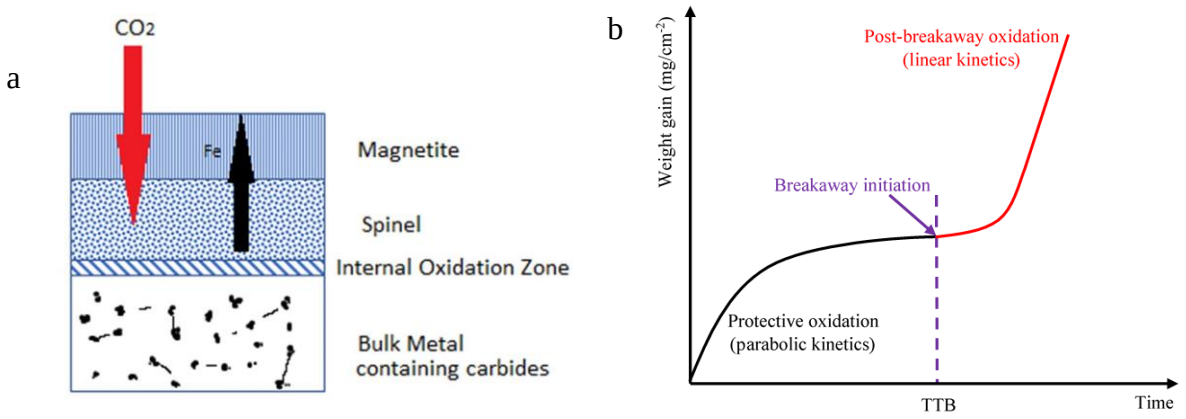

Figure 2-5: (a) Schematic of oxidation process. (b) Weight gain against exposure time for both protective and breakaway oxidation [1]. TTB: time to breakaway [63]. (© Materials at High Temperatures)

2.2.1 Non-breakaway oxidation of Fe-Cr steels

According to Olszewski's study [65], the addition of only 1 wt. % Cr to iron results in a significant increase of oxidation resistance. Ferritic or martensitic steels with 9-12 wt. % Cr, as well as austenitic steel with more than 13 wt. % Cr, show good oxidation resistance when exposed to air at 550-650 °C. The protective oxide scale formed during oxidation has been proved to be Cr-rich spinel with the formula $Fe_{3-x}Cr_xO_4$.

Though FeO is found at the steam side in some steels containing Cr and Mo, e.g. 1.25Cr0.5Mo steel at 585 °C and 2.25Cr1Mo steel at 615 °C, it is hardly to be found in 9Cr-1Mo steel [66]. The protective oxide is mainly composed of two layers: magnetite (Fe_3O_4) and spinel

$Fe_{3-x}Cr_xO_4$ [67][68][69] which is also described as M_3O_4 in some cases (M represents Fe and Cr). Obviously, magnetite is a special form of spinel when x = 0.

The addition of Cr is beneficial to the oxidation resistance of Fe-based alloys. When oxidised at 567 °C in pure oxygen, magnetite (Fe_3O_4) and spinel ($Fe_{3-x}Cr_xO_4$) form as the principal oxides in steels with Cr content in the range of 2-15 wt. % and the oxidation rates decrease with the increase of Cr content [70]. However, the sesquioxides $(Fe,Cr)_2O_3$ form as the principal oxide when the Cr content is above 15 wt. % in Fe-Cr alloys, which are more protective than $Fe_{3-x}Cr_xO_4$ spinel and magnetite [71][72]. Newcomb et al. [73] proposed that in low oxygen partial pressures, the dominant diffusion mechanism changes from the vacancy mechanism to interstitial ion diffusion, encouraging the formation of M_3O_4.

From a thermodynamic aspect, the free energy change is the driving energy of the reaction between metal and oxide. The oxide is formed only when the free energy change is less than zero [61]. Standard free energies can be obtained following Equation 2.3.

$$\Delta G_T = \Delta H + T\Delta S \qquad 2.3$$

As discussed by Newcomb et al. [73], ΔH, ΔS and T (temperature) for the formation of magnetite at the temperature range of 298-700 K can be obtained from the data in Table 2-1. Therefore, the free energy change of the first reaction in Table 2-1 ranges from 13953 to 28023 J/K, -445083 to -179763 J/K for the second reaction and -209572 to -85354 J/mol for the third, at the temperature ranging from 298 to 700 K. The results indicate that the oxide should not be formed following the first reaction while the oxide Fe_3O_4 can be formed following latter two reactions.

Table 2-1: Standard free energies change of reaction $\Delta G_T = \Delta H + T\Delta S$ [73].

Reaction	*ΔH (J/K)*	*ΔS (J/K)*	*Temperature range (K)*
$3Fe + 4CO_2 = Fe_3O_4 + 4CO$	*38453*	*-35*	*298-700*
$3Fe + 4CO = Fe_3O_4 + 4C$	*-641763*	*660*	
$3Fe + 2CO_2 = Fe_3O_4 + 2C$	*-301654*	*309*	

ΔH and ΔS represent the change of enthalpy and entropy, respectively.

The less-protective oxidation is comprised of an outward growth magnetite scale as well as an inward growth spinel scale relative to the original metal surface of ferritic 9Cr-1Mo steel [74]. Figure 2-6 shows two micrographs of oxide formed after 1000 h oxidation in air and 1 % CO-CO_2. A more protective outward growth oxide was formed in the location shown by the arrow in the former micrograph, as well as the less-protective duplex oxide adjacent to it when oxidised in air. When oxidised in 1 % CO-CO_2, an obvious duplex oxide containing an outward growth magnetite (Fe_3O_4) and inward growth spinel (M_3O_4 or $Fe_{3-x}Cr_xO_4$) was formed in which the original metal surface converted to magnetite/spinel interface during oxidation. The growth

of protective oxide is limited by the diffusion rate of Fe and Cr cations, giving a parabolic kinetic [40]. In these two cases, the outward growing columnar Fe_3O_4 was found to be non-porous while the fine grained M_3O_4 was demonstrated to be porous. In the formation of non-breakaway oxidation, no carbon or carbides were observed in either outward growth scale Fe_3O_4 nor inward growth oxide M_3O_4. However, carbon was present in the breakaway oxide, as discussed in Newcomb's work published in 1985 [75].

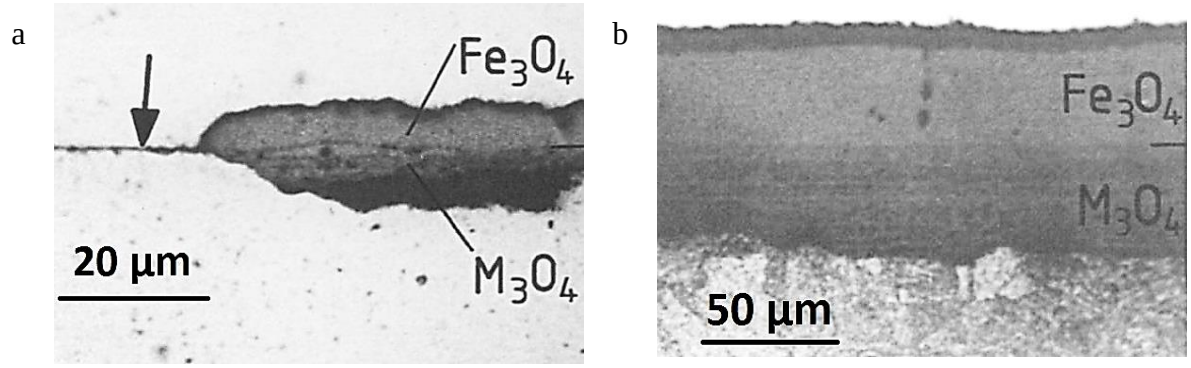

Figure 2-6: The oxide formed in 9Cr-1Mo steel after 1000 h oxidation at 600 °C in (a) air; (b) 1 % CO-CO_2 [74].

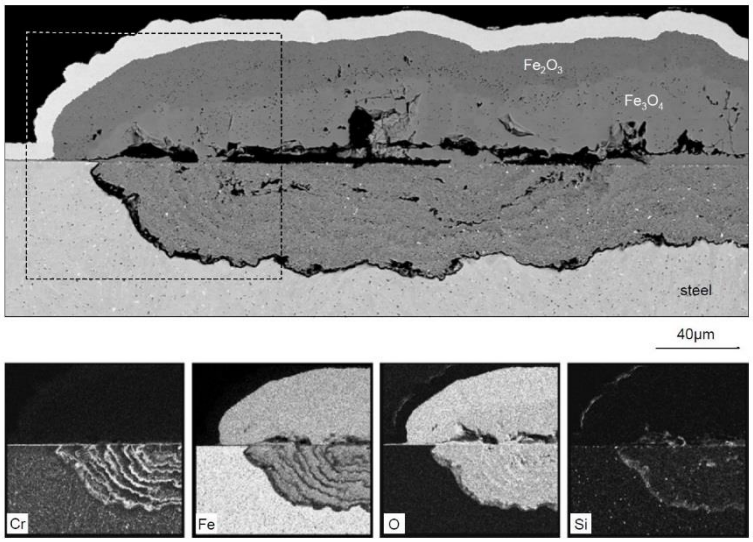

Figure 2-7: SEM images of the cross section (upper image) and corresponding X-ray element mapping from the marked area (lower images) of P92 steel after 1000 h oxidation in Ar/CO_2 at 700 °C [65].

The microstructure and chemical composition of protective oxide from P92 steel is shown in Figure 2-7 [65]. The sample was oxidised in Ar/CO_2 at 700 °C for 1000 hours. It was found that a Fe_2O_3 layer was formed above a magnetite layer, beneath which was a spinel layer. According to x-ray element mapping, Cr-rich spinel exhibits a stringer morphology, with Cr/Si-rich and Cr/Si-depleted bands formed alternately. It illustrates that the composition of spinel is not stable. Zurek et al. also studied the formation of spinel in 9-12% Cr steels [76]. They proposed that the stringer morphology of spinel demonstrates rapid Cr diffusion from the bulk metal in the direction of the oxide scale.

Olszewski demonstrated that the formation of Cr-rich spinel relates to the Si content, which is easily reduced to "zero" level, hence inhibiting the presence of a Cr/Si-rich layer [65]. This leads to a Cr-depleted layer beneath. This process is repeated as long as there is sufficient Cr and Si provided from the bulk metal. However, Zurek has a different explanation for the formation of stringer spinel [76]. He proposed that the preferential oxidation of Cr leads to Cr depletion beneath the Cr-rich layer. With continued Cr depletion during oxidation, Cr-rich spinel could not remain stable. An Fe-rich layer is subsequently formed. The repetition of this process results in the formation of a stringer microstructure of spinel, with Cr-rich and Cr-depleted spinel formed alternately. It can be inferred that the formation of spinel is a repeated process of Cr-rich and Cr-depleted band formation. Therefore, the oxidation rate is strongly influenced by the composition of steels, specifically the Cr concentration, which plays a vital role in the formation of protective oxide.

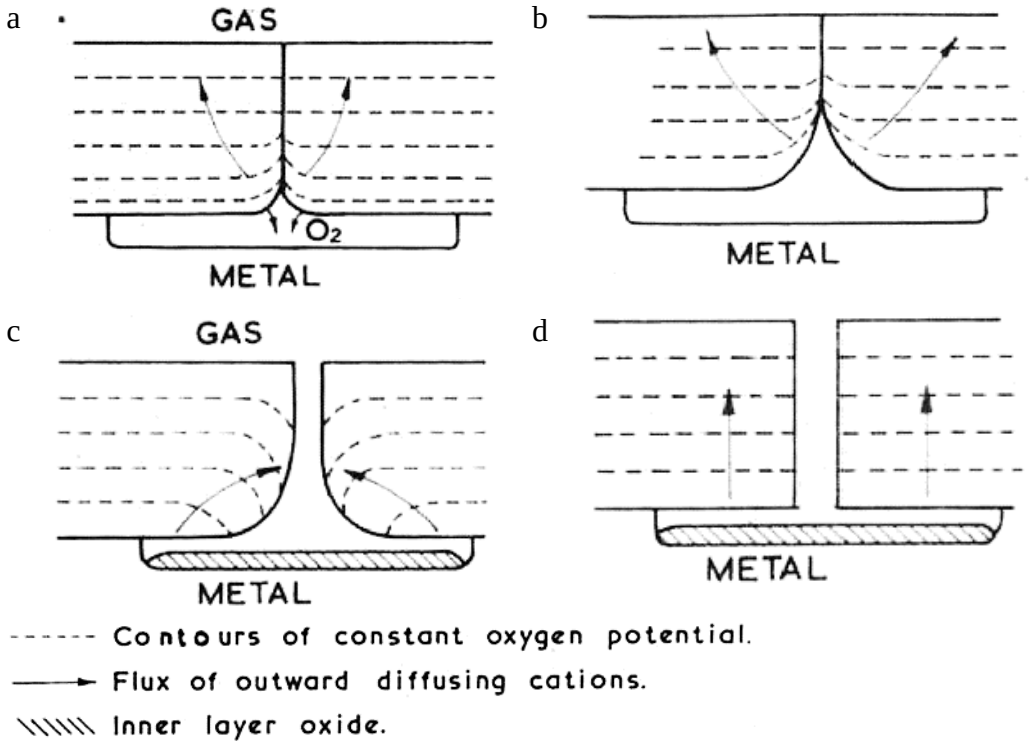

Figure 2-8: Mechanism of oxide growth from Gibbs and Hales: (a) and (b) nano-channel opens up by anisotropic dissociation; (c) and (d) channel heals to equilibrium size. Dashed lines and arrows represent oxygen equipotential and outward diffusion cations respectively [69][77].

Martinelli et al. investigated the oxidation mechanism of 9Cr-1Mo steel by liquid Pb-Bi eutectic alloy [69]. They introduced the concept of nano-channels into the mechanism of oxide formation, according to the concept of micro-channels, to illustrate the mechanism of oxidation proposed by Gibbs and Hales, as shown in Figure 2-8 [77]. The oxygen can be transported in several ways: diffusion via oxide lattice, by grain boundaries, and through nano-channels in the form of oxygen molecules. The latter is the most cited in the literatures [77][78][79]. According to these authors, the oxidant is considered to be transported via nano-channels inside

the scale to the oxide/metal interface. Figure 2-8 illustrates the formation of a nano-channel: the driving force of channel formation is the difference between oxygen pressure in the void formed in oxide scale and the external gas pressure. The continued outward solid-state diffusion of metallic cations, e.g. Fe, leads to a void belt beneath the oxide scale and the porous inner oxide scale, which is the freshly forming oxide formed at the void belt, as shown in Figure 2-8. The diffusion of cations in different directions results in the formation of the nano-channel, which gives external gas access to the metal beneath [77].

It is now seen that fresh Fe_3O_4 is formed at the gas/oxide interface by the outward flux of Fe cations in a duplex oxide scale [1][80]. The inward diffusion of oxygen reacts with Fe and Cr to form $Fe_{3-x}Cr_xO_4$ at the oxide/metal interface. This is consistent with the original gas/metal interface before exposure being the magnetite/spinel interface after exposure [69][80][81].

Gibbs and Hales proposed that the process of oxidation is controlled by defect diffusion, e.g. vacancies [77]. Muller et al. also found that a pore belt is present beneath the oxide scale and above the bulk metal, as shown in Figure 2-9 [82]. Martinelli et al. proposed that nano-cavities are formed during the diffusion of cations at the oxide/metal interface. Considering that nano-cavities are formed by vacancy segregation, this provides spaces for oxidation. The oxidant diffusing through the nano-channels connects with surfaces formed by vacancy clusters. It oxidises the metal inside the space made by vacancy cluster accumulation, i.e. nano-cavities. Therefore, fresh porous spinel is formed at the location of the cavities, which is controlled by metallic vacancies [77]. This is named the "available space model", as shown in Figure 2-10 [80]. As a consequence, it is proposed that outer layer oxide growth, which is magnetite in duplex oxide scale, provides the driving force for outward iron diffusion which makes metallic vacancies, further influencing the formation of nano-cavities [80][81].

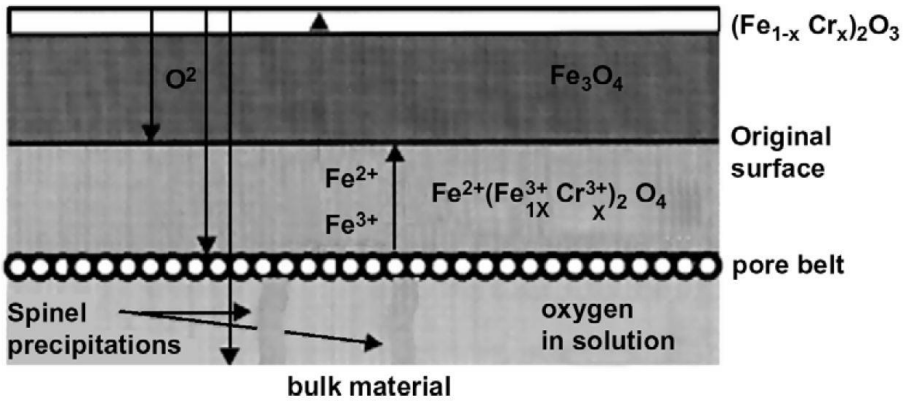

Figure 2-9: Steel oxidation mechanism in liquid lead proposed by Muller et al. [69][82].

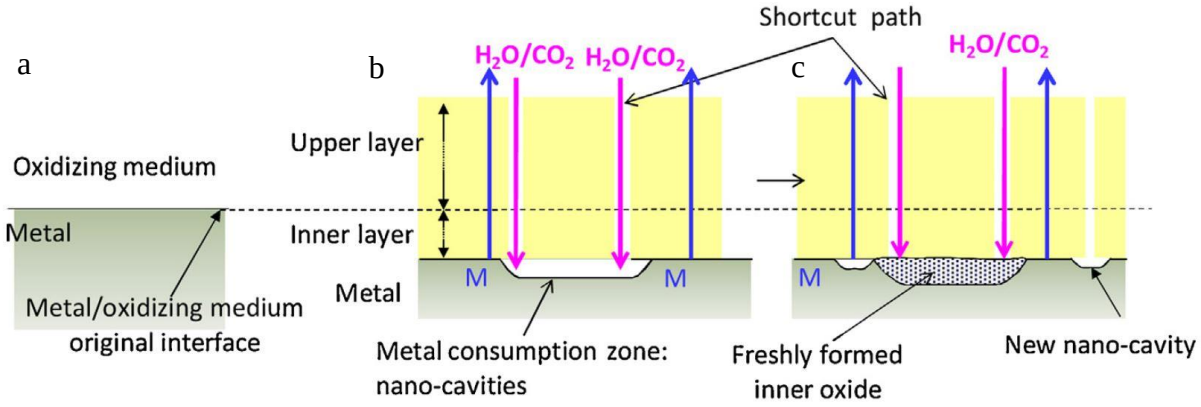

Figure 2-10: Schematic drawings of "available space model": (a) metal before exposure; (b) diffusion of cation leading to metal consumption zone in the form of nano-cavities and molecular oxygen diffusing through nano-channels; (c) oxidation inside nano-cavities to form fresh spinel by vacancy accumulation [80].

2.2.2 Breakaway oxidation of Fe-Cr steels

"Breakaway" oxidation is defined as a rapid acceleration of the reaction rate, which occurs in Fe-Cr steels [83]. It relates to the rapid growth of oxide after the formation of protective Cr-rich oxide in the early stage of oxidation process. It is found that the increase of Cr content in the Fe-Cr steels hinders the breakaway oxidation by forming Cr-rich oxide scale [84]. However, the increase of water vapour accelerates the onset of breakaway oxidation by accelerating nucleation of oxide nodules on the steel surface [83].

Gong et al. has studied breakaway oxidation in ferritic 9Cr-1Mo steel [85]. The assessment was applied at the fin centre 0.5 mm from the fin tip. The scalebar of carbon in at. % shows that carbon (mainly from carbides) is mainly distributed beneath the oxide scale and decreases with increase of depth. Their experimental results include plots of weight gain as a function of exposure time at different temperatures, as shown in Figure 2-11 [85]. It can be seen that samples exposed at 580 °C with 300 vppm H_2O, are still in parabolic kinetics even after 80 kh of exposure. Thus, it is impossible to estimate the time to breakaway in this case. The weight gain plot shows that samples exposed at 600, 620 and 640 °C transfer from parabolic kinetics to linear at approximately 20, 3 and 2 kh of exposure, respectively, which are also the time to breakaway (TTB) at these temperatures. The authors proposed that the carbon deposition is a trigger of breakaway oxidation which relates to the saturation of carbon in the metal. This will be discussed later.

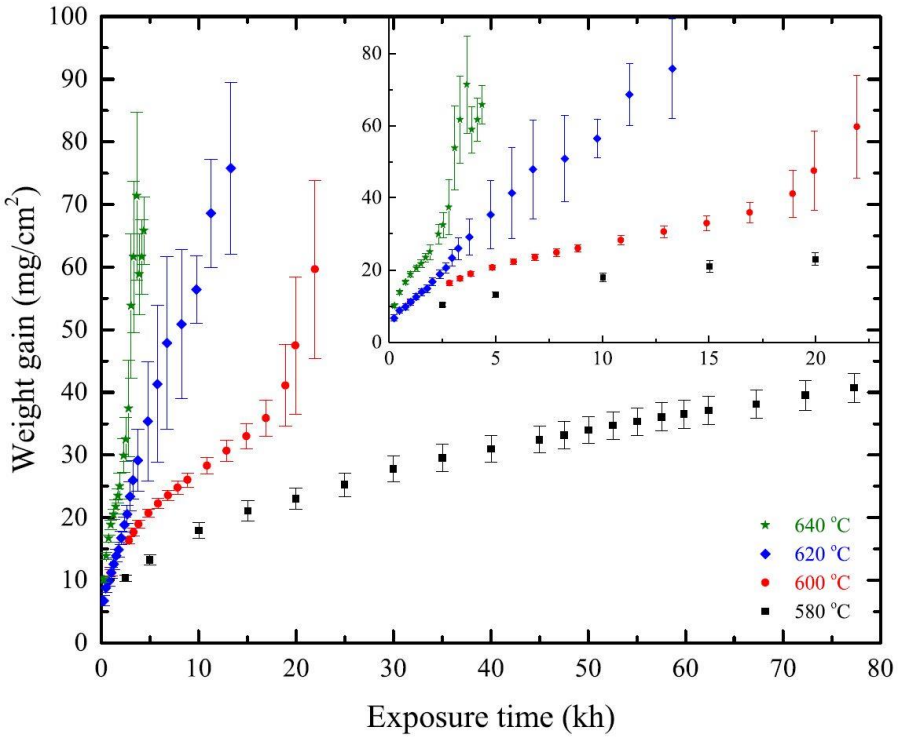

Figure 2-11: Weight gain changes of experimental ferritic 9Cr-1Mo samples exposed at 580 (black), 600 (red), 620 (blue) and 640 °C (green) with gas composition of 100 vppm H_2, 300 vppm CH_4, 1 vol % CO, 300 vppm H_2O and balance CO_2 at gas pressure of 600 psi [85].

Elemental distribution was mapped in the internal oxidation zone (IOZ) layer and adjacent oxide in a non-breakaway location from a breakaway initiation sample exposed at 600 °C for 19924 h, as shown in Figure 2-12 [85]. A duplex oxide was formed in the location examined as well as the IOZ layer. As discussed previously in section 2.1.2, the spinel was formed at the oxide/metal interface in the duplex model. Hence, the IOZ layer and the adjacent oxide were examined in ref [85].

The IOZ layer is mainly comprised of O and Cr, and is Fe-depleted compared with oxide and metal. There are some small dark features in the oxide and IOZ layer which were shown to be Si-rich particles according to EDS. The map of Cr shows the Cr-rich locations to correspond to Fe-depleted dark spots in the oxide layer and O-rich locations in the IOZ layer. The distribution of Mo is consistent with Cr. The Cr, Mo-rich locations are consistent with residual precipitates in the oxide and IOZ layers and carbides in the metal. The big block of dark features in the oxide correspond to C-rich locations, indicating the presence of deposited carbon in the oxide layer. These features are highlighted in Figure 2-13 [85].

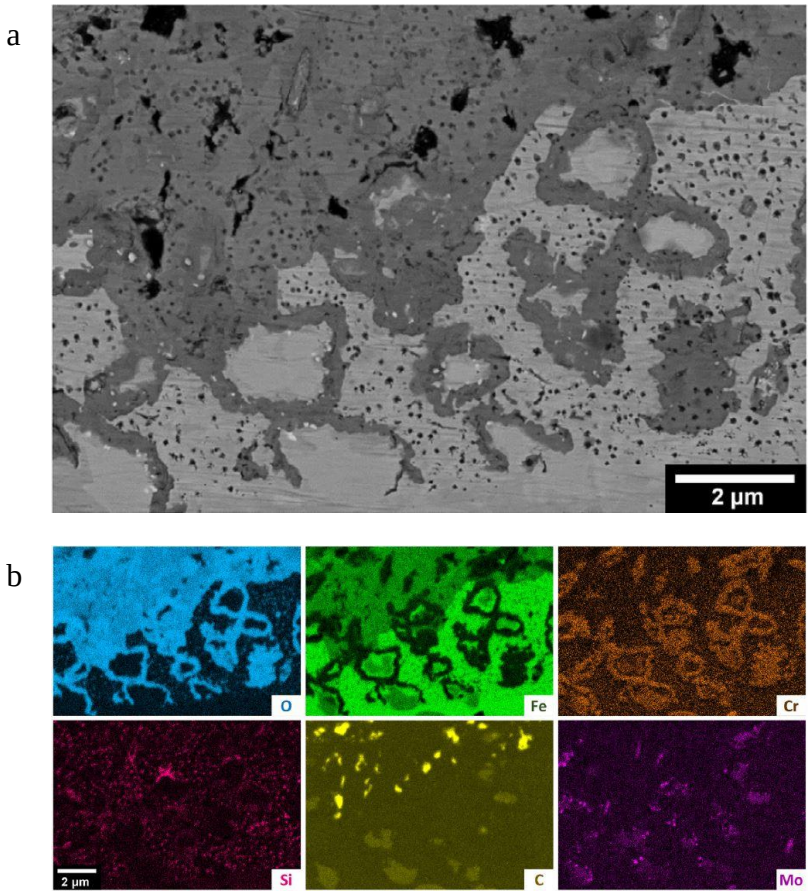

Figure 2-12: (a) Backscattered SEM image from a non-breakaway location containing the IOZ in an experimental 9Cr-1Mo sample exposed at 600 °C for 19924 h and (b) corresponding EDS maps showing elemental distributions [85].

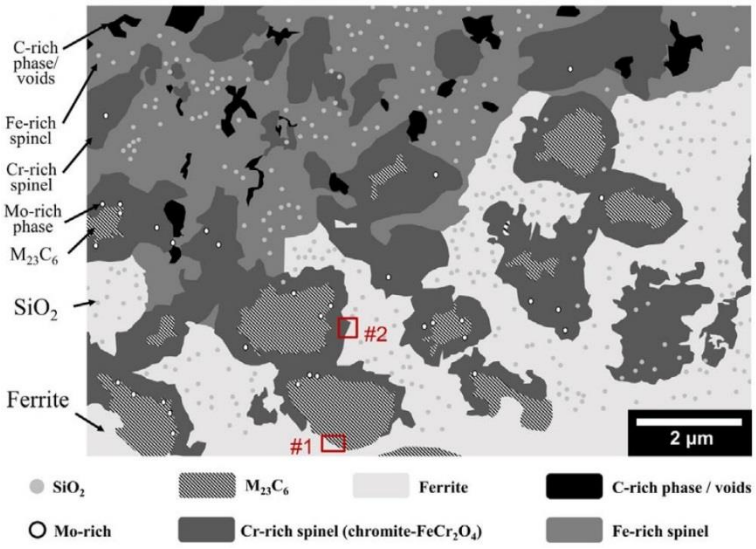

Figure 2-13: Corresponding map with the identified phases present in Figure 2-12 [85].

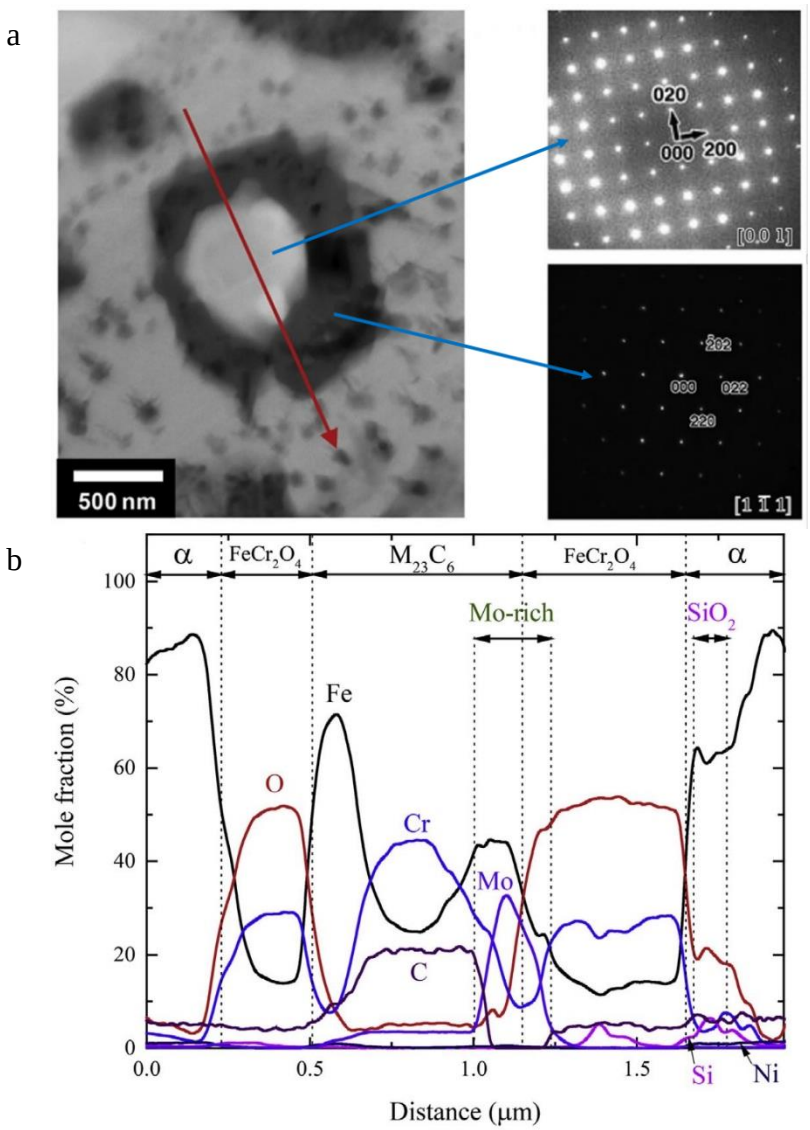

Figure 2-14: (a) TEM dark field image from an area in the IOZ and selected area diffraction (SAD) pattern from the core and the shell; (b) elemental profiles following the red arrow shown in the TEM image [85].

Carbide precipitates present in the IOZ layer surrounded with oxide were identified using TEM as shown in Figure 2-14. The selected area diffraction (SAD) patterns show that the core is $M_{23}C_6$ while the surrounding shell is $FeCr_2O_4$, which is considered as the most stable composition of spinel [85][68]. The elemental profiles following a path across both core and shell, as shown by the red arrow in Figure 2-14a, are consistent with results from TEM diffraction patterns. The work is also indicative of the presence of Mo-rich precipitate in the $M_{23}C_6$ carbide.

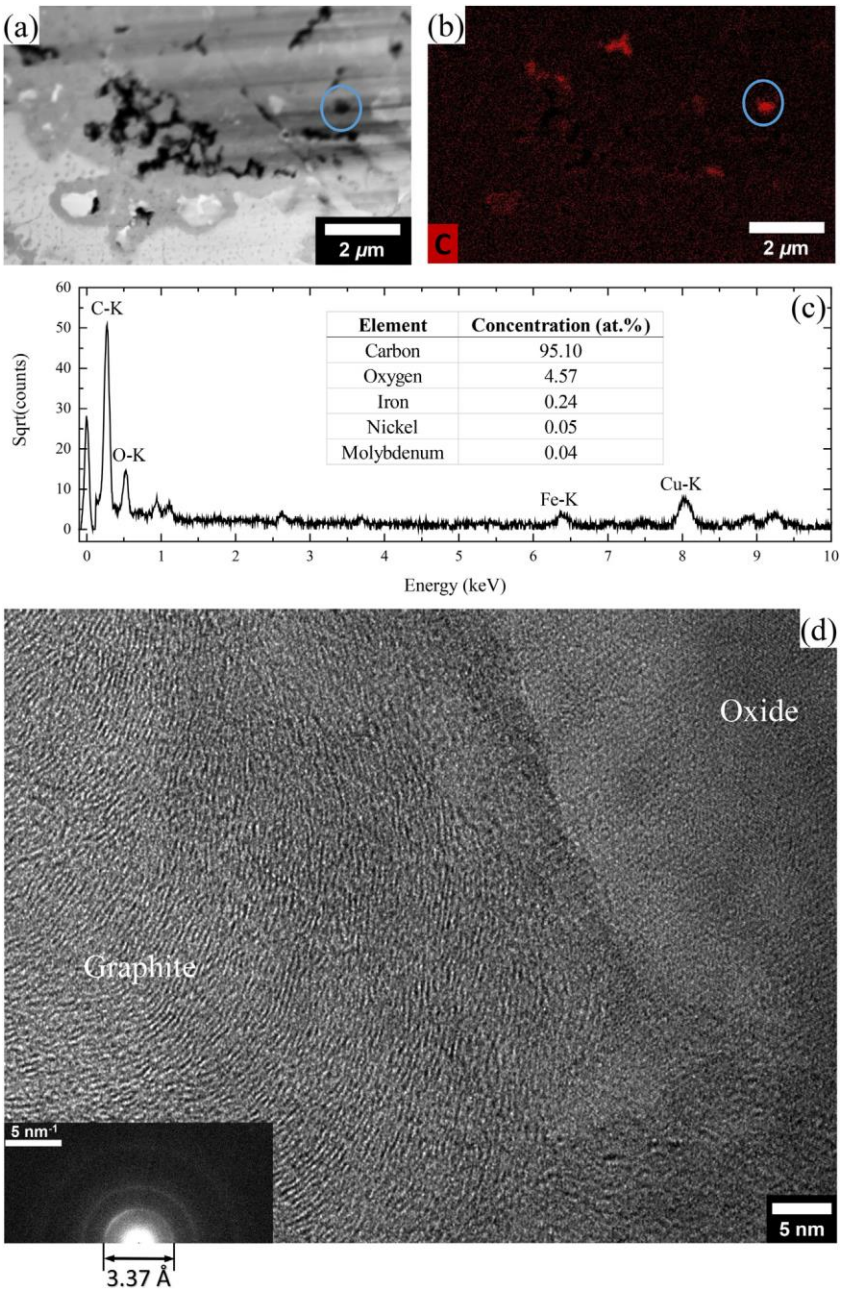

Figure 2-15: (a) TEM dark field image and (b) EDS carbon mapping from the IOZ; (c) EDS spectrum taken from carbon-rich locations; (d) high resolution TEM image of oxide/graphite interface with selected diffraction pattern from the graphite region [85].

Figure 2-15 shows a TEM image of the IOZ layer and adjacent oxide and an EDS map of the corresponding area. Blocky dark features in the oxide show high carbon concentration, indicating the presence of deposited carbon in the oxide during oxidation in CO_2-based gas. Diffraction patterns show that the lattice parameter of this deposited graphite is 3.37 Å with a face-centred cubic structure [85].

Three simple models were established by Robertson to illustrate the changes from protective single layer scale in the very beginning stage of oxidation to the less protective duplex scale

and then the non-protective breakaway scale, as shown in Figure 2-16 [40]. The growth of single layer scale and duplex scale has been discussed in section 2.1.2. Here, a breakaway scale with a laminated morphology from 9Cr steel will be discussed, as shown in Figure 2-17. This type of oxide was formed following linear kinetics (Equation 2.2) after time to breakaway, as seen in Figure 2-5b. The fresh oxide is formed at the oxide/metal interface.

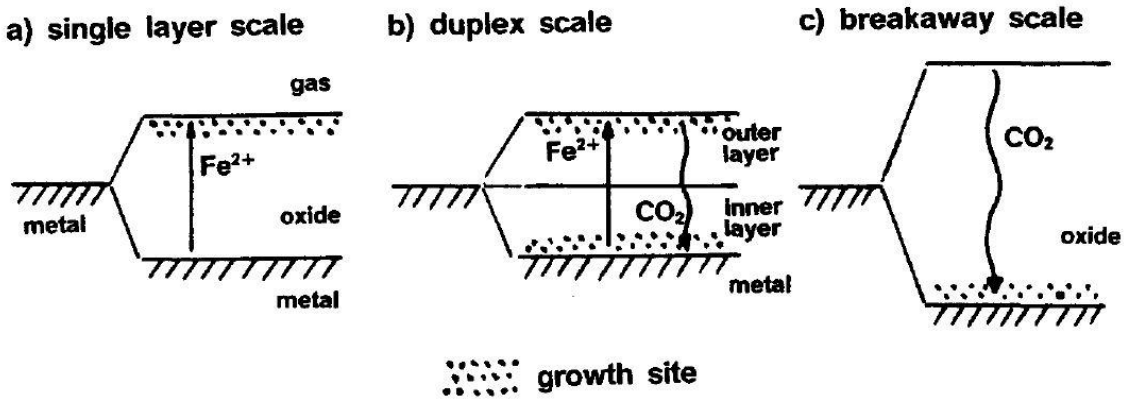

Figure 2-16: Model with the growth sites of (a) single layer; (b) duplex layer and (c) breakaway scales [40].

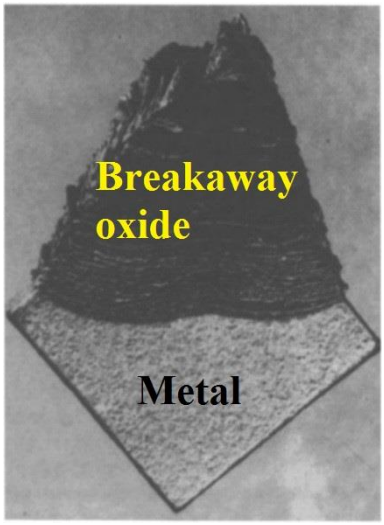

Figure 2-17: A breakaway scale in 9Cr steel [40].

Robertson, Rowlands et al. and Gibbs proposed that breakaway is caused by the deposition of carbon in the oxide scale, which leads to a porous and loose freshly formed oxide which allows continuous access of the oxidant gas, e.g. CO_2, to the metal surface beneath [40][32][78]. Breakaway occurs when continuous percolation paths form across the oxide scale with increase of porosity. In this case, the oxidation rate is limited by the interfacial reaction rate, which then gives linear kinetics.

During the formation of duplex oxide, the inner layer oxide is formed according to the reaction described by the reaction $3Fe + 4CO = Fe_3O_4 + 4C$, as shown in Table 2-1, which produces deposited carbon when the steel is oxidised by CO_2 [40][32]. The deposited carbon, which is

in the form of graphite, is insoluble in the oxide and tends to coat the oxide grains and prevent the formation of boundaries between them.

Olszewski mentioned that commercial alloys are usually exposed under non-isothermal conditions, which causes scale cracking, delamination or spalling in the process of oxidation [65]. The oxide may break down locally due to the oxide growth or thermally induced stress. Some of the oxidation behaviours during exposure at high temperatures are depicted schematically in Figure 2-18. It shows that non-protective and breakaway oxidation exhibit linear kinetics in the plot of weight gain as a function of exposure time, a similar trend to the post-breakaway plot of oxide thickness versus exposure time shown in Figure 2-5b. Olszewski's investigation also show that a chromium content of 9-12% is insufficient to form a protective chromia scale when exposed to a water vapour containing gas. Fast growing Fe-based oxides are formed after the protective oxidation stage due to the absence of the protective chromia scale.

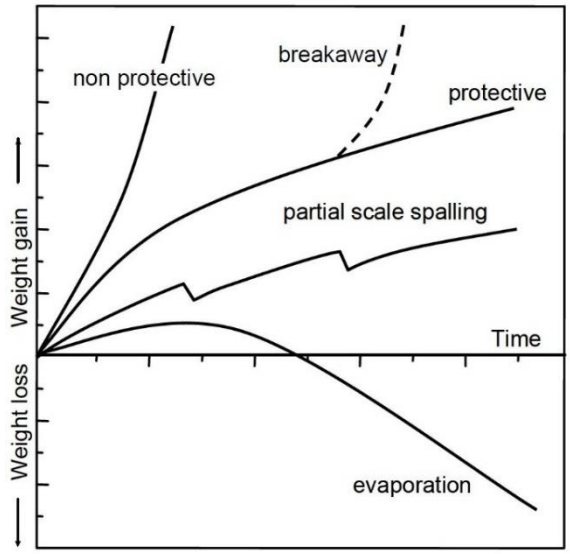

Figure 2-18: Different oxidation kinetics encountered in real metal and alloy systems, especially occurring during long term, discontinuous oxidation [65][86].

A laminated scale was formed by the fast-growing oxide in the breakaway oxidation when continuous percolation paths were formed. In this oxidation stage, oxide formed throughout the oxide scales as well as at the metal surface exposed to oxidant. The Cr-rich and Fe-rich oxide layers formed alternately [74].

Roberson suggested that the Boudouard reaction is the dominant carbon deposition reaction occurring at the pore bases [40]. The deposition of carbon in the oxide initiates breakaway oxidation. It is found that the hydrogen produced from water vapour in the CO_2-based gas accelerates breakaway oxidation by the reverse water gas reaction shown in Equation 2.4 [40]. As proposed by Gong et al., the deposited carbon is a trigger for breakaway oxidation [85].

Thus, samples are more susceptible to enter breakaway oxidation when exposed to wet CO_2 gas than to dry CO_2 gas, which is consistent with the studies in ref [87] and [88].

$$CO + H_2 = H_2O + C \qquad 2.4$$

Olszewski compared the results obtained from different materials after exposure to H_2O- and/or CO_2-containing gases. Two mechanisms were used to explain the conversion from protective into non-protective oxide. A mechanism proposed that hydrogen dissolved in the steel promotes the internal oxidation of the Cr-rich protective oxide formation in a H_2O-containing atmosphere. The second mechanism proposed that the reduction of Cr flux toward the surface impedes the formation of a protective Cr-rich oxide in a dry CO_2-containing atmosphere. Therefore, a wider internal oxidation zone was found in a H_2O-containing gas [65].

Rahmel and Tobolski proposed that voids formed at the oxide/metal interface and within the oxide scale are due to vacancy condensation bridged by mixtures of H_2-H_2O or CO-CO_2 in breakaway oxidation [89], which explains the mechanism for suppression of the formation of chromia-based scale. The oxygen partial pressure in a void near the oxide/metal interface is very low when exposed to dry gas or air. The rate of oxygen transfer to the inner surface of voids is extremely small. Hence, there is sufficient time for Cr to diffuse from the matrix to the void/metal interface to form the protective Cr-rich oxide. In this way, formation of Cr-rich oxide leads to void healing. However, in CO_2- and/or H_2O-rich gases, oxygen transfer in the void is orders of magnitude higher than that in dry gas due to the CO_2 and H_2O molecules, which leads to the suppression of void healing and the growth of non-protective Fe-rich oxides due to the insufficient time for Cr diffusion to the oxide/metal interface [65].

It was proposed by Essuman et al. that hydrogen dissolved in the metal promoted the oxidation of Cr, which is essential for protective oxide (Cr_2O_3) formation [90][91]. This effect can be explained by considering the H-O-H_2O equilibrium at the metal surface, i.e. when the hydrogen concentration is reduced by rapid inward diffusion the oxygen concentration dissolved in the metal will be increased eventually, resulting in a higher inward flux of oxygen to form the internal Cr oxide embedded on the metal (IOZ). Thus the Cr is tied up in the IOZ, leading to a reduction of the outward diffusion Cr cations, and an Fe-rich oxide scale is formed because of the Cr-depleted steel matrix. This is demonstrated in Figure 2-19, where it is seen that P92 steel has much thicker IOZ after exposure to the gas with H_2O than without H_2O [65]. This could be explained by enhanced oxygen diffusion in the alloy due to hydrogen uptake. However, this lock-up of Cr in the IOZ scale results in a reduction of Cr diffusing to the oxide scale, exacerbating the formation of Fe-rich spinel which is usually present in multi-layered and laminated oxide in the breakaway initiation and post-breakaway samples.

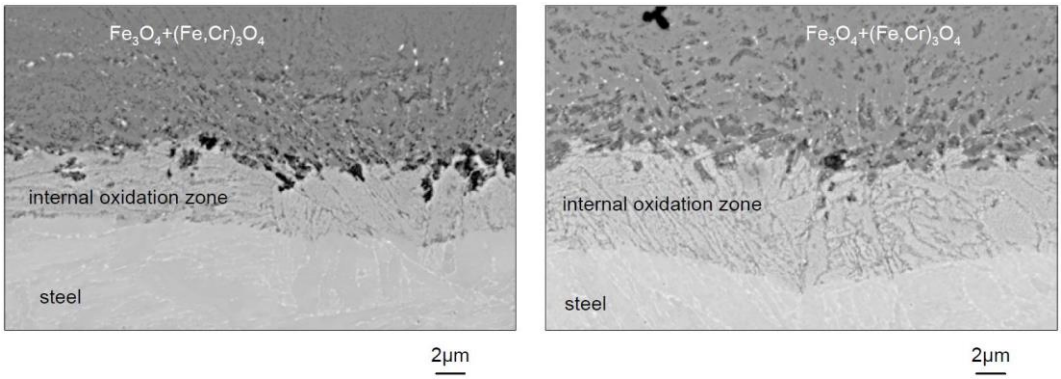

Figure 2-19: SEM images of the cross sections showing the IOZ formed in martensitic P92 during 1000 h exposure to Ar/CO_2 (left) and CO_2/H_2O (right) at 550 °C [65].

Another mechanism that impedes the formation of protective Cr-rich oxide is the Cr activity in CO_2-containing atmospheres. The carburisation of martensite steel would decrease the activity of Cr in the matrix by the formation of internal Cr-rich carbides and consequently decrease the driving force for Cr diffusing outward to the surface. Thus, Fe-rich oxide forms due to the suppression of protective Cr-rich oxide formation. The internal carbides may eventually be converted into internal oxide as the local oxygen potential increases after longer exposure times [92][93].

2.2.3 Phase identification

The oxides formed in 9Cr-1Mo steel after exposure to CO_2-based gas are mainly comprised of three types: Cr_2O_3 in the IOZ scale, spinel and magnetite in oxide scale. Carbon is also deposited during oxidation based on the previous discussion. McCarty has investigated spinel of different compositions with Raman spectroscopy, as shown in Figure 2-20 [94]. The results are summarised in Table 2-2. Magnetite Fe_3O_4 is a special type of spinel when x equals zero in the formula $Fe_{3-x}Cr_xO_4$. Its spectrum has a weak peak at 543 cm^{-1}. The substitution of Cr for Fe causes a reduction in the intensity of this band when x is no more than 0.8, e.g. this peak is not detectable for $Fe_{2.2}Cr_{0.8}O_4$. However, when more Cr is introduced, the band reappears and becomes broad and relatively intense as seen from the spectrum of $Fe_{1.4}Cr_{1.6}O_4$ in Figure 2-20. The A_{1g} mode main peak of spinel ranges from 671 to 686 cm^{-1}, which can be observed in spectra from all six types of spinel oxide.

Gheno et al. made a plot of Raman shift as a function of x in $Fe_{3-x}Cr_xO_4$, as shown in Figure 2-21 [83] and Table 2-2 [94]. The two peaks at around 550 and 675 cm^{-1} are assigned to the T_{2g} and A_{1g} modes respectively while $FeCr_2O_4$ has a peak at 1265 cm^{-1} and a broader peak at 1357 cm^{-1}, which are a combination of different symmetries [94]. The spinel $Fe_{1.4}Cr_{1.6}O_4$ also has a weak broad peak at 1335 cm^{-1}. Therefore, it is possible to obtain the composition of spinel from the Raman shift of the A_{1g} mode, indicating Raman to be a useful method in oxide type (composition) identification.

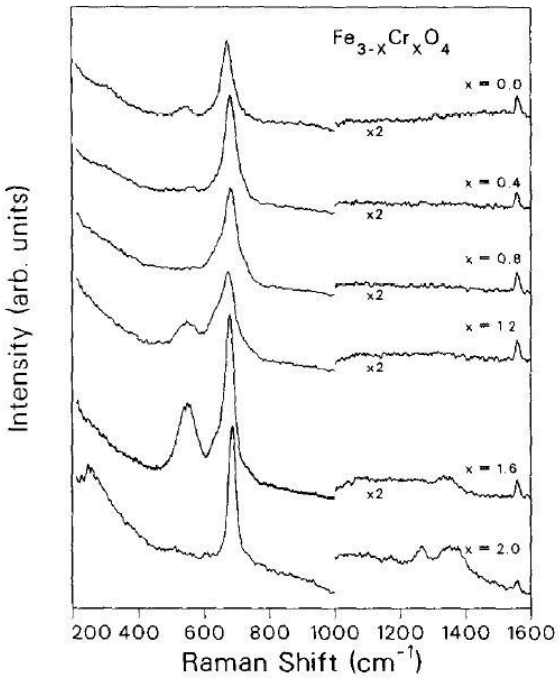

Figure 2-20: Raman spectra of spinel: $Fe_{3-x}Cr_xO_4$ with x = 0.0, 0.4, 0.8, 1.2, 1.6 and 2.0 using a 514.5 nm laser. Peak at 1558 cm^{-1} is from atmosphere O_2 [94].

Table 2-2: Observed Raman bands and lattice parameter for each type of spinel [94].

Spinel type and lattice parameter (Å)	*Raman shift of peak position (cm^{-1})*				
	T_{2g}	E_g	A_{1g}	/	/
Fe_3O_4, a = 8.398	*542*	*/*	*671*	*/*	*/*
$Fe_{2.6}Cr_{0.4}$, a = 8.396	*562*	*/*	*682*	*/*	*/*
$Fe_{2.2}Cr_{0.8}O_4$, a = 8.398	*/*	*/*	*681*	*/*	*/*
$Fe_{1.8}Cr_{1.2}O_4$, a = 8.408	*548*	*636*	*674*	*/*	*/*
$Fe_{1.4}Cr_{1.6}O_4$, a = 8.398	*550*	*636*	*679*	*/*	*1335*
$FeCr_2O_4$, a = 8.381	*/*	*/*	*686*	*1265*	*1357*

A nonpolarized Raman spectrum was obtained from Fe_3O_4 under ambient conditions, as shown in Figure 2-22 [95]. Four peaks present at 193, 306, 538 and 668 cm^{-1} were assigned to $T_{2g}(1)$, E_g, $T_{2g}(2)$ and A_{1g} symmetry, respectively. However, the weak peak at 193 cm^{-1}, and another at 420 cm^{-1} which was absent in this reference, was not often reported [96][97]. It was proposed by Dunnwald and Otto [98] that the presence of a peak at 298 cm^{-1} suggests the beginning of oxidation, because this belongs to the characteristic signature of haematite rather than magnetite [94][99][100][101].

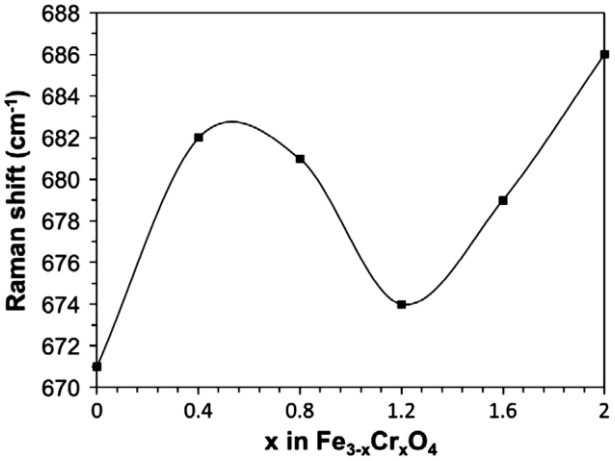

Figure 2-21: Raman shift of the A_{1g} mode of Fe-Cr spinel oxide versus composition [83].

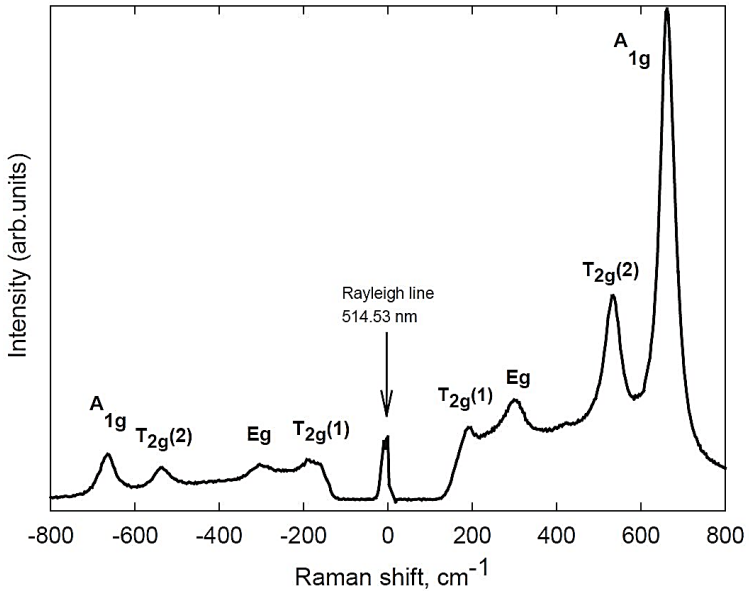

Figure 2-22: Raman spectrum of Fe_3O_4 with the symmetry assignment [95].

The Raman peak at the IOZ location from the previous discussion has two peaks at 550 and 610 cm^{-1} respectively, as shown in Figure 2-23, which is consistent with the two peaks indicative of the presence of chromia (Cr_2O_3).

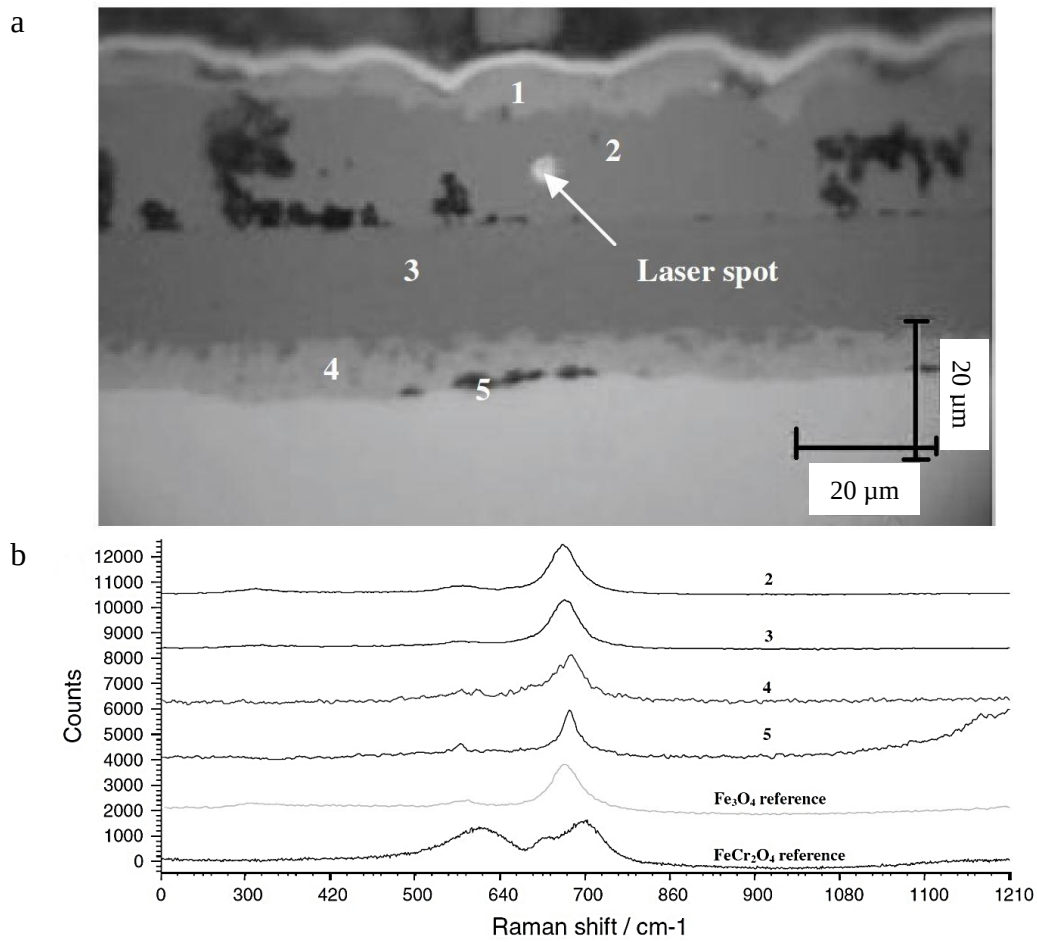

Figure 2-23: (a) SEM image of 9Cr-1Mo sample exposed to flowing CO_2 at 550 °C and 1 atm for 1000 h with different locations examined by Raman spectroscopy; (b) Raman spectra of different locations of the scale marked in (a) [68].

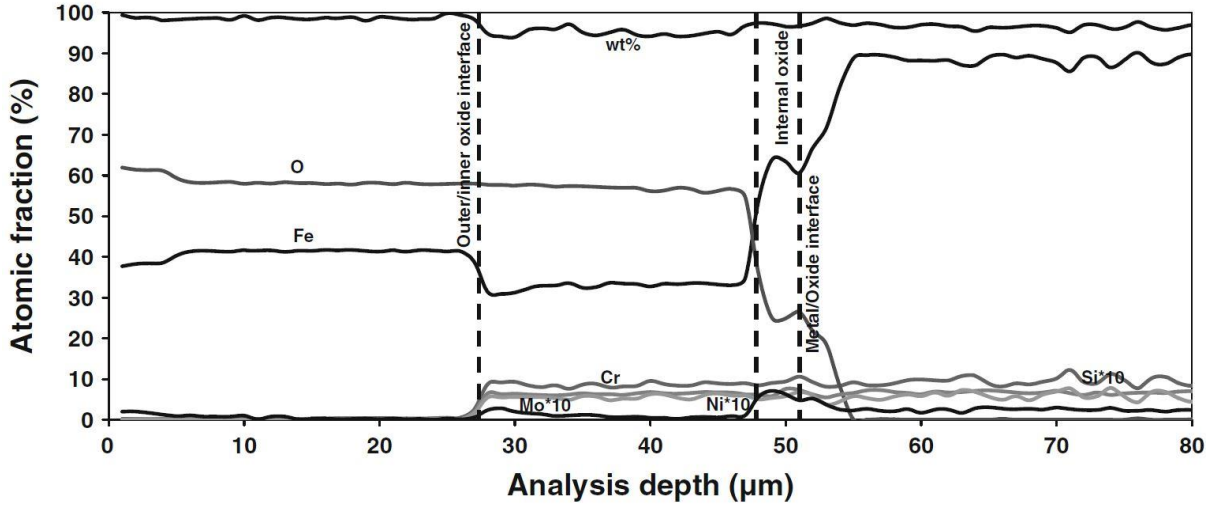

Figure 2-24: Wavelength dispersive X-ray spectroscopy (WDS) elemental profiles of the oxide layer formed on T91 steel after 1000 h at 550 °C and 1 atm of pressure [68].

Raman spectra of different phases formed in the oxide of 9Cr-1Mo steel after exposure for 1000 h in CO_2 are presented in Figure 2-23. It illustrates that the upper bright phase formed at the gas/oxide interface (spot 1) was haematite, followed by the magnetite phase. The Raman

spectrum from spot 3 in Figure 2-23 contains three peaks close to magnetite but differing by small Raman frequency shifts. Figure 2-24 shows that the elements present in the oxide scale were almost only iron, chromium and oxygen, showing that the inner oxide layer was an Fe,Cr-rich spinel with a formula $Fe_{3-x}Cr_xO_4$, where x can be estimated to be approximately 0.6-0.7 based on the atomic fractions of Cr and Fe obtained by WDS. Raman analysis of spot 4 in Figure 2-23 in the IOZ revealed the presence of two peaks characteristic of spinel. It indicates the presence of spinel instead of magnetite. Here in this study, the IOZ was more likely than the T91 matrix to contain small spinel oxide $Fe_{3-x}Cr_xO_4$ precipitates. Figure 2-24 shows that the Fe atomic concentration in the IOZ only reached 65 at. % compared with 90 at. % in the bulk indicating a depletion of Fe in IOZ and the injection of Fe vacancies into the IOZ. Raman analysis of spot 5 near the dark feature at the IOZ/metal interface shows that the feature was of the same nature as the IOZ however slightly richer in chromium. It appears that the stoichiometry of the precipitates in the IOZ tends to have a composition of $FeCr_2O_4$ which is the most stable Fe–Cr rich spinel oxide.

It should be mentioned that an IOZ is often formed beneath a protective oxide, consisting of Cr, Fe and O. Figure 2-24 shows elemental profiles of the oxide scale shown in Figure 2-23a, including the outer layer of magnetite, inner layer of spinel, IOZ and bulk metal beneath [68]. The O fraction remains constant from magnetite to spinel. However, Fe and Cr change in opposition to each other. The Fe fraction decreases with the increase of Cr fraction. The Mo fraction changes in a similar way to Cr. It can be observed that Fe increases to above 65 % in the IOZ while the Cr fraction reduces to approximately 25 %. The Ni fraction reaches a peak in the IOZ compared with other locations, as shown in Figure 2-24.

Birnie et al. has examined Cr_2O_3 with Raman spectroscopy and the spectrum is shown in Figure 2-25 [102]. There are five peaks characteristic of Cr_2O_3 at 290, 352, 528, 547 and 617 cm^{-1}. The peak at 547 cm^{-1} is the A_{1g} mode while all the others are E_g mode. Raman spectra of Cr_2O_3 annealed at different temperatures are shown in Figure 2-26 [103]. The A_{1g} peak ranges from 534 to 551 cm^{-1} while E_g peaks disappear in some cases.

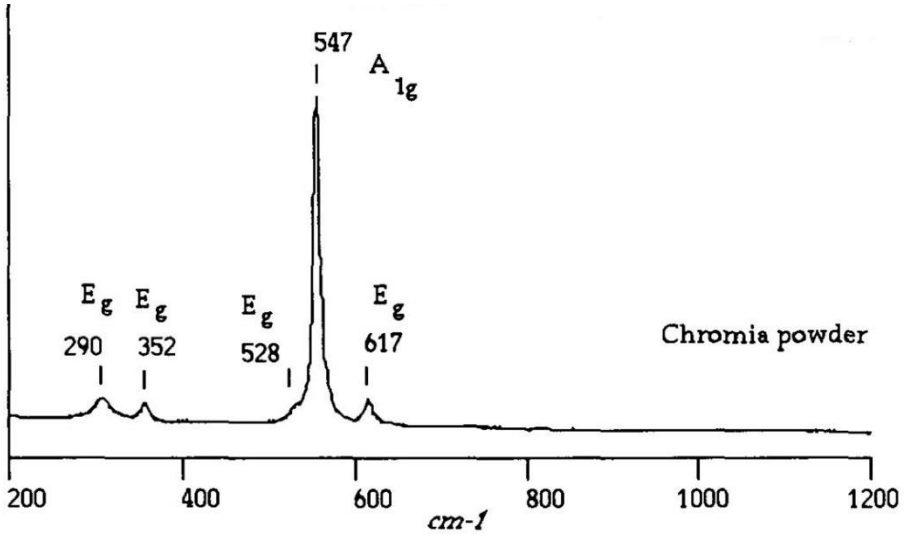

Figure 2-25: Raman spectra of Cr_2O_3 powder [102].

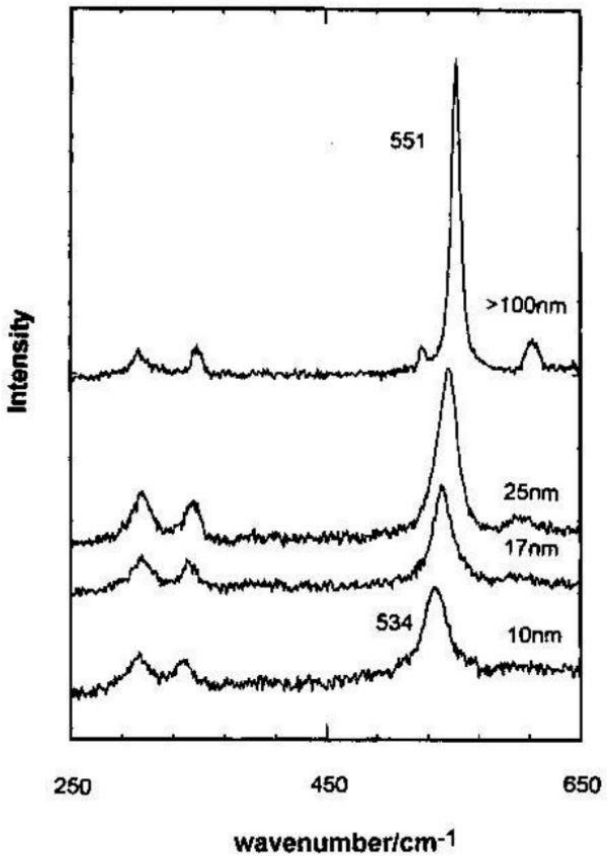

Figure 2-26: Raman spectra of nanometer scale Cr_2O_3 powder annealed in air at different temperatures [103].

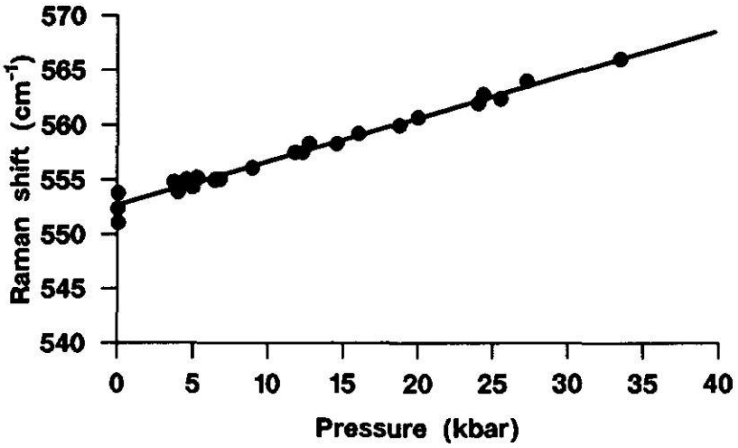

Figure 2-27: Raman shift of the A_{1g} mode peak obtained from single crystal Cr_2O_3 as a function of applied pressure [102].

From the A_{1g} mode peak positions, the corresponding stress can be identified. Compressive stress is present when the peak position is greater than 552 cm^{-1}; a peak position less than 552 cm^{-1} is indicative of tensile stress based on Figure 2-27, where we assume there is no residual stress in the sample.

Raman spectroscopy is also a standard method for characterising crystalline, nanocrystalline and amorphous carbons. Here we focus on the D and G peaks present in Raman spectra of graphite, which are at around 1350 and 1580-1600 cm^{-1}, respectively. The G mode of graphite has E_{2g} symmetry while the D peak is indicative of A_{1g} symmetry, as shown in Figure 2-28a and b, respectively [104].

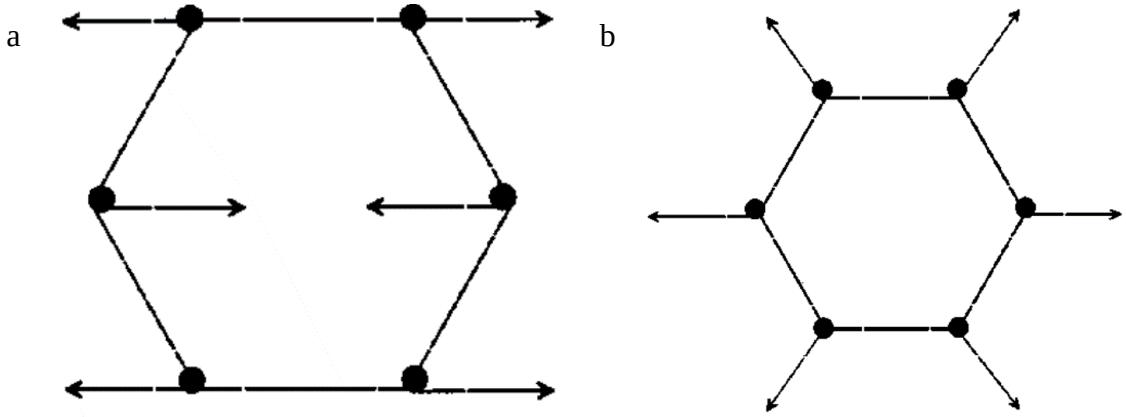

Figure 2-28: Carbon motions in (a) G mode and (b) D mode [104].

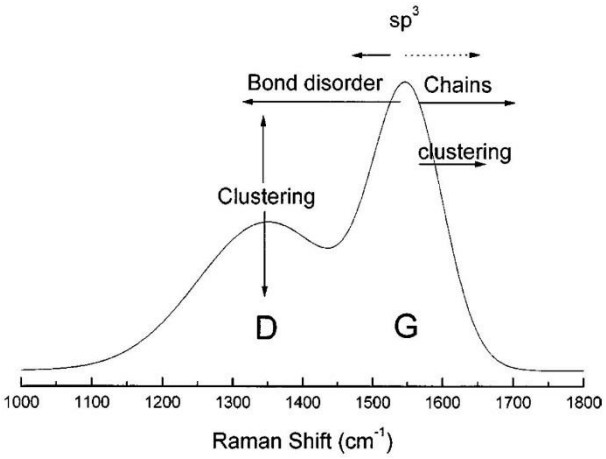

Figure 2-29: Schematic of factors influencing the Raman spectra; a dotted arrow indicates the indirect influence the sp^3 content on the G position of graphite [104].

The schematic in Figure 2-29 shows the factors influencing Raman peak positions of graphite [104]:

1. clustering of the sp^2 phase,
2. bond disorder,
3. presence of sp^2 rings or chains, and
4. the sp^2/sp^3 ratio.

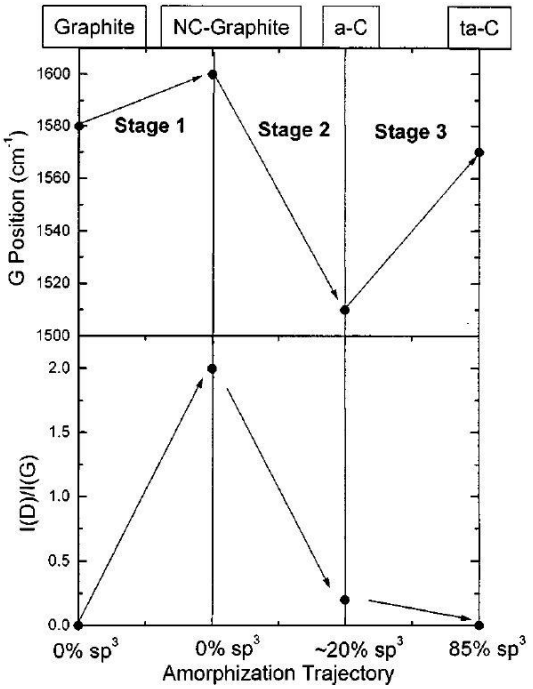

Figure 2-30: Amorphisation trajectory, showing variation of the G position and peak height ratio I(D)/I(G) [104][105].

Ferrari proposed that there are three stages in amorphisation from graphite to diamond-like carbon, as shown in Figure 2-30 [104][105]:

1. Stage 1: from graphite to nanocrystalline graphite, in which the G peak increases from 1580 to 1600 cm^{-1}, and the height ratio I(G)/I(D) increases as well. No dispersion of the G peak is present in this stage.
2. Stage 2: from nanocrystalline graphite to a-C (amorphous carbon), in which the G peak decreases from 1600 to approximately 1510 cm^{-1} and I(G)/I(D) → 0. The G peak dispersion increases.
3. Stage 3: from a-C to defect diamond-like carbon. In this stage, the G peak increase from about 1510 to 1750 cm^{-1} while I(G)/I(D) is very low and reduces to almost 0 and G peak dispersion occurs.

Raman spectra of single crystal graphite give only one band at 1575 cm^{-1} (G), which is assigned to the E_{2g} species of the infinite crystal, as shown in Figure 2-31a. The spectrum is not changed by different orientation of the sample with respect to the incident beam. The Raman spectrum from polycrystalline graphite, however, shows a second peak at around 1355 cm^{-1} (D), as shown in Figure 2-31b. The intensity of the D peak is inversely proportional to the effective crystallite size, L_a. The increase of the D peak intensity corresponds to an increase in unorganised carbon and a decrease in the graphite crystal size. The two plots in Figure 2-32 can be used to determine L_a in the thin surface layer of graphite [104][106][107].

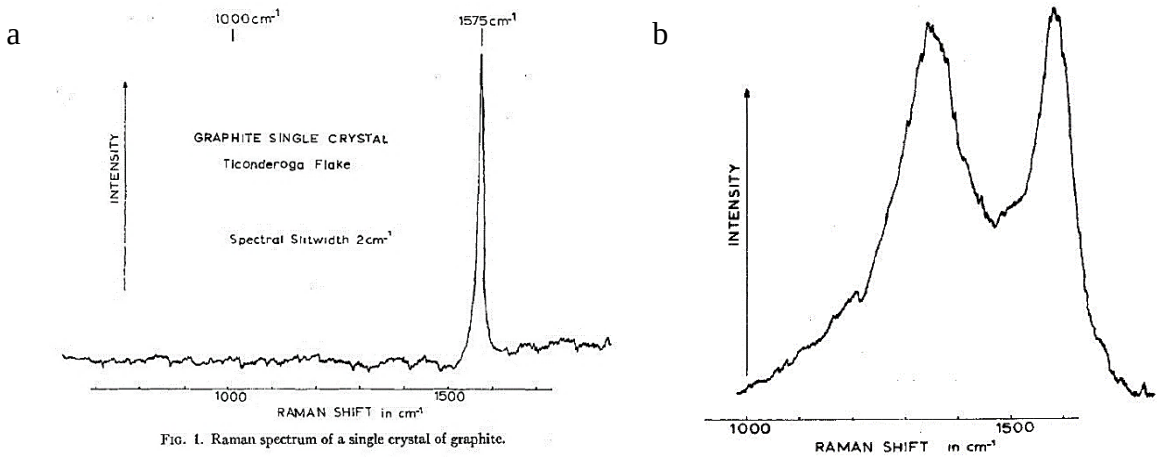

FIG. 1. Raman spectrum of a single crystal of graphite.

Figure 2-31: Raman spectrum of (a) a single crystal of graphite and (b) activated charcoal [106].

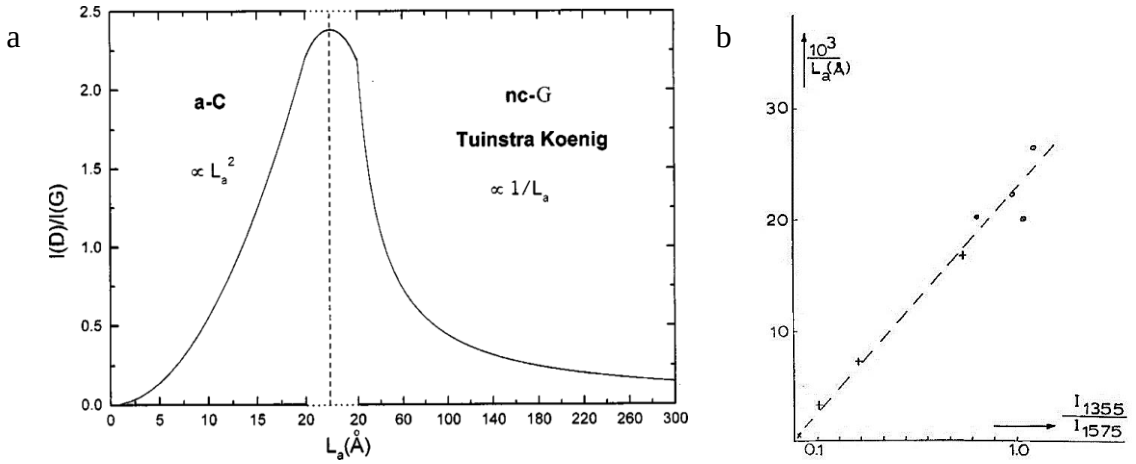

Figure 2-32: (a) Variation of the I(D)/I(G) ratio with L_a [104]. (b) Calibration of Raman intensities versus x-ray data of L_a. L_a represents crystallite size [106].

2.2.4 Modelling work on oxidation

Modelling and simulation is a methodology providing support for the design and evaluation of dynamic systems [108]. The present experimental and theoretical work is possible to provide a frame to fitting the complicated phenomena and providing a guide for the future work.

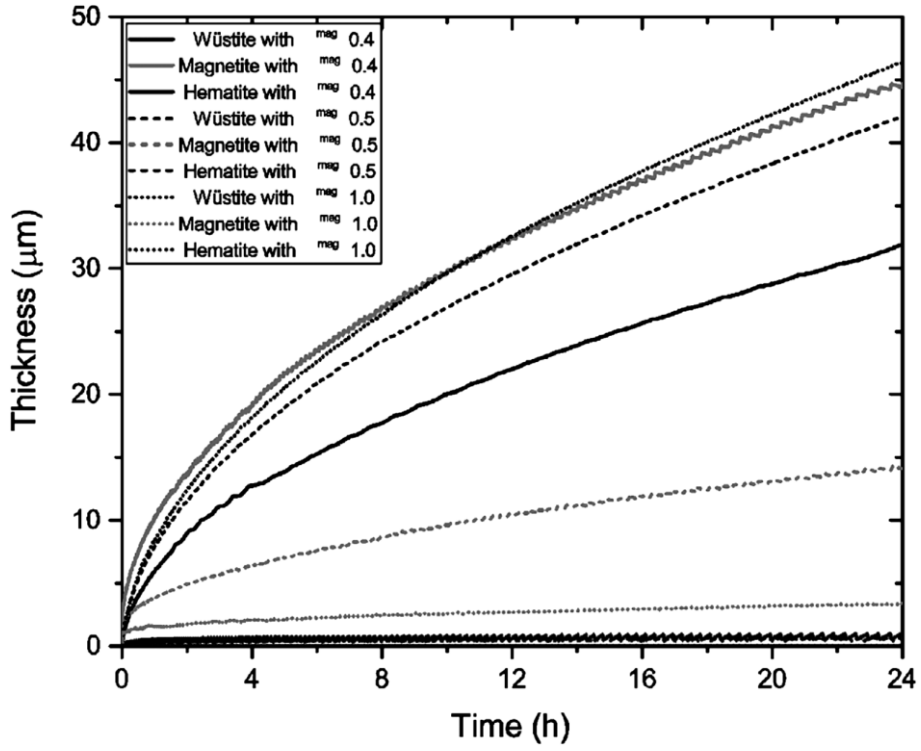

Figure 2-33: Thicknesses of the individual oxide phases as a function of time calculated for various contributions from grain boundary diffusion [85].

Larsson et al. have simulated the growth rate of three types of oxide: wustite, magnetite and haematite, as shown in Figure 2-33, using the Calphad method, which consists of modelling the thermodynamics and kinetics of each phase [85].

Rouillard and Martinelli [109] proposed that when oxidising in CO_2 environment at 550 °C, a duplex oxide layer were formed with an outer magnetite scale and an inner Fe,Cr-rich spinel scale. Their modelling work is based on the void-induced mechanism of oxidation using thermodynamic calculation. The experimental results of oxidation thickness were obtained from samples exposed to flowing CO_2 at 1 atm pressure after different exposure times. It can be observed from Figure 2-34, which shows oxide thicknesses from experimental and modelling work, that the simulated oxide thickness underestimated the real oxide thickness [109].

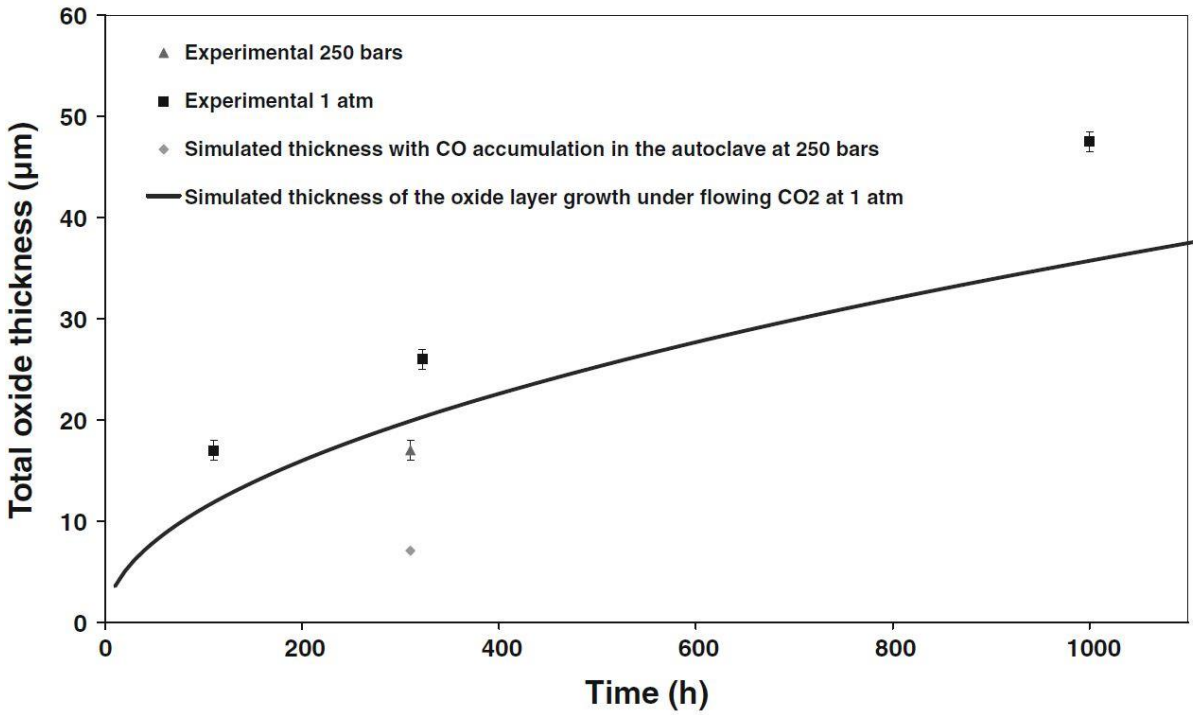

Figure 2-34: Comparison between experimental and simulated oxide thickness on T91 steel after exposure at 1 atm and 250 bar [109].

Evans et al. [110] studied the influence of diffusion by modelling work. They believed that diffusion of cations and anions must be involved in the thermally-activated processes of matter transport and change of defect shape. This process is determined by the slower-moving ion which diffused by vacancy exchange. The ion gradient is strongly influenced by the stress difference between vacancy sources and sinks. Figure 2-35 shows the diffusion fluxes involved during stress-free periods at high temperatures. A lenticular defect tends to a spherical shape due to the diffusion fluxes driven by the differences in surface curvature. The main diffusion path is along the defect surface. This change of shape of the defect by diffusion can reduce the surface energy and inhibit the propagation of fracture [110].

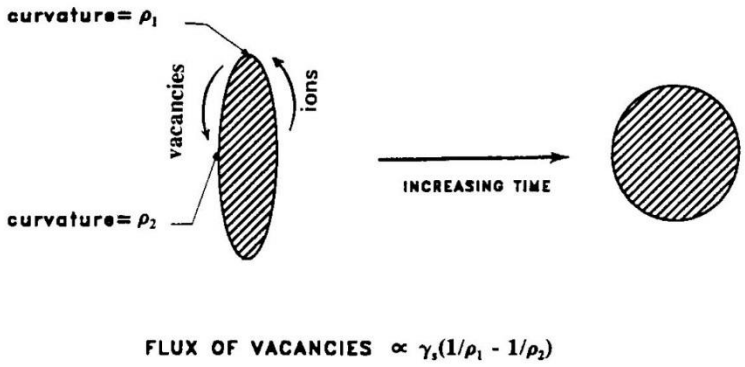

Figure 2-35: Diffusion fluxes involved in the spheroidisation of a lenticular defect [110].

An "available space model" was proposed by Martinelli et al. [81] with the introduction of nano-channels as the diffusion path for oxidising medium. This model can be also used to understand the mechanism of oxide formation, as shown in Figure 2-36.

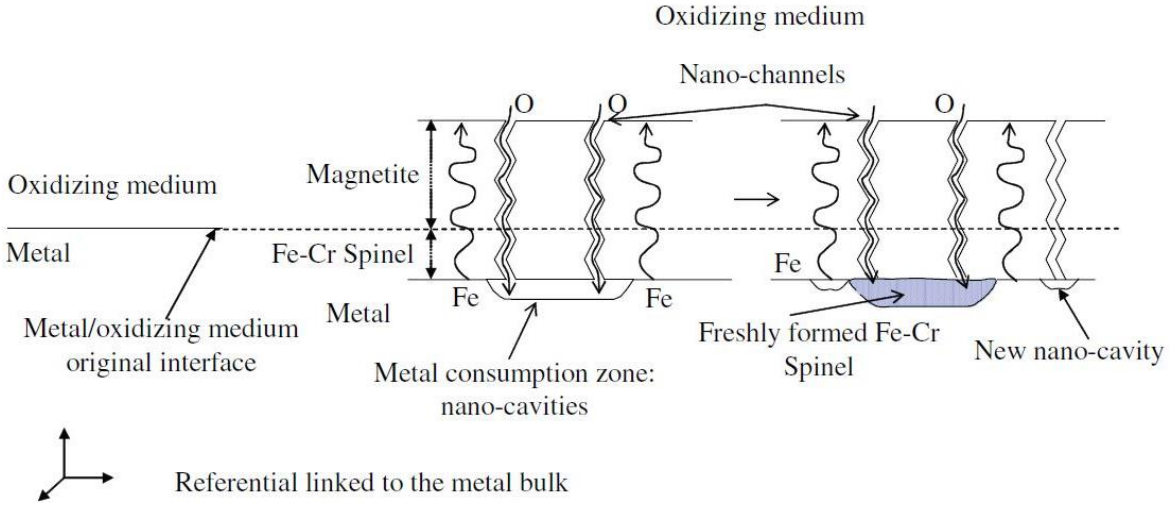

Figure 2-36: "Available space model" illustrating the mechanism of oxide formation [81].

Therefore, different models and simulation work were used to understand the mechanism of oxidation. The experimental results validate the results from modelling work. The experimentation, in turn, will provide information for further improvement of modelling work.

2.3 Carburisation of Fe-Cr steels

2.3.1 The evolution of carbides and their identification

Modelling work on three power plant steels was undertaken to obtain the predicted evolution of precipitates, using MTDATA software based on the experimental results from these three steels: 2.25Cr1Mo, 3Cr1.5Mo and 10CrMoV [111]. Iron carbide cementite (Fe_3C) is reported to be an equilibrium phase (metastable phase) and becomes unstable and decomposes when the

carbon activity a_C decreases [64]. $M_{23}C_6$ Carbides were observed in the form of coarse precipitates in experiments [50][112]. However, the delay of its formation would stabilise the finer carbides or nitrides M_2X and MX (X represents C and N) [111]. The precipitates formed in three power plant materials and their predicated evolution are shown in Figure 2-37 [111]. This gives the evolution of carbide and nitride precipitates. The Fe_3C carbides disappear quickly to a low level after a short time of exposure while M_2X precipitates are formed during this process. However, the M_2C volume fraction in 3Cr1.5Mo is much lower than for the other two steels. M_7C_3 carbides are formed in 2.25Cr1Mo and 3Cr1.5Mo steels and it appears that higher Cr content decreases the time for M_7C_3 formation and its quantity. M_7C_3 is absent in 10CrMoV. $M_{23}C_6$ forms earlier with increase of Cr content. The three evolution processes suggest that Cr and/or V impede the formation of M_7C_3 and accelerate the formation of MX. It also illustrates that $M_{23}C_6$ is the dominant precipitate in these Fe-based steels after a long period of exposure at 600 °C.

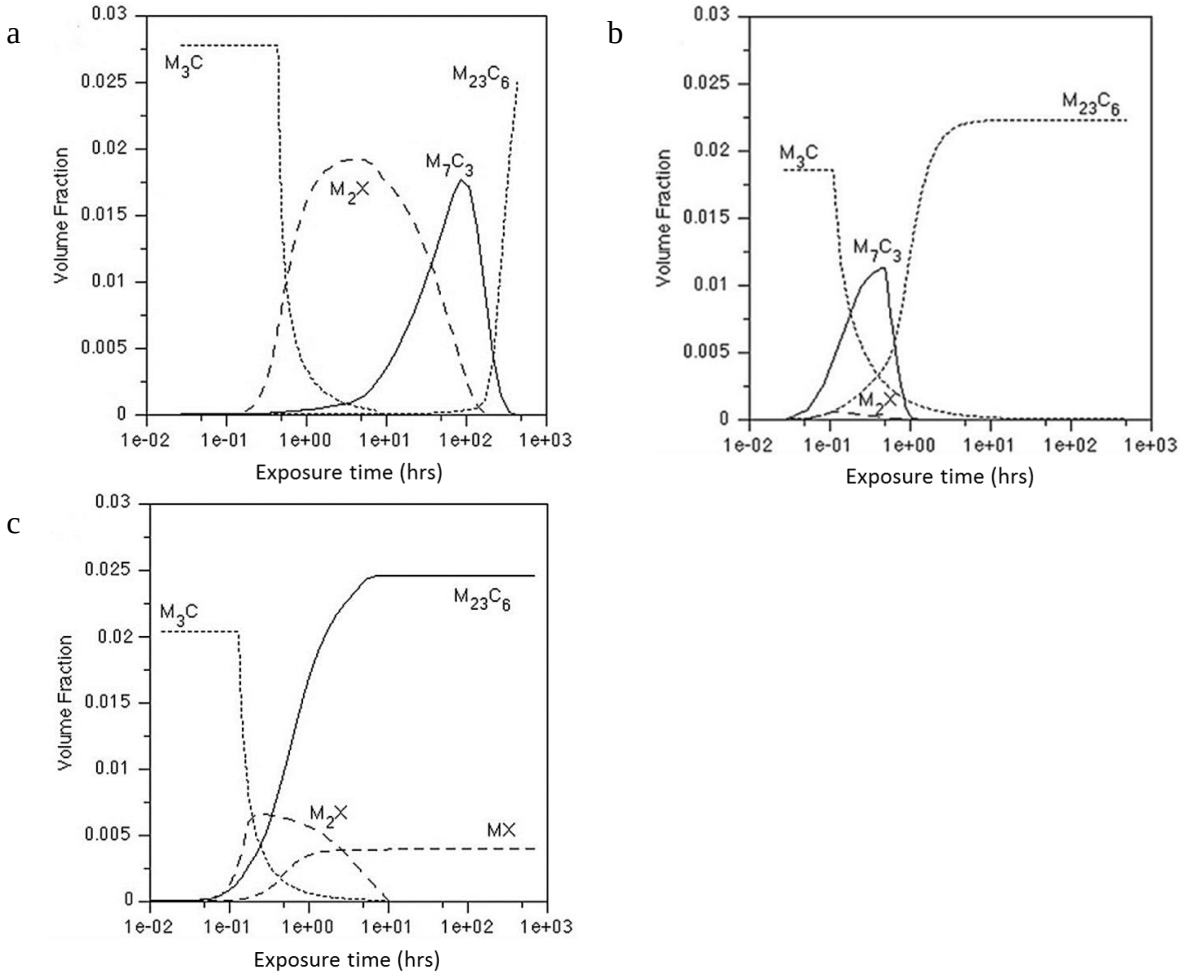

Figure 2-37: The predicted evolution of the precipitates volume fraction as a function of exposure time (in hours) at 600 °C from (a) 2.25Cr1Mo; (b) 3Cr1.5Mo and (c) 10CrMoV [111].

In T91 (9Cr–Mo–Nb–V–N) steel [113], obtained by being austenitised for 30 min at 1050°C, air cooled and then tempered for 1 h at 750 °C, which contains a lath martensite microstructure,

$Cr_{23}C_6$ precipitates along the lath and the prior austenite grain boundaries [37]. Gheno et al. studied precipitates deposited in the IOZ and the internal carburisation zone in martensitic Fe-9Cr steel [114]. The sample was exposed to Ar-20 % CO_2 gas at 800 °C for 20 h. The distribution of elements O, Cr and Fe are shown in Figure 2-38a and b. The Cr-rich locations correspond to carbide precipitates in the internal carburisation zone and Cr oxide forms in the internal oxidation zone. A depletion of Fe is observed in the Cr-rich locations. This is demonstrated by the EDS line scans and maps. Cr is enhanced at the locations containing carbides and in the Cr oxide particles, whilst the Fe concentration is reduced. It is also observed that Cr concentration in the metal is close to 9 wt.%. However, a depletion of Cr occurs in the IOZ. Figure 2-38c and d are the selected area diffraction patterns from α-(Fe,Cr) in the [011] zone axis and $Cr_{23}C_6$ in the [001] zone axis, respectively. However, there is a debate arising from this investigation about the carbide composition formed in Fe-9Cr steel. The Fe in the carbide is not reduced to 0, as shown in Figure 2-38b, indicating that the carbide is comprised of both Cr and Fe, which can be formulated as $M_{23}C_6$ or $(Fe,Cr)_{23}C_6$, where M represents Fe and Cr. Moreover, it appears that the internal carburisation zone is mainly comprised of carbides deposited on ferrite rather than martensite.

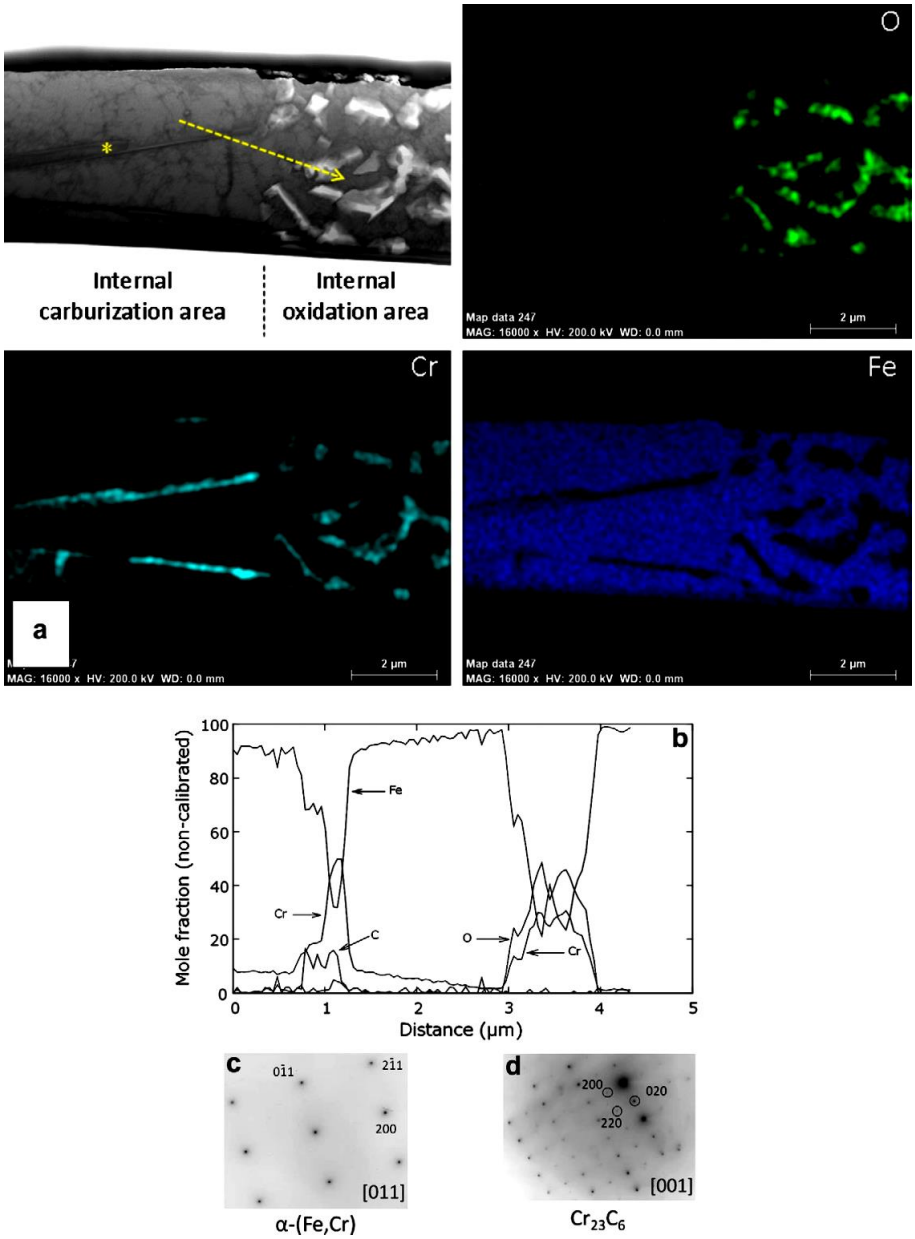

Figure 2-38: TEM analysis at the interface between internal oxidation and carburisation zones in Fe–9Cr after exposure to Ar-20CO_2 at 800 °C for 20 h. (a) Bright field image and corresponding EDS elemental maps; (b) EDS linescan; (c) and (d) selected area diffraction pattern of the α-(Fe,Cr) matrix ([011] zone axis) and of a $(Cr,Fe)_{23}C_6$ carbide ([001] zone axis), respectively. The arrow and star in (a) indicate the location of the linescan in (b) and the pattern in (d), respectively [114].

The T91 steel has also been imaged with transmission electron microscopy, showing the microstructure and dominant carbide precipitates formed, as shown in Figure 2-39. The $M_{23}C_6$ carbides observed were formed along both lath and prior austenite grain boundaries [115].

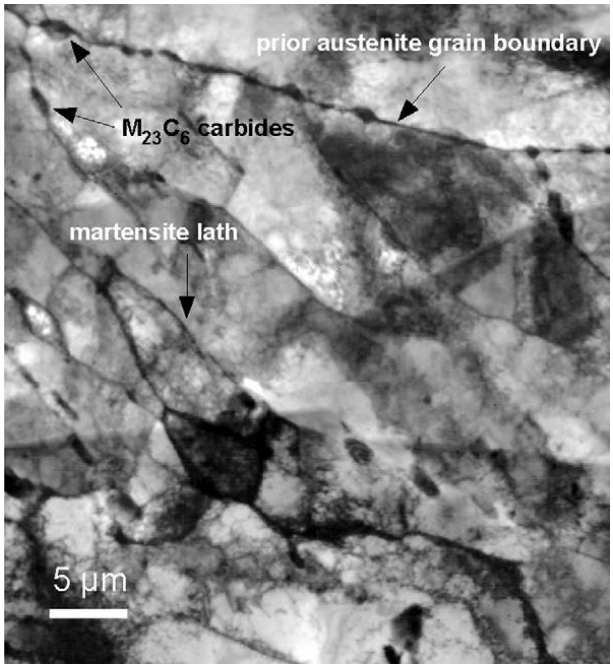

Figure 2-39: TEM observation of T91 (9Cr–Mo–Nb–V–N) microstructure [115].

$M_{23}C_6$ deposited in commercial LDX2101® stainless steel with composition Fe-21.5Cr-5Mn-1.6Ni-0.22N-0.02C (developed by Outokumpu), has been analysed with TEM. A TEM micrograph and diffraction pattern of $M_{23}C_6$ are shown in Figure 2-40 [116]. These illustrate that $M_{23}C_6$ has a face-centred cubic (FCC) structure with a lattice parameter a = 10.65 Å. These crystallographic structures are consistent with data reported elsewhere: 10.66 Å [117], 10.65Å [118], 10.60-10.68 Å [119].

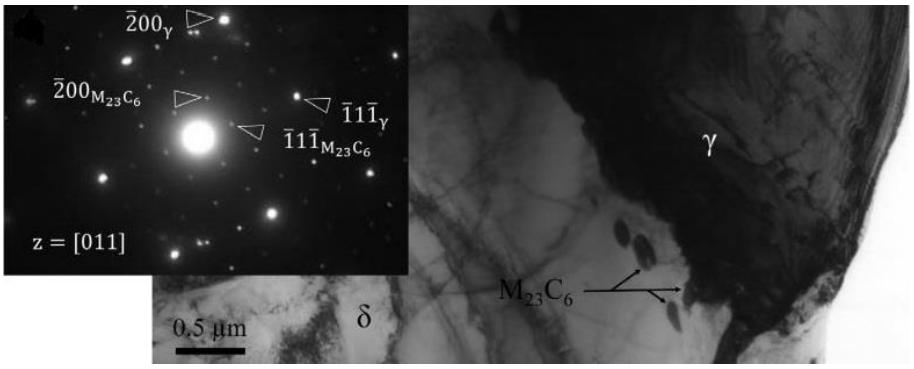

Figure 2-40: A dark field TEM image and corresponding selected area diffraction pattern of the γ austenite and $M_{23}C_6$ carbides in orientation ($Z = [011]||[011]_{M_{23}C_6}$) [116].

Fe carbides tend not to form in Fe-Cr steels due to their low stability. Therefore, $M_{23}C_6$, rather than $Fe_{23}C_6$, carbides can be formed even at low carbon activity (a_C) [85]. Fe and Cr react with the carbon produced in the reactions, as shown in Table 2-1, to form $(Fe,Cr)_{23}C_6$ during the process of oxidation and carburisation, maintaining $a_C < 1$ to inhibit carbon deposition in the oxide in protective oxidation. A sample that had entered a breakaway oxidation regime was analysed using TEM. The blocky precipitates present in the sample were identified as $M_{23}C_6$.

Selected area diffraction patterns showed that the examined needle-shaped precipitates were $M_2(C,N)$ with a hexagonal structure, as shown in Figure 2-41 [85].

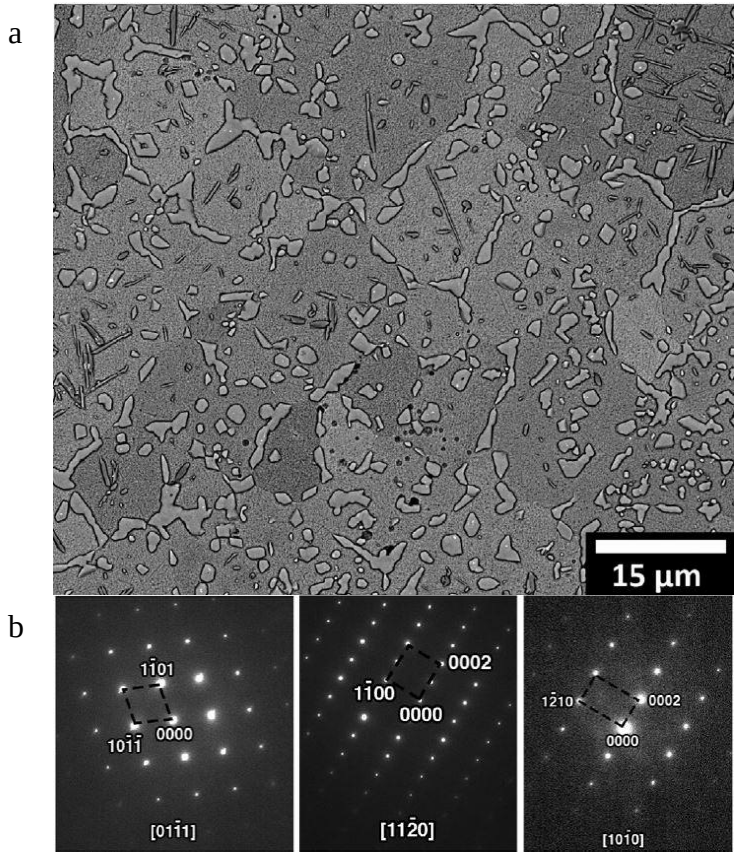

Figure 2-41: (a) Backscatter SEM image of the fin centre after exposure at 600 °C for 19924 h, including blocky $M_{23}C_6$ and needle shape $M_2(C,N)$; (b) selected diffraction patterns of $M_2(C,N)$ phase [85].

In the past, Fe_2C has been studied and the results show that this type of carbide has a hexagonal (HCP) structure. The lattice parameters were obtained and a and c were proximately 2.75 and 3.88 Å, respectively [120]. A study by Dirand and Afqir showed a and c to be 2.754 and 4.349 Å, respectively [121]. Theoretical investigations show that the lattice constants a and c are expected to be 2.888-2.993 and 4.524-4.627 Å, respectively [122].

In the Cr-C system, there are three stable carbide phases: $Cr_{23}C_6$, Cr_7C_3 and Cr_3C_2, and at least two metastable carbides: Cr_2C and Cr_3C [123][124]. Here we only discuss the formation of Cr_2C. When annealed at different temperatures, this fine-grained metastable carbide is first formed at approximately 500 °C, and then converted to other types of carbide at about 650 °C. Figure 2-42 shows three high-resolution images of a cross-section of an a-C/Cr/a-C trilayer film annealed at 300, 400 and 500 °C, respectively, for 30 min, showing the amorphous Cr layer transform to a nano-crystalline phase which has extremely fine-grained Cr_2C with a grain size of approximately 1-2 nm [123]. Zaslavskaya et al. proposed that the alloying element Mo is of benefit to the stabilising of metastable chromium carbide Cr_2C in steel containing 12 wt. % Cr [124]. The chemical composition of M_2C is analogous to Mo_2C, W_2C and the nitrides Cr_2N,

Nb_2N which all have a hexagonal structure. Here the X-ray diffraction pattern result shows the lattice constants of Cr_2C with its hexagonal structure to be a = 2.86 Å, c= 4.47 Å [124].

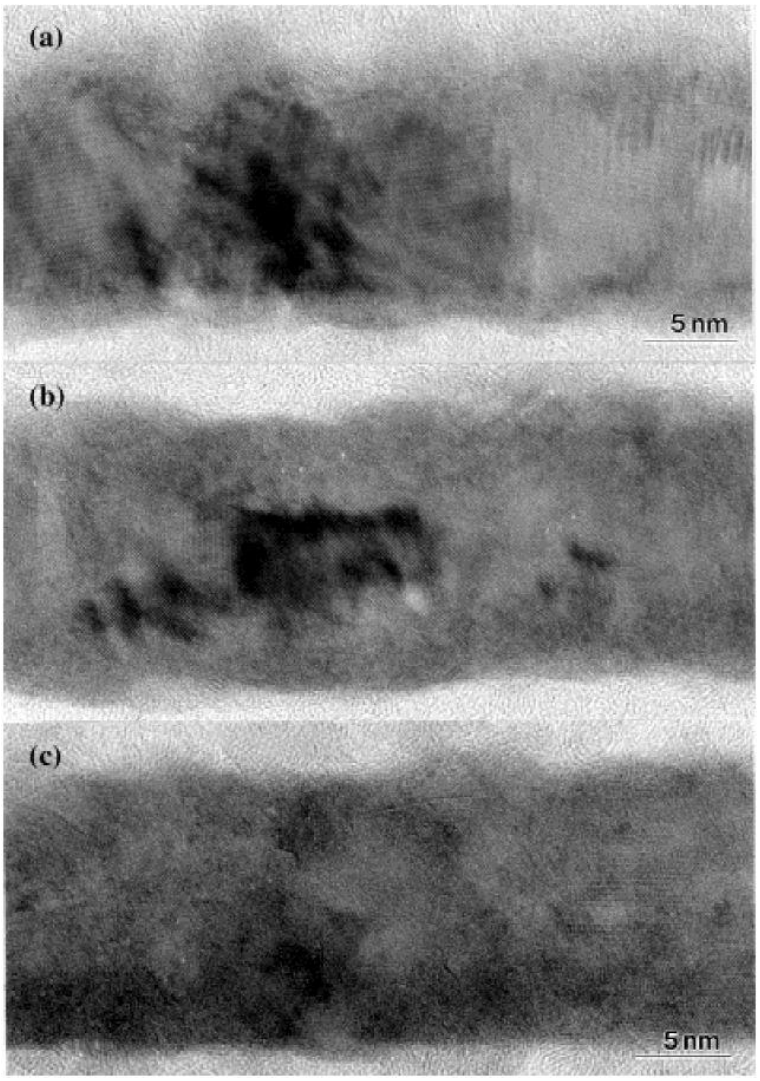

Figure 2-42: Cross-sectional high-resolution images of an a-C/Cr/a-C trilayer film annealed in situ at(a) 300 °C, (b) 400 °C, and (c) 500 °C for 30 min, showing the Cr layer transformation to extremely fine-grained Cr_2C [123].

Table 2-3: Chemical composition (wt. %) of the steels [124].

Steel No.	*C*	*Mn*	*Si*	*Cr*	*Ni*	*W*	*Mo*	*V*	*Ti*	*B*	*Quench temp. (℃)*
1	*0.15*	*0.50*	*0.50*	*13.60*	*3.05*	*1.66*	*/*	*0.20*	*0.043*	*0.005*	*1050 (oil)*
2	*0.24*	*0.30*	*0.46*	*12.70*	*1.70*	*1.77*	*1.70*	*0.24*	*/*	*/*	*1050 (oil)*

Zaslavskaya et al. [124] also compared the elemental concentration of M_2C and $M_{23}C_6$ in two different steels. The composition of these two steels and the corresponding elemental concentrations of two types of carbides were shown in Table 2-3 and Table 2-4, respectively.

Table 2-4 shows the elemental concentrations of M_2X and $M_{23}C_6$ precipitates from the two steels exposed at different temperatures and times. It is seen that the amount of M_2X decreases with the increase of temperature when exposed for 4 h, while the amount of $M_{23}C_6$ shows an

inverse tendency in steel 1. In steel 2, it appears that the sample exposed at a lower temperature (400 °C) but for a longer time (100 h) gives a similar carbide content to that exposed at a higher temperature (680 °C) but for a shorter time (4 h). When two samples from steel 1 exposed for 3 h at 560 and 600 °C, respectively, the Cr concentration in $M_{23}C_6$ is similar while Cr concentration in M_2C decreases with the increase of temperature. The difference in elemental concentration of the two types of carbides between the two samples steel 1 and 2 is not obvious when exposed at different temperatures but for the same time.

Table 2-4: Results of chemical analysis of the M_2X and $M_{23}C_6$ precipitates deposited in 12Cr steels 1 and 2 [124].

Steel No.	*Temp. (℃)*	*Time (h)*	*M_2X*						*$M_{23}C_6$*					
			Amount of phase (%)	*Cr (wt. %)*	*Fe (wt. %)*	*W (wt. %)*	*Mo (wt. %)*	*V (wt. %)*	*Amount of phase (%)*	*Cr (wt. %)*	*Fe (wt. %)*	*W (wt. %)*	*Mo (wt. %)*	*V (wt. %)*
1	*540*	*3*	*1.6*	*74.4*	*10.6*	*11.2*	*/*	*3.7*	*/*	*/*	*/*	*/*	*/*	*/*
	560	*3*	*0.94*	*73.4*	*12.7*	*11.7*	*/*	*2.1*	*0.54*	*64.8*	*18.5*	*9.3*	*/*	*7.4*
	600	*3*	*0.31*	*67.7*	*16.1*	*9.6*	*/*	*6.4*	*1.81*	*64.6*	*21.5*	*12.1*	*/*	*1.7*
2	*680*	*4*	*1.97*	*60.0*	*11.6*	*10.1*	*14.7*	*3.0*	*1.65*	*58.4*	*22.3*	*7.2*	*9.0*	*3.0*
	400	*100*	*2.47*	*64.0*	*10.9*	*9.3*	*11.9*	*2.6*	*0.65*	*56.7*	*30.0*	*4.6*	*7.6*	*1.0*
	680	*4*	*2.51*	*63.8*	*13.9*	*9.2*	*11.1*	*2.0*	*1.57*	*58.8*	*23.1*	*5.4*	*10.1*	*1.25*

Runiewicz et al. analysed the microstructure and type of precipitates M_2X (Cr_2N) deposited in X30CrMoN15-1 steel using TEM and the results are shown in Figure 2-43 [125]. The chemical composition of the steel is given in Table 2-5. It shows that the precipitates deposited in the matrix have a hexagonal structure with lattice parameters a = 4.760 Å and c = 4.438 Å. The precipitates M_7C_3 were also analysed and the results are shown in Figure 2-44 [125]. These have a hexagonal crystal structure with lattice parameters a = 6.979 Å and c = 4.495 Å.

Table 2-5: Chemical composition of X30CrMoN15-1 steel [125]

Steel No.	*C*	*Si*	*Mn*	*Cr*	*Mo*	*Ni*	*V*	*Al*	*Ti*	*Cu*	*N*
X30CrMoN15-1	*0.30*	*0.64*	*0.49*	*15.56*	*1.02*	*0.16*	*0.42*	*0.003*	*0.003*	*0.03*	*0.42*

Shen et al. observed and analysed Nb-rich and Cr-rich nitride phases in the 9Cr steel, which have similar hexagonal crystal structures, but different lattice parameters [126]: Nb-rich M_2N nitrides, a = 2.80 Å, c = 4.45Å, as shown in Figure 2-45 and Cr-rich M_2N nitrides, a = 7.76 Å, c = 4.438 Å, as shown in Figure 2-46. The difference may due to the different tempering temperatures, which is 650 °C for the former and 750 °C for the latter.

Maetz et al. observed nitride Cr_2N in austeno-ferritic duplex stainless steels. Transmission electron microscopy analysis was applied to obtain the microstructures and diffraction patterns of the precipitates, and the results are shown in Figure 2-47. Cr_2N was found to have a trigonal crystal structure in the $[\bar{1}2\bar{1}6]$ zone axis. The lattice parameters a and c were both 4.78 Å, corresponding to 2.58 Å and 4.45 Å in the hexagonal cell, respectively [116].

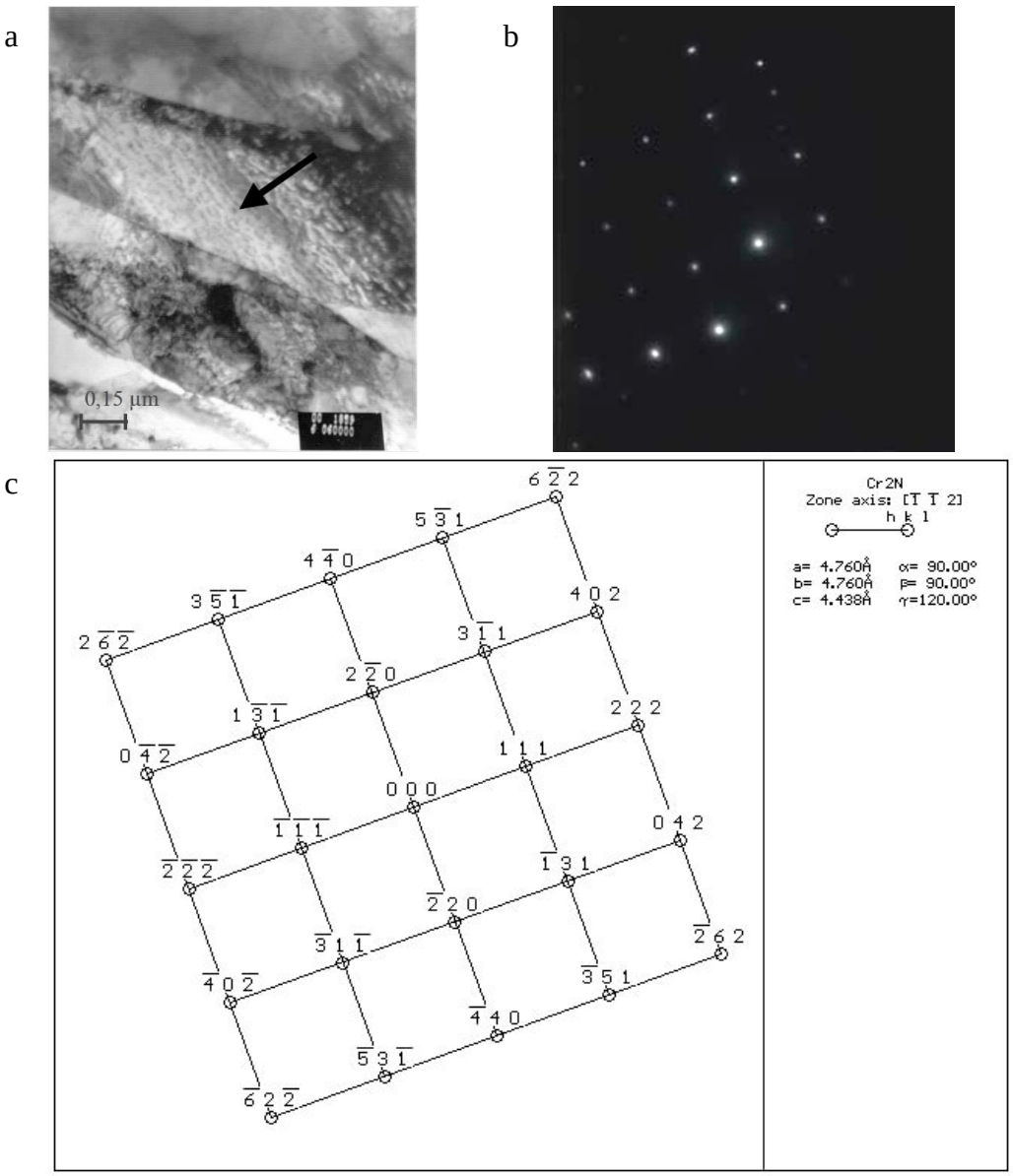

Figure 2-43: (a) TEM image of metal bulk martensite and precipitate M_2C marked with arrow; (b) diffraction pattern of M_2C; (c) interpretation of diffraction pattern [125].

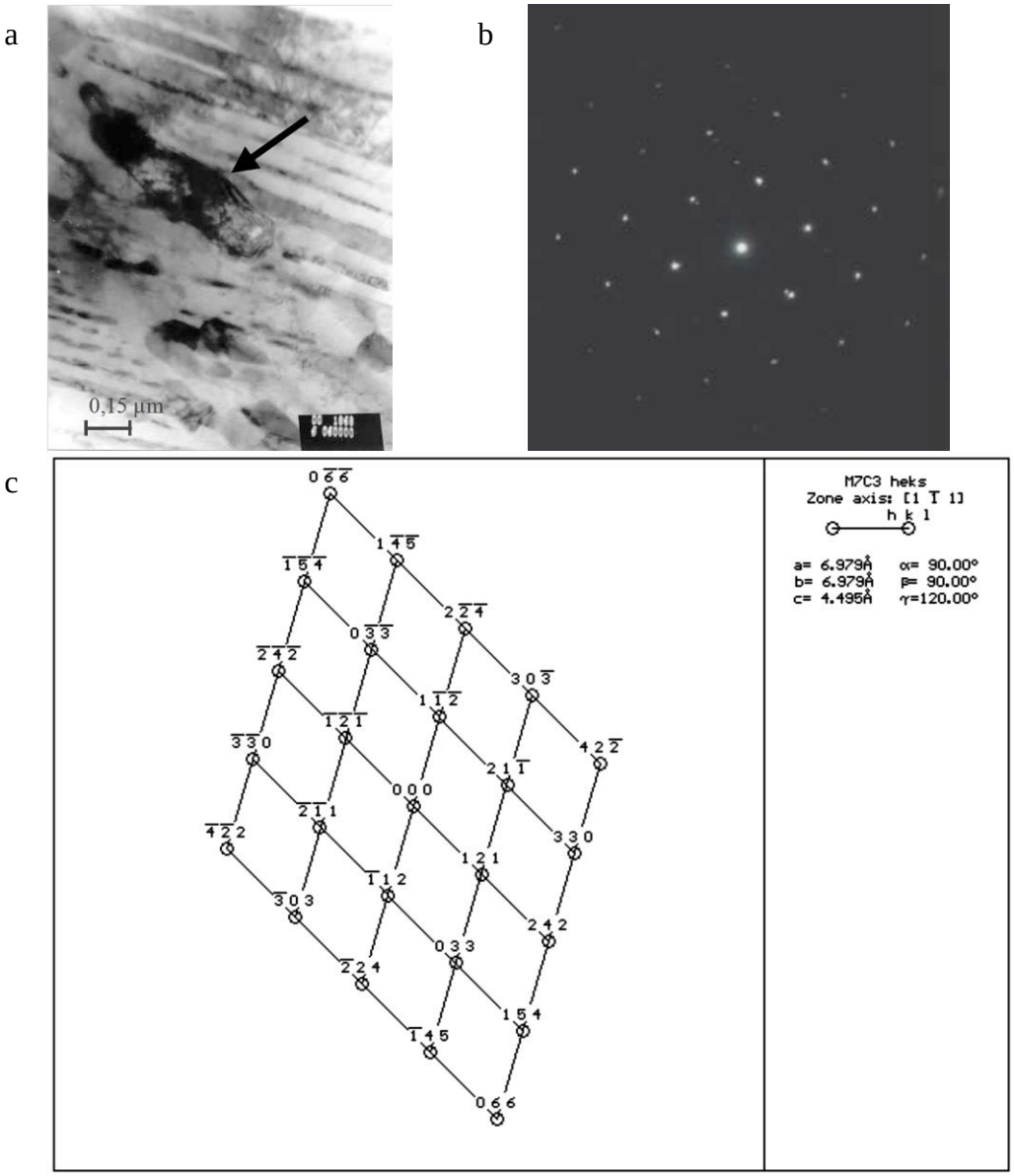

Figure 2-44: (a) TEM image of metal bulk martensite and precipitate M_7C_3 marked with arrow; (b) diffraction pattern of M_7C_3; (c) interpretation of diffraction pattern [125].

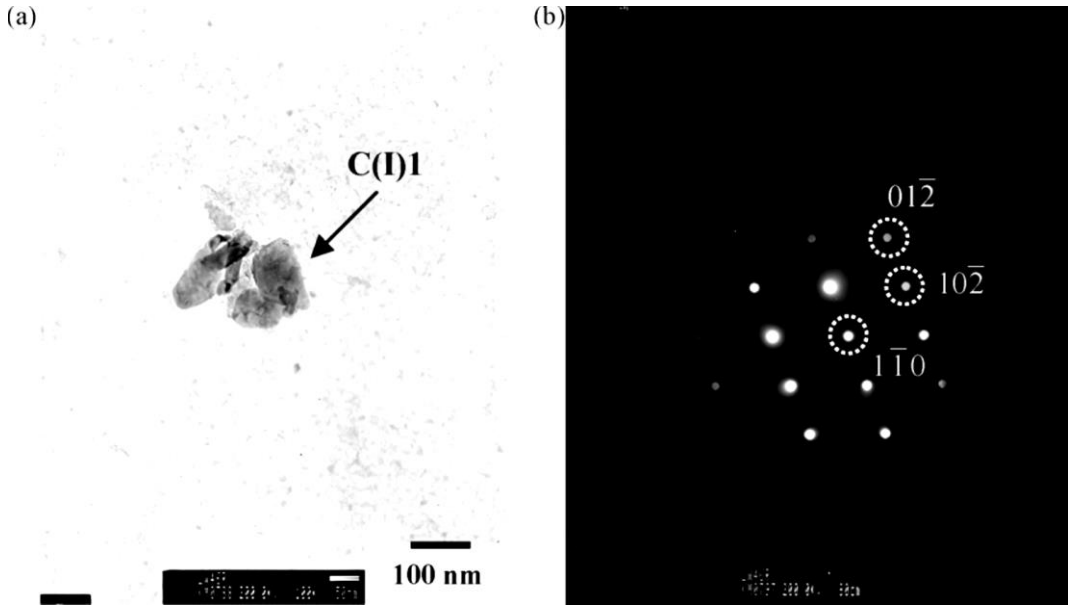

Figure 2-45: TEM micrograph of chromium-rich nitrides, M_2N with lattice parameters a = 2.80 Å, c = 4.45 Å, taken from extraction carbon replica from sample tempered at 650 °C and electron micro-diffraction patterns recorded from the particle C(I)1 in the [223] zone axis [126].

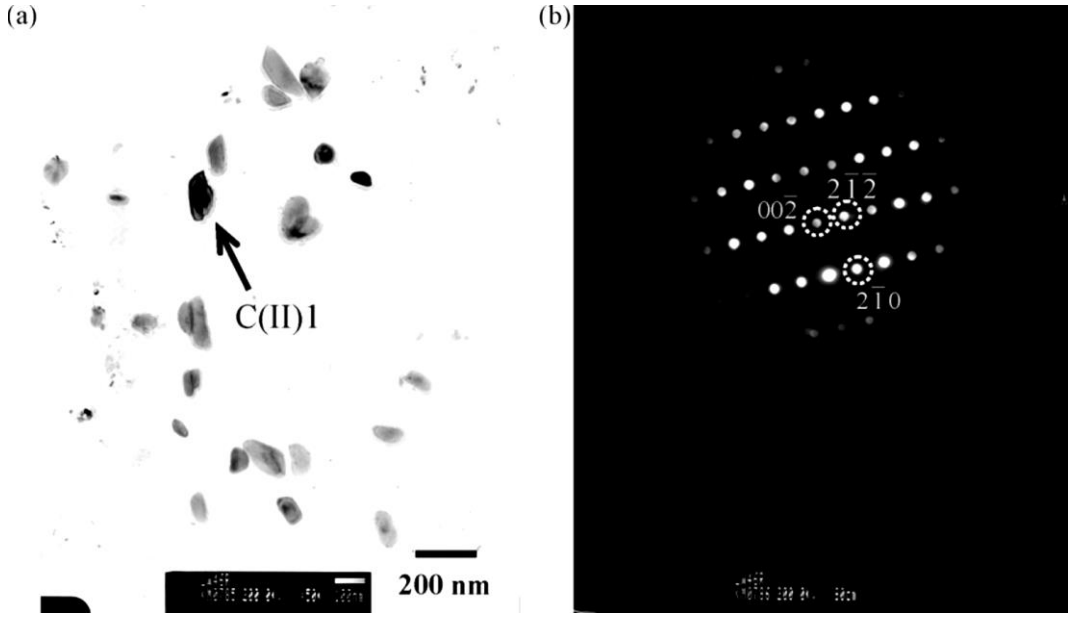

Figure 2-46: TEM micrograph of chromium-rich nitrides, M_2N with lattice parameters a=7.76Å, c = 4.438 Å, taken from extraction carbon replica from sample tempered at 750 °C and electron micro-diffraction patterns recorded from the particle C(II)1 in the [010] zone axis [126].

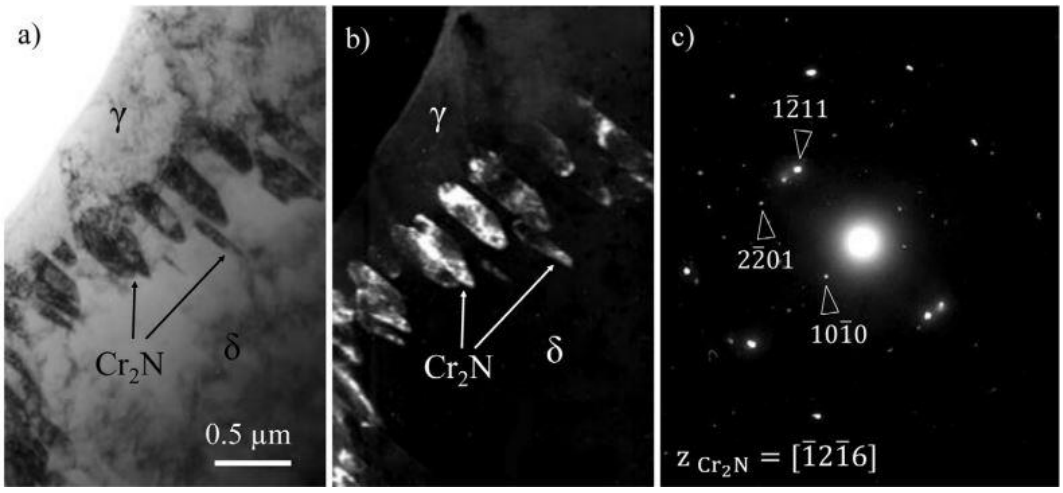

Figure 2-47: TEM analyses after 10 h of ageing at 690 °C: (a) bright-field (BF) image (b) dark-field (DF) image (c) corresponding SAD pattern, respectively, of the Cr_2N nitrides along the zone axis z = $[\bar{1}2\bar{1}6]$ [116].

TEM analysis of the Cr_2N and the matrix show that Cr_2N phases are aligned with one of the two δ ferrite grains [116], as shown in Figure 2-48. Based on the orientation usually reported in the literature [127][128], the orientation in this case is:

$$(0001)_{Cr_2N} \| (110)_{\delta} \text{ and } [\bar{1}100]_{Cr_2N} \| [\bar{1}11]_{\delta}$$

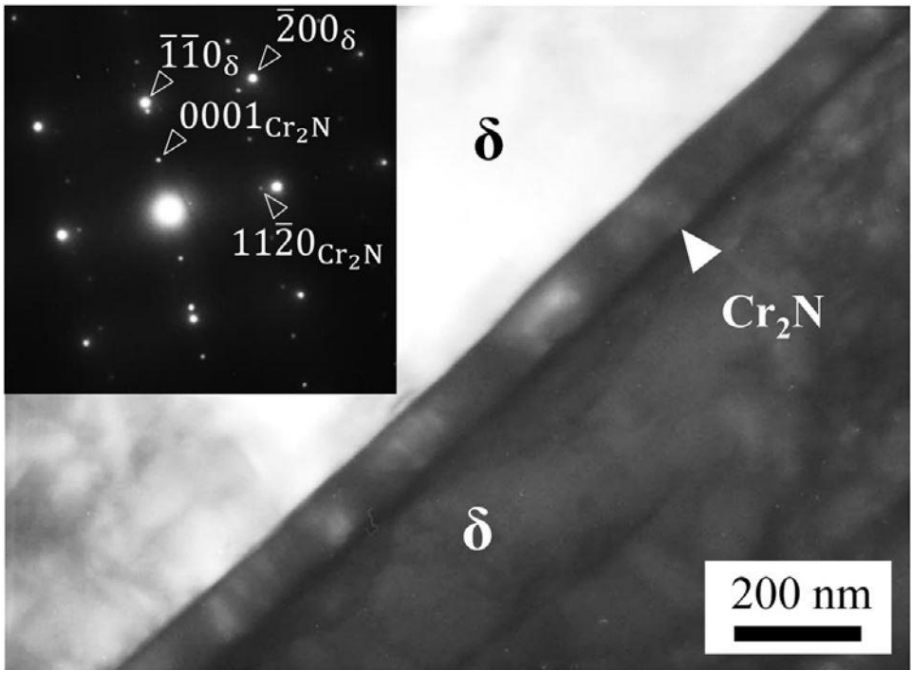

Figure 2-48: Dark field TEM image of the layer of Cr_2N along the δ/δ interface after 120 h of ageing at 690 °C and the corresponding diffraction pattern (z = $[1\bar{1}00]_{Cr_2N} \| [001]_{\delta}$) [116].

Luan et al. investigated a high speed steel (Fe-1.8 %C-4.2 %Cr-5.8 %Mo-6 %V in weight percent), in which MC carbide was present after melting at around 1600 °C, being poured into an iron mould at around 1450 °C and solidifying [129]. Mostly MC carbides were in the form of rods and spheres in 2D, and branch and chrysanthemum structures in 3D. Figure 2-49a and b show the TEM image of a segregated spherical MC carbide and the corresponding diffraction

pattern, respectively. The diffraction pattern shows that MC has a face-centred cubic (FCC) crystal structure.

Figure 2-50 shows the results of X-ray diffraction, including peaks and corresponding d-spacings. The lattice parameter of MC was calculated to be a = 4.144 Å, which is a bit smaller than the experimental result a = 4.170 Å, as shown in ref [129].

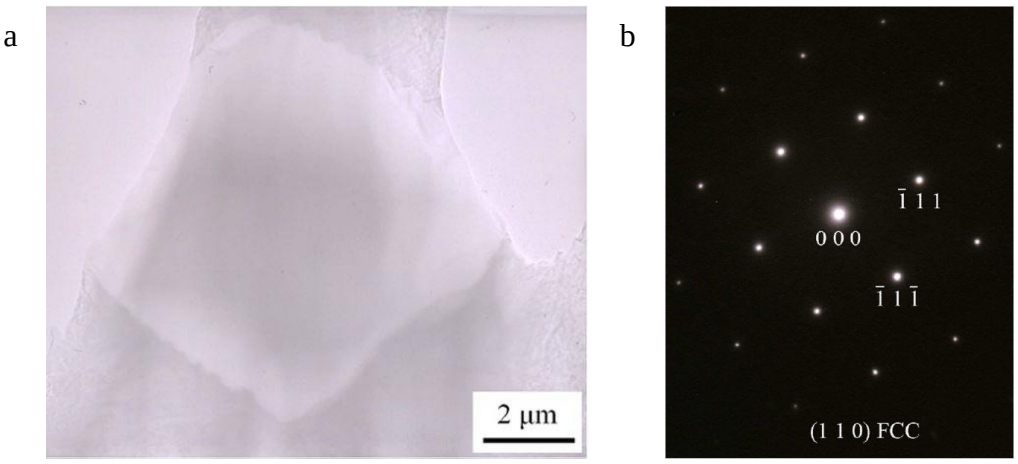

Figure 2-49: (a) TEM micrograph of MC and (b) diffraction pattern of the segregative MC carbide [129].

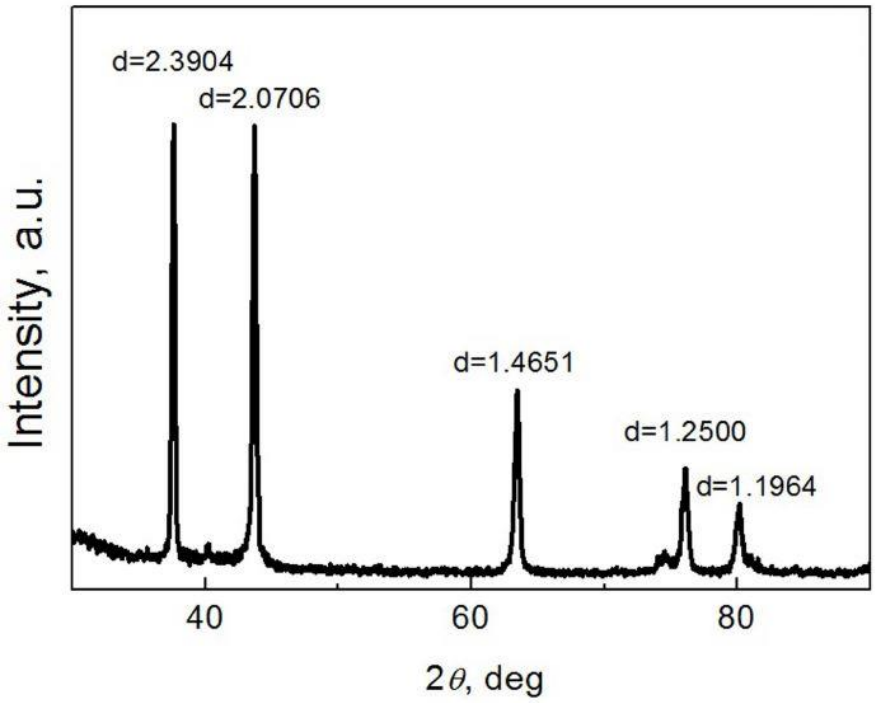

Figure 2-50: X-ray diffraction profile of the MC carbide [129].

Shen studied the precipitate phases in 9Cr steels used for nuclear power reactors [126]. Figure 2-51 shows two precipitates deposited in the matrix from 9Cr steel, the diffraction pattern and the interpretation. The analysis demonstrates that the precipitates are nitrides MN in the [001] zone axis for V(I)1 and [011] zone axis for V(I)3. The lattice parameters were calculated for both of these: a = 4.070 Å and a = 4.232 Å, respectively [126][130].

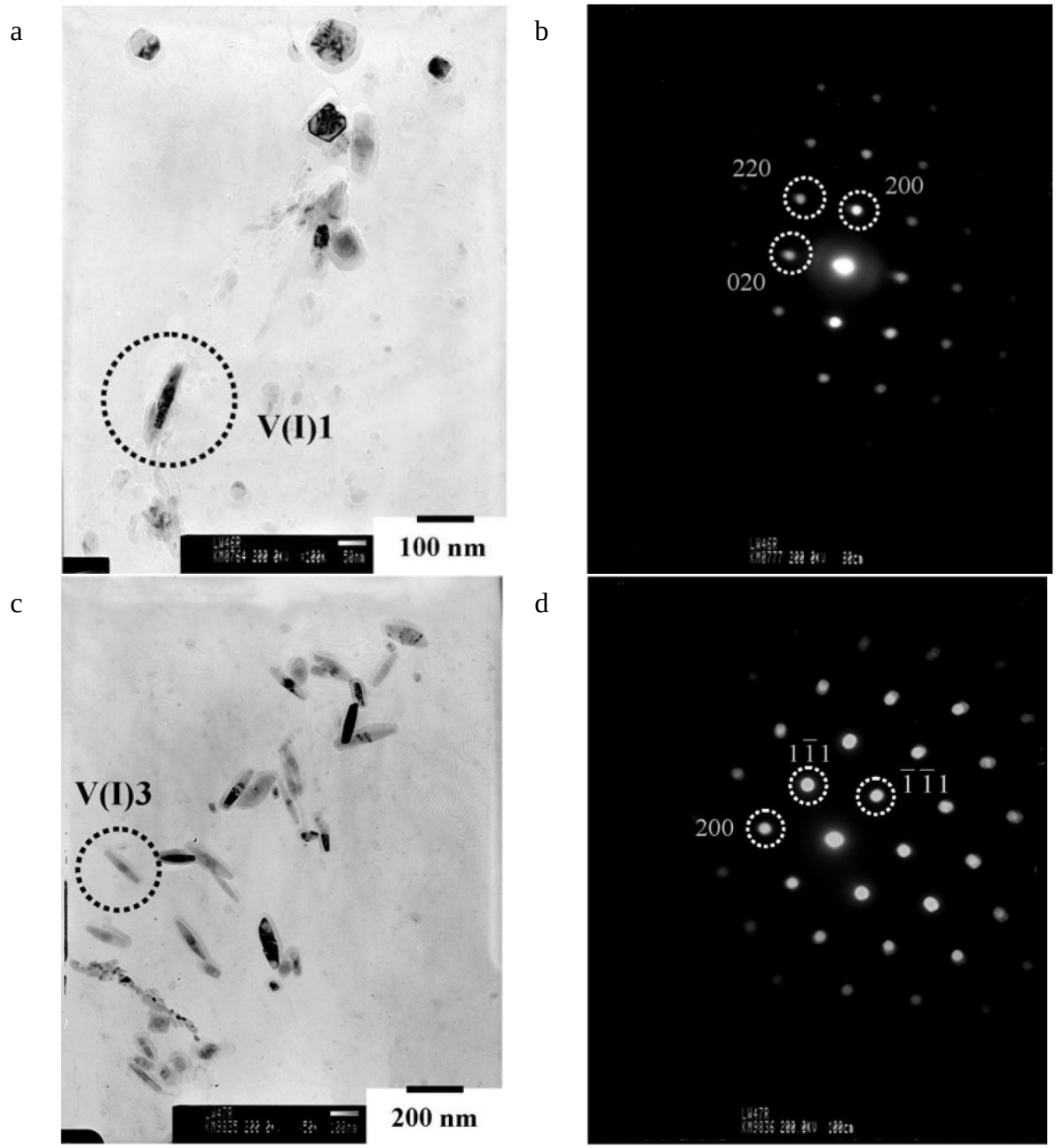

Figure 2-51: TEM micrographs of precipitates MX marked with circle named as V(I)1 and V(I)3 shown in (a) and (c), and the corresponding diffraction patterns in (b) in the [001] zone axis and (d) in the [011] zone axis, respectively [126].

2.3.2 Modelling work on carburisation

Several modelling investigations on the process of carburisation have been proposed by previous researchers. Gong et al. measured carbide volume fractions across a tube fin, as shown in Figure 2-52, and compared them with the predicted carbide volume fractions from modelling and simulation work obtained using Thermo-Calc [85], as introduced in ref [131].

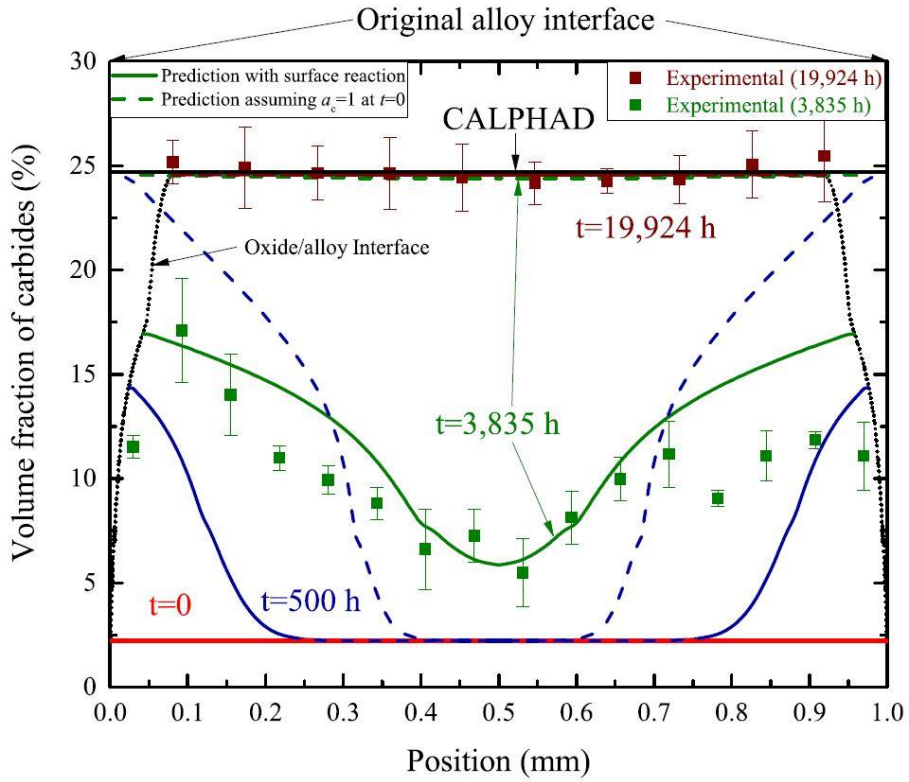

Figure 2-52: Predicted profiles of carbide volume fraction for a fin 1 mm in width exposed to experimental gas conditions at 600 °C for 0, 500 , 3835 and 19924 h, in comparison with experimental measurements [85].

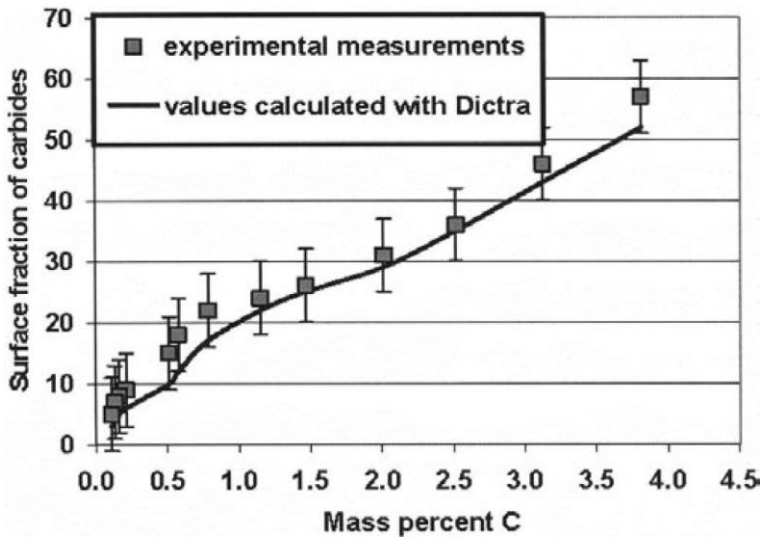

Figure 2-53: Comparison between measured and calculated values of carbide surface fraction as a function of total carbon content in Fe-13Cr-5Co-3Ni-2Mo-0.07C steel at 955 °C [132].

The results from another modelling work on carbide area fractions in Fe-Cr steel is shown in Figure 2-53 [132]. The Fe-13Cr-5Co-3Ni-2Mo-0.07C steel, carburised at 955 and 980 °C in a N_2-CH_4 gas at atmospheric pressure, was analysed using diffusion-controlled transformations (DICTRA) software to predict the carbide area fractions. The calculated results of carbide

volume fractions were consistent with the experimental results, indicating the reliability of the modelling work using DICTRA software.

Thermo-Calc is based on a description of the Gibbs energy of the individual phases at the equilibrium state. It can predict the equilibrium amount and composition of the stable phases as a function of different parameters, e.g. carbon content, temperature, or chemical composition of the analysed sample [131]. The future development of Thermo-Calc is required for experimental data, phase diagram and kinetic process assessment, as well as parameter optimisation for Thermo-Calc models and databases [133].

2.4 Remaining challenges

From the literature review, the following have been identified as challenges:

1. Comparative experiments between ferritic and martensitic steels exposed to simulant coolant gas need to be made to understand the influence of microstructure on oxidation and carburisation.
2. The evolution of oxide during the process of oxidation needs to be understood, e.g. the morphology and composition of oxide formed at different stages as a function of exposure time. The type of oxide needs to be identified as well as the carbon deposited in the oxide. This will give an understanding of the diffusion paths of carbon at different stages of oxidation. Mechanisms of oxidation and carburisation should be established for protective oxidation, breakaway initiation and post-breakaway oxidation.
3. The evolution of carbides in the process of carburisation with regard to their composition, morphology, crystal structure and lattice parameters need to be further understood.
4. Exposure conditions, e.g. temperature, time and moisture, need further consideration to identify their influence on oxidation and carburisation.
5. The definition of the time to initiate breakaway oxidation is important. Breakaway initiation needs to be analysed to establish its links to the types of oxide and carbide formed.
6. Carbide area fractions should also be investigated for carbide quantification. The area fraction needs to be plotted as a function of position and sample topography in order to understand the diffusion paths of carbon from gas to matrix.
7. There is a need to compare the behaviour of samples oxidised at high temperature for short time (HRA autoclave samples) with those oxidised at lower temperature for longer time (OMS) to see whether their mechanisms of oxidation and carburisation are the same.

2.5 Aims of the work

The primary objective of the research undertaken for this thesis is to gain a clear understanding of how the CO_2 coolant gas in AGRs oxidises the 9Cr-1Mo steel currently used as a component

in the reactors. The main areas of this research are geared toward achieving the following goals: (1) Identification of the influence of main environmental parameters which have either positive or negative correlation with oxidation and carburisation of steels. (2) Evaluation of the influence of the microstructure on the steel oxidation behaviour. (3) Identification of the chemical mechanisms and possible triggers which control the onset and subsequent propagation of breakaway oxidation. (4) The determination of accelerated ageing during high temperature short time exposure as a useful insight into the behaviour of lower temperature longer time exposure.

The detailed aims of this thesis are to:

1. Understand the influence of exposure conditions on the process of oxidation by measuring the oxide thickness and observing the morphologies of oxide formed at the different stages of oxidation.
2. Understand the process of oxidation by identifying the type of oxide and deposited carbon in the oxide with SEM-EDS and scanning laser Raman spectroscopy from samples selected from different oxidation regimes, as well as the distribution of key elements, oxide types and carbon deposits.
3. Identify precipitates embedded in the matrix by analysing the elemental distribution, crystal structure and lattice parameters of the precipitates from selected samples at different stage of oxidation and carburisation.
4. Establish the link between oxide thickness and the carburised layer. The process of carburisation can be investigated by calculating the carbide area fractions across the fin of finned samples. Understand the influence of exposure conditions on the process of carburisation by the depth of carburisation and the value of carbide area fractions in the same location from different samples.
5. Understand the mechanisms of oxidation and carburisation and oxide growth models. Understand the evolution of oxide and carbide based on investigation of experimental autoclaved ferritic 9Cr-1Mo steels.
6. Understand whether the basic mechanisms of samples oxidised at lower temperature with longer duration are the same as those oxidised at higher temperature but shorter duration. Ferritic 9Cr-1Mo steels exposed within AGR were compared with experimental autoclave samples oxidised in simulant coolant gas with regards to oxide morphology, elemental distribution and type, carbide morphology and type, and phases present.
7. Understand the influence of microstructure on the process of oxidation and carburisation. A comparison was made of experimental ferritic and martensitic samples, both of which were oxidised in simulant coolant gas. The oxide morphologies, elemental distributions and types, carbide morphologies and types, and phases present in the examined samples were analysed with several techniques to evaluate if the mechanisms of oxidation and carburisation of samples with martensitic microstructure are similar or the same as those with ferritic microstructure. The influence of exposure conditions was also taken into consideration in this investigation.

2.6 Contents of thesis

According to the aims of this investigation discussed above, this thesis constitutes nine chapters, including introduction and literature review chapters which has been discussed, as follows:

Chapter 1: an introduction to the evolution of reactors, AGR reactor structure and the reason 9Cr-1Mo steels were selected as a component material in AGR. Chapter 2: literature review discussing previous work from many researchers on Fe-Cr steels, including mechanisms of oxidation, oxide identification and carbide evolution and corresponding modelling work. The remaining challenges are also discussed together with the aims of this work and the contents of the thesis. Chapter 3: an introduction to the selected samples and techniques used for analysis, specifically the functions used in this thesis. Chapter 4: oxidation and carburisation behaviours are investigated with experimental ferritic 9Cr-1Mo samples under different exposure conditions oxidised in autoclaves in a simulant coolant gas. Several novel technologies are used to establish the mechanisms of oxidation and carburisation. Oxides and carbides formed during exposure were analysed and the data may be useful for future modelling work. Chapter 5: investigations of ferritic experimental 9Cr-1Mo samples oxidised within an AGR environment to compare with those studied in Chapter 4. Oxide close to the oxide/metal interface and internal oxidation zone were identified for a comparison with samples discussed in Chapter 4. Carbide morphologies and types are analysed to confirm if the basic mechanisms of oxidation and carburisation are similar to those oxidised in autoclaves. Chapter 6: investigations of the behaviour of martensitic experimental 9Cr-1Mo samples oxidised in simulant coolant gas to compare with those discussed in Chapter 4, providing information on the influence of microstructure. Morphologies and types of oxide and carbides were analysed to understand the mechanisms of oxidation and carburisation, which will help to confirm the reliability of the established models for oxide and carbide growth discussed in Chapter 4. Comparison of the results from Chapters 6 and 4 helps understanding of the corrosion resistance of steels with different microstructures. A general discussion is provided in Chapter 7, followed by conclusions in Chapter 8 and suggested future work in Chapter 9.

Chapter 3: Materials and analytical techniques

The introduction of SEM-EDS and scanning laser Raman spectroscopy in this chapter is based on my first author paper published in "A study of breakaway oxidation of 9Cr–1Mo steel in a Hot CO_2 atmosphere using Raman spectroscopy" Mater. High Temp. 35 (2018) 50–55. © Materials at High Temperatures

In this chapter, we will discuss material selection, including chemical composition before exposure, exposure conditions, sample preparation and analytical techniques adopted.

3.1 Sample characterisation

3.1.1 Materials

The microstructure of experimental 9Cr-1Mo steel samples denoted "HRA" and "DNB" are ferrite and martensite respectively, and these were provided with different heat treatments. (1) Experimental 9Cr-1Mo DNB steels were normalised and tempered to produce martensitic microstructure. (2) The experimental 9Cr-1Mo HRA steels were given an anneal heat treatment to produce a ferritic microstructure [134]. Virgin DNB samples were cut from DNB experimental Cast 1543 finned tube while virgin HRA samples were cut from HRA experimental X375424C finned tube.

3.1.2 Exposure to CO_2-based gas

Experimental ferritic finned 9Cr-1Mo steels provided by Wood PLC were exposed to two different types of atmosphere: (1) experimental HRA samples were exposed to a simulant CO_2-based coolant gas in a laboratory autoclave. The samples will be described as A-temperature-time for moisture that is 400 vppm, otherwise as A-temperature-time (moisture) in this investigation; (2) experimental HRA ferritic 9Cr-1Mo steels oxidised within AGR coolant gas known as oxidation monitoring scheme (OMS) samples will be described as sample ID-temperature-time.

Experimental DNB finned 9Cr-1Mo steels provided by Wood PLC were all exposed to a simulant CO_2-based coolant gas in a laboratory autoclave. These samples will be described as B-temperature-time for moisture that is 400 vppm, otherwise as B-temperature-time (moisture).

Chemical compositions of HRA and DNB experimental samples before and after exposure within AGR with different types of cast are shown in Table 3-1. Related information on OMS

samples, autoclave samples and analytical techniques used are detailed in Table 3-2, Table 3-3 and Table 3-4, respectively.

Table 3-1: Chemical composition (in wt. %) for HRA and DNB tubes and within AGR samples with different cast.

AGR		*C*	*S*	*Si*	*Mn*	*P*	*Cr*	*Mo*	*Ni*	*Co*	*Cu*	*Fe*
Autoclave Samples	*HRA*	*0.093*	*0.008*	*0.67*	*0.47*	*0.011*	*9.2*	*1.04*	*0.21*	*0.02*	*0.16*	*Balance*
	DNB	*0.083*	*0.007*	*0.42*	*0.43*	*0.010*	*8.6*	*0.99*	*0.21*	*0.02*	*0.09*	*Balance*
HRA OMS samples	*Cast 756*	*0.11*	*0.08*	*0.53*	*0.57*	*0.001*	*8.9*	*1.00*	*0.29*	*0.02*	*0.01*	*Balance*
	Cast FA171	*0.12*	*0.008*	*0.62*	*0.48*	*0.010*	*9.1*	*0.94*	*0.18*	*0.02*	*0.14*	*Balance*

Table 3-2: Information and exposure conditions of HRA OMS samples

AC/carriers	*Sample ID*	*Indicative temperature (℃)*	*Duration (kh)*	*Moisture*	*Description*	*BA*
Lo9Cr	*T01M26*	*495*	*~172*	*Variable*	*9% Cr Tube Type 1 Cast 756*	*N*
AC5	*M92M02*	*580*	*~147*	*Variable*	*HYA T6M Spares: Finned 9% Cr Tube Type A Cast FA171*	*Y*
AC5	*M96M01*	*580*	*~147*	*Variable*	*HYA T14M Spares: Finned 9% Cr Tube Type B Cast FA171*	*Y-initiating*

AC indicates that sample was oxidised in the autoclave, but with the coolant gas from the reactor; Lo9Cr indicates that the sample was oxidised within the reactor [135]. BA: breakaway; kh: one thousand hours.

Table 3-3: Information and exposure condition of autoclave samples

Category	*Sample ID Wood*	*Gas condition (vppm)*	*Temperature (℃)*	*Duration (hrs)*	*Weight gain ($mg \cdot cm^{-2}$)*	*BA*
HRA	*Virgin*	/	/	/	/	/
HRA	*8133*	*400*	*580*	*2542*	*8.9*	*N*
HRA	*8525*	*400*	*600*	*1510*	*17.1*	*N*
HRA	*8734*	*1200*	*600*	*1520*	*13.7*	*N*
HRA	*8525*	*400*	*600*	*3835*	*18.4*	*N*
HRA	*8726*	*1200*	*600*	*17065*	*93.1*	*Y*
HRA	*8195*	*400*	*640*	*245*	*10.0*	*N*
HRA	*8147*	*400 to 800 @ 245*	*640*	*1495*	*25.0*	*Y*
HRA	*8187*	*400*	*640*	*2526*	*30.6*	*N*
HRA	*8179*	*400*	*640*	*3074*	*56.5*	*Y*
HRA	*8203*	*400*	*640*	*3334*	*69.7*	*Y*
HRA	*8204*	*400*	*640*	*3639*	*90.8*	*Y*
HRA	*8211*	*400*	*640*	*3883*	*54.3*	*Y*
DNB	*Virgin*	/	/	/	/	/
DNB	*8104*	*400*	*580*	*5000*	*13.0*	*N*
DNB	*8666*	*1200*	*600*	*3020*	*30.4*	*Y*
DNB	*8418*	*400*	*600*	*3835*	*23.8*	*N*
DNB	*8667*	*400*	*620*	*3736*	*23.3*	*Y*
DNB	*8273*	*400*	*640*	*245*	*10.1*	*N*
DNB	*8295*	*400*	*640*	*4887*	/	*Y*

vppm: volume parts per million; hrs: hours; 400 to 800 @ 245: moisture gas changes from 400 to 800 vppm after 245 hours; BA: breakaway.

Three constant gas conditions existed in this investigation for samples exposed under simulated autoclave conditions: (1) Low moisture gas 400 vppm, (2) High moisture gas 800 vppm and (3) Very high moisture gas 1200 vppm. The respective contents of the gases were as follows:

1. 400 vppm: 300 vppm H_2O, 100 vppm H_2, 300 vppm CH_4, 1 vol % CO, balance CO_2.
2. 800 vppm: 700 vppm H_2O, 100 vppm H_2, 300 vppm CH_4, 1 vol % CO, balance CO_2.
3. 1200 vppm: 1100 vppm H_2O, 100 vppm H_2, 300 vppm CH_4, 1 vol % CO, balance CO_2.

The main difference between the three was the water vapour content. Therefore, the influence of water vapour was taken into consideration as a factor which influences the process of oxidation and carburisation together with exposure temperature and time. Moreover, all autoclave samples exposed in the simulant coolant gas provided were oxidised under 600 psi pressure.

Table 3-4: Techniques used for all the samples selected (within AGR +Autoclave)

Station	***Sample ID***	***Oxidation techniques***			***Carburisation techniques***				
		OM	*SEM*	*Raman*	*XRD*	*TEM*	*STEM*	*FIB*	*HS-AFM*
HRA-OMS	*T01M26-495-171888 (Variable)*				✓			✓	
HRA-OMS	*M92M02-580 -146760 (Variable)*	✓	✓	✓	✓			✓	
HRA-OMS	*M96M01-580-146760 (Variable)*	✓	✓	✓				✓	
HRA	*Virgin*	✓			✓	✓	✓	✓	
HRA	*8133-580-2542*	✓	✓	✓	✓	✓	✓	✓	✓
HRA	*8525-600-1510*	✓						✓	
HRA	*8734-600-1520 (1200)*	✓						✓	
HRA	*8525-600-3835*	✓						✓	
HRA	*8726-600-17065 (1200)*	✓						✓	
HRA	*8195-640-245*	✓						✓	
HRA	*8147-640-1495 (400-800@245)*	✓	✓	✓	✓	✓	✓	✓	
HRA	*8187-640-2526*	✓						✓	
HRA	*8179-640-3074*	✓						✓	
HRA	*8203-640-3334*	✓						✓	
HRA	*8204-640-3639*	✓						✓	
HRA	*8211-640-3883*	✓	✓	✓	✓	✓	✓	✓	✓
DNB	*Virgin*	✓			✓			✓	
DNB	*8104-580-5000*	✓						✓	
DNB	*8666-600-3020 h (1200)*	✓						✓	
DNB	*8418-600-3835*	✓						✓	
DNB	*8667-620-3736*	✓						✓	
DNB	*8273-640-245*	✓	✓	✓	✓			✓	
DNB	*8295-640-4887*	✓	✓	✓	✓			✓	

3.1.3 Sample preparation

Samples were mounted in cross-section and polished following the same procedure for most of the experiments except for the high speed atomic force microscopy (HS-AFM). Specimens were polished with silicon carbide paper followed by diamond paste down to 1 µm and finished with vibro-polishing with silica colloidal liquid for a few hours, depending on the initial condition of samples. The surface of sample, as shown in Figure 3-1, was then ready for most of the analyses.

However, higher quality surfaces were required for HS-AFM examination. Warren et al. [136] described a procedure to prepare samples for HS-AFM. The details will not be discussed here. The main differences of sample preparation between HS-AFM and other experiments are as follows:

1. Samples for HS-AFM were polished with two new silicon carbide papers with each grit number 600, 1200, 2500 and 4000.

2. Samples for HS-AFM were subjected to further cleaning steps. They were thoroughly rinsed with de-ionised water and detergent.
3. The length × width × height of the sample (including mounting material) for HS-AFM is up to 2 × 2 × 1 cm.
4. Vibro-polishing of the sample for HS-AFM took three days in general. However, there were some exceptions due to the corrosion resistance of particular samples.

Samples for transmission electron microscopy (TEM) were prepared using an FEI Helios 600i dualbeam workstation described later, which provides imaging using both SEM and FIB. The samples were milled to less than 100 nm in thickness to ensure electron transparency. The size of the thin foils was approximately 15 × 6 × 0.1 µm.

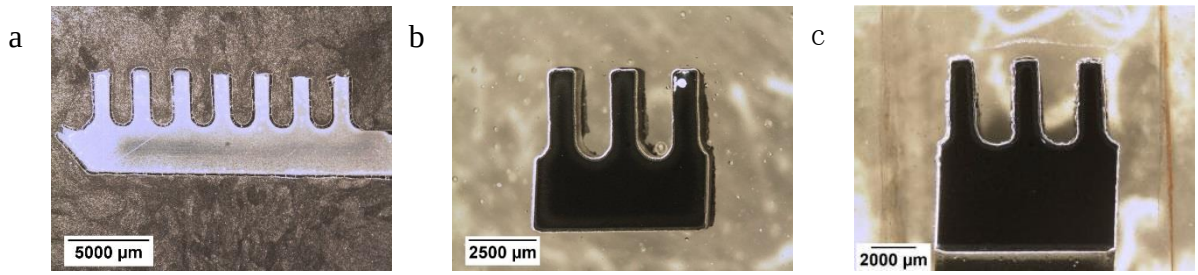

Figure 3-1: Cross-section overview of (a) within AGR sample, (b) autoclave HRA sample and (c) autoclave DNB sample.

3.2 Optical microscopy

The optical microscopy (OM) is widely used for surface and structure observation of metallic samples. The limit resolution d_{min} of optical microscopy can be deduced from the following Equation 3.1 according to ref [137]:

$$d_{min} = \frac{K\lambda}{2NA} \qquad 3.1$$

where K is a constant which has a value of 1.22 when the objective is filled with light from a suitable condenser; λ is the wavelength of the monochromatic incident light; and NA is the numerical aperture. Microscopes are usually provided with a series of NA ranging from 0.1 to 1.3. Visible light wavelength ranges from ~650 nm at the red end of the visible spectrum to ~400 nm at the blue end of the spectrum. Therefore d_{min} at the blue end provides 1.5 times better resolution than at the red end.

3.3 Scanning laser Raman spectroscopy

Infrared absorption and Raman scattering are the main spectroscopies used to observe vibrational, rotational, and other low-frequency modes in a system [138]. Therefore, Raman spectroscopy is often used to provide structural fingerprints which can identify molecules.

3.3.1 Background

Raman spectroscopy relies on inelastic scattering of monochromatic light, which is usually a laser. The laser light interacts with molecular vibrations, phonons or other excitations in the system, resulting in an energy shift of laser photons which provide information of the vibrational modes [139]. The associated energy shifts are those required to cause nuclear motion. If only electron cloud distortion is involved in scattering which is elastic, the photons will be scattered with very small frequency changes, because the electron has low mass, 9.1×10^{-31} kg [140]. For molecules it is called Rayleigh scattering. However, if nuclear motion is induced during the scattering process, energy will be transferred either from the incident photon to the molecule or from the molecule to the scattered photon. Inelastic scattering results in the energy of the scattered photon being different from that of the incident photon by one vibrational unit. This is Raman scattering, which is inherently a weak process in that only one in every 10^6–10^8 photons are affected. For some laser Raman spectroscopy instruments, manual calibration with silicon with a wavelength peak at 520.5 cm^{-1} is recommended [141].

Figure 3-2 shows the basic process for Raman scattering. At room temperature, most molecules tend to be present in the lowest vibration level (m). Rayleigh scattering is the most intense process as most photons are scattered in this way. No energy changes are involved in this process, leading to the light returning with the same energy. If the Raman scattering process starts from the ground vibrational state, m, molecules absorb energy during the process and are eventually excited to a higher vibrational state, n. This process is called Stokes scattering. Molecules exist in an exited vibration at state, e.g. n. The scattered photon returns at a lower energy. Scattering from higher vibrational states to the ground state is called anti-Stokes, involving energy transferred to the scattered photon so it returns at a higher energy.

Raman mapping is used in this investigation. For the previous works, a Raman spectrum is acquired from each point in a rectangular area 40 × 40 μm by moving the sample stage, as will be discussed in the following section.

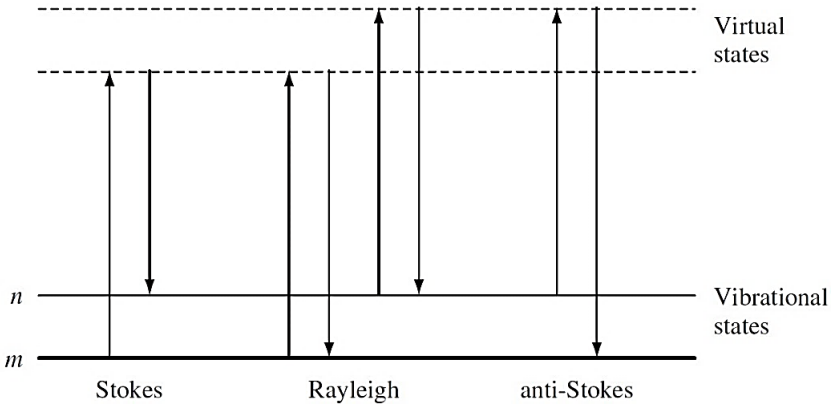

Figure 3-2: Diagram of the Rayleigh and Raman scattering processes [142].

3.3.2 Area mapping

The advantage of the Raman instrument used in this project is the area Raman mapping, which is capable of producing images by rastering the surface of the sample to determine spatially resolved chemical composition and classification. Chemical composition is often used to obtain contrast for spatial distribution of chemical components. Mapping is used especially when the number of pixels is small, i.e. from 100-1000 pixels. The intensity at each pixel is proportional to the amount of chemical component at the point corresponding to that pixel. The relative composition can also be determined based on the ratio of two components intensity [143].

An auto-calibration Renishaw inVia Raman spectrometer incorporating a Leica optical microscope with a Leica N-plan 50× objective lens (NA = 0.75) was used for acquisition of Raman spectra and maps in this investigation. The resolution is approximately 0.4 μm calculated by Equation 3.1. The instrument uses a 532 nm wavelength Nd: YAG laser. Raman maps were obtained by scanning over a 40 × 40 μm region, moving the stage in 1 μm steps and acquiring for 40 s per point. 10 % laser power was used to limit sample damage, corresponding to 3 mW power at the sample surface. Calibration was performed automatically using a silicon sample integral to the instrument. The maps and spectra were processed using Renishaw Wire version 4.3 software with peaks fitted and baselines removed.

3.3.3 Composition and phase identification

The oxide formed on steels can be identified by laser Raman spectroscopy. Figure 3-3 shows Raman spectra recorded from samples exposed in different environments in which different oxides were formed [144]. These oxides were identified from Raman shifts of peaks. Peaks at 295 and 408-414 cm^{-1} are indicative of the presence of haematite, 547-557 cm^{-1} for chromia, 664–685 cm^{-1} for corundum solid solution and 680-690 cm^{-1} for spinel phases [145][146][147][148]. In this way, the composition of certain oxides can be obtained based on the peaks present in Raman spectra.

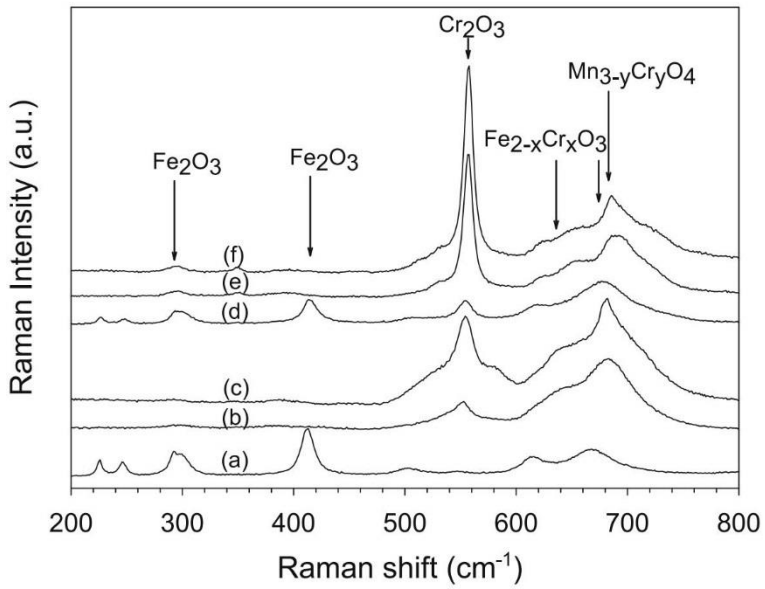

Figure 3-3: Raman spectra of AISI 441 ferritic stainless steel samples oxidised in air: (a) 650 °C, 5 min; (b) 850 °C, 5 min; (c) 850 °C, 60 min; in water vapour: (d) 650 °C, 5 min; (e) 850 °C, 5 min; (f) 850 °C, 60 min [144].

Figure 3-3 shows that the peak at around 295 cm^{-1} is obvious in spectra (a) and (d), indicating the presence of haematite, low intensity in spectrum (e), indicating the reduction of haematite and almost none in (c) and (d). It illustrates that Fe_2O_3 is mainly formed in the samples exposed at 650 °C and decreases with the increase of exposure temperature and time. The peaks for $Fe_{2-x}Cr_xO_3$ are not clear in the spectra.

The peak for chromia at 547-557 cm^{-1} is absent in spectrum (a) and has low intensity in (b) and (d) while high intensity of this peak is shown in (c), (e) and (f). It appears that Cr_2O_3 increases with the increase of exposure temperature and time. The stress of the examined sample can be obtained from a plot of Raman shift as a function of pressure discussed in ref [102]. It seems that $Mn_{3-y}Cr_yO_4$ exhibits a similar tendency with Cr_2O_3.

Raman spectra provide information of phases formed in the examined samples as well as changes due to the environment by comparing samples exposed to different conditions.

3.4 Scanning electron microscopy

Unlike an optical microscope, a scanning electron microscope (SEM) produces images with electrons rather than light. Electrons interact with atoms close to the surface to produce various signals containing information relating to surface topography and composition. SEM is capable of achieving better than 1 nm resolution but this is controlled by the incident beam diameter [149]. Therefore, it is very effective for studying crystal morphology on a microscale.

3.4.1 Instrument

In a typical SEM, an electron beam emitted from an electron gun is focused by one or two lenses to a spot 0.4-5 nm in diameter. The beam then passes through deflection coils which deflect the beam in the x and y axes, as shown in Figure 3-4, resulting in the scanning in a raster fashion over a rectangular area of the sample surface. Several types of detectors installed in the instrument can be used to collect information from different signals to image the examined area.

The instrument used in this investigation was a Zeiss Sigma VP FEG-SEM, a field emission gun SEM, equipped with a silicon drift detector (SDD) converting emitted X-rays into electronic signals. The samples were analysed at 15-20 kV. The working distance was around 8 mm, which is the best distance to obtain high resolution images in this instrument.

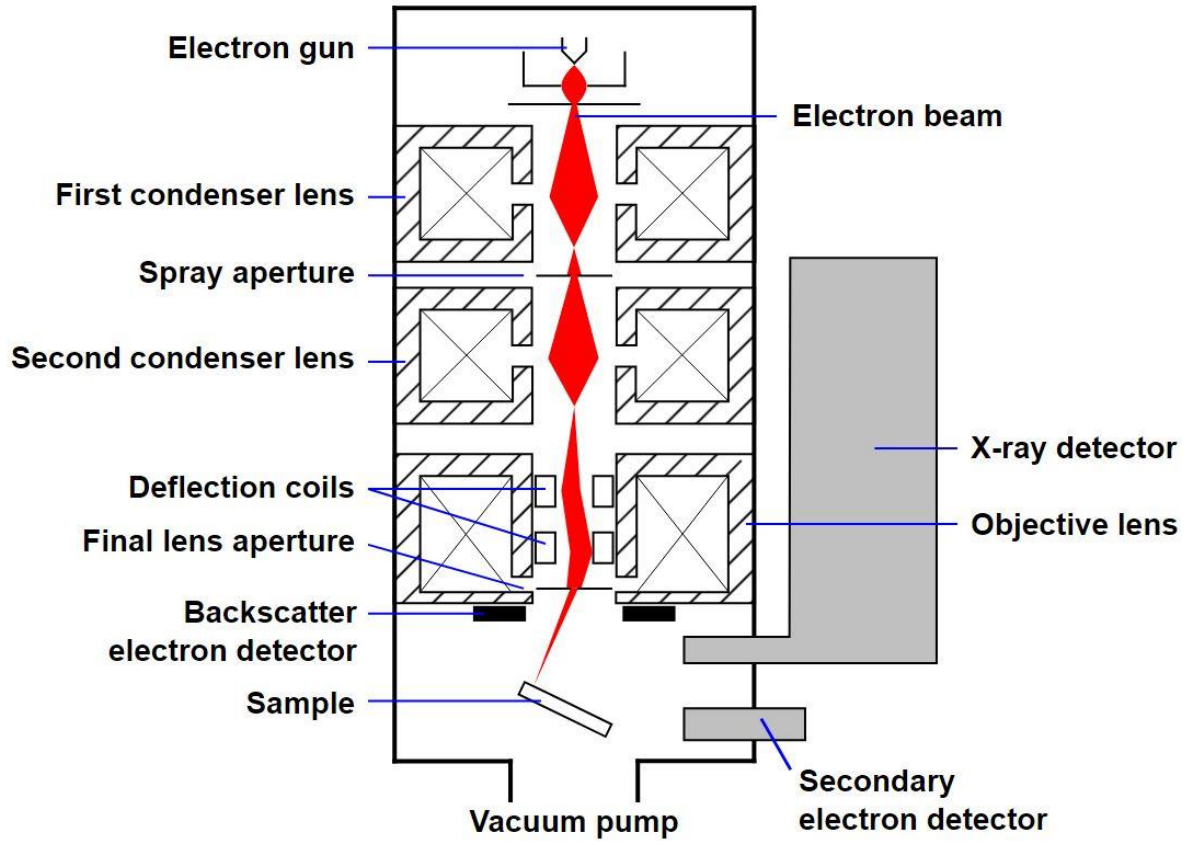

Figure 3-4: Schematic diagram of an SEM [150].

3.4.2 Electron emission

The signals used by an SEM to produce images are due to interactions of the electron beam with atoms at various depths within the sample. The types of signals used in this investigation are produced by secondary electrons (SE), reflected or back-scattered electrons (BSE), and characteristic X-rays, absorbed current (sample current) and transmitted electrons. Secondary

electron detectors are standard equipment in all SEMs, but it is rare that a single machine would have detectors for all other possible signals.

In secondary electron imaging, the secondary electrons (SE) are emitted from a depth very close to the sample surface. Scanning electron microscopy is capable of producing very high-resolution images of the surface, revealing details less than 1 nm in size. The emission process is shown in Figure 3-5a. The primary electron (PE) ejects an electron from the surface of sample which escapes to the detector. That escaping electron is the SE captured by a detector to produce a signal and form the image.

Backscattered electrons (BSE) are produced when the incident beam electrons are reflected from the sample surface by elastic scattering, as shown in Figure 3-5b. They emerge from deeper locations within the sample than SE as demonstrated by Figure 3-6. Therefore, the resolution of BSE images is less than SE images because the interaction volume is larger, as explained below. Back-scattered electrons are often used in SEM, along with the characteristic X-ray spectra, because the intensity of the BSE signal is strongly related to the atomic number (Z) of the sample. It provides information about the elemental distribution in the examined sample. Figure 3-5b demonstrates that BSE are produced by the Coulomb repulsion between PE and nucleus of sample atom.

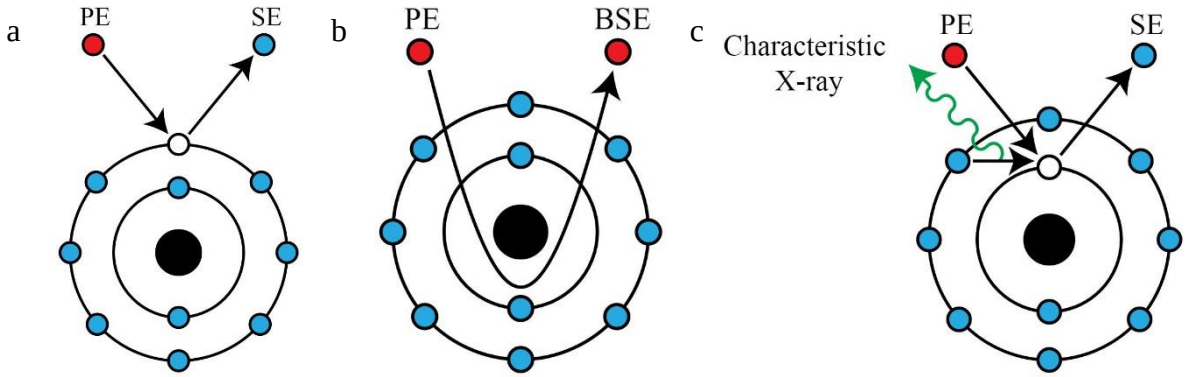

Figure 3-5: Mechanisms of emission of (a) secondary electrons (SE); (b) backscattered electrons (BSE); and (c) characteristic X-rays from atoms of the sample. PE represents primary electron [150].

A characteristic X-ray is produced when the incident PE removes an inner shell electron from a sample atom. A higher-energy electron subsequently fills the inner shell, leading to the energy release as shown in Figure 3-5c. These characteristic X-rays are used to identify the composition and measure the abundance of elements in the sample. It will be discussed in detail later.

3.4.3 Sample interaction volume

When the beam collides with the sample surface, several signals are produced to provide information from different depth within the sample, as shown in Figure 3-6. The signals used

in this thesis are secondary electrons, backscattered electrons and characteristic X-rays which will be discussed later in this chapter. Secondary electrons provide most topographic information among the four types of signals discussed. The interaction area of BSE is beneath the area of SE. It shows the different atomic number and phase with different colours. Characteristic X-rays provide signals from an extended area providing information on atomic composition.

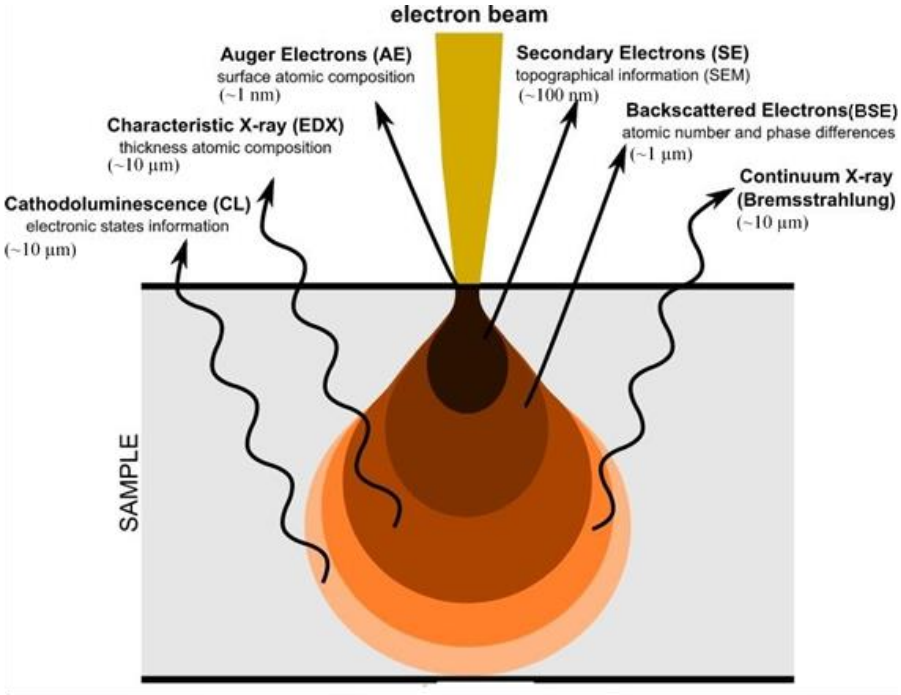

Figure 3-6: Signals emitted from different depth of sample and corresponding interaction volume [151].

3.5 Transmission electron microscopy

3.5.1 Instrument

Transmission electron microscopy (TEM) is an imaging technique in which a beam of electrons is transmitted through a sample to form an image. An image is formed from interaction of the electrons with the thin sample (<100 nm) as the beam is transmitted through the sample. TEM is an efficient tool for the characterisation of materials over spatial ranges from the atomic scale, through the nanometre regime (from <1 nm to ~100 nm) up to the micrometre level and beyond.

Signals generated resulting from interactions between a high energy electron beam and a thin sample are shown in Figure 3-7. Most of these signals can be detected by different detectors within a TEM. They provide images together with crystallographic and chemical information. With X-ray spectra from small regions, which exhibit characteristic peaks, it is possible to

identify the different elements present in different regions with high spatial resolution, as discussed in section 3.6 later.

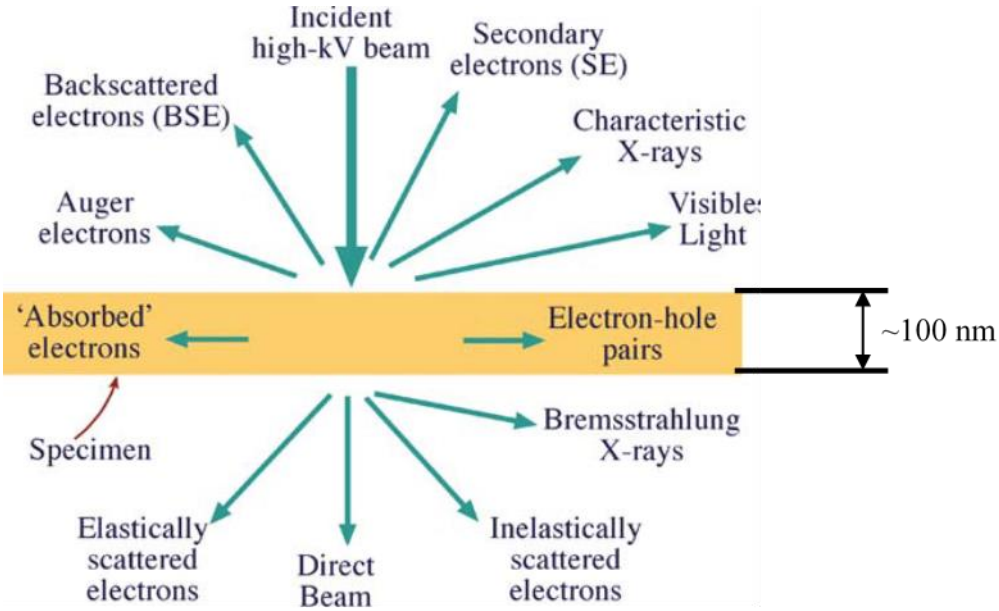

Figure 3-7: Signals generated when a high-energy beam interacts with a thin sample [152].

There are four main components to a TEM: an electron source and electron optical column, a vacuum system, the necessary electronics (lens supplies for focusing and deflecting the beam and the high voltage generator for the electron source), and control software. A typical modern TEM consists of an operating console surmounted by a vertical column, the vacuum system, and control panels (Figure 3-8) [152].

The microscope is often fully enclosed to reduce interference from the environment. In some cases, it can even be operated remotely, ensuring the operator is away from the instrument environment to benefit both the operator and the instrument. As shown in Figure 3-8, the electron column of a TEM includes elements analogous to those of a light microscope. According to ref [153], the light source of the light microscope is replaced by an electron gun, which is built into the top of the column and connected to a high voltage source (approximately 100-300 kV). The glass lenses are replaced by electromagnetic lenses. Unlike glass lenses, the power (focal length) of magnetic lenses can be changed by changing the current through the lens coil. (In the light microscope, variation in magnification is obtained by changing the lens or by mechanically moving the lens.) These focus the electron beam to the required size and location. The eyepiece or ocular is replaced by a fluorescent screen or a digital camera. The electron beam emerges from the electron gun and is condensed into a nearly parallel beam at the sample by the condenser lenses. The sample must be thin enough to transmit the electrons, typically 0.5 µm or less (less than 0.1 µm in this work). After passing through the sample, transmitted electrons are collected and focused by the objective lens and a magnified real image

of the sample is projected by the projection lens(es) onto the viewing device at the bottom of the column. The entire electron path from gun to camera must be under vacuum to prevent the scattering and absorbing of the electrons when colliding with air molecules [154][153].

The instrument used for the present work is a Philips EM430 operated at 200 kV to get the diffraction patterns of phases examined.

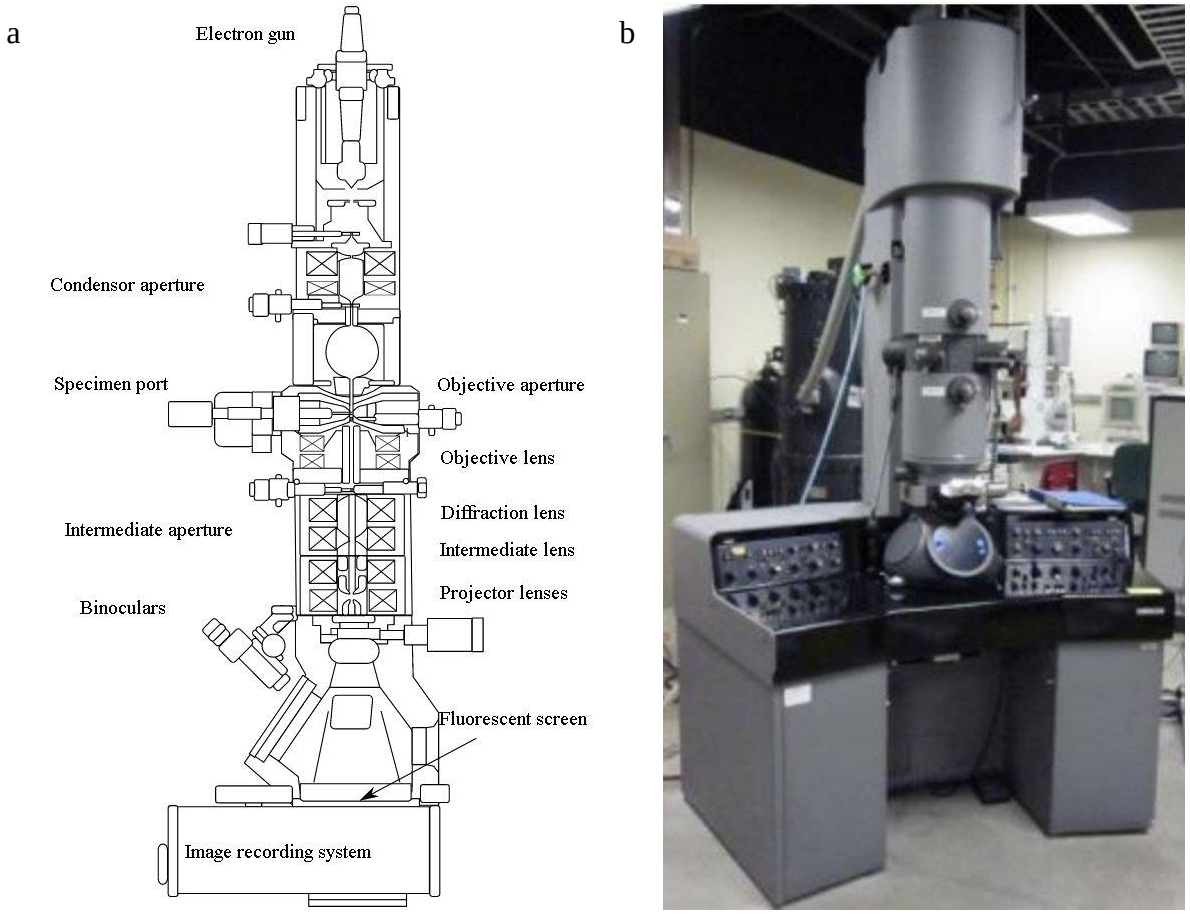

Figure 3-8: (a) Cross section of the column of a typical transmission electron microscope [152] and (b) a photograph of Philips EM430 TEM instrument used in this work [155].

3.5.2 Selected-area diffraction pattern

The standard way to obtain a diffraction pattern with a parallel beam of electrons is to use a selected-area aperture. However, it is impractical to insert an aperture at the sample plane. Consequently, an aperture in a plane conjugating with the sample is inserted to create a virtual aperture at the plane of the sample. This operation is called selected-area diffraction (SAD). As shown in Figure 3-9, the conjugate plane is the image plane of the objective lens. Selected-area diffraction patterns were created by inserting an SAD aperture into the image plane, leading to the formation of a virtual aperture. This aperture is centred on the optic axis in the middle of the viewing screen. Only electrons falling inside the virtual aperture are

allowed go through into the imaging system and contribute to the formation of SAD patterns. All other electrons (dotted lines) are blocked by the SAD diaphragm.

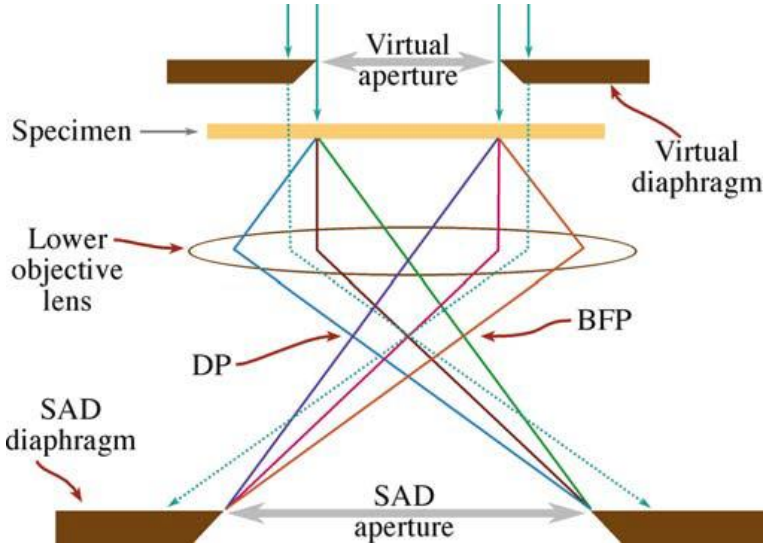

Figure 3-9: Ray diagram showing SAD pattern formation [152]. BFP represents back-focal plane

3.5.3 Principle of scanning transmission electron microscopy

Scanning transmission electron microscopy (STEM) is an extension to TEM. The electron beam is focused to a fine spot which is scanned over the sample surface in a raster. A typical STEM is a conventional TEM equipped with additional scanning coils, detectors and necessary circuitry which switch between STEM and TEM modes. High resolution STEM is usually established in an exceptionally stable room in order to obtain atomic resolution images protected from vibration, temperature fluctuation, electromagnetic waves and acoustic waves [156]. The image resolution of a TEM is governed by the ability of the objective lens, while STEM image resolution is governed by the incident electron beam size [157].

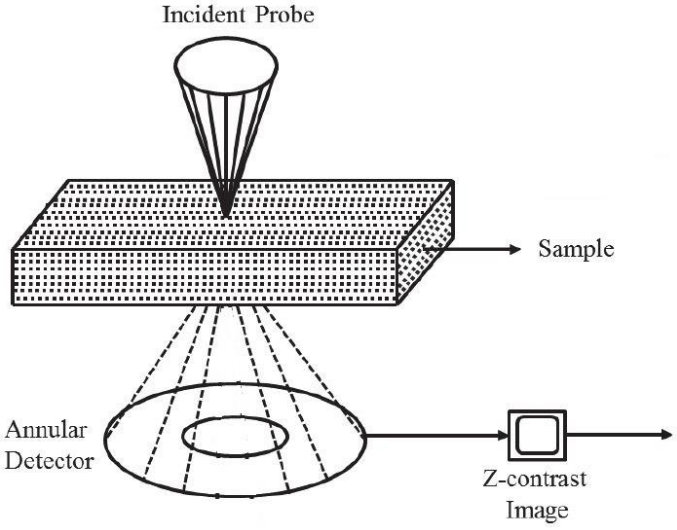

Figure 3-10: Schematic of STEM [158].

A schematic of STEM is presented in Figure 3-10. A wide range of signals are available in the STEM, but commonly collected signals for characterisation are bright field (BF), annular dark field (ADF) and EDS. In BF mode, only those transmitted electrons that leave the sample at relatively low angles with respect to the optic axis (smaller than the incident beam convergence angle) are collected. However, those electrons that leave the sample at relatively higher angles are collected as ADF. Transmitted electrons which lose energy are responsible for X-rays generated from the electron excitation and collected for EDS analysis.

Removing the SAD aperture and focusing the image with the objective lens leads to the formation of a BF image which is formed by the direct-beam electrons, as shown in Figure 3-11a, and a dark-field (DF) image formed by scattered electrons shown in Figure 3-11b. Both BF and DF images can be viewed at any magnification simply by adjusting the intermediate lenses of the microscopes. The two basic calibrations for TEM are the magnification and the fixed camera length when the diffraction pattern is formed. From Figure 3-11c, the electrons selected by the aperture travel off the optic axis, because the aperture is placed to select the scattered electrons. It is not easy to focus such a displaced-aperture DF image on an older TEM. The image moves on the screen when adjusting the objective-lens strength. The backscattered electrons need to be back on the optic axis, resulting in the formation of a DF image under this condition. This operation is called centred dark-field (CDF) imaging.

The thin foils in this work were analysed in STEM mode using an Oxford Instruments AztecTEM equipped with an advanced EDS system and X-Max 80 detector.

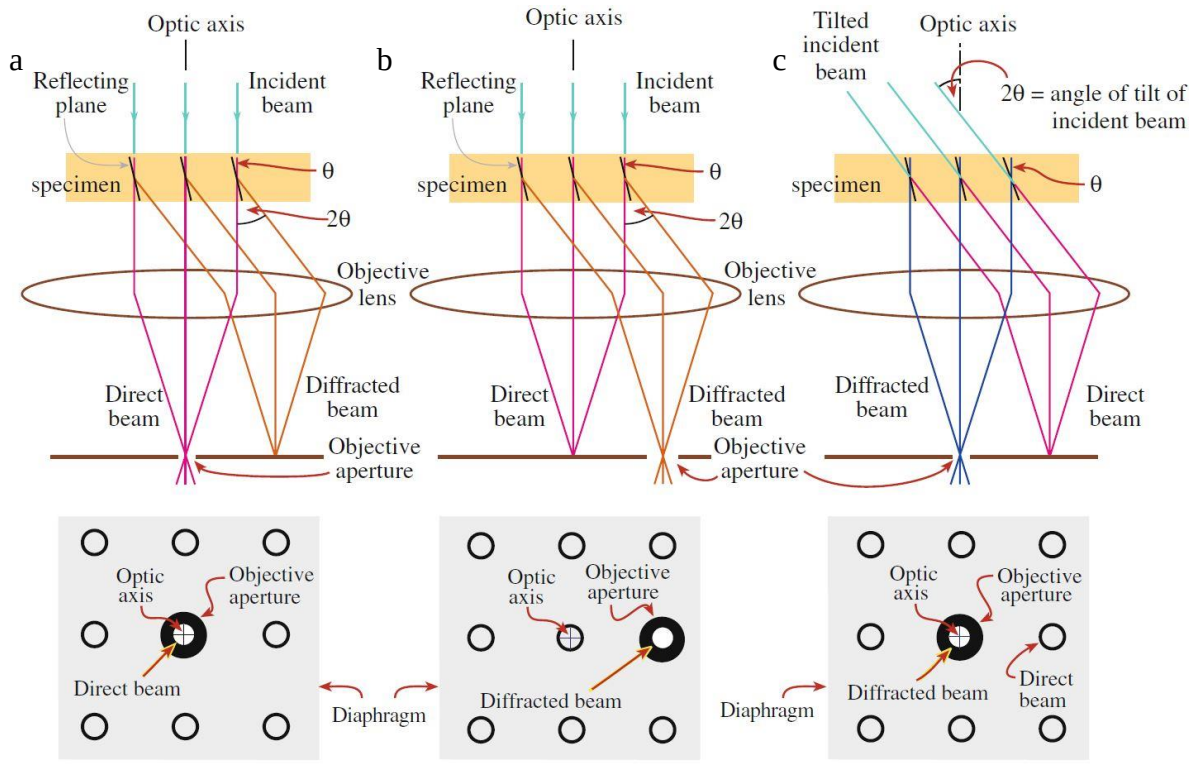

Figure 3-11: Ray diagrams showing the way to use the objective lens and aperture in combination to produce (a) a bright field image; (b) a displaced-aperture dark field image and (c) a centred dark field image [152].

3.6 Energy dispersive X-ray spectroscopy

Characteristic X-ray analysis is also called energy dispersive X-ray spectroscopy (EDS, EDX, EDXS or XEDS) [159]. It is an analytical technique for elemental analysis and chemical characterisation. Moreover, EDS is capable of gathering a spectrum of all elements above lithium within limits from the examined sample. It is also often used to estimate the relative abundance of chemical elements. However, the accuracy of quantitative analysis is affected by various factors. For instance, EDS often provides inaccurate results for light element analysis, i.e. for elements with atomic number from 4 to 9. The difficulty for analysis is due to the low count rates caused by insufficient beam current at low voltage and small spot sizes which make it difficult for microanalysis [160].

The formation of peaks in EDS spectra is explained in Figure 3-12. The ground state (K) is the most stable atomic shell which is closest to the nucleus. External stimulation, by a primary electron, excites an electron in an inner shell, which consequently leads to an electron in an outer higher energy shell filling the hole in the inner lower energy shell. Radiation energy is released, as shown in Figure 3-12. Kα represents the energy release when an electron moves

from the L to K shell. Similarly, Kβ, and Lα represent the energy release when an electron changes from M to K shell, and M to L shell, respectively [161].

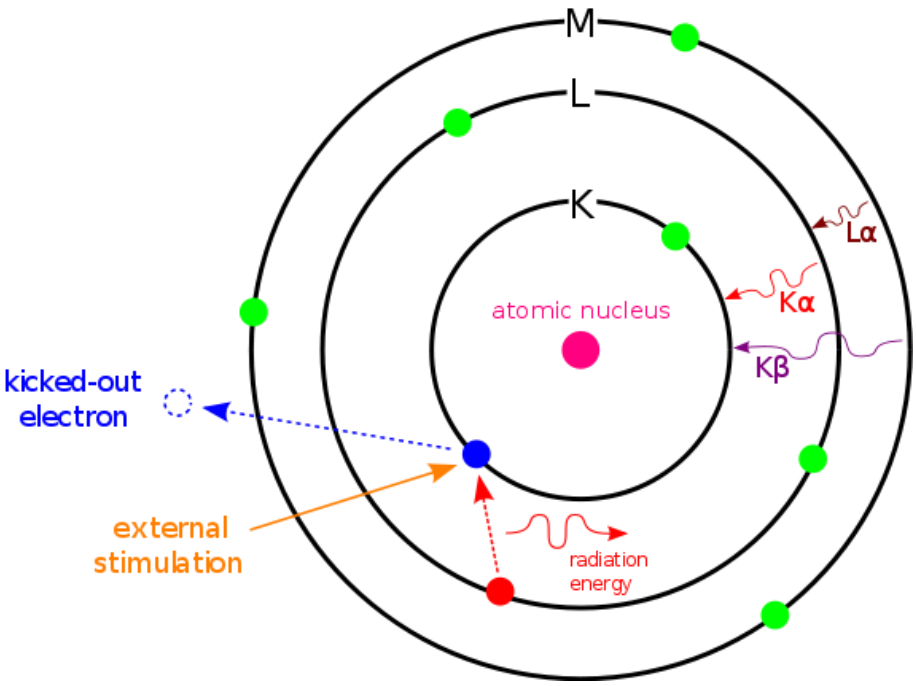

Figure 3-12: schematic drawing for EDS stimulation [162].

A Carl Zeiss Sigma field emission gun scanning electron microscope (FEG-SEM) fitted with an Octane PlusTM EDS system from EDAX^{TM} was used for SEM-EDS analysis in this investigation. High resolution secondary electron (SE) images were obtained. TEAM EDS software was used for acquiring spectra and mapping. All EDS analysis was undertaken at 15 keV primary electron energy. The electron beam interaction volume for this analysis was estimated to be approximately 500 nm in diameter. The penetration depth in a bulk sample has been discussed in Figure 3-6. According to previous investigation [163], the spatial resolution of microanalysis on thin foils for STEM has been related to the diameter of the electron probe at the lower surface of the foil while Doig, Lonsdale and Flewitt's study shows that the spatial resolution is determined by a combination of the incident beam intensity and the elemental distribution within the foil. ZAF correction was used to process the obtained data.

ZAF is an approach used in quantitative electron probe microanalysis to convert the intensity ratios into concentration units [164]. It refers to three types of corrections, Z for atomic number correction, A for absorption correction and F for fluorescence correction which are calculated separately. The Z factor deals with the difference of generated X-rays between specimen and standard, the A factor is adopted to calculate the absorption of X-ray generation, and the F factor is based on the model of Reed in most correction procedures [165].

3.7 Focused ion beam

3.7.1 Ion used for milling and imaging

Focused ion beam (FIB) is a technique used in material science for site-specific analysis, deposition and ablation of materials. It is similar to SEM except that the beam rastered over the sample is a gallium (Ga) ion rather than an electron beam [166]. In this work, FIB was used for milling and imaging. The former was used to prepare thin foil samples for TEM and STEM analysis while the latter was used for carbides revealing and carbide area fraction calculation by processing FIB images with image processing software ImageJ. Secondary electrons are emitted from the sample surface to give high-spatial resolution images.

3.7.2 Instrument

A schematic diagram of a typical FIB ion column is shown in Figure 3-13. The structure of the column is similar to that of an SEM. As discussed previously, the main difference is the use of a gallium ion (Ga+) beam rather than an electron beam. Also, lenses in FIB are electrostatic rather than magnetic due to the high mass of gallium ions compared with electrons. Reyntjen and Puers proposed that a vacuum of about 1×10^{-7} mbar is maintained inside the column [167]. The ion beam is generated from a liquid-metal ion source by the application of a strong electric field which causes the emission of positively charged ions from a liquid gallium cone formed on the tip of a tungsten needle. After a first refinement through the spray aperture, the ion beam is condensed in the first electrostatic lens. The upper octopole adjusts the beam stigmatism. The ion beam energy is typically between 10 and 50 keV, with beam currents varying between 1 pA and 20 nA. Using the variable aperture mechanism, the beam current can be varied over four decades, allowing both a fine beam for high-resolution imaging and a heavy beam for fast and rough milling. Blanking of the beam is accomplished by the blanking deflector and aperture, while the lower octopole is used for raster scanning in a user-defined pattern. The beam is focused to a fine spot by the second electrostatic lens, which enables a best resolution in the sub 10 nm range. A continuous dynode electron multiplier (CDEM) is used to collect secondary particles for imaging.

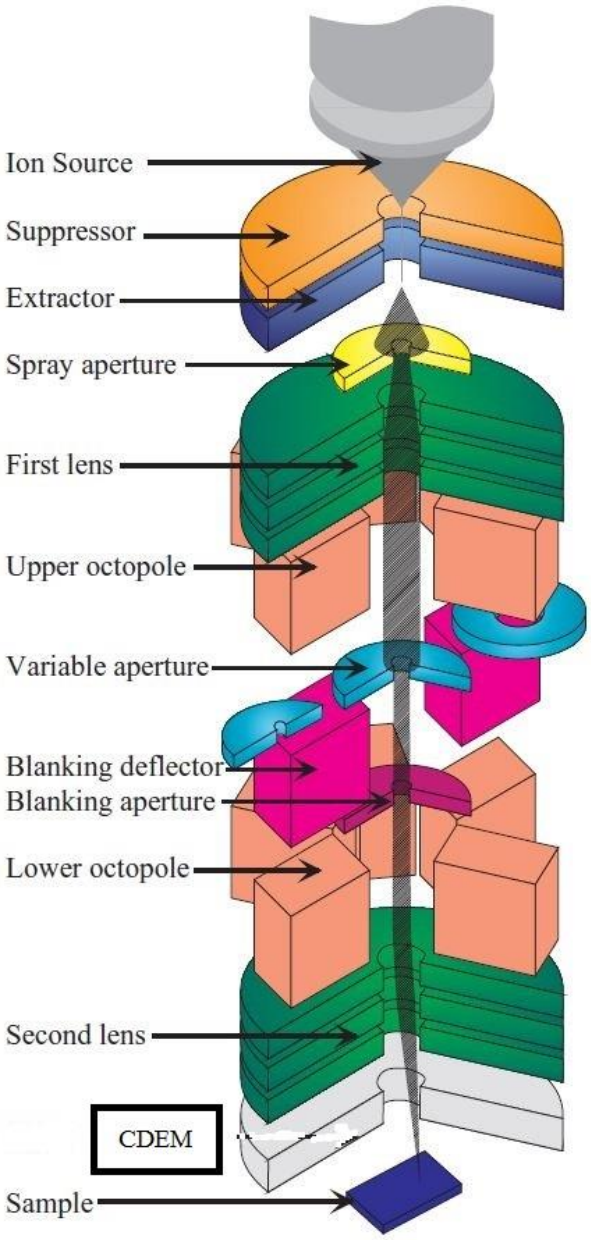

Figure 3-13: Schematic diagram of FIB ion column [167].

3.7.3 Milling, imaging and deposition

As shown in Figure 3-14a, the FIB is raster scanned over a substrate during FIB imaging. Secondary particles, including neutral atoms, ions and electrons, are generated and collected on a CDEM. Thus, the contrast shown in FIB images depends on the quantity of secondary ions and electrons reflected from different features. In this study, it causes a dark colour of carbide precipitates and a light colour of the matrix. The detector bias is a positive or negative voltage to collect secondary electrons or secondary ions, respectively. In crystalline materials, the ion penetration depth varies due to channelling along open columns in the lattice structure. Thus, FIB can be used to image crystal grains, revealing differences in crystal orientation. However, imaging with FIB causes some damage to the sample, because Ga^+ ions enter the

sample surface leading to ion implantation. The interaction volume is determined by the ion energy and the angle of incidence of the ion beam.

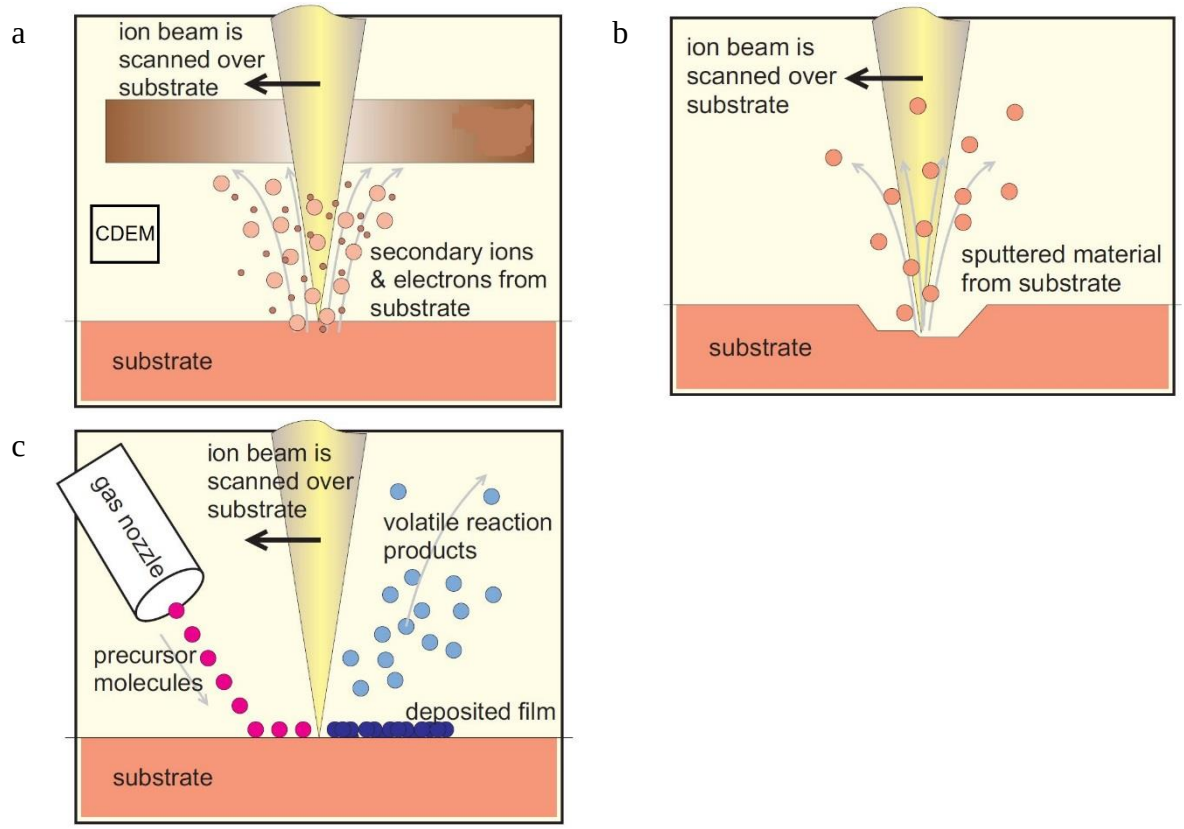

Figure 3-14: Principle of FIB (a) imaging; (b) milling; (c) deposition [167][168]. CDEM represents continuous dynode electron multiplier.

Figure 3-14b illustrates the physical sputtering of the sample schematically. An arbitrary shape can be etched by scanning the substrate with a high ion current beam. The introduction of XeF_2 was applied for precipitate observation after communicating with Drs. Geoff West and Peter Heard. An etching gas, e.g. XeF_2, can be introduced to speed up the etching process for some materials. However, it is also found that XeF_2 is useful in revealing the distribution of precipitates embedded in a matrix. It is believed that the XeF_2 gas either adheres to the cleaned metal surface or reacts within a very thin layer, e.g. a monolayer, on the sample surface which significantly increases the secondary electron yields of these regions and giving a uniform 'bright' background. The gas doesn't appear to adhere to precipitates and has varying adherence to secondary phases.

Figure 3-15 shows a schematic diagram illustrating how the XeF_2 gas reveals carbides from the matrix. The critical gas XeF_2 adheres to the metal surface changing the work function of metal surface. The work function represents the minimum energy required to remove an electron from the metal [169][170][171]. The work function has been changed with XeF_2 gas, which either adheres to the metal surface or reacts with a monolayer of metal to reduce the work function of the metal, thus more secondary electrons are yielded by the metal surface and

detected by the detector, showing a higher brightness in the corresponding FIB XeF_2 image. However, it appears that the gas doesn't tend to adhere to the precipitate surface, thus the work function keeps the same which is higher than the metal surface, leading to a dark region of these secondary phases in the corresponding FIB XeF_2 image. Michaelson's work has detailed the work function of many elements, showing that the work functions of Fe, Cr, Mo and C are 4.5, 4.5, 4.6 and 5 eV, respectively [170]. Fujii et. al studied the work function of a few types of MC carbides and Cr_3C_2, with the results ranging from 4.8 to 5.2 eV [172]. It appears more energy is required to bring free electrons from carbon and carbides than the metal Fe, Cr and Mo. Gas XeF_2 further reduces the work function of metal surfaces which are mainly comprised of elements Fe, Cr and Mo. Thus, more electrons are removed from metal surfaces than carbide precipitates after exposing to XeF_2.

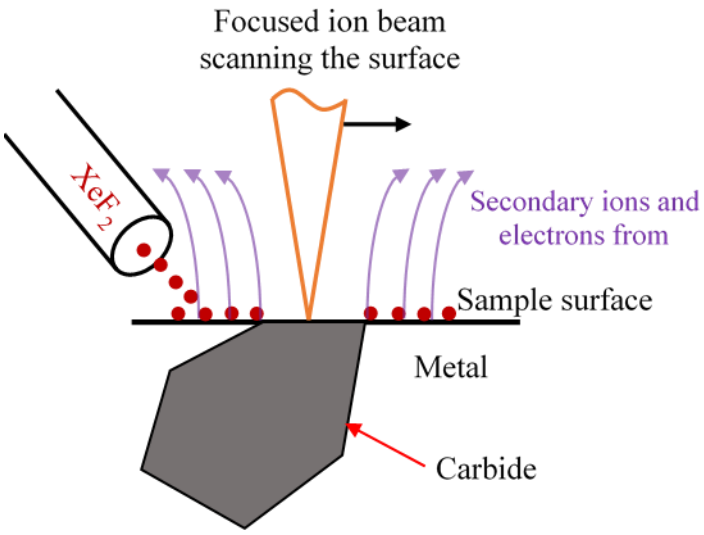

Figure 3-15: A schematic diagram illustrating the work function of XeF_2 in FIB system on the metal surface.

Focused ion beam technology can also be used for localised deposition of metals and insulators. The process of deposition is illustrated in Figure 3-14c. A precursor gas is sprayed onto the surface by a fine needle, where it is adsorbed. The incident ion beam then decomposes the adsorbed precursor gas. The volatile reaction products desorb from the surface and are removed through the vacuum system, while the desired products remained on the surface as a thin film.

The focused ion beam instrument used for this work was an FEI FIB-201 single gallium ion beam instrument, operating at 30 keV beam energy using insulator enhanced etch (IEE) mode, which introduces XeF_2 gas into the system. FIB images were obtained by initially cleaning regions of the sample by sputtering an area of 120 × 100 μm at 11 nA beam current and 30 kV for about 10 s to remove surface contamination and oxide. Ion-induced secondary electron images were then obtained at 150 or 90 pA beam current showing topographical and ion channelling contrast. Following acquisition of the initial image, XeF_2 gas was introduced into the system for a few seconds to functionalise the surface, and further images were obtained at

low and high magnification. The resulting images have reduced ion channelling contrast but show carbide precipitates as darker regions.

3.7.4 The dualbeam instrument

Dualbeam is a technique that combines SEM and FIB in one system. Nowadays, most modern FIB instruments with a FIB column are combined with an additional SEM column to become a "dualbeam" platform. It is often applied for transmission electron microscopy (TEM) sample preparation and microstructural analysis [166].

It can be seen from Figure 3-16 that in a dualbeam platform both electron beam and Ga^+ ion beams interact with the sample at the same location. However, there is an angle between the incident electron beam and ion beam. Emitted electrons and sputtered particles are generated and collected by the corresponding detector to form SEM and FIB images, respectively.

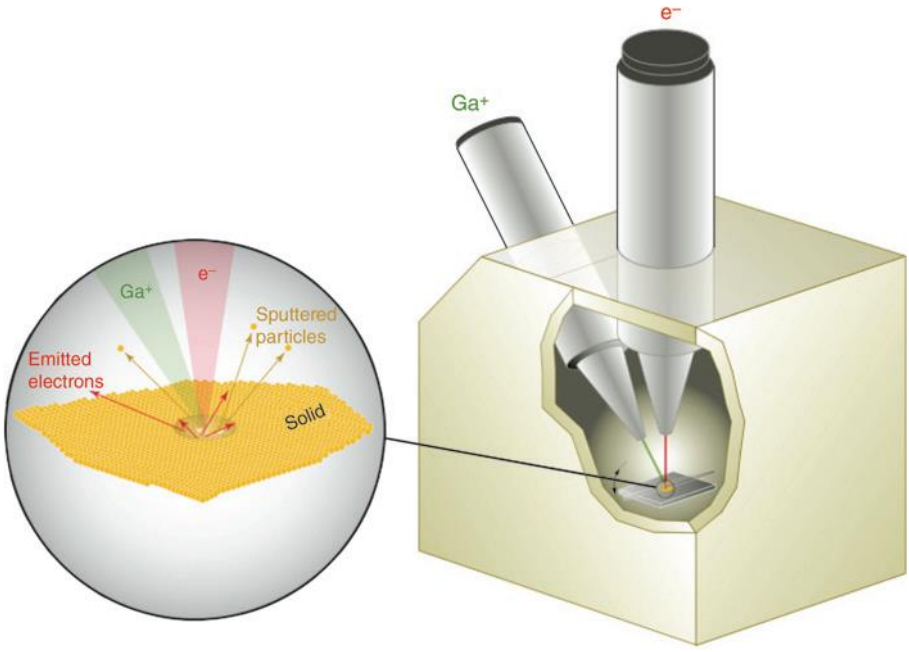

Figure 3-16: Schematic illustration of dualbeam and expanded view showing electron and ion beam sample interaction [166][168].

Thin foils of 15 × 6 × 0.1 μm in size were prepared using the ion milling, lift-out method in a FEI Helios NanoLab 600i combined FIB/SEM dualbeam system, as described below.

3.7.5 Preparation of TEM thin foils by dualbeam

A TEM sample is prepared in the form of a thin foil which is less than 100 nm in thickness, as discussed previously, to ensure that the incident electron beam penetrates the foil to obtain the corresponding diffraction pattern, which is used for phase identification determined by crystal structures and lattice parameter(s) obtained.

The dualbeam is used in sample preparation for TEM thin foils due to the ability to add or remove materials with high precision. A 52 ° angle between the SEM and FIB beams makes it possible to observe samples in both SEM and corresponding FIB images at different angles, as shown in Figure 3-17 [173]. An in-situ lift-out needle was used to pick up thin foil samples for further low energy milling after being attached to a copper grid in this work.

Using low energy Ga^+ ions, it is possible to avoid many scanning artefacts and physical effects (e.g. ion channelling). Moreover, the thin foil is less damaged by an ion beam with low energy milling and thus suitable for further TEM and STEM analysis. The ion energy was reduced to 5 keV or even lower for low energy milling, in the final polishing step for a TEM thin foil preparation, resulting in a higher quality surface for high resolution imaging [173].

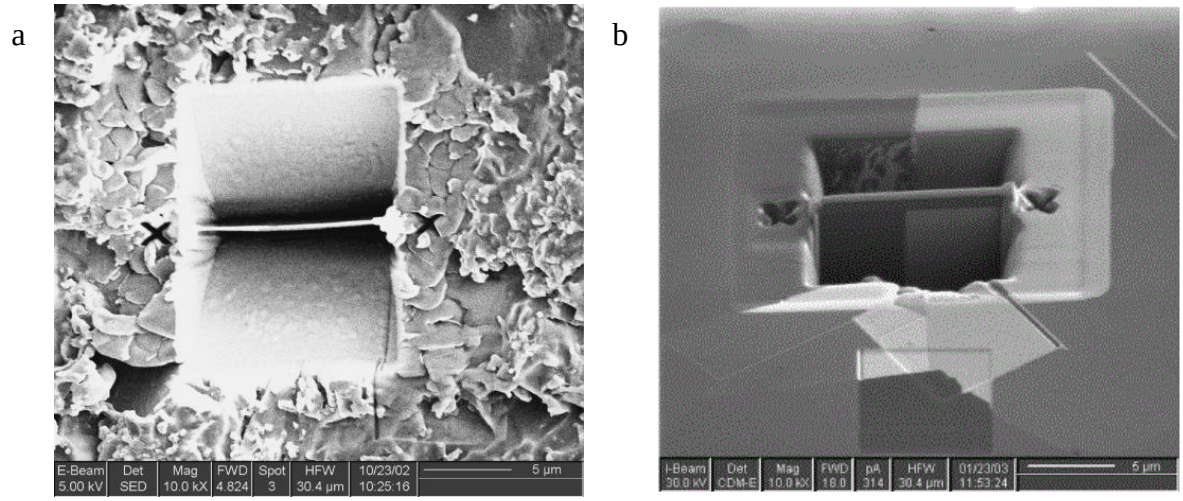

Figure 3-17: The thin foil observed from (a) SEM image at a final state and (b) FIB image in the midway through the preparation process [173].

3.8 High speed atomic force microscopy

3.8.1 Background

Atomic force microscopy (AFM) is a technique that allows imaging and measurement of a sample surface structure with unprecedented resolution and accuracy [174]. Atomic force microscopy (AFM) is different from other microscopies, e.g. optical microscopy and SEM, which form images with light or electrons, AFM physically contacts a surface of the sample with a sharp probe forming maps according to the height of the surface. It often provides higher resolution than SEM. As we know, SEM is operated in a vacuum environment. However, AFM can be operated in an ambient atmosphere. Atomic force microscopy scanning is generally a slower process than SEM imaging. Atomic force microscopy is able to form an image in three dimensions (3D) so that the height, length, width or volume of any feature can be obtained.

The design of a typical AFM is as shown in Figure 3-18 [174]. The force between the probe and sample surface is measured by a force transducer. Feedback control is used to keep the force constant by controlling the expansion of a z piezo transducer, which moves up and down to follow the sample surface. This distance is measured to give the sample topography. The force between the tip and sample is kept at a set value. This also effectively maintains the distance between tip and sample at a fixed value. The xy piezo actuator is used to scan the probe across the surface. Then, a map of the surface shape is formed by monitoring the voltage of the z piezo.

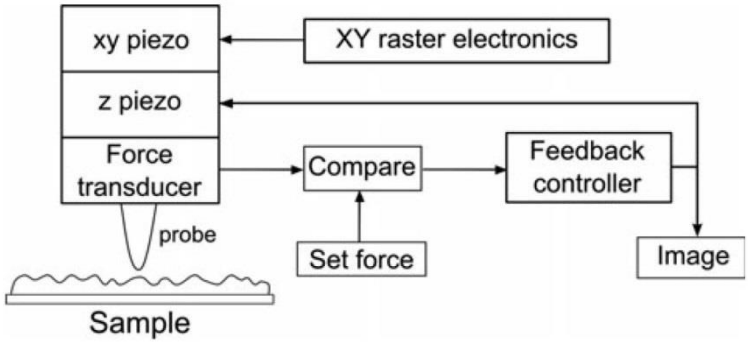

Figure 3-18: Schematic block diagram of AFM operation and functions used during this process [174].

3.8.2 Instrument

A higher quality of sample surface is required for HS-AFM analysis. Thus a special procedure is required for sample preparation which has been discussed in section 3.1.2 [136]. To resolve the time-consuming disadvantage of AFM, the development of HS-AFM resolved this limitation and improved the slow scan speed of AFM. The sample analysed by HS-AFM moves in a raster pattern and the surface is scanned with a sharp tip to map the topography with nanometre lateral resolution. The HS-AFM used in this investigation has the ability to measure not only the height but also the local stiffness, thermal and electrical properties at the same time [35].

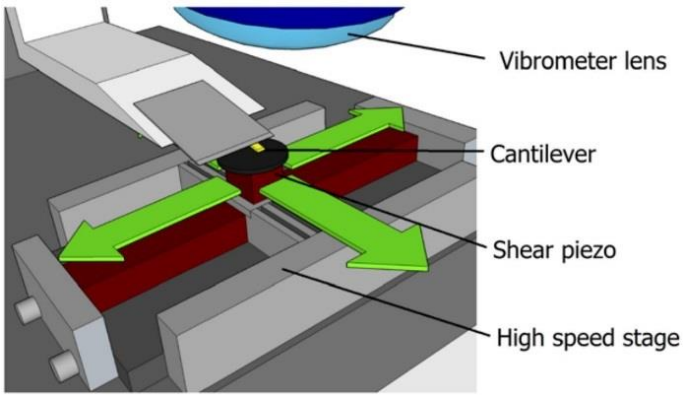

Figure 3-19: Schematic diagram showing the experimental arrangement. The arrows show the direction of motion of the scan stage [175].

Before using the instrument for an experiment, the accuracy of the laser doppler vibrometer detection system, which is used as a non-contact means of vibration measurement [176], is calibrated with a 1 µm pitch silicon calibration grid. Then the HS-AFM topographical images created from the laser Doppler vibrometer vertical displacement data are compared with deflection images collected by a standard optical beam deflection sensor. The laser spot is located at the free end of the cantilever shown in Figure 3-19 and periodic line scans are performed by the stage as shown in Figure 3-20, in which the data are collected by the vertical displacement measurement on the tip of the cantilever. It can be observed that the vertical displacement data are overlaid on one another and exhibit the correct horizontal pitch and vertical height.

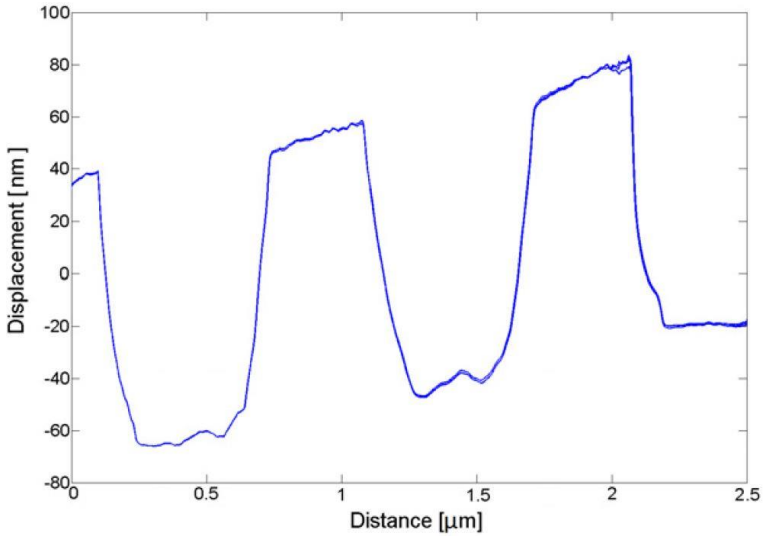

Figure 3-20: Line scan traces over a 1 µm pitch silicon calibration grid. A fast scan frequency of 1 kHz is applied on the calibration grid [175].

The HS-AFM technique images samples by measuring the height of different features. Higher features give higher intensity in the HS-AFM image. Figure 3-21 shows an HS-AFM image and height profiles following the red line in the image. The features with high intensity are deposited TiS_2 precipitates while the mica substrate exhibits low intensity indicating the precipitates are higher than the substrate [177]. The height of precipitates is approximately 1 nm, according to the height profile as a function of distance. It also demonstrates that the HS-AFM technique is capable of analysing samples at the nanometre scale.

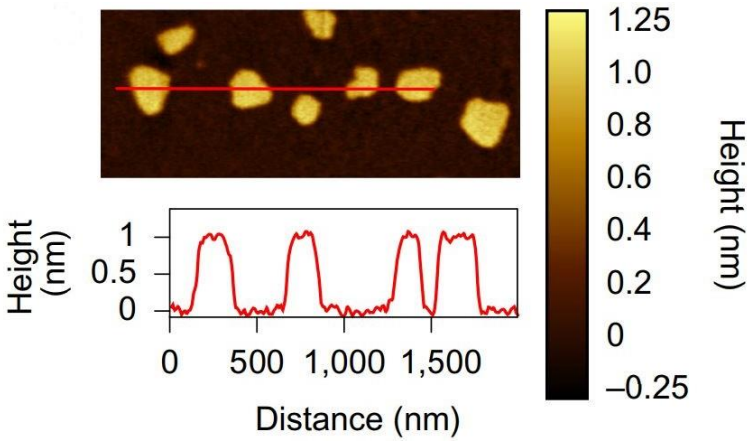

Figure 3-21: the upper image is a HS-AFM image of TiS_2 on a mica substrate; the lower image shows a height profile following the red line in the upper image. The right scale bar shows the corresponding height of feature in different intensities [177].

Figure 3-22 shows schematic diagrams of carbide precipitates formed in the matrix before and after polishing. The observed carbide surface has the same height as the sample surface before polishing. However, the height of metal reduces faster than that of the carbide due to the lower hardness of the former, making it possible to analyse carbide precipitates with HS-AFM technology.

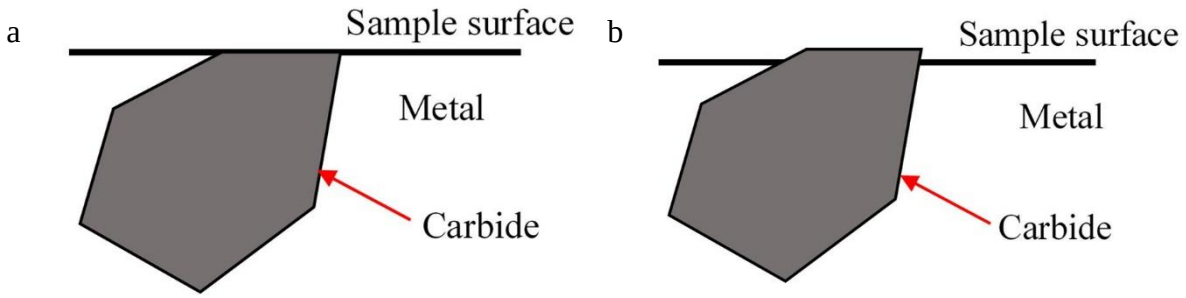

Figure 3-22: Schematic diagrams of carbide formed in the sample surface which is prepared for HS-AFM analysis (a) before polishing and (b) after polishing.

High-speed AFM images in this thesis were acquired using a Bristol Nano Dynamics Ltd system which is capable of imaging at up to 2 megapixels per second. High-speed AFM is used to cover significantly larger areas than can be mapped using a conventional AFM in a fraction of the time. Considering the pixel rates, it allows the HS-AFM to image millimetre sized areas within a day, which the conventional AFM would take a year of continuous imaging to achieve. Custom software is used to extract the precipitate features and characterise them according to their area, height and aspect ratio. An extended map from HS-AFM is generated by acquiring a series of HS-AFM images of 4.5 × 4.5 μm in size. Several such images are obtained and stitched together to provide a large area high resolution image for comparison with FIB results. Features with higher intensity indicate greater height than those with lower intensity, as will be discussed in chapter 4.

3.9 X-ray diffraction (XRD)

X-ray diffraction is a technique which reveals information about the crystal structure, chemical composition and physical properties of materials and thin films. It is based on observing the scattered intensity of an X-ray beam interacting with a sample as a function of incident and scattered angle, polarisation and wavelength or energy.

3.9.1 Background

Bragg's law is a special case of Laue diffraction which provide angles for coherent and incoherent scattering from a crystal lattice [178]. Bragg's law can be described as Equation 3.2 [179][154]:

$$2d\ sin\theta = n\lambda \qquad 3.2$$

where d represents the lattice interplanar spacing of the crystal; θ is the X-ray incidence angle (Bragg angle); n represents a positive integer; λ is the wavelength of the incident wave. Figure 3-23 shows the interaction between incident beams and a crystalline solid, and the scattered atoms from lattice planes. The lower beam travels an extra length of 2dsinθ compared with the upper beam [154]. Moving particles, e.g. electrons, photons and neutrons, have the de Broglie wavelength, as described by Equation 3.3 [180].

$$\lambda = \frac{h}{p} \qquad 3.3$$

Where h represents Planck constant; p represents the momentum of the particle.

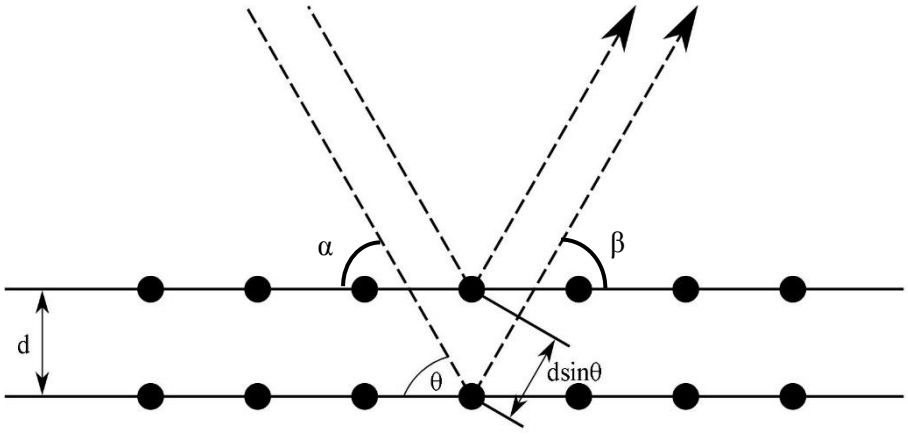

Figure 3-23: schematic of Bragg diffraction [154][181].

Electron transitions are not observed between all pairs of energy levels based on the spectral phenomena. Some of the diffraction from certain sets of planes are absent in XRD spectra at the position predicted by Bragg's Law because these transmissions are forbidden by a set of

selection rules. The Schrodinger equation is used to explain the absence of the transitions governed by selection rules:

$$\Delta n = anything$$

$$\Delta l = \pm 1 \ (not\ zero)$$

$$\Delta j = 0 \ or \ \pm 1 \qquad 3.4$$

where Δn is the change in the principal quantum number; Δl is the change in the orbital angular momentum quantum number; and Δj is the change in the total angular-momentum quantum number. When the change in l equals zero, the transitions are forbidden, e.g. 2s-1s. Therefore, the transition between L_1 and K is not allowed, as shown in Figure 3-24.

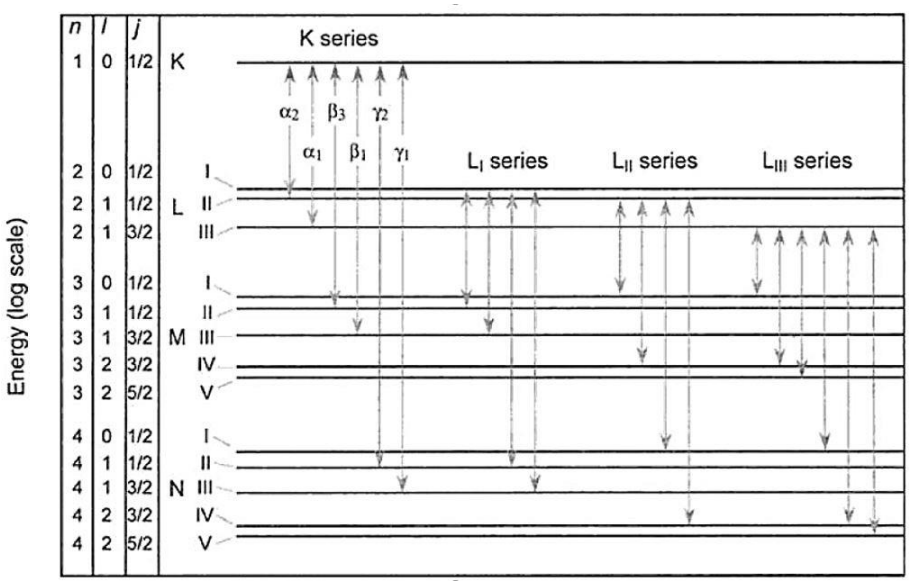

Figure 3-24: Energy level diagram showing all the allowed transitions in a Mo atom [182].

These selection rules determine which reflections are permitted in XRD from the various crystal lattice types as shown in Table 3-5.

Table 3-5: Selection rules for the Miller indices with a few typical Bravais lattices [181].

Unit cell type	*Allowed reflections*	*Forbidden reflections*
Primitive cubic	*Any h, k, l*	*None*
BCC	*h + k + l = 2n (even)*	*h + k + l = 2n+1 (odd)*
FCC	*h, k, l all odd or all even*	*h, k, l mixed odd, even*
FCC diamond	*h, k, l all odd;* *h, k, l all even and h + k + l = 4n*	*h, k, l mixed odd, even* *h, k, l all even and h + k + l ≠4n*
HCP	*l even and h + 2k ≠3n*	*l odd and h+2k = 3n*

where BCC, FCC and HCP represent body-centred cubic, face-centred cubic and hexagonal from Bravais lattices, respectively. h, k and l are the Miller indices which are the three integers used to describe a family of lattice planes.

3.9.2 Diffractometer recording of polycrystalline patterns

Polycrystalline samples can be analysed using XRD. A Cu Kα doublet X-ray source is used in this work with a wavelength, λ, of 1.5406 Å. For any set of planes d(hkl), there are sufficient crystal orientations to make the correct Bragg's law angle θ with respect to the incident beam, as shown in Figure 3-23. Considering that the crystals have random orientations, a cone of half apex angle 2θ is formed. Therefore, for each d(hkl), there is a corresponding 2θ(hkl). Polycrystalline patterns are registered by film recording or diffractometers [181]. The plot of peak intensities as a function of 2θ was processed using VESTA software and comparing with those in the ICSD database to confirm phases present in the examined samples.

The XRD instrument is calibrated prior to experiment. The angles of the spectrometer arms are initially set to zero. Then the X-ray is detected by the counter without interacting with the sample to obtain the full intensity of the beam. The height of the sample is then adjusted to reduce the detected intensity to half of the full intensity. This half-intensity height is the correct height of the sample.

Figure 3-25 shows a schematic of the X-ray diffractometer used for recording the polycrystalline patterns. The sample is placed in the middle of the stage. Monochromatic radiation enters from the divergent slits which are adjusted to be line focused on the target. The diffracted radiation is then selected by narrow receiving slits equipped with a filter. The distance between sample stage and X-ray tube is designed to be equal to the distance between sample and the counter. Meanwhile, the sample face is maintained symmetrical with respect to the primary and diffracted beams. The radiation passing by the receiving slits is detected by a type of counter, e.g. Geiger counter, gas proportional counter or crystal scintillation counter. The produced pulses are then amplified and fed to the recorder which records the 2θ values for each reflection [181].

In this work, a Philips Xpert diffractometer with a Cu Kα radiation source was used for XRD analysis. The generator voltage used was 40 keV, tube emission current was 30 mA. The XRD spectra were acquired between 10 ° and 120 ° with a step of 0.02 ° and 1 s dwell time. The monochromator used in this technology is a PW3123/10 graphite monochromator for Cu Kα source, as shown in Figure 3-25.

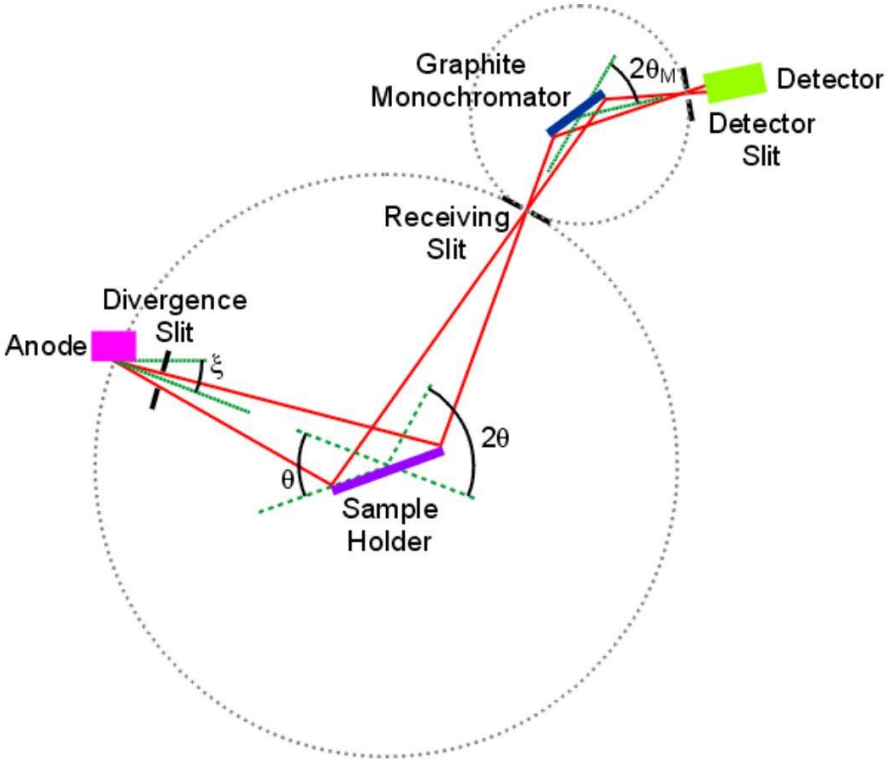

Figure 3-25: Schematic of the diffractometer used for recording polycrystalline patterns [181][183].

3.9.3 The X-ray penetration depth

Penetration depth is defined as the depth at which the intensity of the radiation inside the material falls to $1/e$ (about 37 %) of the original value at the surface, or the depth where the intensity is reduced by an arbitrary amount of absorption, e.g. 99 % of the original intensity when the X-ray beam exits the sample. Since the information obtained is the average value from the interaction volume, the penetration depth becomes an important parameter in XRD analysis [184].

Equation 3.5 gives the integrated intensity diffracted by an infinitesimally thin layer located at a depth of x below the surface of sample [185]:

$$dI_D = \frac{I_0 ab}{\sin\alpha} e^{-\mu x(1/\sin\alpha + 1/\sin\beta)} dx \qquad 3.5$$

where I_0 is the incident beam intensity; α is the incident angle; β is the diffracted angle; and μ represents the absorption coefficient. a, b and I_0 are unknown constants, which will cancel out if we express the intensity diffracted by the layer considered as a fraction of the total integrated intensity diffracted by a sample of infinite thickness. This fraction is called G_x. If we assume 99 % of the total intensity is contributed from this surface layer, the contribution from material below this layer can be ignored, and x is the effective depth of penetration. In the case of α = β

= θ, the fraction G_x can be described as a function of penetration depth x, as shown in Equation 3.6 [185]:

$$G_x = (1 - e^{-\frac{2\mu x}{\sin\theta}}) \quad 3.6$$

Equation 3.6 is described in the following form which is more suitable for penetration depth calculation [185]:

$$\frac{2\mu x}{\sin\theta} = ln\left(\frac{1}{1 - G_x}\right) = K_x \quad 3.7$$

$$x = \frac{K_x \sin\theta}{2\mu} \quad 3.8$$

Based on the study from B.D. Cullity, values of K_x corresponding to G_x are given in Table 3-6.

Table 3-6: The fraction G_x and corresponding K_x [185].

G_x	0.50	0.75	0.90	0.95	0.99	0.999
K_x	0.69	1.39	2.30	3.00	4.61	6.91

In this study, the incident angle θ ranges from 5 to 60 °. As discussed above, assuming the fraction G_x is 0.50, then the corresponding K_x is 0.69. The absorption coefficient μ of ferritic steel is 100 cm^{-1} from ref [186], then the penetration depth can be calculated and it ranges from 3 to 30 μm. The length and depth of the examined area in XRD analysis is 5mm × 5mm, indicating an interaction volume ranging from 0.075 to 0.75 mm^3.

Chapter 4: Studies on ferritic 9Cr-1Mo steel exposed to a simulant AGR coolant gas

Oxidation and carburisation processes within experimental autoclave samples from HRA will be discussed in this chapter. The influence of exposure conditions, including temperature, time and moisture, will be evaluated in the investigation. Optical microscopy, scanning electron microscopy and energy dispersive X-ray spectroscopy were used to observe oxide morphologies and elemental distribution. Oxide types were identified using scanning laser Raman spectroscopy. Carbides were observed with focused ion beam and high-speed atomic force microscopy techniques and identified using X-ray diffraction. Thin foil transmission electron microscopy samples were prepared within a dual beam instrument and carbide precipitates were observed and identified using (scanning) transmission electron microscopy.

4.1 Oxide observation and identification

4.1.1 Samples used for oxidation analysis and techniques used

Experimental autoclave ferritic HRA samples listed in Table 4-1 were used for oxide investigation. Selected autoclave samples in this chapter are marked as A-temperature-time, e.g. A-580-2542 represents sample HRA 8133-580 °C-2542 h (400 vppm). However, different moistures are highlighted in brackets, e.g. A-640-1495 (400 to 800 @ 245) represents sample HRA 8147-640 °C-1495 h (400 to 800 vppm @ 245), indicating that moisture changes from 400 vppm to 800 vppm after 245 h. Three samples were used for oxide identification: A-580-2542, A-640-1495 (400 to 800 @ 245) and A-640-3883 in non-breakaway, breakaway initiation and post breakaway oxidation regimes respectively.

Table 4-1: Techniques used for all the autoclave HRA samples selected.

Sample ID	***Oxidation***			***Carburisation***				
	OM	*SEM-EDS*	*Raman*	*FIB*	*XRD*	*TEM*	*STEM-EDS*	*HS-AFM*
A-Virgin	✓			✓	✓		✓	
A-580-2542	✓	✓	✓	✓	✓	✓	✓	✓
A-600-1510	✓			✓				
A-600-1520 (1200)	✓			✓				
A-600-3835	✓			✓				
A-600-17065 (1200)	✓			✓				
A-640-245	✓			✓				
A-640-1495 (400 to 800 @ 245)	✓	✓	✓	✓	✓	✓	✓	
A-640-2526	✓			✓				
A-640-3074	✓			✓				
A-640-3334	✓			✓				
A-640-3639	✓			✓				
A-640-3883	✓	✓	✓	✓	✓	✓	✓	✓

The techniques used for investigation are shown in Table 4-1. Optical microscopy was adopted for morphology observation of the oxide formed on a fin. Scanning electron microscopy was applied to samples which were also analysed with scanning laser Raman spectroscopy for comparison.

4.1.2 Oxide observation and thickness measurement from optical microscopy

Figure 4-1 shows examples of the optical images recorded from cross-sections prepared from an HRA virgin sample and a sample subject to breakaway oxidation. The samples from HRA were approximately 3 mm thick at the base and 3 mm long for the fins. They were all exposed in a flowing CO_2-based coolant gas. Figure 4-1a shows that there is a sharp edge at the fin tip corner where oxide grows faster than the other locations, e.g. fin side, during exposure to the CO_2-based gas. Figure 4-1b shows a non-breakaway sample with a duplex oxide formed during oxidation. Eventually, breakaway occurs and a "fan-shaped" oxide was formed, as shown in Figure 4-1c. Due to the influence of geometry, the oxide at fin tip corner and fin side were measured to make a comparison.

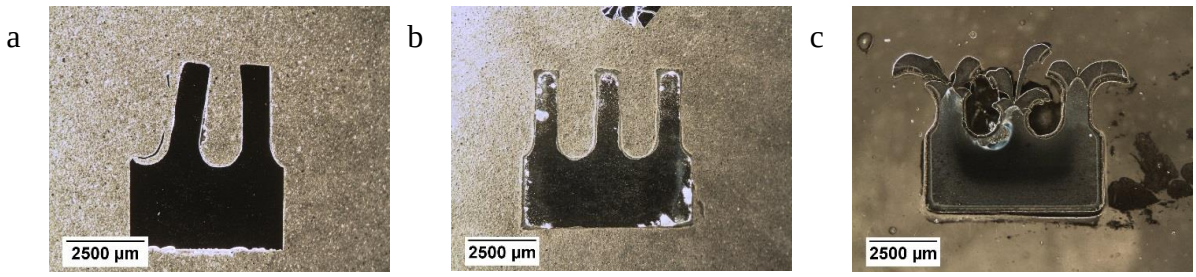

Figure 4-1: Cross-sections of experimental sample (a) A-virgin and (b) A-640-2526 (breakaway initiation) and (c) A-640-3639 (post-breakaway).

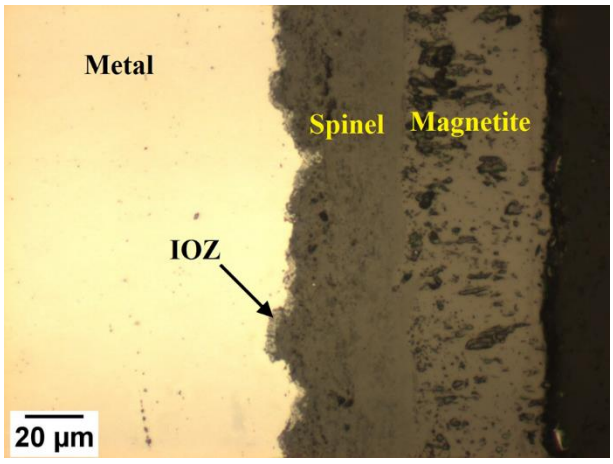

Figure 4-2: An optical micrograph recorded from the fin side of sample A-600-1510 showing the microstructure of a duplex oxide.

Considering the reality that fins of the components made of 9Cr-1Mo steels serviced in the reactor were oxidised in CO_2-based coolant gas and the crack were first present at the fin tip

corners. The investigation were therefore focused on the fins to understand the process of oxidation and carburisation.

An optical image at high magnification Figure 4-2, shows the microstructure of the duplex oxide formed at the fin side of sample A-600-1510, which is comprised of magnetite, spinel and internal oxidation zone (IOZ) layers. The IOZ layer appears to be oxide embedded in the matrix, which will be examined later.

A schematic drawing of finned experimental samples, with the marked locations analysed using optical microscopy and SEM-EDS, is shown in Figure 4-3. The optical micrographs, from which the oxide thickness can be measured, were obtained from fin tip corner and fin side while SEM-EDS was applied to the fin tip of the examined fin. Optical micrographs recorded from fin tip and fin side of samples listed in Table 4-1 are shown in Figure 4-4 and Figure 4-5.

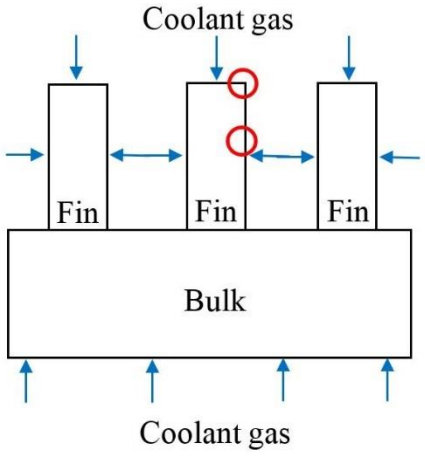

Figure 4-3: Schematic drawing of finned samples, directions of coolant gas diffusion (blue solid lines) and locations for optical micrographs (red circles).

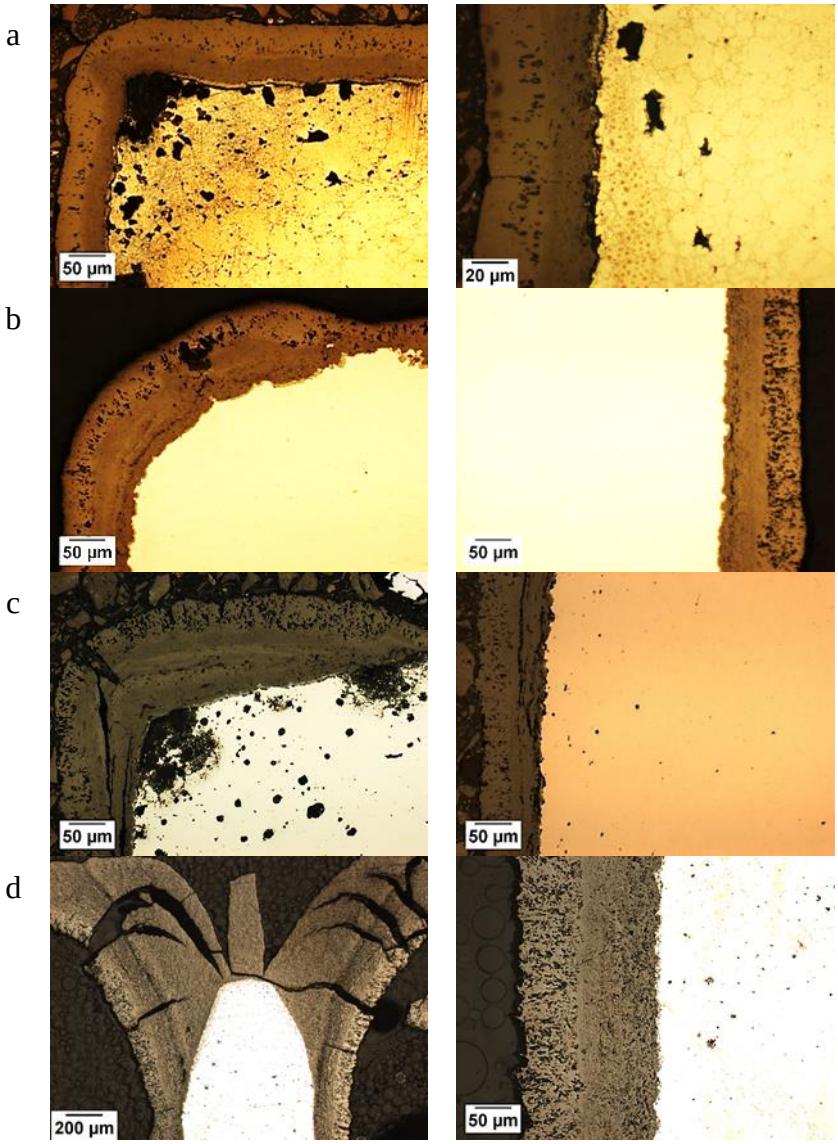

Figure 4-4: Optical micrographs at the fin tip (left) and fin side (right) of samples exposed at 580 and 600 °C: (a) A-580-2542; (b) A-600-1510; (c) A-600-1520 (1200); (d) A-600-17065 (1200).

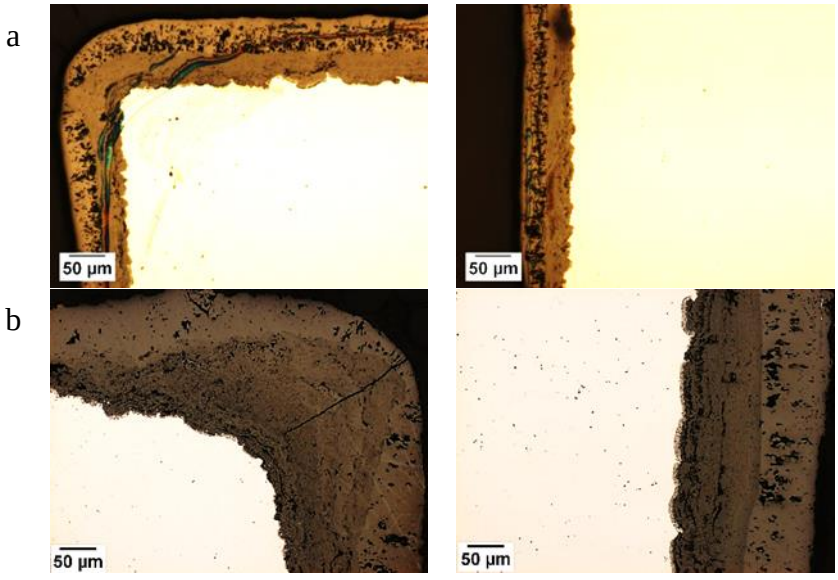

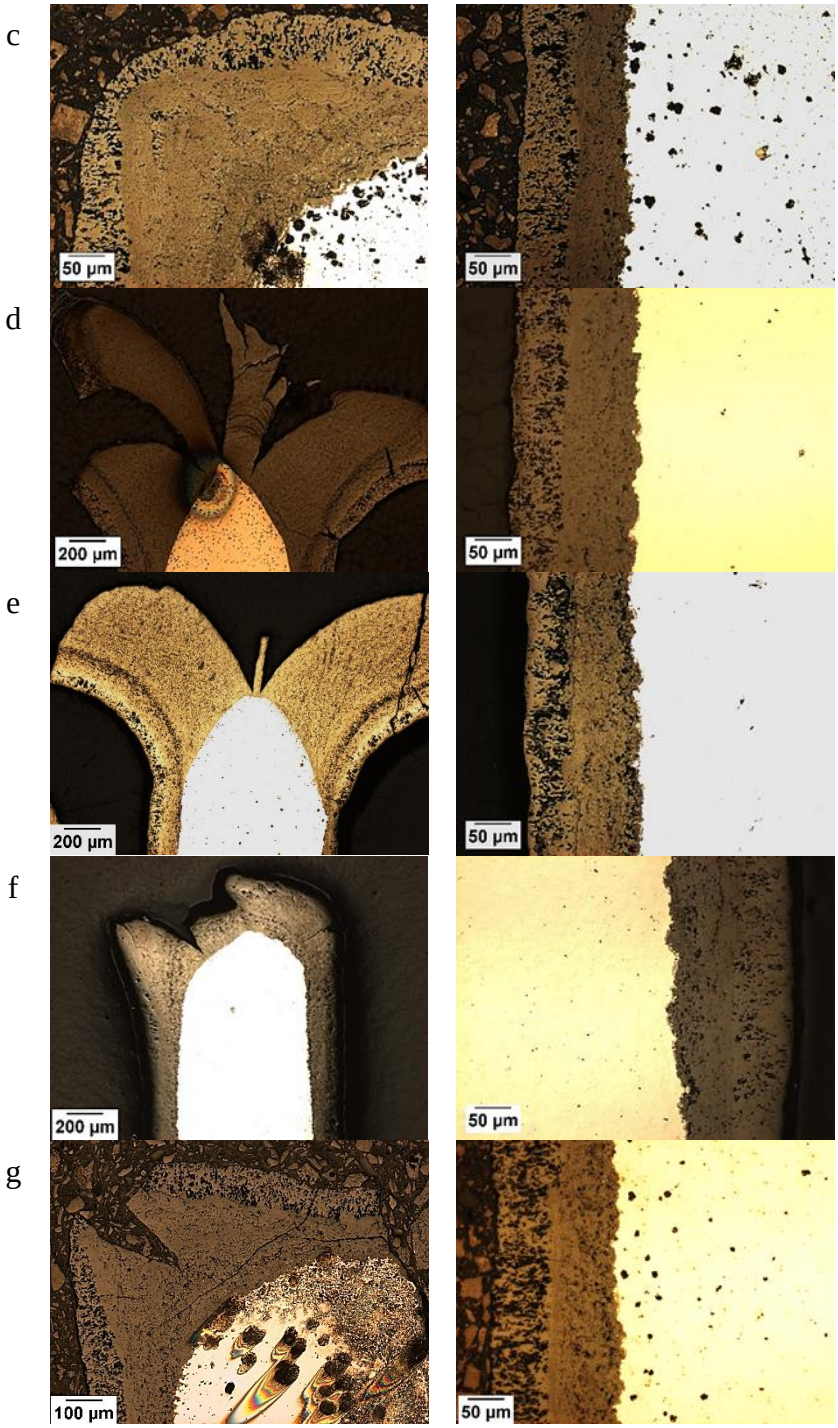

Figure 4-5: Optical micrographs at the fin tip (left) and fin side (right) of samples exposed at 640 °C: (a) A-640-245; (b) A-640-1495 (400 to 800 @ 245); (c) A-640-2526; (d) A-640-3074; (e) A-640-3334; (f) A-640-3639 and (g) A-640-3883.

Table 4-2: Oxide morphology and oxidation regime of each HRA sample.

Sample ID	*Oxide morphology at fin tip corner*	*Oxidation regime*
A-580-2542	*Duplex*	*Non-breakaway*
A-600-1510	*Duplex*	*Non-breakaway*
A-600-1520 (1200)	*Multi-layered*	*Breakaway initiation*
A-600-17065 (1200)	*Laminated fan-shaped*	*Post-breakaway*
A-640-245	*Duplex*	*Non-breakaway*
A-640-1495 (400 to 800 @ 245)	*Multi-layered*	*Breakaway initiation*
A-640-2526	*Multi-layered*	*Breakaway initiation*
A-640-3074	*Laminated fan-shaped*	*Post-breakaway*
A-640-3334	*Laminated fan-shaped*	*Post-breakaway*
A-640-3639	*Laminated fan-shaped*	*Post-breakaway*
A-640-3883	*Laminated fan-shaped*	*Post-breakaway*

Figure 4-4 and Figure 4-5 show optical micrographs of samples listed in Table 4-1 from fin side and fin tip. The oxide from the fin side of all examined samples exhibited a duplex layer in which the thicknesses of outer magnetite and inner spinel layers were roughly equal. Oxide at the fin tip corner was more complicated, as shown in Table 4-2 and described as follows:

1. Duplex oxide, in which the thicknesses of spinel and magnetite are roughly the same, was formed on A-580-2542, A-600-1510 and A-640-245. The absence of cracks indicates non-breakaway oxidation had occurred in these samples. It seems that duplex oxide was mainly found in samples exposed at low temperature or with short time, which means that these samples were in a protective oxidation regime following parabolic kinetics.
2. Multi-layered oxide, in which magnetite bands were present in the spinel layer, was formed on samples A-600-1520 (1200), A-640-1495 (400 to 800 @ 245) and A-640-2526. Cracks were also observed in the oxide at the fin tip corner in these samples, indicating the initiation of breakaway oxidation. However, A-600-1520 (1200) and A-640-2526 were marked as non-breakaway as received. Therefore, they are in a stage close to breakaway initiation. Moreover, sample A-600-1520 (1200) was exposed at lower temperature and shorter time but higher moisture than A-640-2526. However, multi-layered oxide was formed in both samples, illustrating the accelerating effect of moisture in the process of oxidation.
3. A laminated oxide, which is often present in a fan shape beneath a multi-layered oxide, was observed on samples A-600-17065 (1200), A-640-3074, A-640-3334, A-640-3639 and A-640-3883. Compared to those with duplex and multi-layered oxide, these samples were exposed at higher temperature for longer time, or in high moisture. Cracks were formed in the oxide, allowing gas to access the metal directly through, giving a higher rate of oxidation in these samples which were in post-breakaway oxidation and following linear kinetics.

Table 4-3: Average thickness (in µm) of oxide scales in ferritic 9Cr-1Mo steel samples.

Samples	*A-Virgin*	*A-580-2542*	*A-600-1510*	*A-600-1520 (1200)*	*A-600-17065 (1200)*	*A-640-245*
Fin tip	*/*	*71*	*120*	*136*	*/*	*93*
Fin side	*/*	*45 ± 2*	*91 ± 5*	*82 ± 4*	*184 ± 5*	*55 ± 4*
Samples	*A-640-1495 (400 to 800 @ 245)*	*A-640-2526*	*A-640-3074*	*A-640-3334*	*A-640-3639*	*A-640-3883*
Fin tip	*244*	*310*	*/*	*/*	*/*	*282*
Fin side	*189 ± 5*	*145 ± 8*	*153 ± 5*	*156 ± 6*	*168 ± 4*	*187 ± 6*

Table 4-4: Thickness of magnetite, spinel and the continuous IOZ layer in µm.

Samples	*A-Virgin*			*A-580-2542*			*A-600-1510*			*A-600-1520 (1200)*		
Oxide type	*/*			*Fe_3O_4*	*Spinel*	*IOZ*	*Fe_3O_4*	*Spinel*	*IOZ*	*Fe_3O_4*	*Spinel*	*IOZ*
Fin tip	*/*			*40*	*31*	*5.8 ± 0.8*	*60*	*60*	*2.4 ± 0.4*	*/*	*/*	*4.6 ± 0.6*
Fin side	*/*			*33 ± 2*	*22 ± 3*	*4.7 ± 0.4*	*46 ± 2*	*45 ± 3*	*3.0 ± 0.7*	*43 ± 3*	*39 ± 2*	*3.8 ± 0.9*
Samples	*A-600-17065 (1200)*			*A-640-245*			*A-640-1495 (400 to 800 @ 245)*			*A-640-2526*		
Oxide type	*Fe_3O_4*	*Spinel*	*IOZ*	*Fe_3O_4*	*Spinel*	*IOZ*	*Fe_3O_4*	*Spinel*	*IOZ*	*Fe_3O_4*	*Spinel*	*IOZ*
Fin tip				*41*	*52*	*/*	*/*	*/*	*/*	*/*	*/*	*/*
Fin side	*85 ± 4*	*99 ± 5*	*/*	*30 ± 2*	*25 ± 2*	*/*	*90 ± 6*	*99 ± 4*	*5.8 ± 1.0*	*75 ± 6*	*70 ± 2*	*/*
Samples	*A-640-3074*			*A-640-3334*			*A-640-3639*			*A-640-3883*		
Oxide type	*Fe_3O_4*	*Spinel*	*IOZ*	*Fe_3O_4*	*Spinel*	*IOZ*	*Fe_3O_4*	*Spinel*	*IOZ*	*Fe_3O_4*	*Spinel*	*IOZ*
Fin tip	*/*	*/*	*/*	*/*	*/*	*/*	*/*	*/*	*/*	*/*	*/*	*/*
Fin side	*70 ± 4*	*83 ± 9*	*/*	*63 ± 4*	*82 ± 4*	*/*	*80 ± 1*	*88 ± 3*	*/*	*77 ± 3*	*110 ± 5*	*/*

Beneath the oxide at the fin tip corner, an IOZ layer was formed in some samples. A continuous IOZ layer was formed in non-breakaway samples A-580-2542, A-600-1510 and A-600-1520 (1200) while a discontinuous IOZ was formed in samples A-640-1495 (400 to 800 @ 245) and A-640-2526.

It was found that the sample exposed at 580 °C for 2542 h was in non-breakaway oxidation with a duplex oxide formed at the fin tip corner while the sample exposed at 640 °C for 2526 h exhibited a multi-layered oxide with a small crack present in the oxide at the fin tip corner, indicating breakaway initiation in this sample. This comparison demonstrates that temperature is the dominant parameter influencing oxidation.

Cracks were observed at the fin tip corner in samples entering breakaway, indicating that geometry affects the process of oxidation. As shown in Figure 4-6, the growth of oxide at the fin tip corner resulted from the two dimensional (2D) diffusion of cations (Equation 4.1) [187].

$$\frac{\partial C}{\partial t} = D\left(\frac{\partial^2 C}{\partial x^2} + \frac{\partial^2 C}{\partial y^2}\right) \qquad 4.1$$

where $C = C(x, y, t)$, t represents time, x and y are the distance following the horizontal and vertical directions, as shown by blue arrows in Figure 4-6a, D represents the diffusion coefficient which is constant. At the fin tip corner, CO_2 diffuses in from both the vertical and horizontal directions, increasing the oxidation rate at this location. The metal is gradually converted into oxide during oxidation when exposed to the coolant gas. However, it appears that the oxide tended to keep the original shape of the fin during the oxidation process. Therefore, the spinel layer gradually became thicker than the magnetite at the fin tip corner before it reached post-breakaway oxidation, during which fan shape oxide was formed. Figure 4-6b shows contours of streamlines in the two-dimensional corner flow. The velocity potential $\phi(x, y) = u_0(y^2 + x^2)/2$ [188]. Therefore, the diffusion of CO_2 at the fin tip corner diffuses faster compared with the fin side.

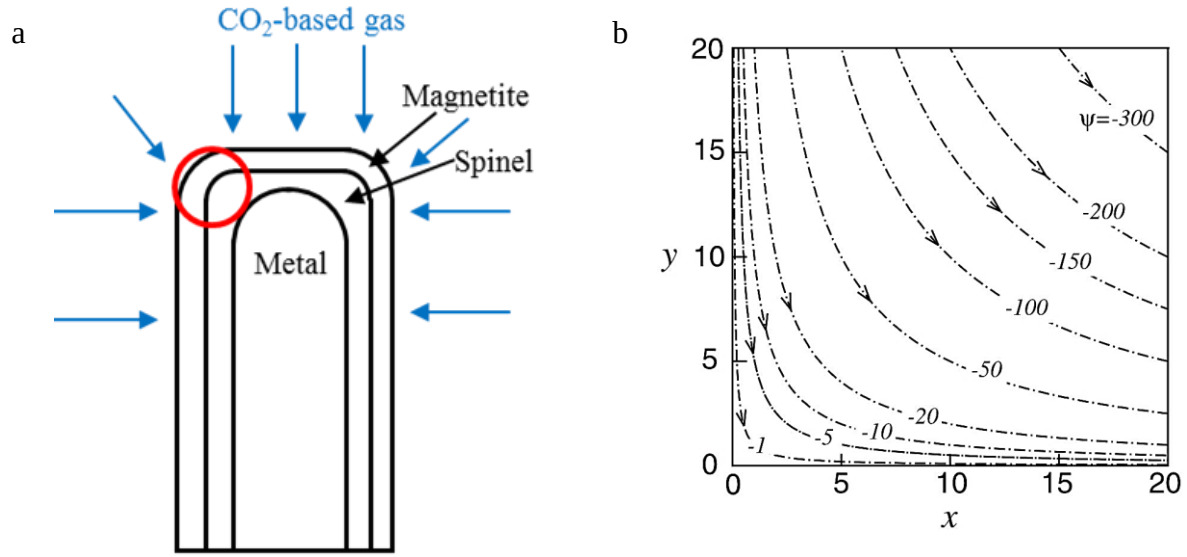

Figure 4-6: (a) A schematic drawing illustrating the oxide formed on the fin tip and diffusion directions of CO_2-based coolant gas and (b) Contours of streamlines in the 2D corner flow with $u_0 = 1$, where x and y are Cartesian coordinates. u_0 is the coordinates of the original location (fin tip corner in this work). The stream function $\Psi(x,y) = -u_0xy$ [188].

The average oxide thickness at these two locations of samples were measured in each case as shown in Figure 4-4 and Figure 4-5 and the results are given in Table 4-3. The thickness of the oxide scale at the locations examined for each sample was measured at twelve positions and mean values were calculated together with the associated standard deviation ±1σ. It is worth noting that the oxide at the fin tip centre has grown separately from other fan-shaped oxide in breakaway samples. Oxide thickness from virgin sample and fan-shaped oxide was not recorded because there was no oxide in the former and the definition of the fan-shaped oxide thickness was ill-defined in the latter.

The results shown in Table 4-3 indicate that the oxide scale at the fin tip is thicker than that at the fin side, and thicker oxide is obtained in the samples exposed at higher temperature and for longer exposure time. The thicknesses of magnetite, spinel and continuous IOZ layer were

measured and the results were shown in Table 4-4. At the location of fin tip corner, the continuous IOZ is only present beneath duplex oxide. At the fin side, a continuous IOZ layer is present beneath duplex and multi-layered oxide, however, it became discontinuous or disappeared beneath laminated oxide which is usually present in post-breakaway oxidation. Furthermore, there is an unclear difference in oxide thickness resulting from moisture. The mean value of oxide thickness obtained from non-breakaway location at the fin side should follow parabolic kinetics with respect to exposure time, as shown in Figure 4-7a which is plotted for the samples exposed at 640 ºC and 400 vppm moisture. However, the influence from geometry is not taken into consideration in this case due to the difficulty in defining the oxide thickness at the fin tip corner in post-breakaway samples (fan-shaped oxide). Figure 4-7b shows a plot of weight gain against exposure time with the data provided by Wood PLC, in which the influence from geometry is taken into account. It consists of a curve exhibiting sub-parabolic kinetics (power 0.4262 rather than 0.5) followed by a plot exhibiting linear kinetics after 1900 h. The time of the change from sub-parabolic kinetics to the linear kinetics is defined as the time to breakaway (TTB). The oxidation occuring at the TTB is defined as breakaway initiation oxidation.

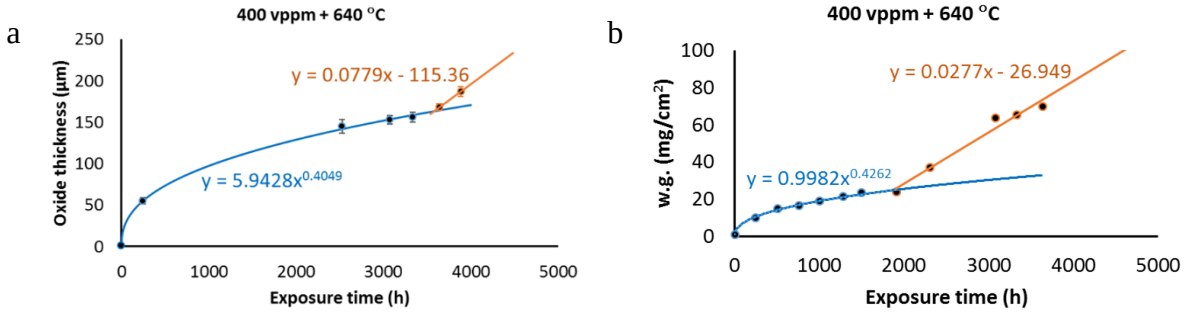

Figure 4-7: Fitted curve of oxide thickness vs exposure time for the samples exposed at 640 ºC with 400 vppm moisture: (a) oxide thickness vs exposure time from non-breakaway location fin side using the data provided by Table 4-3; (b) weight gain vs exposure time using the data provided by Wood PLC.

According to Figure 4-7, it appears that samples exposed up to 2000 h follow sub-parabolic kinetics while those after 2000 h follow linear kinetics. A power fitting was adopted for the two sub-parabolic plots. In Figure 4-7a, the curve was separated into two parts: (1) the sub-parabolic curve with a fitting equation $y = 5.94x^{0.40}$ and (2) the curve following linear kinetics: $y = 0.078x - 115.36$. The fitting equation of the plot of weight gain versus time before 2000 h in Figure 4-7b is $y = x^{0.43}$, which is also sub-parabolic. The linear fitting equation for the plot in Figure 4-7 after 2000 h is $y = 0.028x - 27$. Gong et al. plotted weight gain as a function of exposure time, shown in Figure 2-11 in Chapter 2. The plot in Figure 4-7b from our results is the plot of 640 °C in the publication [85].

Optical micrographs show that oxide in different morphologies, including duplex, multi-layered and laminated forms, need to be investigated to elucidate the mechanism of oxidation. Duplex oxide is present in samples following sub-parabolic kinetics, as shown in

Figure 4-7. It is also present in the non-breakaway locations, e.g. fin side, in samples entering the breakaway regime. Multi-layered oxide is observed at fin tip of samples experiencing breakaway corresponding to the samples close to TTB. Laminated oxide is present at the fin tip corner in post breakaway samples which is normally in a fan-shaped morphology. Optical micrographs in Figure 4-5 show that duplex, multi-layered and laminated oxides were present in samples A-580-2542, A-640-1495 (400 to 800 @ 245) and A-640-3883 respectively.

4.1.3 Oxide observation and elemental distribution from SEM-EDS

According to the discussion on Figure 2-10 in Chapter 2, fresh spinel is formed at the oxide/metal interface. A line scan using EDS was applied at the fin side of sample A-580-2542 and fin tip corner of the sample, together with an area 40 × 40 μm in size including oxide/metal interface analysed with EDS mapping in each case. Figure 4-8 shows a SEM image and EDS line scan of the oxide formed on the fin side of sample A-580-2542 which is comprised of magnetite and spinel, as well as a thin layer of IOZ, which penetrates the matrix [189]. According to the EDS line scan results, Cr concentration in the spinel ranges from 9 to 25 wt. %, indicating the composition of spinel ranges from $Fe_{2.60}Cr_{0.40}O_4$ to $Fe_{1.91}Cr_{1.09}O_4$. The red line (without arrow) illustrates the line scan trace and the results are shown in Figure 4-8b. The magnetite is mainly comprised of Fe and O. However, Si-rich oxide particles were formed occasionally in the IOZ and magnetite/spinel interface. The Cr concentration increases immediately from < 1 wt. % in magnetite to 9-25 wt. % in the spinel layer. It appears that a few narrow Cr-rich bands (> 20 wt. %) were formed in the spinel layer. The Cr concentration drops in the IOZ layer. However, it shows a high level in the residual carbide precipitates. The alloying element Mo exhibits a similar tendency to Cr in the oxide scale. The Cr-rich locations in the metal correspond to the carbides formed in the matrix.

The corresponding EDS elemental maps are shown in Figure 4-9 and are consistent with the line scan results. It seems that the Cr distribution in the location close to the oxide/metal interface follows the grain boundaries in the metal. The Cr is mainly distributed at the grain boundaries in the metal, consistent with the Fe-depleted locations. The maps of Fe and Cr indicate that the IOZ layer is comprised of oxide embedded in the matrix. The filamentary structure of Mo exhibits a similar distribution with Cr-rich locations. It can be seen that Si is mainly distributed at the magnetite/spinel and oxide/metal interfaces.

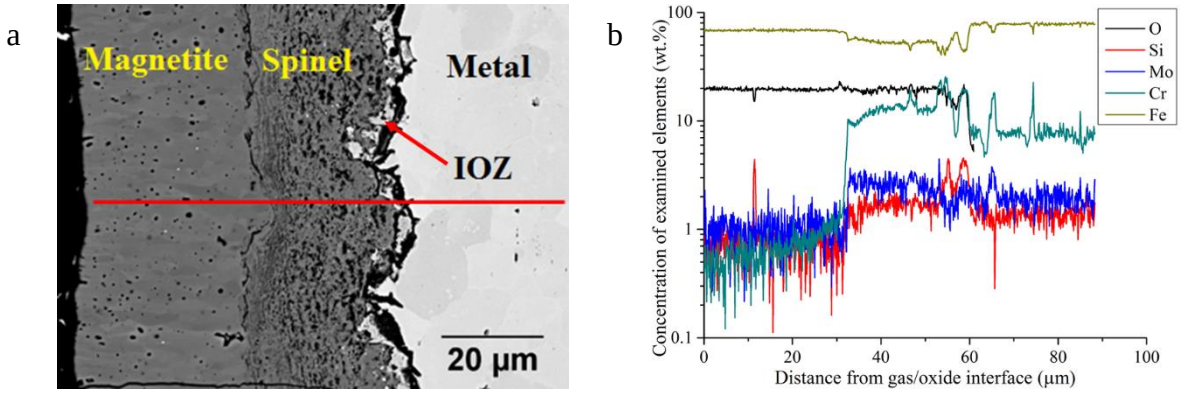

Figure 4-8: (a) SEM image on the fin side and line scan trace; (b) concentration of elements as a function of distance from gas/oxide interface from EDS line scan from sample A-580-2542.

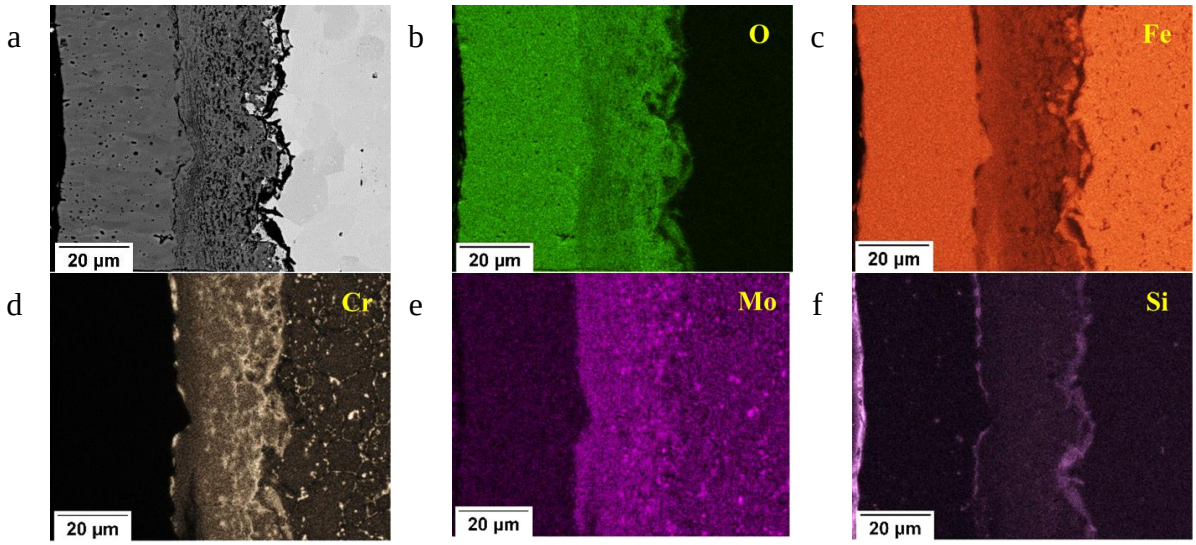

Figure 4-9: (a) SEM image on the fin side and marked area for EDS mapping; EDS maps of (b) O; (c) Fe; (d) Cr; (e) Mo; (f) Si from sample A-580-2542.

A duplex oxide at the fin tip corner of sample A-580-2542, which is in a non-breakaway oxidation regime, was analysed with EDS line scanning and mapping and the results are shown in Figure 4-10 and Figure 4-11, respectively. The concentration profiles show that the levels of Cr and O are indicative of the presence of magnetite about 30 μm thick as the outer layer oxide and spinel about 40 μm thick as an inner oxide layer. The chemical formulae for magnetite and spinel are Fe_3O_4 and $Fe_{3-x}Cr_xO_4$, respectively, inferred from the weight percentage in these two oxide layers. The composition of spinel changes with the Fe/Cr ratio. The evaluated area using EDS mapping includes spinel, a small area from magnetite and matrix, as shown with the outlined region in Figure 4-11. According to the EDS line scan results, Cr concentration in the spinel ranges from 6 to 25 wt. %, indicating the composition of spinel range from $Fe_{2.73}Cr_{0.27}O_4$ to $Fe_{1.91}Cr_{1.09}O_4$. Figure 4-11b shows an oxygen map which is used to distinguish oxide from matrix. Maps of Mo and Si show a similar distribution to that of Cr, while opposite to that of Fe. Silicon is mainly distributed in spinel and at the IOZ/metal interface. Elemental distribution is indicative of the presence of Cr, Mo-rich particles in the analysed oxide scale.

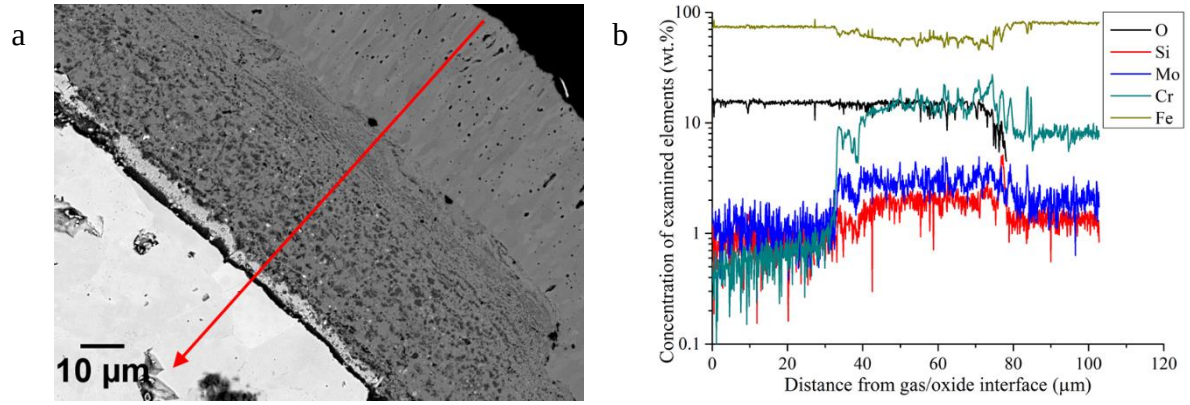

Figure 4-10: (a) SEM image on the fin tip and line scan trace; (b) concentration of elements as a function of distance from gas/oxide interface from EDS line scan from sample A-580-2542.

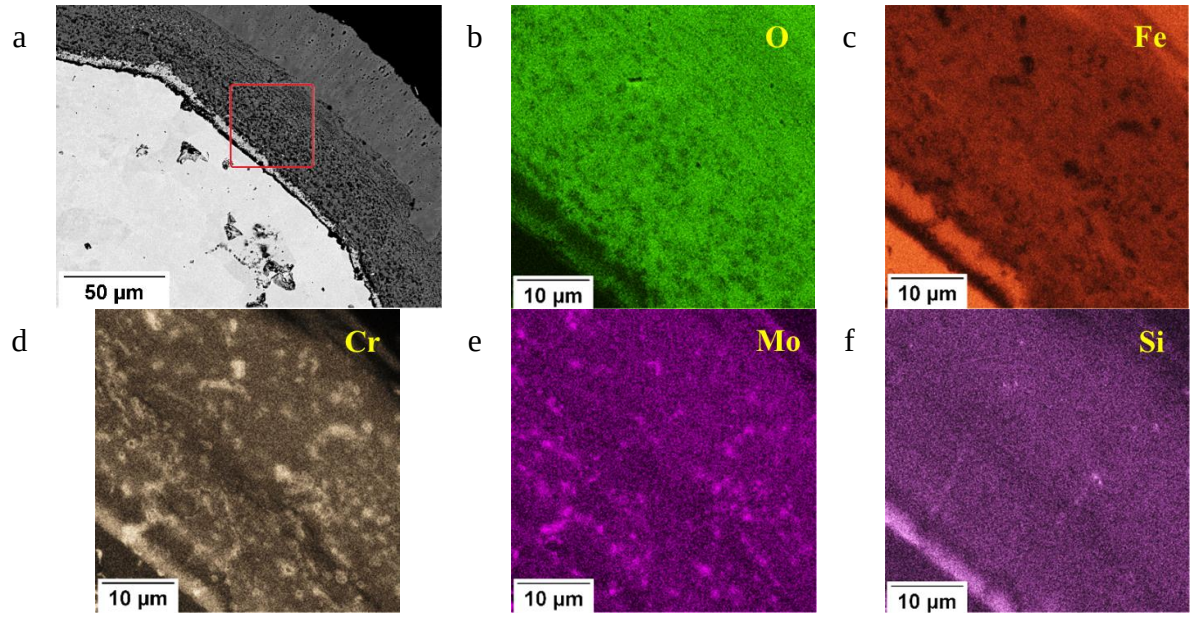

Figure 4-11: (a) SEM image on the fin tip and marked area for EDS mapping; EDS maps of (b) O; (c) Fe; (d) Cr; (e) Mo; (f) Si from sample A-580-2542.

Multi-layered oxide present in sample A-640-1495 (400 to 800 @ 245), which is in breakaway oxidation initiation, was evaluated using EDS line scanning and mapping, as shown in Figure 4-12 and Figure 4-13, respectively. The concentration profiles indicate that the oxide is composed of a thin layer of magnetite about 25 μm thick and a layer of spinel about 220 μm thick in which Cr-rich and Cr-depleted bands are present alternately. According to the EDS line scan results, the Cr concentration in the Cr-rich layers in the spinel ranges from 5 to 25 wt. %, indicating that the composition of the spinel ranges from $Fe_{2.78}Cr_{0.22}O_4$ to $Fe_{1.91}Cr_{1.09}O_4$. Cr-depleted thin layers are Fe_3O_4, inferred from the very low Cr concentration. The small Cr signal was possibly obtained from the spinel beneath due to the interaction volume, as described in Figure 3-6 in Chapter 3. Spinel and matrix close to the oxide/metal interface were examined with EDS mapping to evaluate the freshly formed spinel. EDS maps show that Cr is present in filamentary structures in the examined oxide. It appears that the distribution of

Cr-rich areas in the oxide corresponds to grain boundary and carbide precipitates in this area which had been oxidised. Filamentary Cr in the matrix corresponds to carbide precipitates.

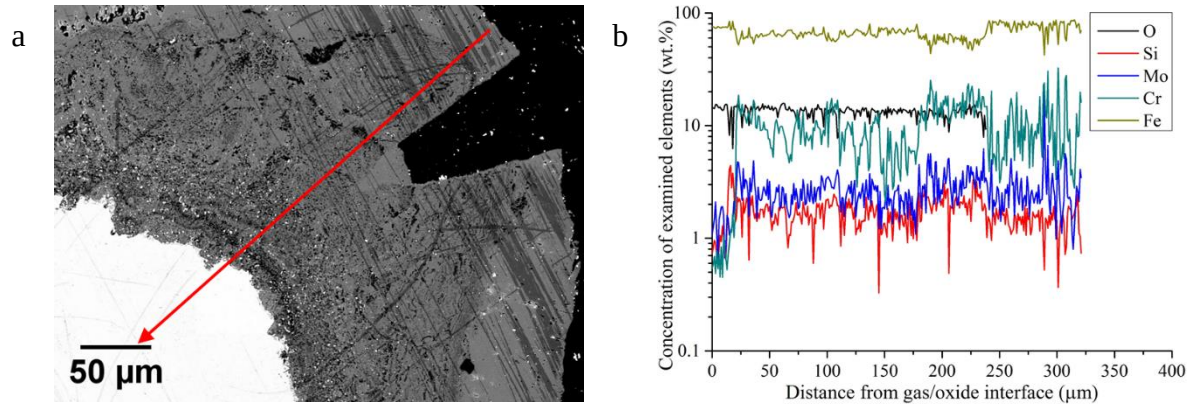

Figure 4-12: SEM image on the fin tip and line scan trace; (b) concentration of elements as a function of distance from gas/oxide interface from EDS line scan from sample A-640-1495 (400 to 800 @ 245).

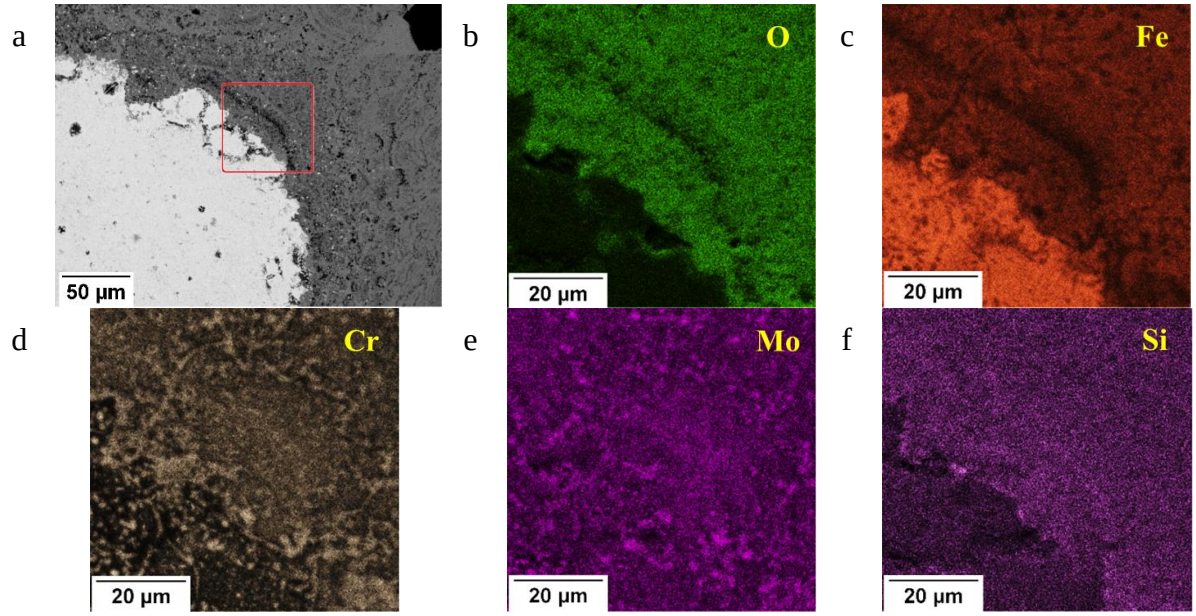

Figure 4-13: (a) SEM image on the fin tip and marked area for EDS mapping; EDS maps of (b) O; (c) Fe; (d) Cr; (e) Mo; (f) Si from sample A-640-1495 (400 to 800 @ 245)

The presence of cracks and fan shape oxide which is defined as laminated oxide, are evidence that sample A-640-3883 has entered a post-breakaway oxidation regime. It appears that the outer layer of magnetite has peeled off during storage or mounting. Therefore, only laminated oxide was analysed using EDS line scanning and mapping, and the results are shown in Figure 4-14 and Figure 4-15, respectively. The concentration profiles show that Cr-rich and Cr-depleted oxide are present alternately, and it appears that the level of Mo changes in a positive correlation with Cr in the oxide layer. According to the EDS line scan results, the Cr concentration in the Cr-rich layers in the spinel ranges from 8 to 26 wt. %, indicating the

composition to range from $Fe_{2.65}Cr_{0.35}O_4$ to $Fe_{1.86}Cr_{1.14}O_4$. The Cr-depleted oxide corresponds to Fe_3O_4, as will be confirmed by Raman spectroscopy in the following section.

The EDS map of Cr from the outlined area in Figure 4-15a indicates that the distribution of Mo has some similarities with Cr and is opposite to Fe, consistent with concentration profiles. However, it appears that the Si distribution has little relationship with other examined elements in the oxide and there are some Si-rich particles present in the matrix in this post-breakaway sample.

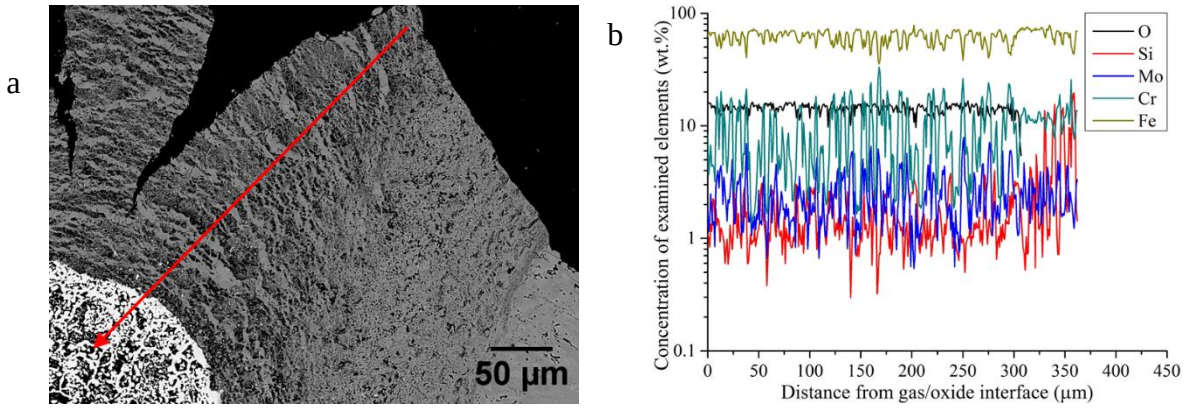

Figure 4-14: SEM image on the fin tip and line scan trace; (b) concentration of elements as a function of distance from gas/oxide interface from EDS line scan from sample A-640-3883.

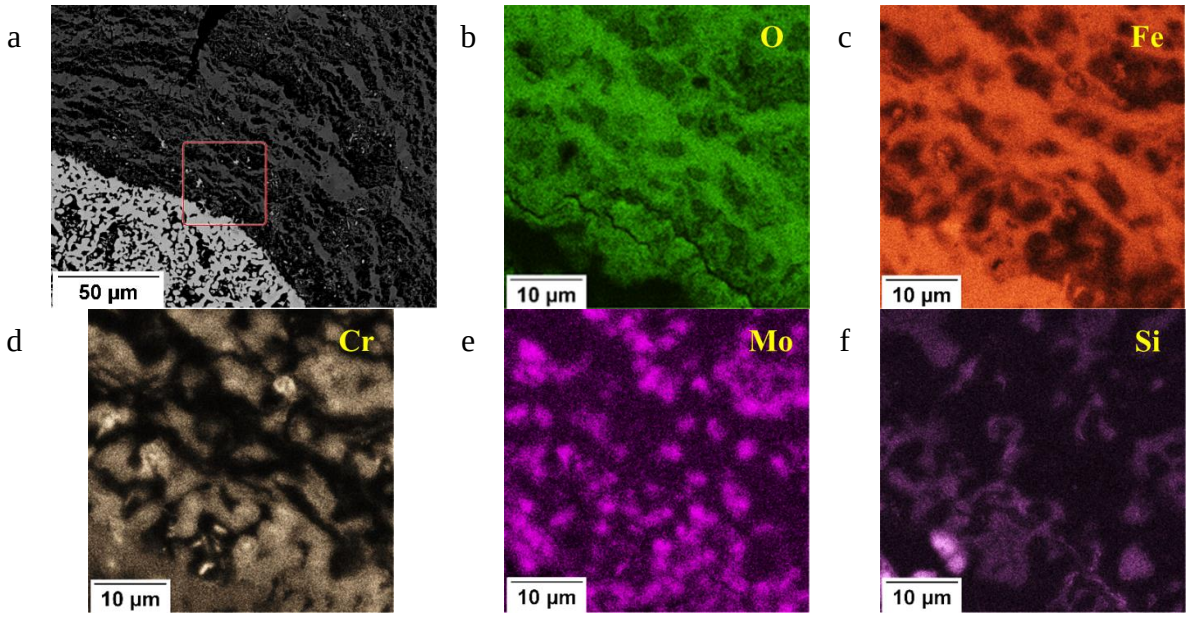

Figure 4-15: (a) SEM image on the fin tip and marked area for EDS mapping; EDS maps of (b) O; (c) Fe; (d) Cr; (e) Mo; (f) Si from sample A-640-1495 (400 to 800 @ 245)

The line scan results show clearly that more Cr-depleted spinel or magnetite was formed in multi-layered and laminated oxide. A few Cr-depleted Cr bands (3-5 wt. %) were present in the multi-layered oxide, while in the laminated oxide Cr-rich (10-20 wt. %) and Cr-depleted (1-2 wt. %) bands were present, alternately. The oxide thickness increases from duplex to multi-layered and then laminated morphology, which suggests that residual stress should be

developing in the oxide scale, potentially leading to the generation of cracks. Therefore, scanning laser Raman spectroscopy was used for oxide identification as well as possible stress distribution measurement.

4.1.4 Oxide identification using scanning laser Raman spectroscopy

The oxide elemental concentration and distribution were evaluated in the above discussion. To elucidate the mechanism of oxidation, it is necessary to identify the types of oxide present. Areas close to the oxide/metal interface from samples in the non-breakaway, breakaway initiation and post-breakaway oxidation regimes were evaluated using scanning LRS to obtain Raman spectra and specific peak intensity maps.

A white light illuminated optical micrograph of sample A-580-2542 and Raman spectra from two positions A in IOZ and B from a dark spot marked in the optical micrograph are shown in Figure 4-16. The spectra obtained in this work were fitted using Wire 4.3 software. The outlined area was selected for analysis. Several peaks were present in the spectra from the two examined locations, A and B. The peaks from spectrum in Figure 4-16b were present at 554, 609, 682, 1352 and 1598 cm^{-1} while the peaks in Figure 4-16c were present at 307, 550, 668, 1353 and 1584 cm^{-1}. These peaks can be used to identify the types of oxide and other features present in the oxide scale by comparing with reference Raman spectra.

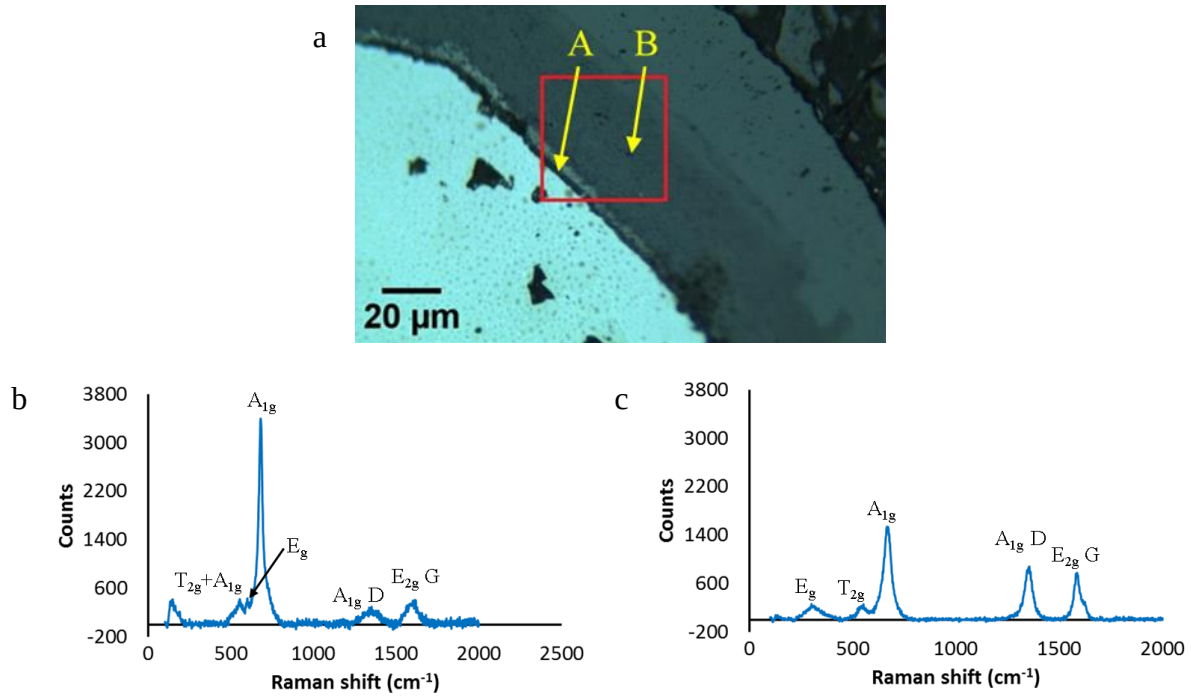

Figure 4-16: (a) White light optical micrograph of sample A-580-2542 showing region mapped by Raman spectroscopy; Raman spectra from (b) point A and (c) point B.

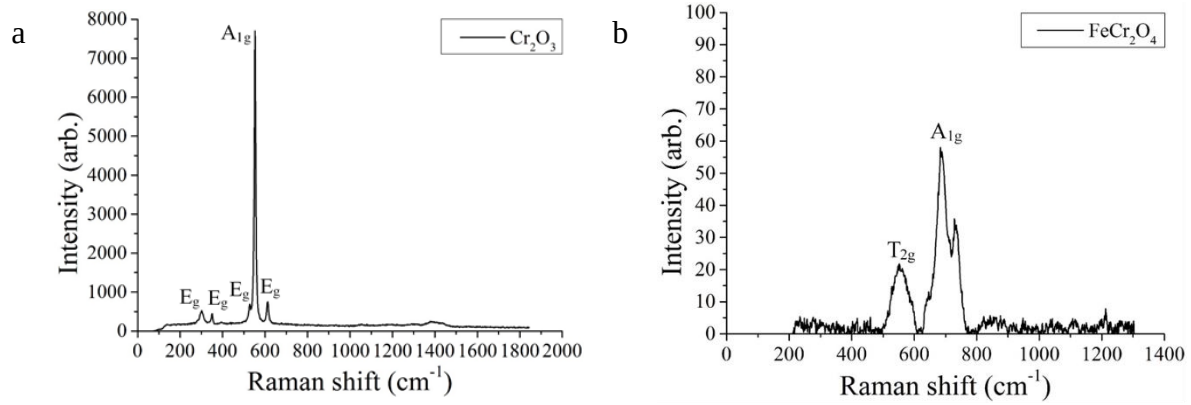

Figure 4-17: Raman spectra from (a) Cr_2O_3 and (b) $FeCr_2O_4$ from the RRUFF database [190]. Raman shift of peak in A_{1g} mode is 553 cm^{-1} in (a) [102] while peaks in T_{2g} and A_{1g} mode at 554 and 688 cm^{-1}, respectively, in (b) [95] (© Materials at High Temperatures).

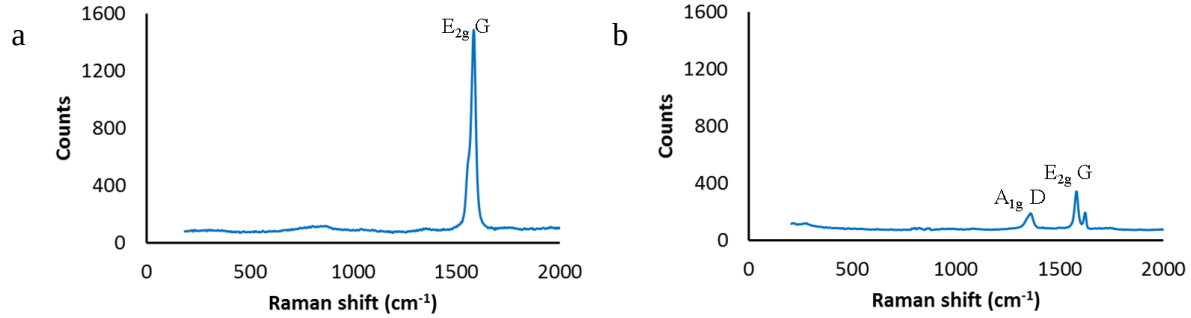

Figure 4-18: Raman spectra from (a) perfect graphite/single crystal graphite [191] and (b) graphite from the RRUFF database [192]. Raman shift of peak in E_{2g} mode in (a) is at 1582 cm^{-1} while the two peaks in A_{1g} and E_{2g} mode in (b) are at 1360 and 1585 cm^{-1}, respectively [104].

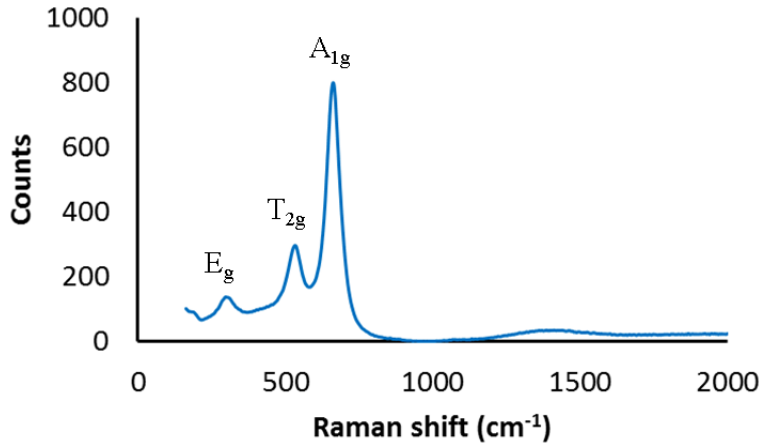

Figure 4-19: Raman spectra from Fe_3O_4 from the RRUFF database [193]. Raman shift of peaks in E_g, T_{2g} and A_{1g} mode are 295, 540 and 667 cm^{-1}, respectively [95].

A Raman spectrum was obtained from a pure sample of chromium (III) oxide (chromia, Cr_2O_3), obtained from the U.S. Department of Commerce to compare with experimental results from sample A-580-2542. According to Birnie et al., a main A_{1g} mode peak at 547 cm^{-1} and four small E_g mode peaks at 390, 352, 528 and 617 cm^{-1} were identified from Cr_2O_3, as shown in Figure 4-17a. Figure 4-17b shows a reference Raman spectrum obtained from the spinel

chromite ($FeCr_2O_4$), taken from the Raman database RRUFF [190], which is comprised of two peaks A_{1g} and T_{2g}, at 554 and 688 cm^{-1}, respectively.

Two small peaks at 554 cm^{-1} and 609 cm^{-1} from point A of sample A-580-2542 in the IOZ are indicative of the presence of Cr_2O_3 by comparing with the reference spectra from Figure 4-17a. Both Cr_2O_3 and $FeCr_2O_4$ contain peaks at about 541 cm^{-1} (A_{1g} mode for the former and T_{2g} mode for the latter) but the later contains a further peak at around 667 cm^{-1}, which is indicative of the presence of spinel at this location. Additionally, D and G peaks from graphite are present at 1352 and 1589 cm^{-1}, respectively, as shown in Figure 4-18 [104]. Peaks at 307, 550 and 668 cm^{-1} from the spectrum of point B indicate the presence of magnetite, by comparison with the reference spectrum from Fe_3O_4 shown in Figure 4-19, or a mixture of magnetite and spinel. The spectrum also contains a D peak at 1353 cm^{-1} and a G peak at 1584 cm^{-1} from graphite. The presence of D and G peaks indicates that the carbon was deposited in the oxide in the form of graphite.

Peak intensity maps at 541 cm^{-1} and 667 cm^{-1}, as shown in Figure 4-20a and b, indicate that Cr_2O_3 is mainly distributed at the IOZ/metal interface and is comprised of a mixture of spinel and Cr_2O_3. However, it can be seen from Figure 4-17 that the peak at 541 cm^{-1} is broad for the spinel and narrow for chromia. Oxide from the outlined area is mainly comprised of spinel with deposited carbon of a low-degree of order inferred from the similar intensity distributions in the maps at 1353 and 1590cm^{-1}, as shown in Figure 4-20c and d. Comparing the intensity maps at 667 cm^{-1} and 1590 cm^{-1}, it is found that the carbon is not distributed at the top right corner in the map, which is magnetite.

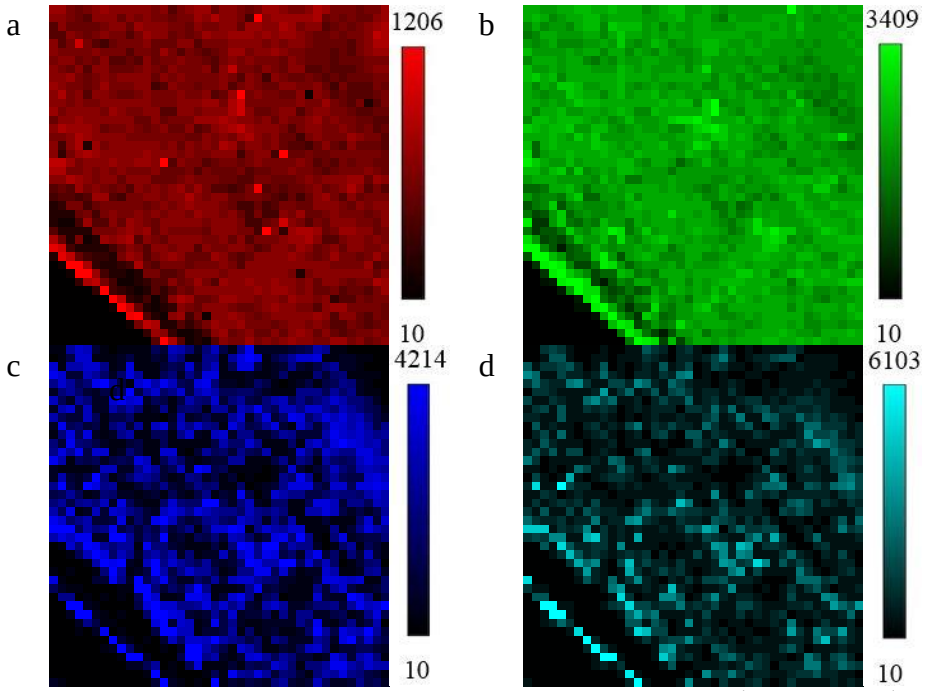

Figure 4-20: Raman peak intensity maps of A-580-2542 for peaks at (a) 541 cm^{-1}; (b) 667 cm^{-1}; (c) 1353 cm^{-1}; and (d) 1590 cm^{-1}. The intensity scale markers in counts per pixel are shown for each map.

The intensities of D and G peaks of graphite present in the spectrum of spot A are 120 and 298 counts, respectively, while in spot B they are 956 and 853 counts, respectively. As discussed in Chapter 2, the crystallite size can be derived from the I(D)/I(G) ratio [106], which can be obtained by curve fitting with Wire 4.3 software. These ratios of spots A and B in sample A-580-2542 are 0.40 and 1.12 respectively, suggesting the crystallite sizes to be 10 and 4 nm, respectively.

Sample A-640-1495 (400 to 800 @ 245) has entered breakaway initiation and was evaluated following the same method adopted for sample A-580-2542. A white light optical micrograph and the Raman spectra of two positions, A close to the oxide/metal interface and B in the band with dark colour, are shown in Figure 4-21. The outlined area was examined with Raman mapping and the results are shown in Figure 4-22. The absence of the small peak at 610 cm^{-1} in Figure 4-21b indicates that the oxide in position A is spinel, as confirmed by the peaks present at 548 and 669 cm^{-1}. The absence of a D peak and the presence of a G peak at around 1568 cm^{-1} in spot A indicates that the deposited carbon is in the form of highly ordered or single crystal graphite. The spectrum from Position B in Figure 4-21c shows that the dark band in the optical micrograph is composed of carbon with a low-degree of order due to the presence of a D peak at 1352 cm^{-1} and a G peak at 1575 cm^{-1}, as well as spinel, inferred from the peak present at 676cm^{-1}.

The Raman intensity maps of sample A-640-1495 (400 to 800 @ 245) were extracted from the peaks at 671 cm^{-1} and 1575 cm^{-1}, which are the main peaks of spinel and carbon, respectively, and the results are shown in Figure 4-22. The intensity map at 671 cm^{-1} indicates that the spinel is distributed in the evaluated outlined area while graphite is mainly distributed in the dark band discussed previously, which is consistent with the results from the spectra.

The intensities of the D and G peaks present in the spectrum of spot A shown in Figure 4-16a are 0 and 383, respectively, while in spot B they are 446 and 2200, respectively. The crystallite size is determined by the I(D)/I(G) ratio [106]. The ratios of spots A and B in sample A-580-2542 are 0 and 0.2, respectively, indicating the corresponding crystallite sizes are 0 (signal crystal) and 20 nm, respectively.

As observed in Figure 4-5g, sample A-640-3883 has entered the post-breakaway regime. The outlined area in the white light optical micrograph was analysed using scanning LRS. Spectra from two locations, spots A and B, marked in the optical micrograph were extracted from the results, as shown in Figure 4-23. The presence of a peak at 675 cm^{-1} and absence of peaks at around 540 and 610 cm^{-1} are indicative of the presence of spinel and absence of Cr_2O_3. Two additional peaks are present at 1349 cm^{-1} and 1585 cm^{-1}, indicating the presence of low-degree order carbon. As for the spectrum from spot B, which corresponds to the Cr-depleted location, three peaks are present at 309, 548 cm^{-1} and 671 cm^{-1}, indicative of the presence of magnetite

[95]. Therefore, spot B is comprised of magnetite or a mixture of magnetite and spinel, because peaks at 548 and 671 cm^{-1} are also present in spinel. Moreover, D and G peaks from carbon are present at 1351 and 1592 cm^{-1}, respectively.

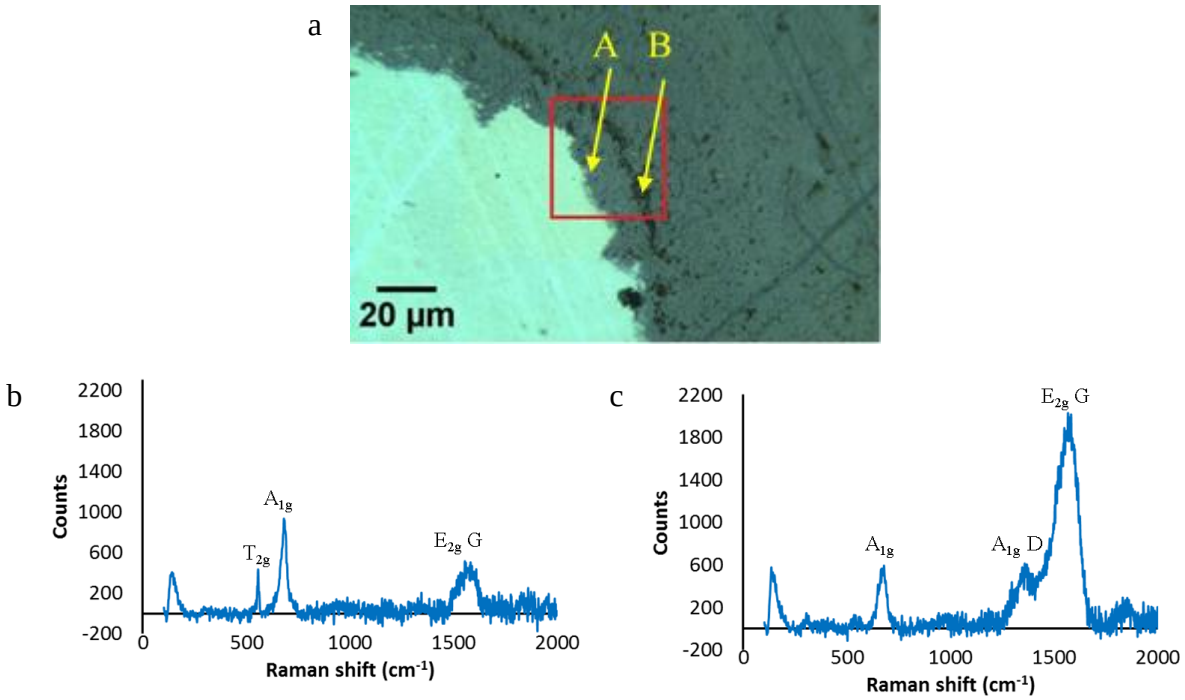

Figure 4-21: (a) White light optical micrograph of sample A-640-1495 (400 to 800 @ 245) showing region mapped by Raman spectroscopy. Raman spectra from (b) point A and (c) point B [95][104].

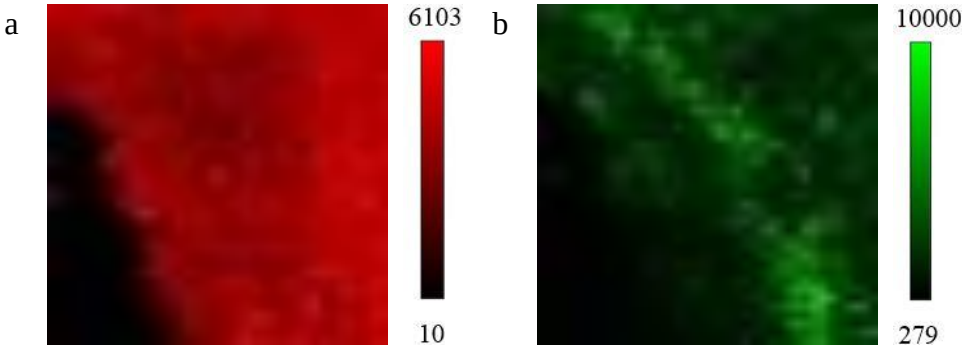

Figure 4-22: Raman peak intensity maps of sample A-640-1495 (400 to 800 @ 245) for peaks at (a) 671 cm^{-1}; (b) 1575 cm^{-1}. The intensity scale markers in counts per pixel are shown for each map.

The intensities of the D and G peaks of spot A are 2347 and 2343 respectively while for spot B they are 1140 and 821, respectively. Therefore, the I(D)/I(G) ratios of spot A and B are 1 and 1.39, respectively. According to the I(D)/I(G) ratio and the G peak Raman shift, the graphite formed in this sample is in transition from graphite to nanocrystalline graphite. The crystallite sizes obtained from spot A and B are 4.5 and 3 nm, respectively [106][104].

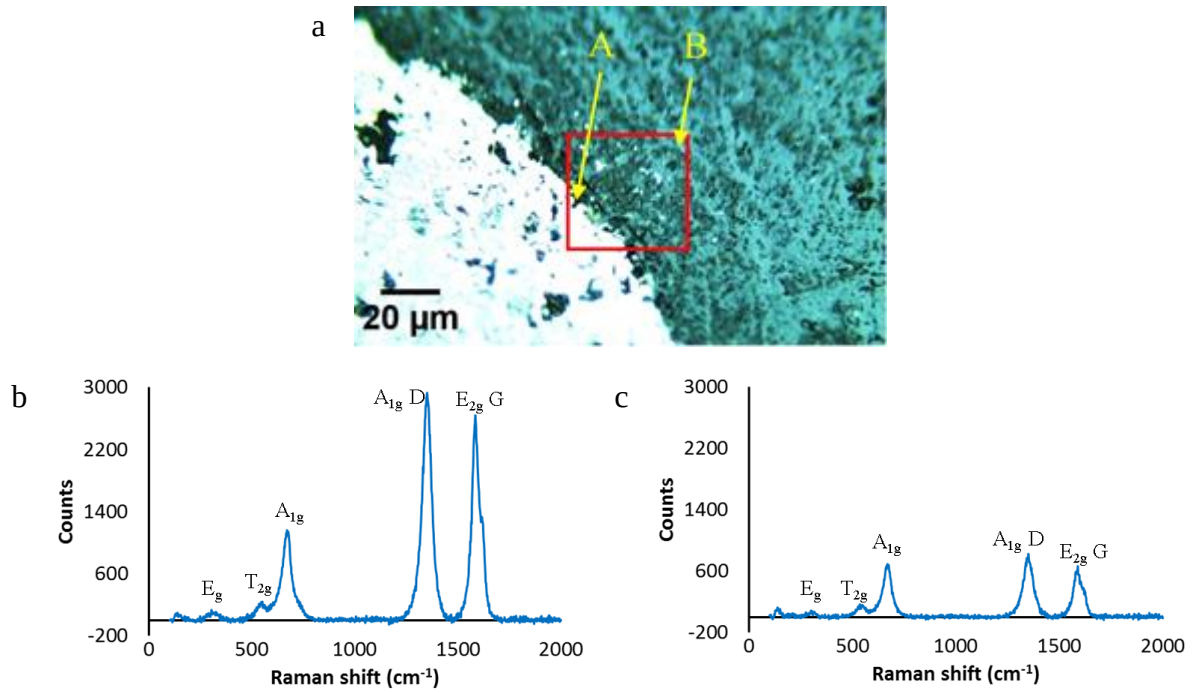

Figure 4-23: (a) White light optical micrograph of sample A-640-3883 showing region mapped by Raman spectroscopy. Raman spectra from (b) point A and (c) point B [95][104].

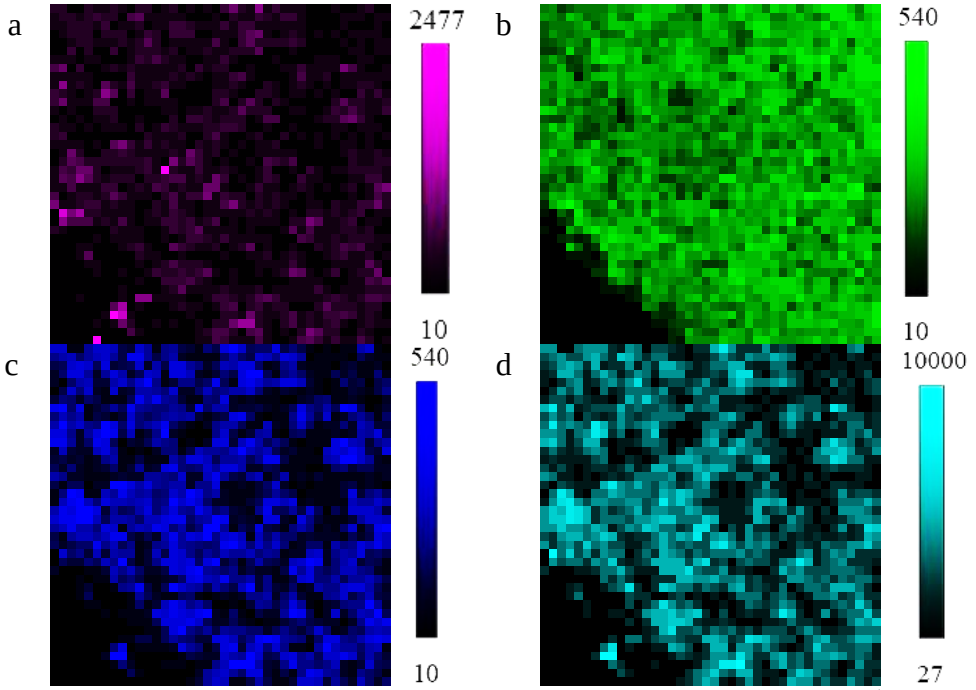

Figure 4-24: Raman peak intensity maps of sample A-640-3883 for peaks at (a) 308 cm^{-1}; (b) 669 cm^{-1}; (c) 1351 cm^{-1} and (d) 1589 cm^{-1}. The intensity scale markers in counts per pixel are shown for each map.

Raman intensity distribution maps of sample A-640-3883 were obtained from the 308, 669, 1351 and 1589 cm^{-1} peaks. The peak intensity map at 308 cm^{-1} is indicative of the presence of magnetite. Both magnetite and spinel include the peak at 546 cm^{-1}. Therefore, the representative map from the peak at 308 cm^{-1} is shown in Figure 4-24a instead of that from the 546 cm^{-1} peak. Magnetite is obviously present in the oxide. The low intensity locations correspond to spinel in the oxide. The intensity maps at 308 and 669 cm^{-1} indicate the

distribution of magnetite and spinel. The intensity maps from the D and G peaks at 1351 and 1589 cm^{-1}, respectively, show that carbon with a low-degree of order is present in most of areas in the examined oxide.

Table 4-5 presents the Raman shifts of peaks from spectra for the two locations in three examined experimental HRA samples, A-580-2542, A-640-1495 (400 to 800 @ 245) and A-640-3883. The obtained D and G peak intensities and their ratios are given in Table 4-6. Chromia is only present in the IOZ layer from sample A-580-2542. Magnetite was present in the examined oxide from samples A-580-2542 and A-640-3883. However, it is only found occasionally in A-580-2542 while it is present within the spinel from spectra of sample A-640-3883.

Table 4-5: The Raman peak positions for each location examined in three selected experimental HRA samples: A-580-2542, A-640-1495 (400 to 800 @ 245) and A-640-3883.

Sample ID and examined locations		*(Fe_3O_4) E_g (cm^{-1})*	*T_{2g}(spinel)/A_{1g} (Cr_2O_3) (cm^{-1})*	*(Cr_2O_3) E_g (cm^{-1})*	*A_{1g} (cm^{-1})*	*A_{1g} D (cm^{-1})*	*E_{2g} G (cm^{-1})*
A-580-2542	*Spot A*	*/*	*554*	*609*	*682*	*1352*	*1598*
	Spot B	*307*	*550*	*/*	*668*	*1353*	*1584*
A-640-1495 (400 to 800 @ 245)	*Spot A*	*/*	*548*	*/*	*669*	*/*	*1568*
	Spot B	*/*	*/*	*/*	*676*	*1352*	*1573*
A-640-3883	*Spot A*	*/*	*/*	*/*	*675*	*1349*	*1585*
	Spot B	*309*	*548*	*/*	*671*	*1351*	*1592*

Table 4-6: The D and G peak intensity, their ratio and crystallite size of graphite for each location examined in three selected experimental HRA samples: A-580-2542, A-640-1495 (400 to 800 @ 245) and A-640-3883.

Sample ID	*Location*	*Intensity*		*I(D)/I(G) ratio*	*Graphite crystallite size (nm)*
		D	*G*		
A-580-2542	*Spot A*	*120*	*298*	*0.40*	*10*
	Spot B	*956*	*853*	*1.12*	*4*
A-640 -1495 (400 to 800 @ 245)	*Spot A*	*/*	*383*	*0*	*/*
	Spot B	*446*	*2200*	*0.20*	*20*
A-640-3883	*Spot A*	*2347*	*2343*	*1*	*4.5*
	Spot B	*1140*	*821*	*1.39*	*3*

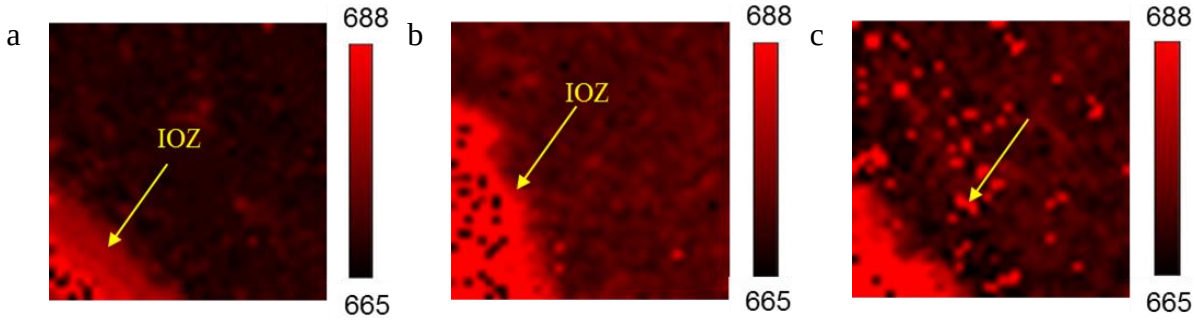

Figure 4-25: Raman peak position maps at around 675 cm^{-1} from sample (a) A-580-2542; (b) A-640-1495 (400 to 800 @ 245) and (c) A-640-3883.

The peak shift may be caused by a change in composition, stress or a combination of both. According to ref [194], the positive shift of peak indicates a compressive stress while tensile

stress produces a negative shift. Assuming there are no composition changes in the examined regions, Figure 4-25a, b and c show the peak position maps of the outlined region marked in Figure 4-16a, Figure 4-21a and Figure 4-23a, respectively. The peak shifts from 665 to 688 cm^{-1}, as shown in the intensity scale bar. The high intensity in the areas corresponding to the matrix are due to the effects of signal noise and should be ignored. It can be seen that the peaks of sample A-580-2542 have high intensity in the IOZ layer and a relatively lower intensity in the spinel, suggesting a relative compressive stress in the IOZ layer, as the arrow shows in Figure 4-25a. The peak position map from sample A-640-1495 (400 to 800 @ 245) shows about 8 cm^{-1} higher intensity in the discontinuous IOZ (as the arrow shows in Figure 4-25b) than the adjacent oxide. Some high intensity spots (as arrow shows in Figure 4-25c) are present in the peak position map of sample A-640-3883, indicating higher Raman shift and, hence, relative compressive stress in these spots.

4.2 Carbide observation and carburisation characterisation

During exposure to the CO_2-based simulant coolant gas, oxidation and carburisation occurred simultaneously. The diffusing carbon reacts with Fe and some alloying element, e.g. Cr, Mo, etc., leading to the formation of carbides and possibly other precipitates embedded in the matrix. Precipitates of different types and morphologies, which were formed in different stages of oxidation, were identified and analysed. Precipitates may be linked to the mechanisms of oxidation and carburisation, and the triggers of breakaway oxidation. The carbide area fractions were examined to understand the influence of exposure conditions on the overall carburisation process.

4.2.1 Samples used for carburisation analysis

Four samples, including A-virgin, A-580-2542, A-640-1495 (400 to 800 @ 245) and A-640-3883, were selected for XRD, TEM, and STEM analysis to identify the types of carbides with different morphologies observed from FIB XeF_2 images. Experimental autoclave HRA samples listed in Table 4-1 were analysed using FIB, following the three paths shown in Figure 4-26, and the FIB XeF_2 images were processed with ImageJ software to obtain plots of carbide area fraction against distance to the oxide/metal interface.

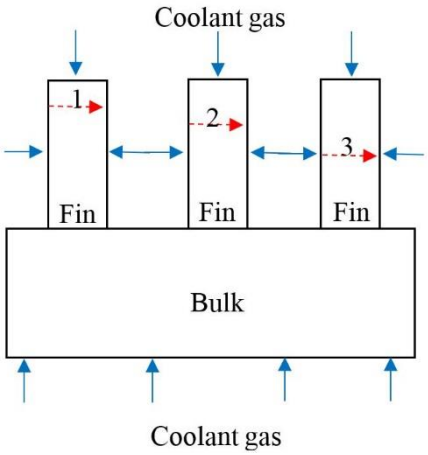

Figure 4-26: Schematic drawing of finned samples, directions of coolant gas diffusion (blue solid lines), and three paths for FIB milling (red dashed lines). The experiment following three paths should be on the same fin.

Comparison experiments between FIB and HS-AFM were applied to non-breakaway sample A-580-2542 and post-breakaway sample A-640-3883. X-ray diffraction was used for phase identification. Transmission electron microscopy was used to identify the precipitates of different morphologies, including crystal structure, lattice parameter, etc. Scanning transmission electron microscopy was then used for elemental distribution evaluation to obtain the weight percentage of elements in the precipitates as well as their surrounding matrices. Finally, high-speed atomic force microscopy was used to obtain the morphologies of precipitates present in non-breakaway and post-breakaway samples, for comparison.

4.2.2 Carbide precipitates identification

All the autoclave HRA samples plus A-virgin were examined with XeF_2-assisted FIB imaging and precipitates with four different morphologies were observed. As shown in Figure 4-27, carbides with different morphologies formed in different stages of oxidation were observed: fine needles, large needles, coarse carbide, and cored carbides. Coarse precipitates (diameter > 1 μm) were observed at grain boundaries as well as in the grains. Additionally, intragranular fine needle precipitates (length < 700 nm) were present in samples in the early stage of non-breakaway oxidation, e.g. A-580-2542. Cored coarse precipitates and intragranular large needle precipitates (length > 1 μm) were present in samples entering breakaway initiation, e.g. A-640-1495 (400 to 800 @ 245). Cored coarse precipitates were observed in samples entering the post-breakaway oxidation regime, e.g. A-640-3883. It can be inferred that the carbon diffused both along grain boundaries and within grains to form both intergranular and intragranular precipitates.

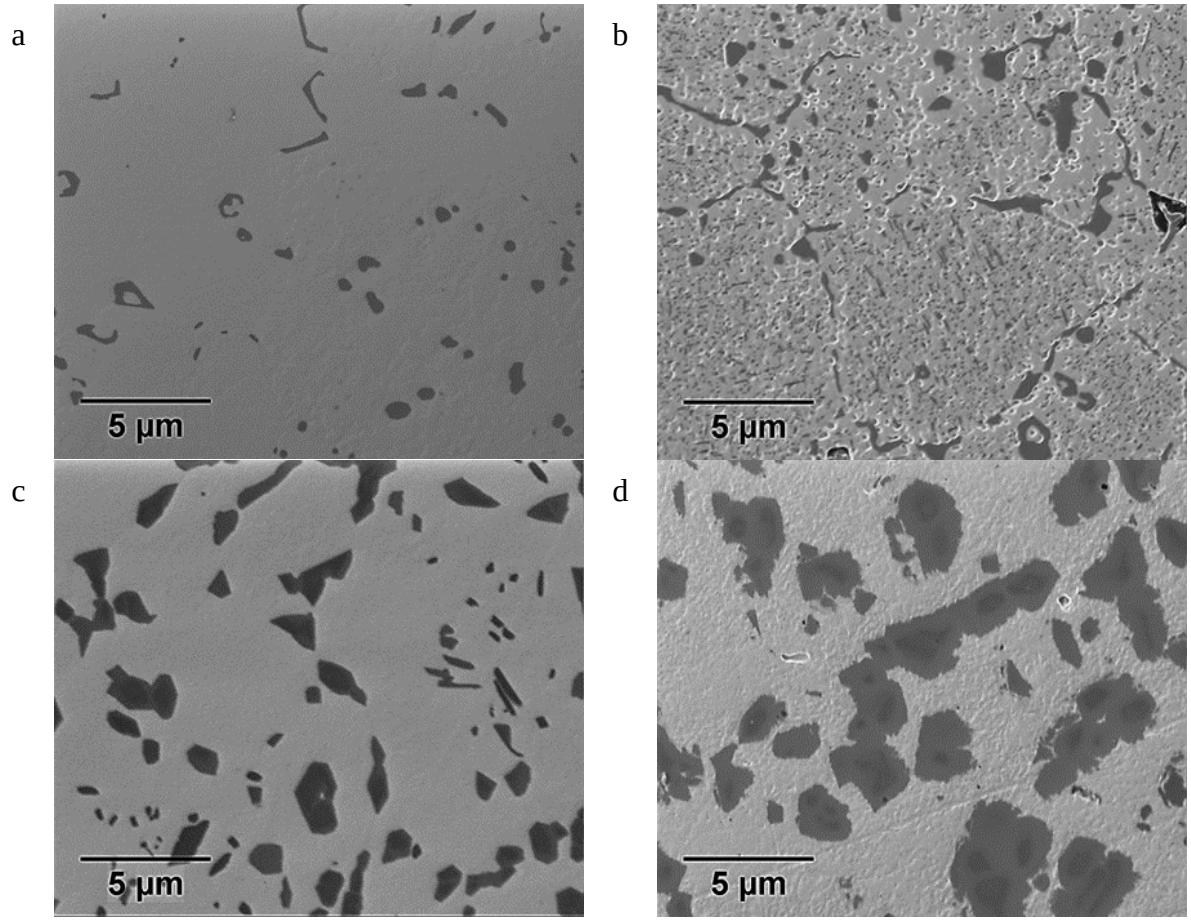

Figure 4-27: FIB XeF_2 images from sample (a) A-virgin; (b) A-580-2542; (c) A-640-1495 (400 to 800 @ 245) and (d) A-640-3883.

Figure 4-28 shows results from XRD analysis using Cu Kα x-radiation. Mounting materials were examined separately and the corresponding peaks were identified in the resulting spectra. The only phase present in A-virgin was identified as α-Fe. This phase was also detected in the other examined samples. Additionally, oxide M_3O_4 (including magnetite and spinel) was detected in sample A-580-2542. However, there was no signal from precipitates, probably due to their low volume fractions. The spectrum from sample A-640-1495 (400 to 800 @ 245) indicated the presence of MC, $M_{23}C_6$, and M_2C carbides plus α-Fe and M_3O_4. It appears that MC and $M_{23}C_6$ were also present in sample A-640-3883, plus α-Fe and oxide. Though it shows the phases seen in the micrographs in Figure 4-27, XRD is incapable of identifying the specific precipitates. Therefore, TEM was adopted to identify the precipitates with different morphologies, including coarse, fine needle, large needle and cored coarse.

a

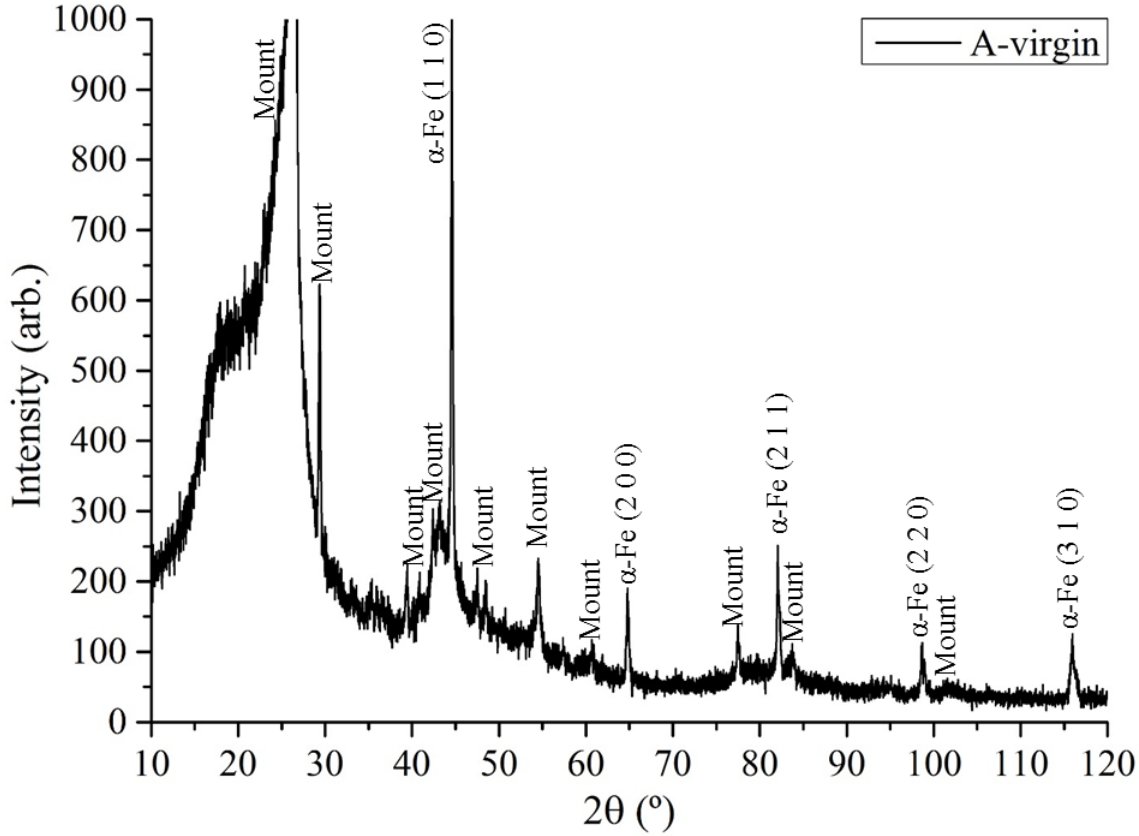
A-virgin
Intensity (arb.)
2θ (°)
Mount
α-Fe (1 1 0)
α-Fe (2 0 0)
α-Fe (2 1 1)
α-Fe (2 2 0)
α-Fe (3 1 0)

b

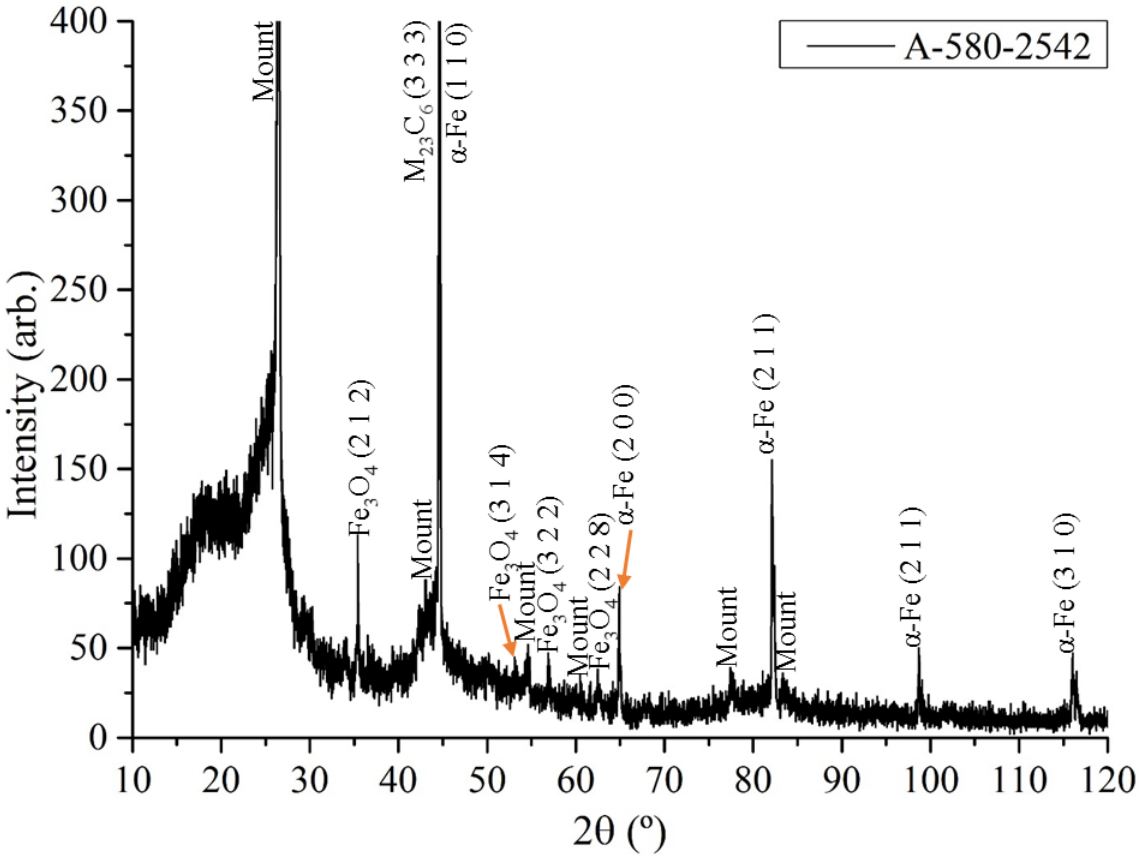
A-580-2542
Intensity (arb.)
2θ (°)
Mount
$M_{23}C_6$ (3 3 3)
α-Fe (1 1 0)
Fe_3O_4 (2 1 2)
Fe_3O_4 (3 1 4)
Fe_3O_4 (3 2 2)
Fe_3O_4 (2 2 8)
α-Fe (2 0 0)
α-Fe (2 1 1)
α-Fe (3 1 0)

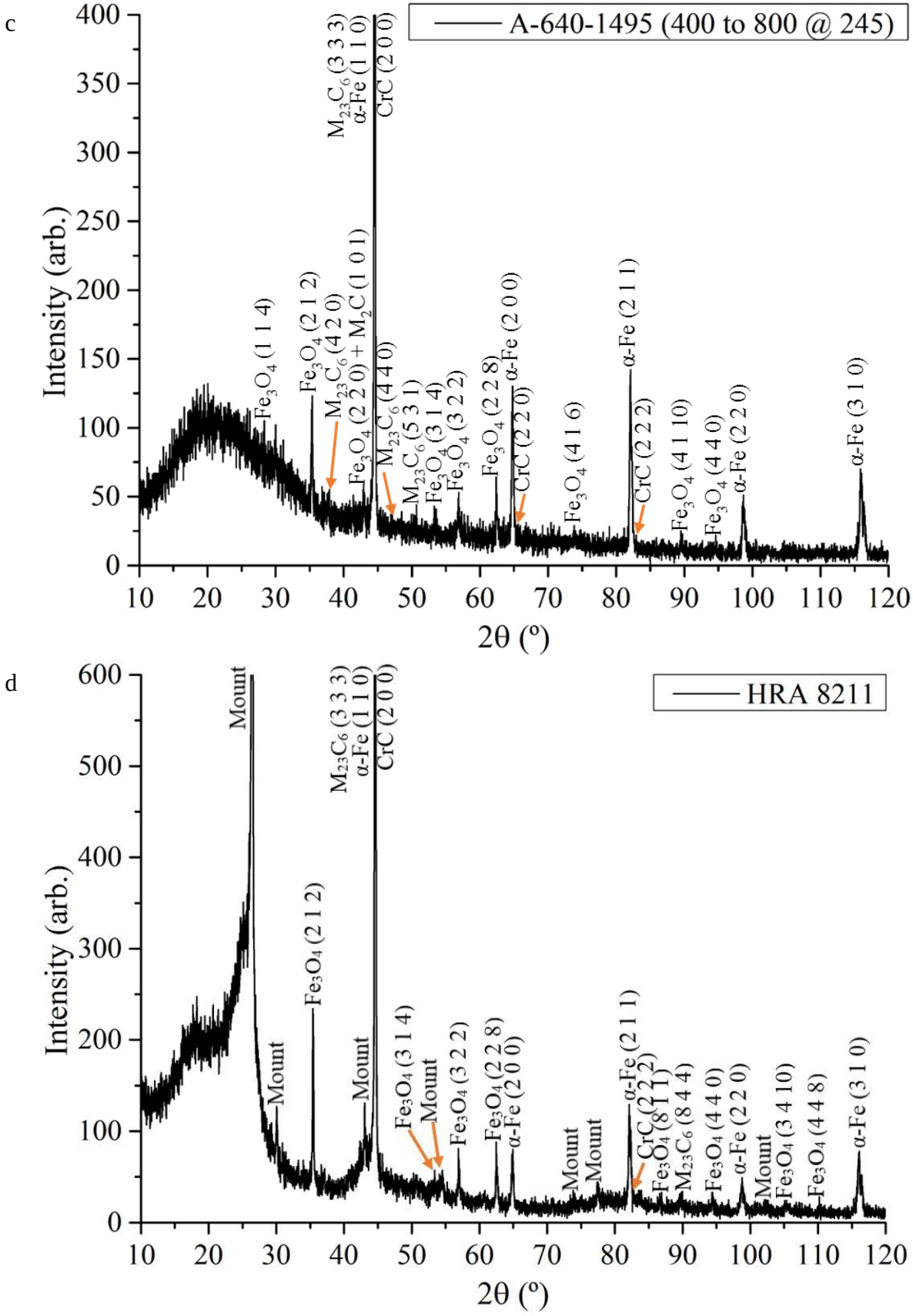

Figure 4-28: XRD results of the four examined samples (a) A-virgin; (b) A-580-2542; (c) A-640-1495 (400 to 800 @ 245); (d) A-640-3883.

Thin foils 15 × 6 × 0.1 μm in size were prepared using the ion milling, lift-out method in a FEI Helios NanoLab 600i combined FIB/SEM system (see Section 3.7.4) from four samples in different stages of oxidation, and examined with TEM and STEM-EDS for precipitate identification and the elemental distribution analysis of carbides of different morphologies.

A Philips EM430 operated at 200 kV (see Section 3.5.1) was used to obtain the diffraction patterns of the phases examined. Precipitates with four different morphologies and corresponding adjacent parent metal were evaluated using electron diffraction patterns to identify the crystal structures and lattice parameters. A TEM image from sample A-580-2542 of the evaluated fine needle precipitate, the corresponding selected area diffraction (SAD) pattern and the equivalent from the adjacent parent matrix are shown in Figure 4-29. It appears that the fine needle precipitate has a hexagonal (HCP) structure with lattice parameters a and c of 2.510 Å and 4.199 Å, respectively. According to ref [195], the fine needle is identified as M_2C (M represents Fe and Cr) and is in the [011] zone axis. Since there is no evidence of N present in the metal chemical composition given in Table 3-1 exposure environment (comprised of H_2O, H_2, CH_4, CO and balance CO_2), it is more reasonable to identify the precipitates as carbides, M_2C, rather than nitrides, M_2N, which has a similar crystal structure and lattice parameters. Furthermore, from SAD, the adjacent matrix is α-Fe with a body-centred cubic (BCC) structure and in the [011] zone axis. The lattice parameter a is 3.161 Å, which is larger than the theoretical value 2.866 Å [195]. Slater investigated the atomic radius of elements, which demonstrates that the atomic radius of Fe, Cr and Mo are 1.40, 1.40 and 1.45 Å respectively [196]. Ref [197] shows that the atomic radius of Fe, Cr and Mo cations is 1.72, 1.85 and 2.01 Å respectively, Therefore, the larger lattice parameter from our analysis is likely to be a result of the alloying elements Cr and Mo in the steel. The orientation relationship between fine needle M_2C and matrix is $(10\bar{1})_{M_2C} \| (01\bar{1})_{\alpha-Fe}$ and $[011]_{M_2C} \| [011]_{\alpha-Fe}$.

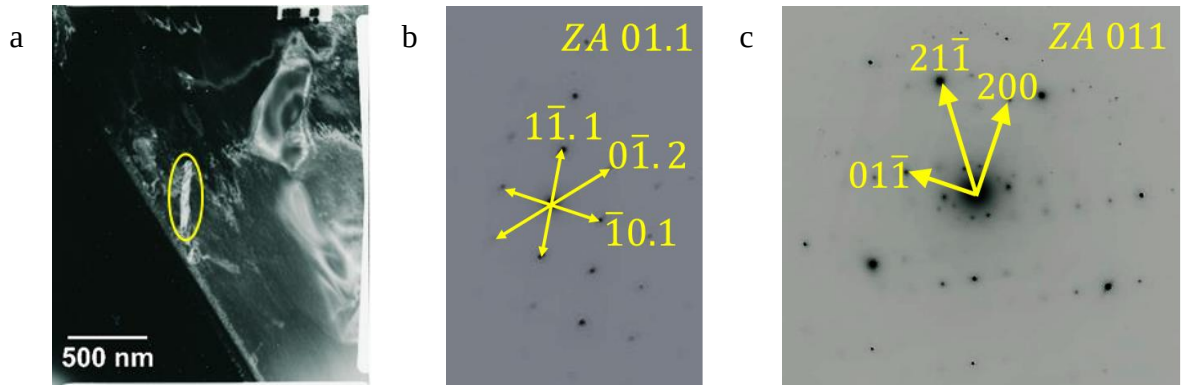

Figure 4-29: (a) The dark field TEM image of sample A-580-2542; (b) corresponding SAD of the small needle marked in TEM image and (c) corresponding SAD of matrix adjacent to the small needle.

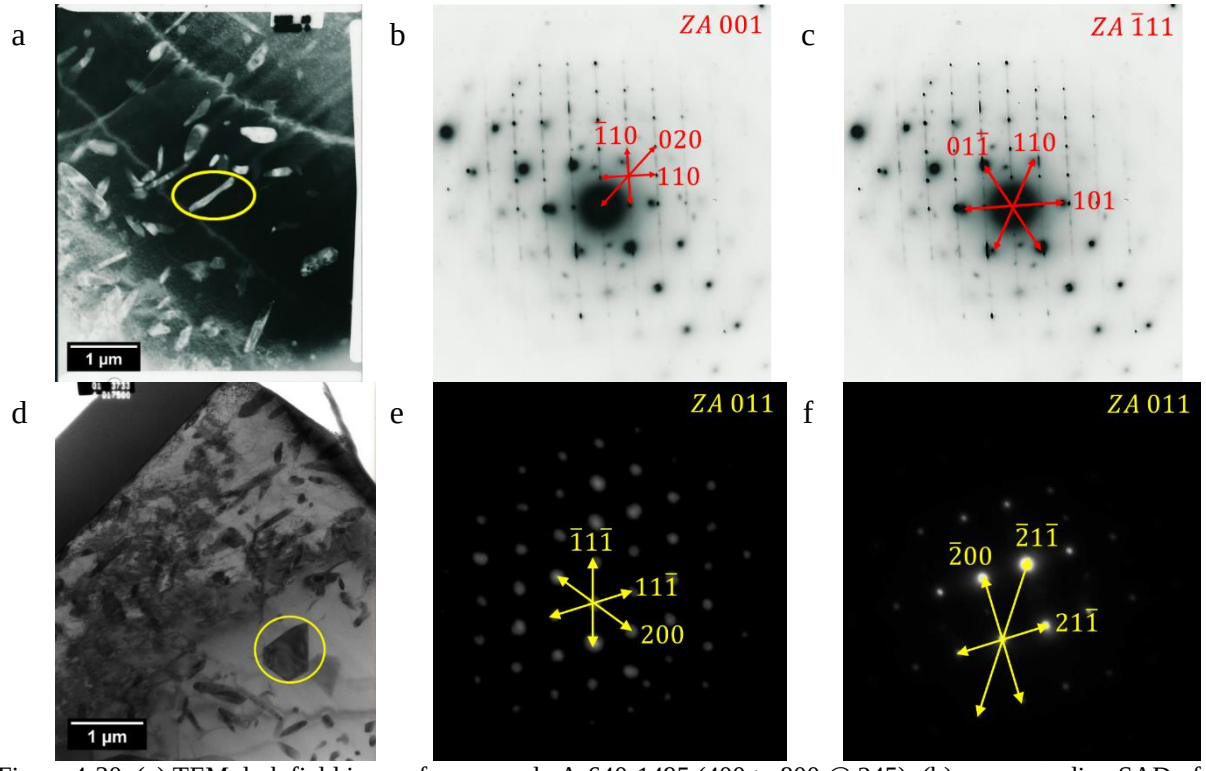

Figure 4-30: (a) TEM dark field image from sample A-640-1495 (400 to 800 @ 245); (b) corresponding SAD of the large needle marked in TEM image and (c) corresponding SAD of matrix adjacent to the small needle. (d) TEM image from another grain including a coarse carbide; (e) corresponding SAD of the coarse carbide marked in TEM image and (f) corresponding SAD of matrix adjacent to the coarse carbide.

TEM images and SADs from a large needle and adjacent matrix for sample A-640-1495 (400 to 800 @ 245) are shown in Figure 4-30a, b and c. From SAD, the large needle is identified as MC, which has a body-centred cubic (BCC) structure in the [001] zone axis, while the adjacent metal is α-Fe in the $[\bar{1}11]$ zone axis. The lattice parameter of the former is 4.714 Å and the latter 2.673 Å. A coarse carbide in another grain from the same thin foil was also analysed and the TEM image and SADs of the carbide and adjacent metal are shown in Figure 4-30d, e and f. The coarse carbide is identified as $M_{23}C_6$ with a lattice parameter of 10.230 Å, which is close to the theoretical value of 10.621 Å, with a face-centred cubic (FCC) structure in the [011] zone axis, while the adjacent metal is α-Fe with lattice parameter of 2.727 Å in the [011] zone axis in the analysed grain. Therefore, the orientation relationship between the large needle MC and the matrix is $(110)_{MC}\|(101)_{\alpha-Fe}$ and $[001]_{MC}\|[\bar{1}11]_{\alpha-Fe}$, while the relationship between the coarse carbide $M_{23}C_6$ and the matrix is $(11\bar{1})_{M_{23}C_6}\|(21\bar{1})_{\alpha-Fe}$ and $[011]_{M_{23}C_6}\|[011]_{\alpha-Fe}$.

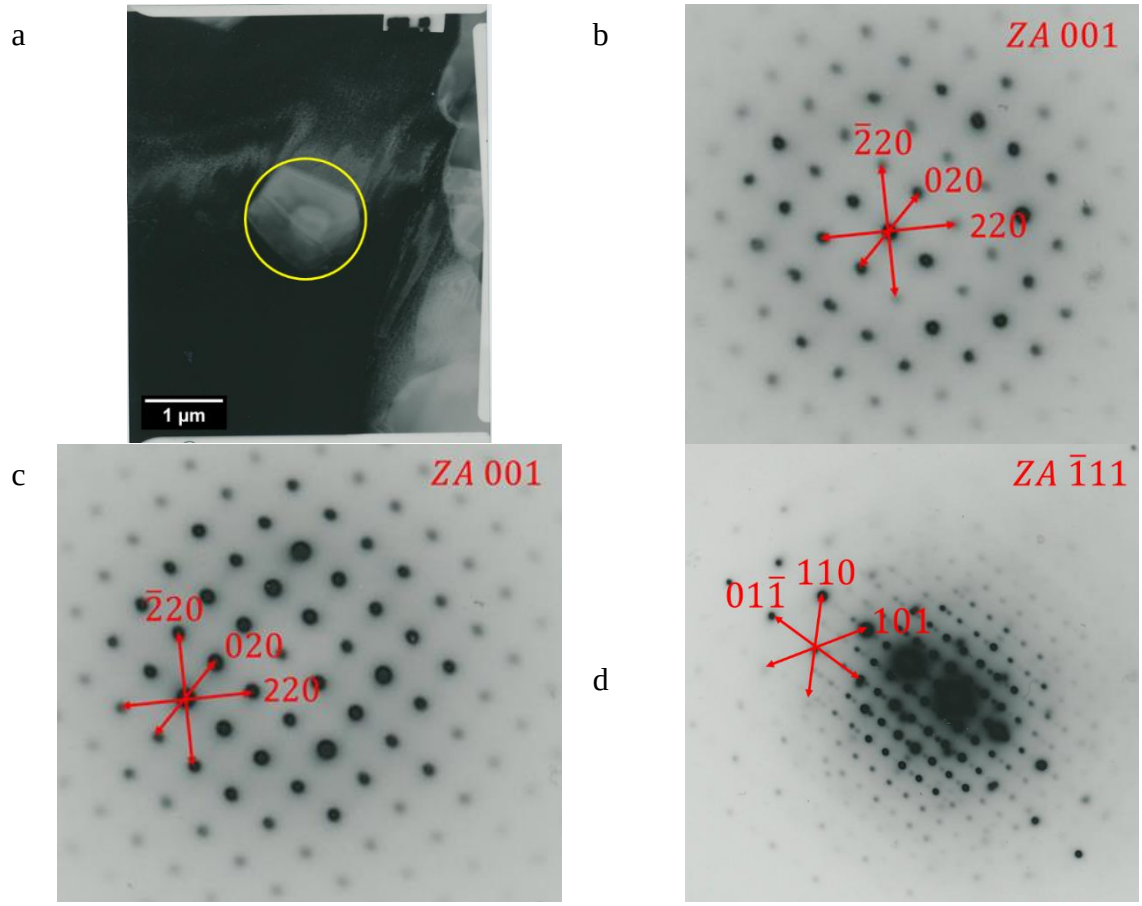

Figure 4-31: (a) TEM image from sample A-640-3883; (b) corresponding SAD of the inner core from cored coarse carbide marked in TEM image; (c) corresponding SAD of the outer layer from cored coarse carbide and (d) corresponding SAD of matrix adjacent to the cored coarse carbide.

Figure 4-31 shows that cored coarse carbides were present in sample A-640-3883. SADs of inner core and outer layer carbide were evaluated, together with the adjacent matrix. The results show that the core and the outer layer carbide have grown in the same orientation with the [001] zone axis. However, a small difference is present in the lattice parameters of the two, with the former being 9.86 Å and the latter 10.07 Å. Though the atomic radius of Cr (0.130 nm) [198] is larger than that of Fe (0.126 nm) [199], both Fe^{2+} (0.076 nm) and Fe^{3+} (0.064 nm) have larger ionic radius than Cr^{3+} (0.062 nm) [200]. Therefore, the difference in lattice parameter between the inner core and surrounding carbide is very likely a result of the different Fe/Cr ratio. Diffraction patterns of the adjacent parent metal identified it as α-Fe in the $[\bar{1}11]$ zone axis, with lattice parameter 3.071 Å. Therefore, the orientation relationship between cored coarse carbide $M_{23}C_6$ and matrix is $(200)_{M_{23}C_6} \| (0\bar{1}\bar{1})_{\alpha-Fe}$ and $[001]_{M_{23}C_6} \| [\bar{1}11]_{\alpha-Fe}$.

Since carbides with different morphologies had been identified with TEM, their chemical compositions were analysed using STEM-EDS to obtain the elemental profiles.

4.2.3 Carbide composition

The thin foils were analysed in the STEM mode using an Oxford Instruments AztecTEM advanced EDS system with X-Max 80 detector and STEM-EDS Kα1 maps of elements were obtained. Bearden and Burr evaluated X-ray atomic energy levels and results showed that the Kα1 energy of Fe, Cr, Mo, Mn and S are 7.11, 5.99, 2.00, 6.54 and 2.47 keV, respectively [201]. The composition of carbides and the surrounding matrices were analysed using STEM with EDS analysis. Line scan analyses followed the direction shown by the arrows in STEM images and ended at the point of the arrows. From the FIB images in Figure 4-27, it appears that only coarse carbides were present both at grain boundaries and within the grains in the A-virgin sample. A thin foil sample was examined using STEM-EDS, as shown in Figure 4-32 based on line scan results. The Cr concentration of intergranular carbide is approximately 80 wt.% with a very low Fe content, while the Cr and Fe concentrations of the intragranular carbide are approximately 50 wt.% and 30 wt.%, respectively. Chromium concentration in the surrounding matrix is around 9 wt.%, consistent with the Cr content of 9Cr-1Mo steels. Peaks from Mn and S confirm the presence of MnS inclusions.

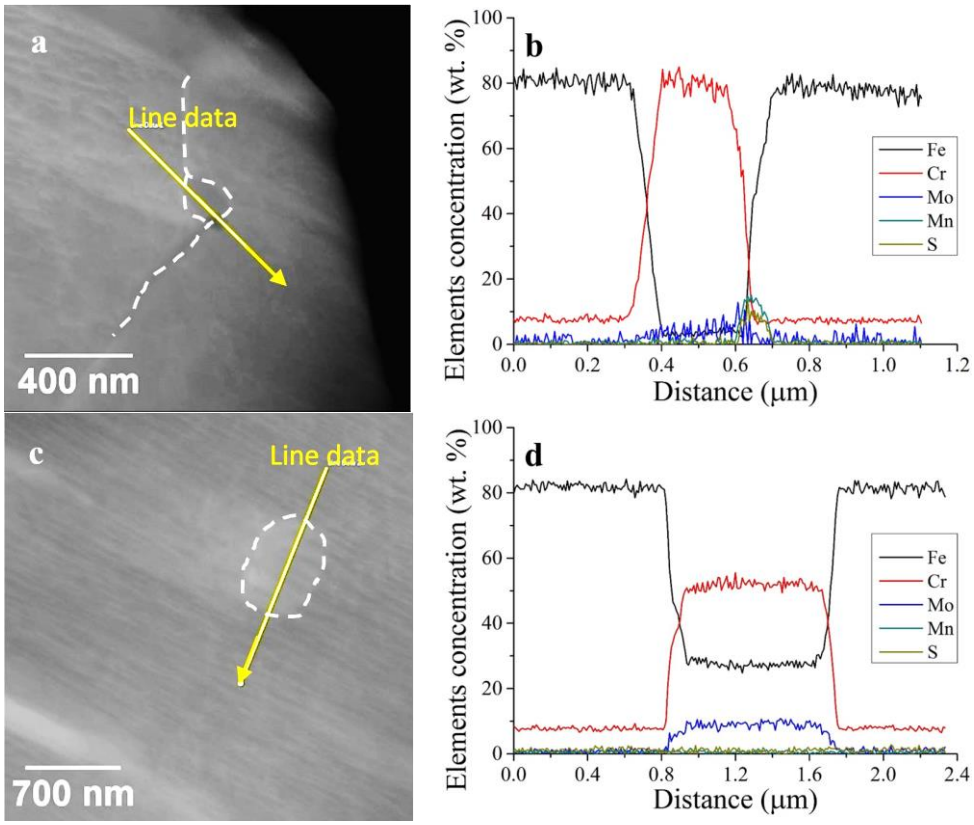

Figure 4-32: (a) STEM image of an intergranular coarse carbide in A-virgin sample; (b) EDS line scan profile from the line in (a); (c) STEM image of an intragranular carbide in A-virgin sample; (d) EDS line scan profile from the line in (c).

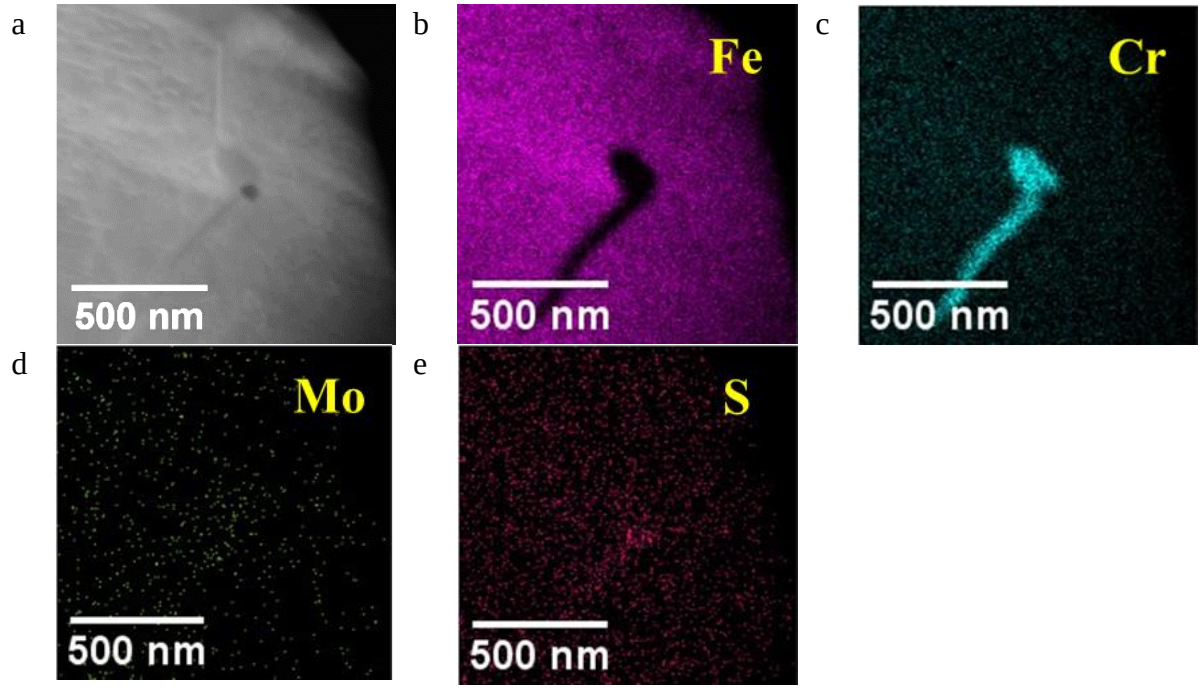

Figure 4-33: (a) STEM image of an intergranular coarse carbide in A-virgin sample; EDS maps of (b) Fe; (c) Cr; (d) Mo and (e) S.

The EDS maps in Figure 4-33 examined the same area evaluated in Figure 4-32a, showing elemental distributions. Obviously, the carbide is mainly composed of Cr. The dark precipitate in the micrograph on the side of the carbide shows a higher concentration in S, corresponding to the elemental profiles in Figure 4-32b. It confirms that this dark feature is an MnS inclusion.

Images obtained by FIB XeF_2 imaging and presented in Figure 4-27 show that coarse carbides and fine needles are present in the region close to the oxide in sample A-580-2542. Coarse carbides are present both at grain boundaries and within the grains while fine needles are distributed within the grains. In order to identify these two types of carbides with different morphologies, a thin foil was extracted using dualbeam and analysed with STEM to obtain the elemental distribution of these two types of carbides, as shown in Figure 4-34. A cross-section perpendicular to the c axis of a fine needle was selected to minimise any contribution from the matrix. EDS line scan results of the examined small needle and coarse carbide are shown in Figure 4-34b and d, respectively. The concentration profiles show that the fine needle is mainly comprised of Cr (50-90 wt. %) and Fe (less than 5 wt. %), whereas the Cr and Fe concentrations in the coarse carbide are approximately 50 and 30 wt. %, respectively.

Figure 4-35 shows an area including cross-sections of two fine needle precipitates and the matrix between. The fine needles are Cr-rich, with the concentration profiles shown in Figure 4-34d.

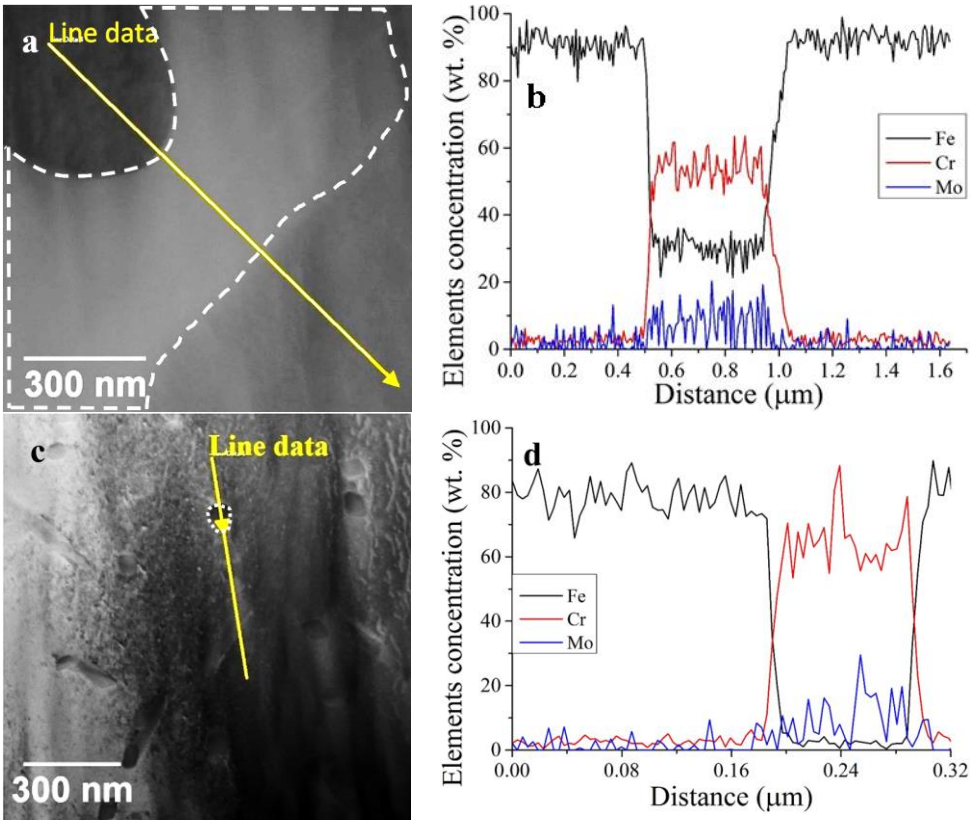

Figure 4-34: (a) STEM image of a coarse carbide in sample A-580-2542; (b) EDS line scan profile from the line in (a); (c) STEM image of needle carbides in sample A-580-2542; (d) EDS line scan profile from the line in (c).

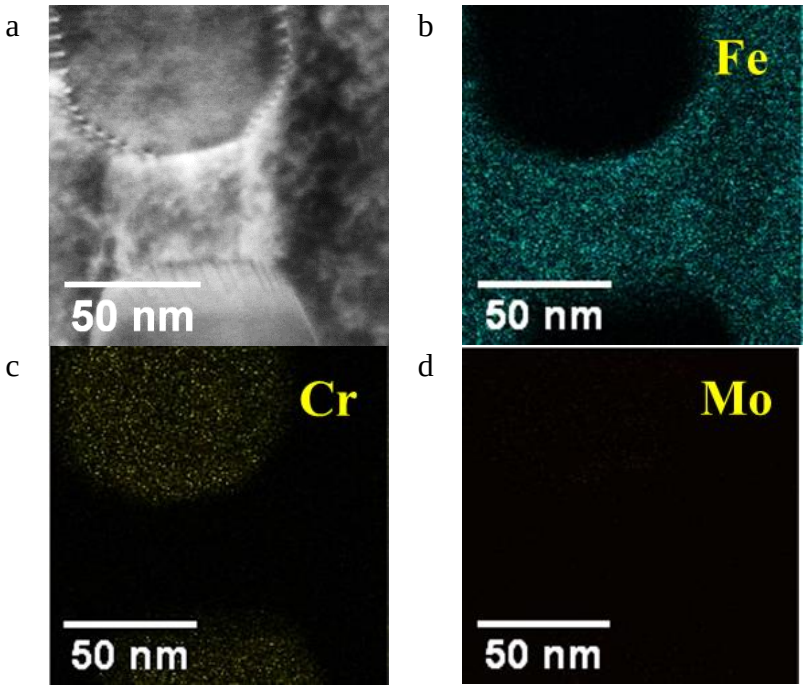

Figure 4-35: (a) STEM image of a fine needle cross-section in A-580-2542; EDS maps of (b) Fe; (c) Cr and (d) Mo.

Cores are present in the coarse carbide formed in sample A-640-1495 (400 to 800 @ 245), which has entered breakaway initiation. Concentration profiles of elements from cored coarse carbide and a large needle are shown in Figure 4-36. These show that the Cr concentration in

the core is as high as 80 wt. %, but reduced to around 50 wt. % in the outer layer carbide. The profiles also indicate that Cr is depleted in the surrounding matrix (less than 5 wt. %). The concentration profiles of large needles show Cr and Fe concentrations of 40-60 wt. % and 20-40 wt. %, respectively. The Fe concentration is roughly equal to that of Cr in the outer layer carbide, while the Cr concentration is higher than that of Fe in the cores.

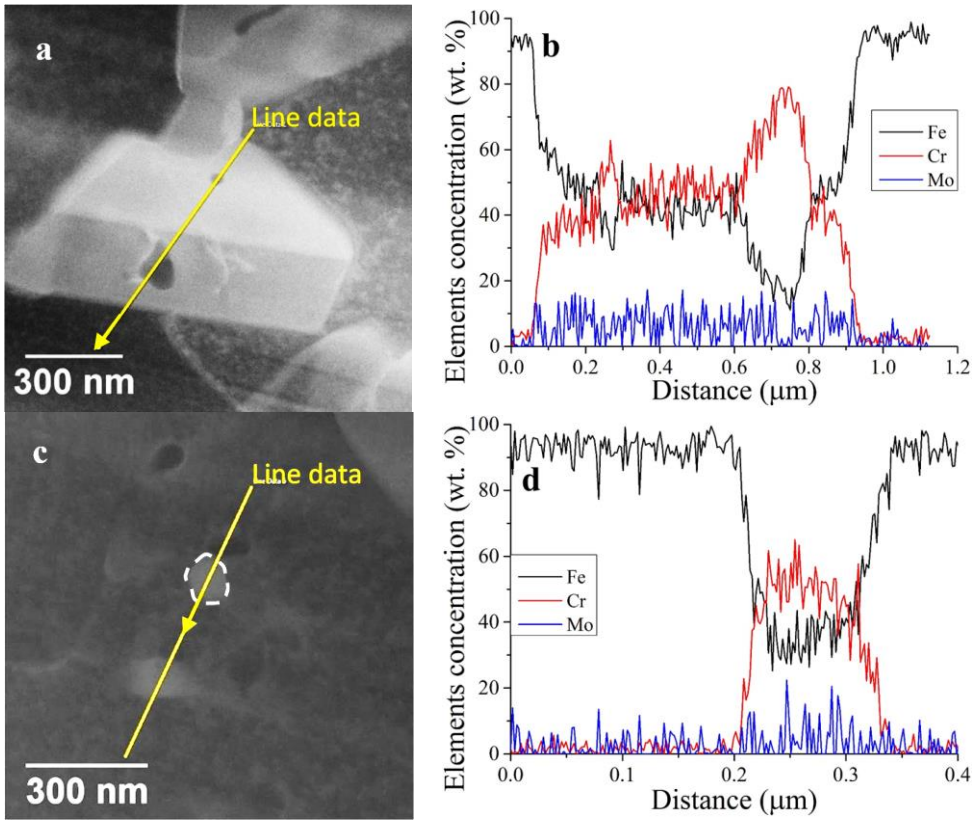

Figure 4-36: (a) STEM image of an fine needle cross-section in A-640-1495 (400 to 800 @ 245); (b) EDS line scan profile from the line in (a); (c) STEM image of an intragranular carbide in A-virgin sample; (d) EDS line scan profile from the line in (c).

Figure 4-37 shows the elemental distribution of the area evaluated in Figure 4-36a. The EDS maps demonstrate that the cored coarse carbide is mainly composed of Cr and Fe, accompanied with some Mo and S. However, the difference between core and surrounding carbide is difficult to observe in the EDS maps.

An area including both coarse carbides and large needles was evaluated by STEM, and the EDS maps are shown in Figure 4-38. Large needles are Cr-rich carbides based on the Cr distribution, corresponding to the elemental profiles shown in Figure 4-36d.

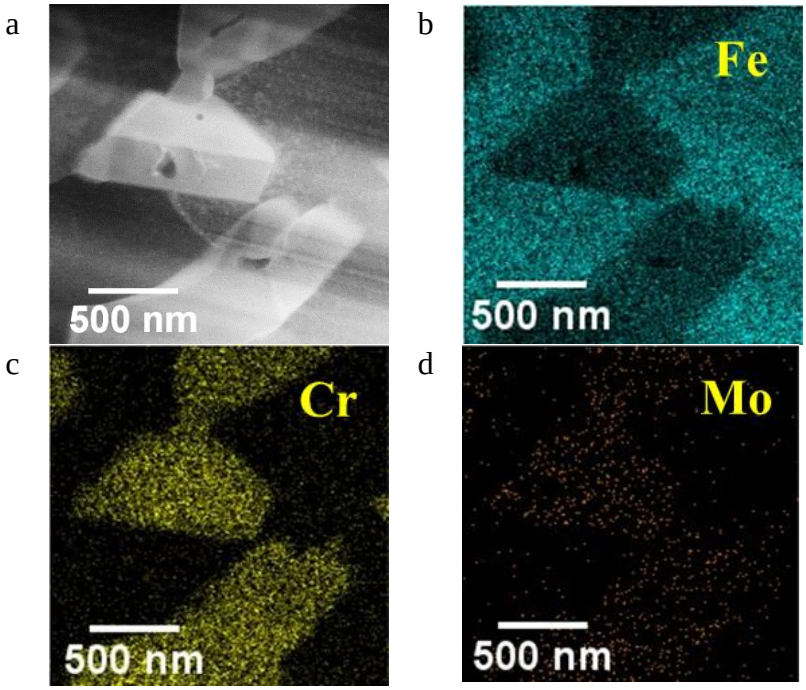

Figure 4-37: (a) STEM image of an intergranular cored coarse carbide in A-640-1495 (400 to 800 @ 245); EDS maps of (b) Fe; (c) Cr and (d) Mo.

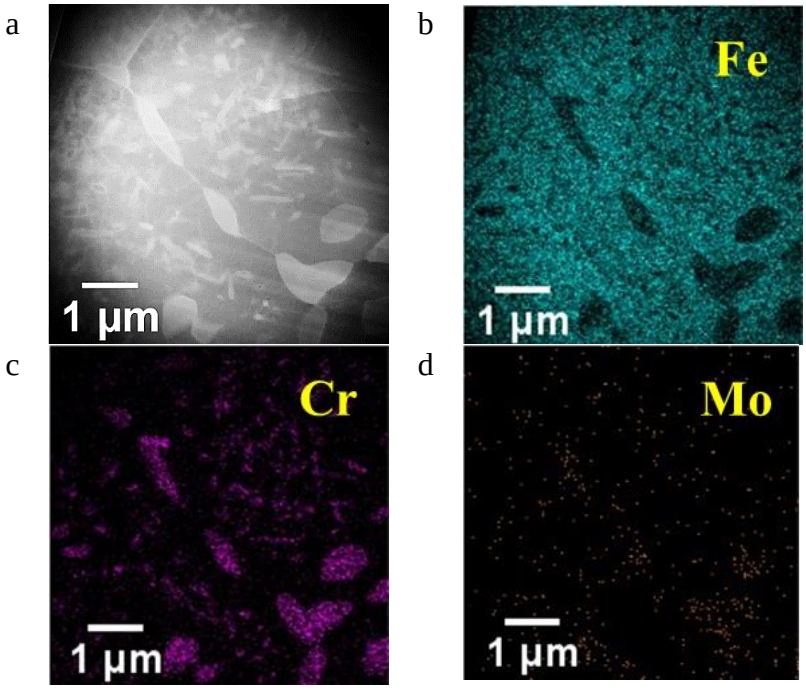

Figure 4-38: (a) STEM image of both coarse carbides and large needles in A-640-1495 (400 to 800 @ 245); EDS maps of (b) Fe; (c) Cr and (d) Mo.

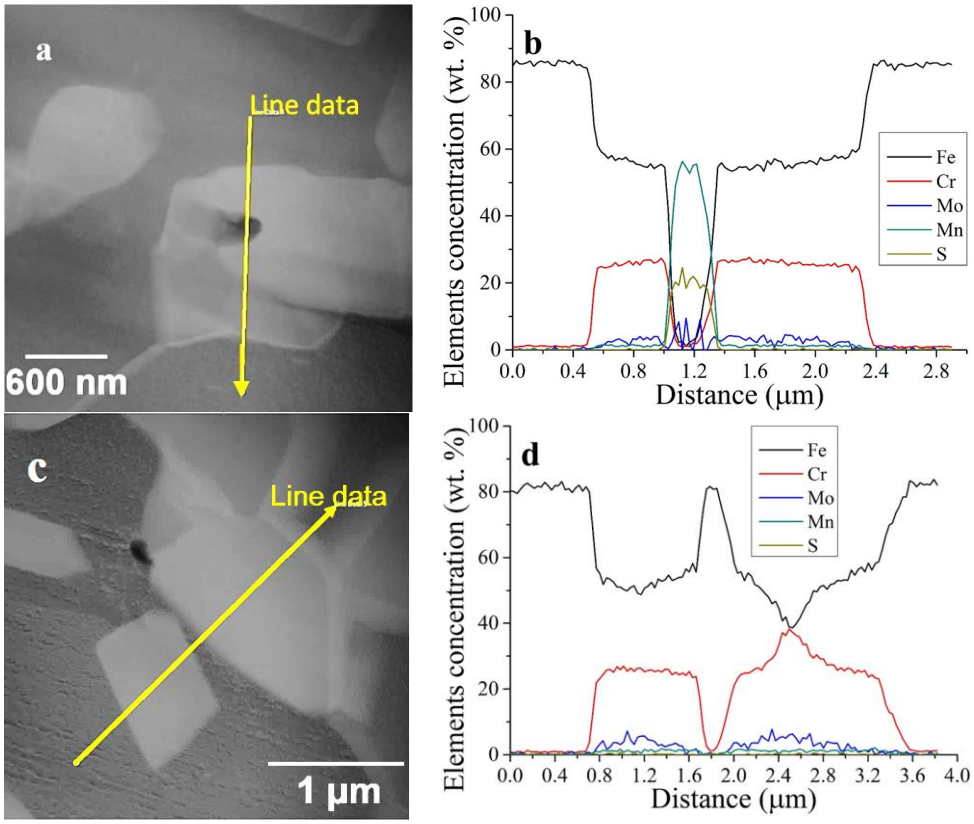

Figure 4-39: (a) STEM image of an intergranular carbide in A-640-3883; (b) EDS line scan profile from the line in (a); (c) STEM image of an intragranular carbide in A-virgin sample; (d) EDS line scan profile from the line in (c).

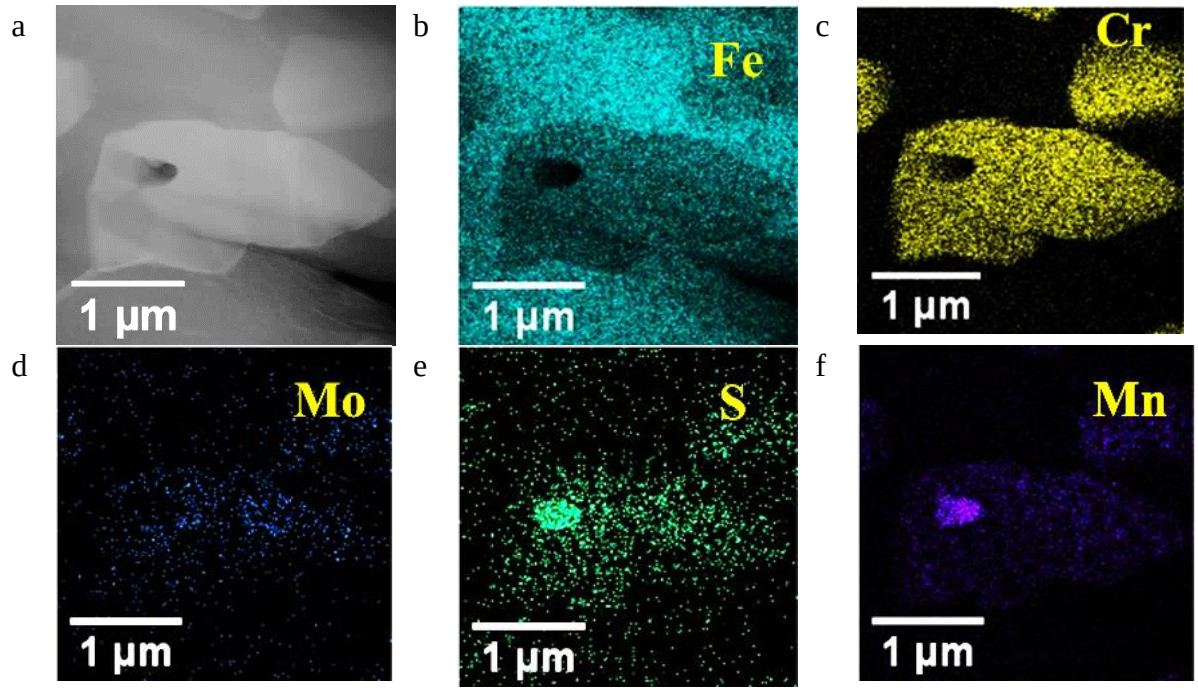

Figure 4-40: (a) STEM image of coarse carbides with an MnS inclusion in A-640-3883; EDS maps of (b) Fe; (c) Cr; (d) Mo; (e) S and (f) Mn.

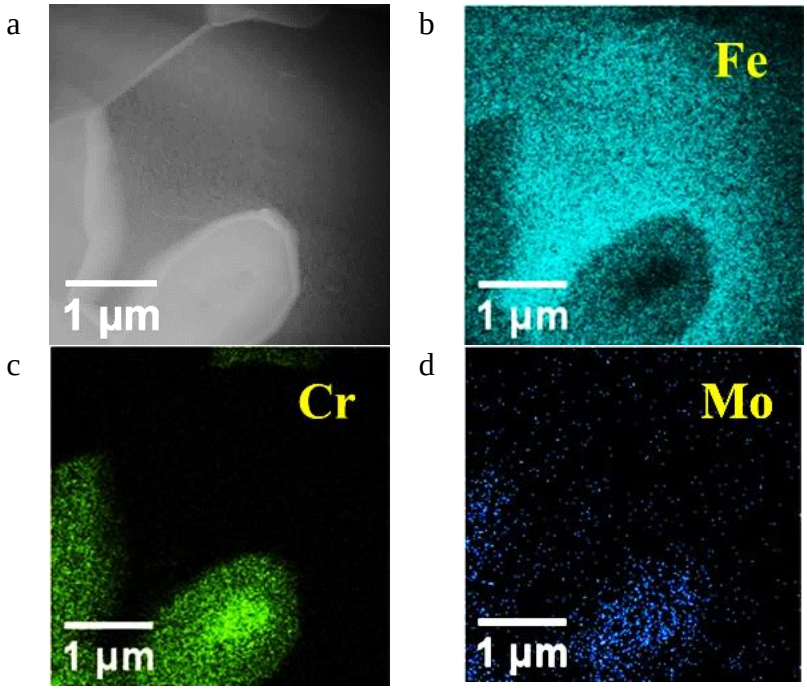

Figure 4-41: (a) STEM image of a cored coarse carbide in A-640-3883; EDS maps of (b) Fe; (c) Cr and (d) Mo.

Figure 4-39 shows STEM images of coarse carbide and cored carbide, and the corresponding concentration profiles from EDS line scans obtained from sample A-640-3883. It shows that the Cr and Fe concentrations in coarse carbide are around 30 and 55 wt. %, respectively. However, a dark feature in the STEM image is present in the carbide examined, as shown in Figure 4-39a. The profiles (Figure 4-39b) indicate that it is mainly comprised of Mn and S, indicating the presence of an MnS inclusion, which can be formed together with carbides occasionally. The outer layer of cored coarse carbide in Figure 4-39c has a similar elemental distribution (Figure 4-39d) as the coarse carbide in Figure 4-39b. However, both Cr and Fe concentrations in the core are around 40 wt. %. In addition, there is an obvious Cr depletion in the surrounding parent matrix down to around 1 wt. %. Therefore, the Fe concentration is higher than the Cr concentration in the coarse carbide and cored carbide in general, apart from the inner core in which the Fe concentration is roughly equal to that of Cr.

It is evident that an accompanying MnS inclusion was formed together with carbide, according to the EDS maps in Figure 4-40. The coarse carbide is mainly comprised of Fe and Cr, accompanied with some Mo and S. A cored coarse carbide was also examined in Figure 4-41. A heavy Fe-depleted region corresponds to the Cr, Mo-rich region in the examined carbide.

4.2.4 Carbide area fraction calculation using FIB and HS-AFM

The types of carbides, their corresponding morphologies and elemental distributions have been identified using XRD, TEM and STEM-EDS techniques. However, it is also important to understand the distribution of carbides in the matrix, which can be described by the carbide area fractions. Here, profiles of carbide area fractions will be plotted on each HRA autoclave

sample plus A-virgin using FIB/XeF_2 imaging. A comparison of carbide area fractions obtained from HS-AFM and FIB/XeF_2 for the same locations will also be made. Images from HS-AFM provide information on height of examined features.

As discussed in Chapter 3, high quality sample surface preparation is required to ensure a deformation-free surface for HS-AFM analysis. A suitable protocol has been described previously [136]. Carbides and other features were identified by their height following sample polishing and utilising the difference in carbide hardness compared with the parent material to leave them proud of the surface [202]. Custom software was used to extract the carbide precipitate features and characterise them according to their area, height and aspect ratio. An optical micrograph of a polished sample is shown in Figure 4-42a, with the three paths across the fin and one path from the fin tip centre down through the fin for FIB imaging, while a FIB image of the central fin is shown in Figure 4-42b. The marked area in Figure 4-42b shows a region that was analysed with both HS-AFM and FIB imaging at high resolution for direct comparison. Figure 4-43a and b show FIB and XeF_2 images, respectively, of the region marked in Figure 4-42b. The carbide area fraction as a function of position across the middle part of the central fin in Figure 4-42a was obtained by acquiring a series of HS-AFM images of 4.5 × 4.5 µm in size. Twenty such images were obtained and the carbide area fractions plotted as a function of position from the centre of the fin to the oxide/metal interface. Carbide area fractions were extracted from these and colour coded to indicate the area fraction as a function of position. Finally, a FIB XeF_2 image (Figure 4-43c) from the outlined region close to the oxide/metal interface, as shown in Figure 4-42b, was used to compare with the high-resolution HS-AFM image provided by stitching a set of 1600 overlapping HS-AFM images (Figure 4-43d).

The focused ion beam instrument used for this work was a FEI FIB-201 single gallium ion beam instrument, operating at 30keV beam energy. FIB images were obtained by initially cleaning regions of the sample by sputtering an area of 120 × 100 µm at 11nA beam current for about 10s to remove surface contamination and oxide. Ion-induced secondary electron images were then obtained at 150 or 90pA beam current showing topographical and ion channelling contrast. Following acquisition of the initial image, XeF_2 gas was introduced into the system for a few seconds to functionalise the surface, and further images were obtained at low and high magnification. The resulting images have reduced ion channelling contrast but show carbide precipitates as darker regions. The centre fin of the sample was analysed by FIB imaging following three horizontal paths at 500, 1000 and 1500 µm from the fin tip, as shown in Figure 4-42a. Five images were obtained at each position, and carbide area fractions were obtained using standard image processing software (ImageJ) to threshold the images according to greyscale and pixel counts. A further set of images was obtained from the tip of the fin

travelling down through the centre, as shown in Figure 4-42a. The image used for comparison with HS-AFM was obtained in the same way.

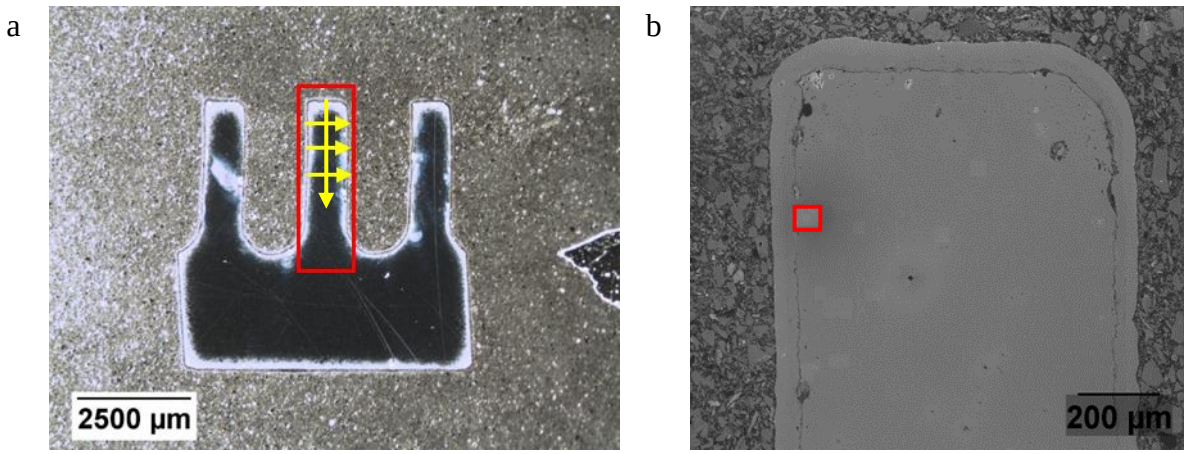

Figure 4-42: (a) Optical image of the prepared sample and the paths for FIB imaging. (b) FIB image of the middle fin showing an area analysed using HS-AFM and FIB imaging.

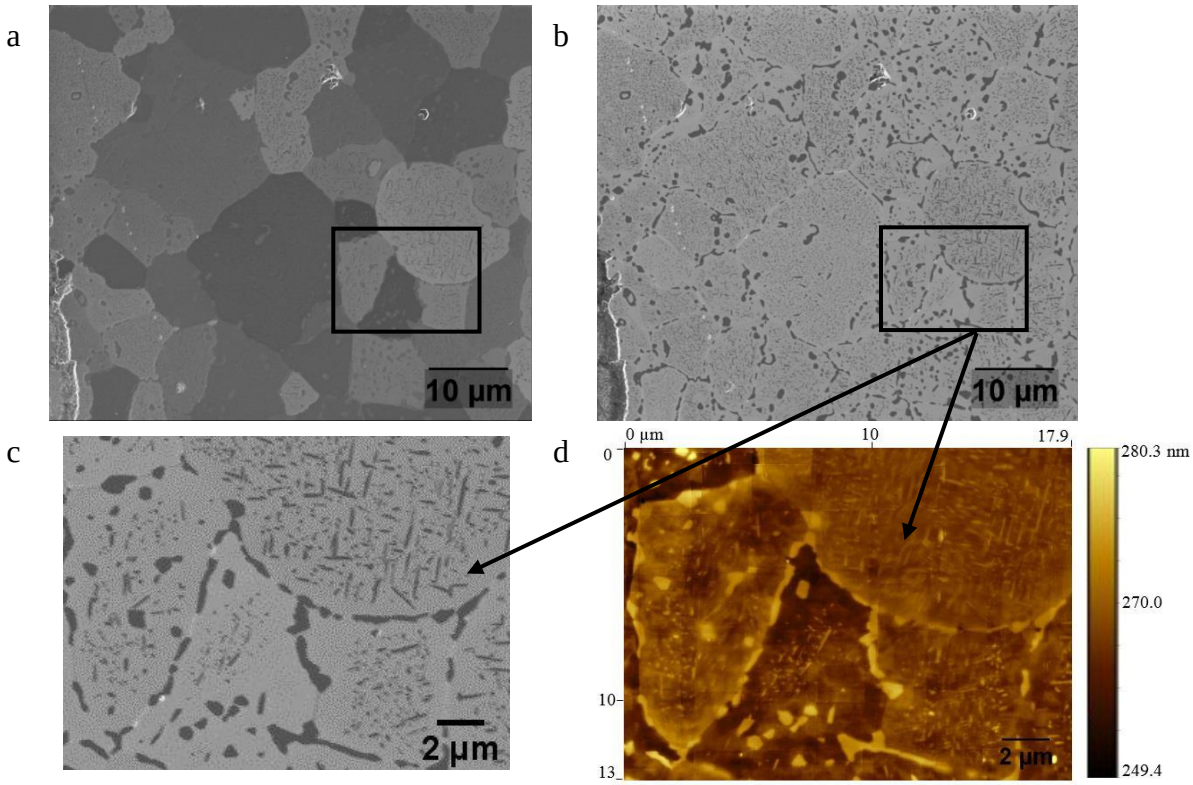

Figure 4-43: (a) Initial FIB micrograph of the area marked in Figure 4-42b from sample A-580-2542. (b) The corresponding FIB XeF_2 image. (c) Detailed FIB XeF_2 image; (d) Composite HS-AFM image from same area showing 31 nm height range.

A focused ion beam induced secondary electron image after surface cleaning producing channelling contrast is shown in Figure 4-43a. The corresponding image of the same area after exposure to XeF_2 gas is shown in Figure 4-43b. The channelling contrast is now suppressed and the carbides are visible as darker regions in the image. It is evident that larger carbides are

present at the grain boundaries, together with smaller intragranular carbide precipitates. A section of the same image at higher magnification is displayed in Figure 4-43c, together with the corresponding HS-AFM image in Figure 4-43d. Clearly the FIB XeF_2 image and the HS-AFM image are in general agreement regarding the morphology and distribution of carbides which are shown as dark areas in the FIB image and as brighter raised areas in the HS-AFM image. From the previous work described, the larger carbides at the grain boundaries are assumed to be $M_{23}C_6$, and both FIB and HS-AFM images show a similar distribution. The smaller needle-like intragranular carbide distribution is also in general agreement between the two images, although there are small differences at high magnification. The reason for this is not clear, but there are some estimations. This difference may be caused by the software threshold. Considering that the HS-AFM images were based on the height of the features, those with low height may be neglected during processing by the image software. Another reason may be due to the sharpness of the tip which is used for the measurement of the height. Some material was removed due to the sputtering phase to remove oxide before FIB imaging. This is the most likely reason for the slightly different heights in the sample. However, it can be seen that the HS-AFM image reveals additional height changes from grain to grain.

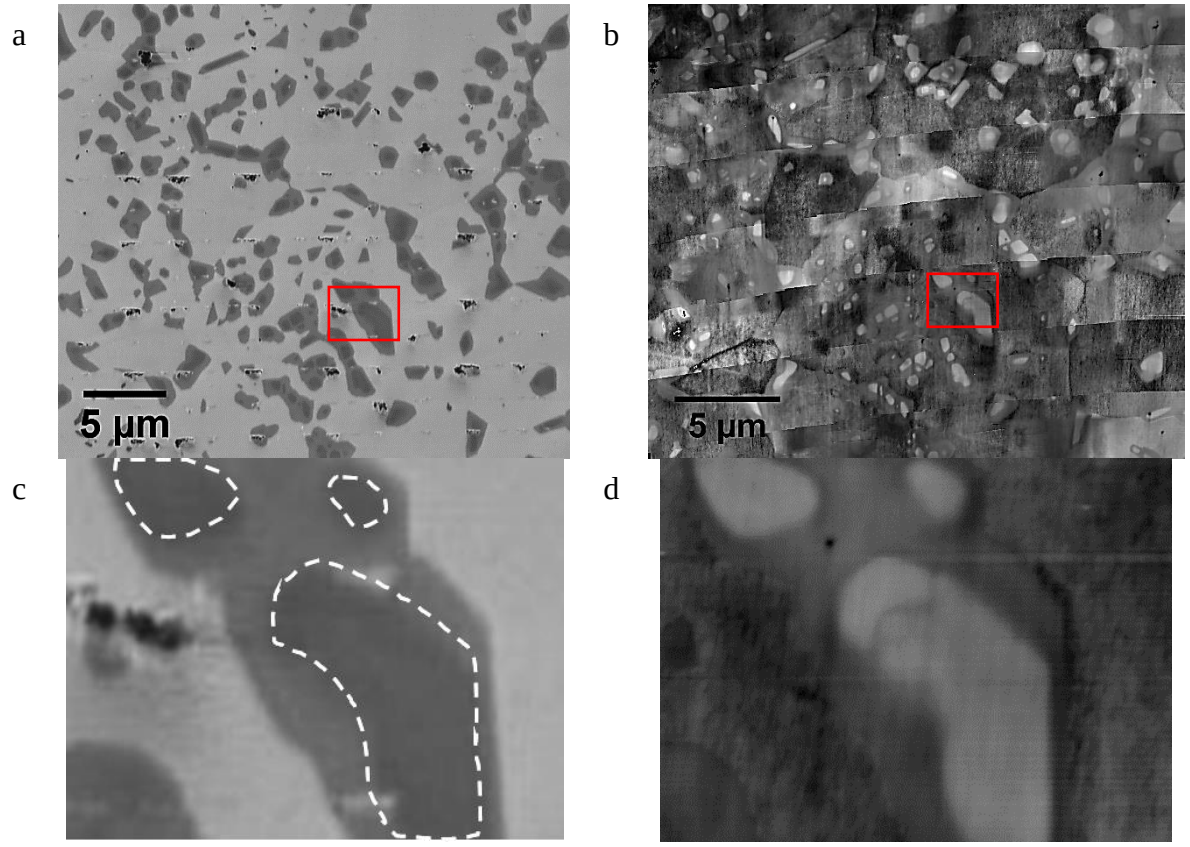

Figure 4-44: (a) FIB XeF_2 micrograph of the examined area in sample A-640-3883; (b) Composite HS-AFM image from same area; (c) FIB XeF_2 image with the cores marked and (d) HS-AFM image of the area marked in red box shown in (a) and (b). The brightness represents the height of the feature.

Figure 4-44a and b show a FIB XeF_2 micrograph from post breakaway sample A-640-3883 with a corresponding HS-AFM image. A small area was selected to show details of a cored

coarse carbide, as shown in Figure 4-44c and d. The features with high brightness are consistent with cores in dark colour shown in the FIB XeF_2 image; the brightness in the HS AFM image indicates the height of the feature. Therefore, the core is higher than the surrounding outer layer carbide, whose height is greater than the matrix.

Thresholding based on the brightness of FIB XeF_2 images and the height of the features in HS-AFM images (Figure 4-45) was used to obtain carbide area fraction. The results are presented in Figure 4-46. FIB images were obtained along the direction of the arrows and from the fin tip downwards through the middle of the fin as shown in Figure 4-42a. Figure 4-46 shows that the carbide area fraction at the edge of the fin is higher than that at the fin centre. However, there are small differences between the three profiles at different distances from the fin tip. A carbide area fraction map of the right-hand side of the middle fin obtained from sparse HS-AFM images is shown in Figure 4-45. The map shows that most carbides are distributed in the region about 200 µm from the fin side and 570 µm from the fin tip. As described in the experimental section, the area fraction from the FIB images was extracted from an area of 120 × 100 µm, while for the HS-AFM images extracts were obtained from an area of 4.5 × 1.5 µm. The plots from the HS-AFM measurements, have more spatial detail, and show that the carbide area fraction in the region next to the oxide is lower than that obtained from the FIB, which can be also observed from Figure 4-46b.

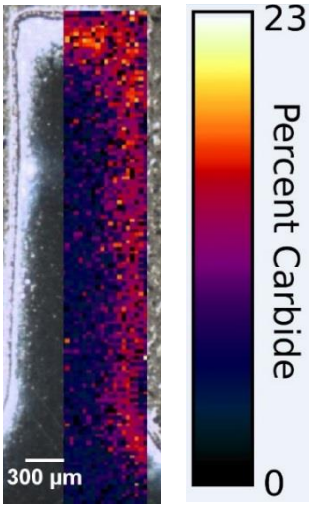

Figure 4-45: Optical image of middle fin overlaid with HS-AFM map of measured carbide percentage using thresholding software on a sparse data set of frames from sample A-580-2542.

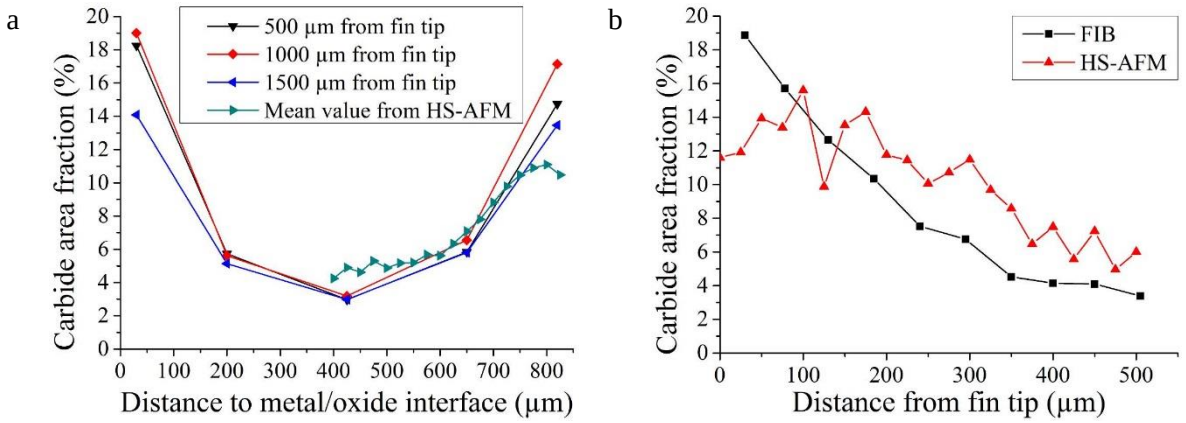

Figure 4-46: Carbide area fraction of sample A-580-2542 from both FIB and HS-AFM images against distance from oxide/metal interface (a) across the fin; (b) From the fin tip downwards through the centre of the fin.

An image in Figure 4-45 shows the carbide percent image from HS-AFM results overlaid on the optical image. To characterise the carbide coverage further, a sparse matrix of images, each of 4.5×1.5 µm in size and spaced at 25 µm intervals, was obtained, covering the entire right-hand side of the central fin. It is seen that carbides were mainly distributed beneath the oxide scale. It can be seen that the highest carbide percent from the HS-AFM map is approximately 20 %, consistent with the 19 % obtained from FIB, as shown in Figure 4-46. Furthermore, the carbide percentage decreases with increase of distance from the oxide/metal interface and reaches its lowest percentage at the fin centre, following the three paths across the fin and the path from the fin tip centre down through the fin, as with previous observations of the carbide area fraction obtained by processing FIB XeF_2 images with ImageJ software.

Carbide area fractions were obtained following the three horizontal paths shown in Figure 4-42a from the samples listed in Table 4-1 and plotted as a function of distance to the oxide/metal interface by processing FIB XeF_2 images with ImageJ software. The carbide area fraction results from the A-virgin sample together with samples exposed at 600 °C, are shown in Figure 4-47, while those exposed at 640 °C are shown in Figure 4-48. According to these plots, the carbide area fractions in the fin centre from those samples exposed at low temperature or with a short time are consistent with those from the virgin sample. The area fractions from these samples are high at the fin side, but low at the fin centre. Samples exposed at high temperature or for long time exhibit a saturation state, where the carbide area fraction is roughly equal from the fin side and the fin centre. In addition, the Cr concentration in the carbide is approximately 50 wt. % in the coarse carbide without the presence of cored carbides. The absence of an area fraction from path 1 in breakaway samples A-600-17065 (1200) and A-640-3334 results from the conversion from metal to oxide at this location during oxidation. Figure 4-47d shows that the area fraction on the fin side of sample A-600-17065 (1200) is less than that from sample A-640-3334, as shown in Figure 4-48e, following the same path 1500 µm from the fin tip. Area fractions from sample A-580-2542 in Figure 4-46a and A-640-2526 in Figure 4-48, which were exposed for similar times and at the same moisture

level show that the former obtained a lower area fraction than the latter due to the lower exposure temperature of the former sample.

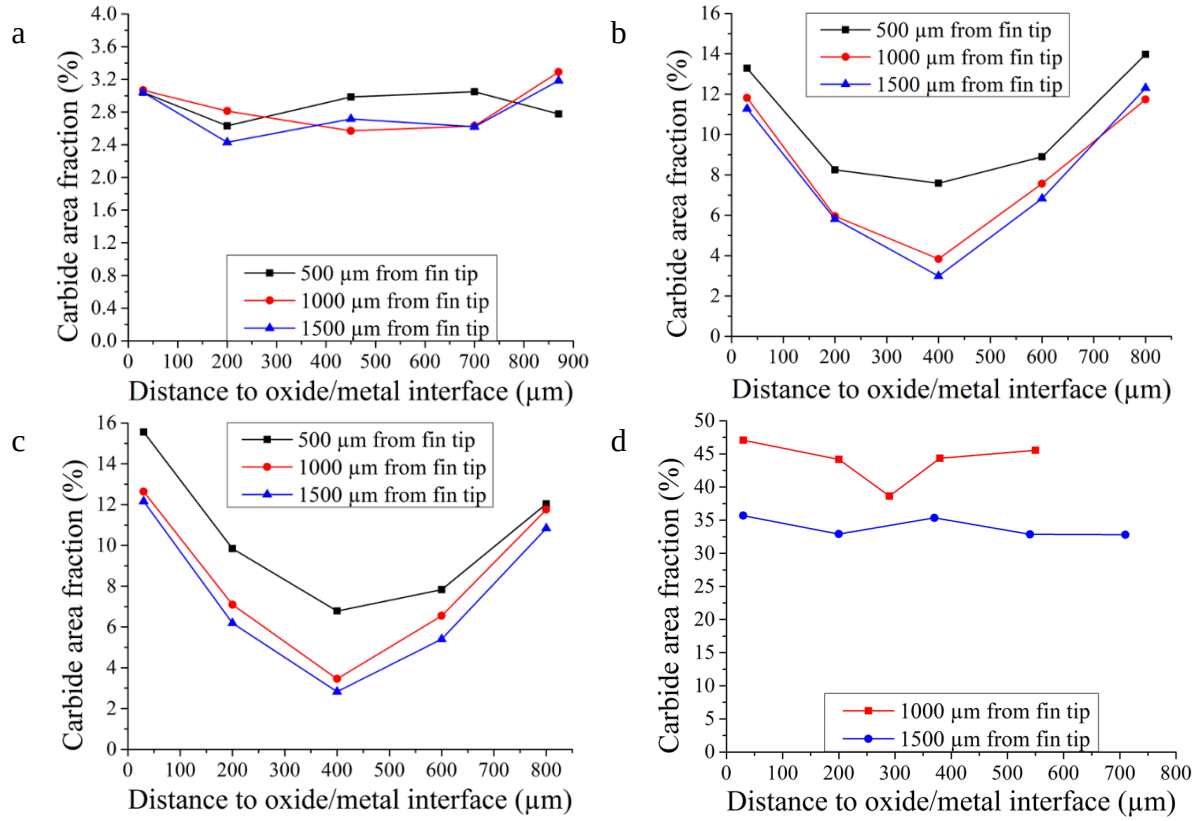

Figure 4-47: The plots of carbide area fraction against the distance to oxide/metal interface of (a) A-virgin and samples exposed at 600 °C: (b) A-600-1510; (c) A-600-1520 (1200) and (d) A-600-17065 (1200).

The carbide area fraction results from autoclave HRA samples exposed at 640 °C are shown in Figure 4-48. The lowest area fraction present in sample A-640-245 is similar to that from samples A-580-2542, A-600-1510, A-600-1520 (1200) and A-virgin, as shown in Figure 4-47. These plots show a high area fraction on the fin side and low at the fin centre. Moreover, the saturated carbide area fraction is present at 17-20 % for breakaway initiation sample A-640-1495 (400 to 800 @245) (Figure 4-48b) and then increases with time and temperature until the metal is converted into the oxide. It is also observed that the carbide area fraction keeps increasing with the increase of temperature and time after saturation state is observed, resulting from the formation of cored carbide with more Fe introduced into the carbides. During this process, the carbide area fraction at the fin side beneath the fan-shaped laminated oxide grows faster than that in the fin centre, leading to higher area fractions at the fin side and lower at the fin centre, as shown following path 2 in Figure 4-47d and Figure 4-48d, path 3 in Figure 4-48e and path 1 in Figure 4-48f.

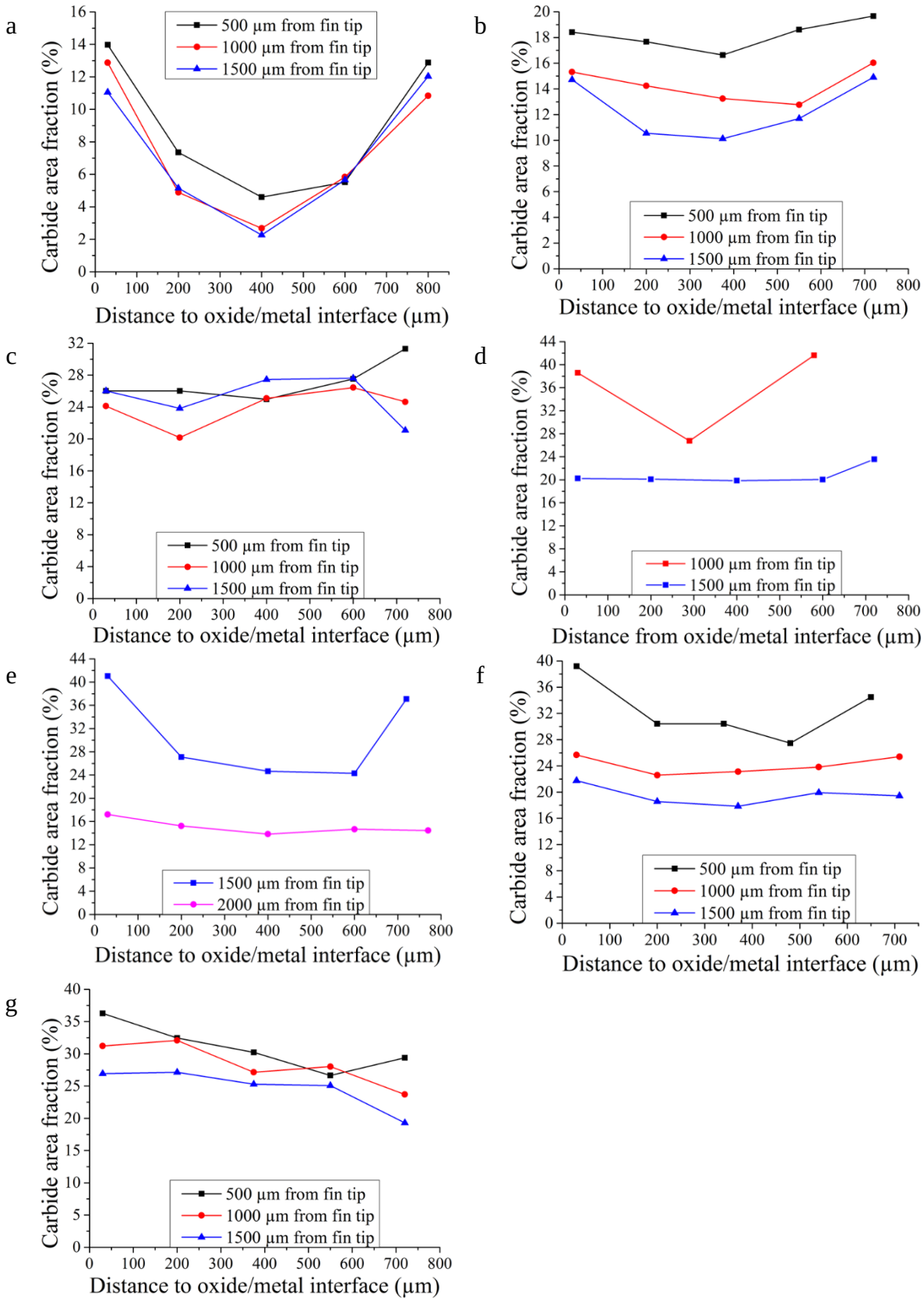

Figure 4-48: The plots of carbide area fraction against the distance to oxide/metal interface of samples exposed at 640 °C: (a) A-640-245; (b) A-640-1495 (400 to 800 @ 245); (c) A-640-2526; (d) A-640-3074; (e) A-640-3334; (f) A-640-3639 and (g) A-640-3883;

Table 4-7: Carbide area fractions at fin side and fin centre of experimental HRA samples exposed in simulant coolant gas following three paths described in Figure 4-3.

Sample ID	*Carbide area fraction (%)*					
	Fin side			*Fin centre*		
	Path 1	*Path 2*	*Path 3*	*Path 1*	*Path 2*	*Path 3*
A-virgin	*~3*	*3-3.3*	*3-3.3*	*~3*	*~2.6*	*~2.8*
A-580-2542	*15-19*	*17-19*	*14-15*	*~3*	*~3*	*~3*
A-600-1510	*13-15*	*11-13*	*11-13*	*~8*	*~4*	*~3*
A-600-1520 (1200)	*12-16*	*12-13*	*11-13*	*~7*	*~3.5*	*~3*
A-600-17065 (1200)	*/*	*45-48*	*33-37*	*/*	*~38*	*~35*
A-640-245	*13-15*	*11-13*	*11-13*	*~5*	*~3*	*~2.5*
A-640-1495 (400 to 800 @ 245)	*18-20*	*15-17*	*14-16*	*~17*	*~13*	*~10*
A-640-2526	*26-32*	*24-26*	*20-26*	*~25*	*~25*	*~28*
A-640-3074	*/*	*38-42*	*20-24*	*/*	*~26*	*~20*
A-640-3334	*/*	*/*	*36-42*	*/*	*/*	*~24*
A-640-3639	*34-40*	*26-28*	*20-22*	*~32*	*~24*	*~18*
A-640-3883	*28-37*	*23-27*	*18-27*	*~30*	*~27*	*~25*

Table 4-7 shows the carbide area fractions obtained from fin side and fin centre following the three paths described in Figure 4-26. The area fractions at the fin side are often higher than those from fin centre, excluding samples which exhibit a saturation state and the virgin sample. When a saturation state occurs, the carbide area fractions increase with the decrease of distance from fin tip. This phenomenon indicates that differences in carbide area fraction are mainly determined by carbon diffusing in from the fin side before the presence of the saturation state and fin tip after saturation state. The area fractions following path 1 show a higher value than path 2 followed by path 3, indicating the influence of carbon diffusing in from the fin tip. The saturation state was observed following path 1 in sample A-640-1495 (400 to 800 @ 245) which shows that the saturation area fraction begins from approximately 17 %. Furthermore, since granular $M_{23}C_6$ is considered as the dominant carbide, the carbide area fraction can also be considered as carbide volume fraction. According to Table 4-7 and Table 4-2, the saturation state is mainly present in samples with multi-layered and laminated oxides, which indicates a potential relationship between saturation state and breakaway oxidation. In ferritic 9Cr-1Mo steels, breakaway may initiate when the saturation state occurs at around 17 % carbide area fraction.

The carbide area fractions from sample A-580-2542 and A-640-1495 (400 to 800 @ 245) were also obtained by analysing FIB XeF_2 images using Labview software, which distinguished the needle carbides from coarse carbides. As observed from Figure 4-27, sample A-580-2542 contains fine needle and coarse carbides while sample A-640-1495 (400 to 800 @ 245) contains large needle and coarse carbides. The needle carbides and coarse carbides in these two samples were separated and plotted as a function of distance to the oxide/matrix following the three paths shown in Figure 4-26, together with the total carbide area fraction, as shown in Figure 4-49 and Figure 4-50. A slight difference in total area fraction between the result from ImageJ and Labview was caused by a difference in thresholding.

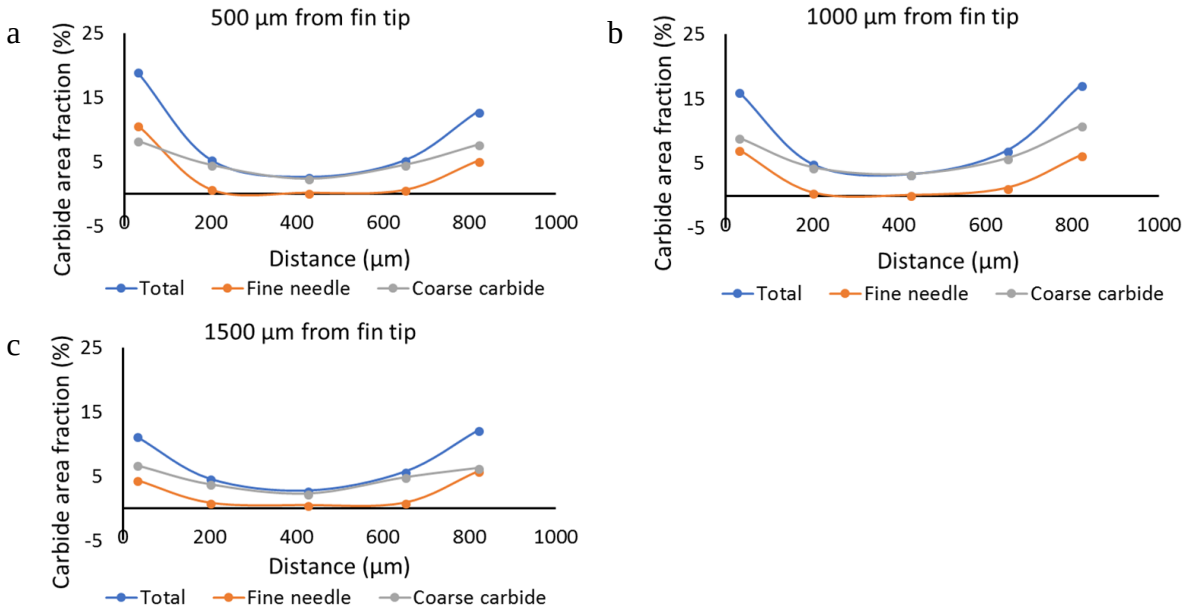

Figure 4-49: Carbide area fraction of sample A-580-2542 obtained from FIB imaging following the three paths shown in Figure 4-26.

The plots in Figure 4-49 show that there was a higher area fraction of fine needles close to the oxide/metal interface in sample A-580-2542 but this reduced quickly to a very low level close to the fin centre (0 in some regions). Therefore, the carbide area fraction in the fin centre mainly arises from the coarse carbides.

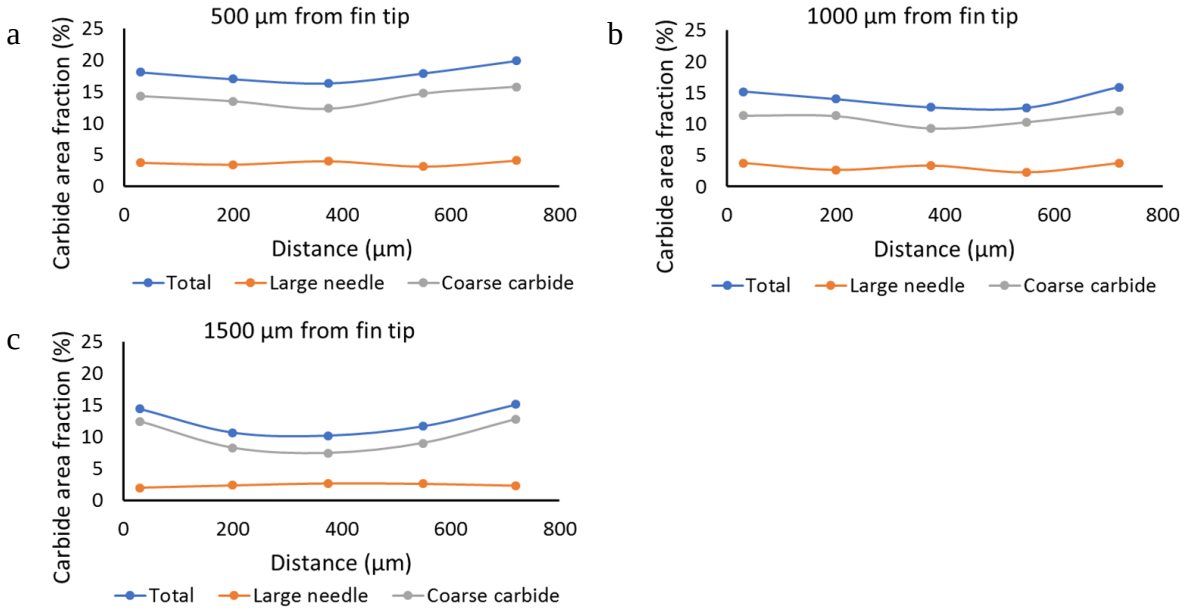

Figure 4-50: Carbide area fraction of sample A-640-1495 (400 to 800 @ 245) obtained from FIB imaging following the three paths shown in Figure 4-26.

Figure 4-50 shows the carbide area fractions obtained from sample A-640-1495 (400 to 800 @ 245). The plots following path 1 and 2 for FIB imaging exhibit the saturation state, which is consistent with the results processed by ImageJ. It appears that the levels of large needles and

coarse carbides remain stable when the saturation state is present. The area fraction of coarse carbides is always higher than that from large needles in this sample.

FIB images in Figure 4-27 show that fine needles were present after exposure at a lower temperature (580 °C) in a non-breakaway sample and dissolved into the metal with the increase of temperature and time. Large needles were formed in the sample which had entered breakaway initiation oxidation at a higher temperature (640 °C). Coarse carbides were formed in both samples. Area fractions were higher in the sample exposed at 640 °C for 1495 h than in the sample exposed at 580 °C for 2542.

4.3 Discussion

4.3.1 Oxidation

Optical micrographs show that non-breakaway samples have a duplex oxide without the presence of any cracks at the fin tip corners. Multi-layered oxide and small cracks extending from oxide to fin tip corner were present in breakaway initiation samples. Laminated oxide with large cracks at the fin tip corner indicates post-breakaway oxidation, and laminated oxide is often in the form of a fan shape. The oxide from non-breakaway fin sides exhibit a duplex layer. Continuous IOZ was mainly present in non-breakaway samples, with discontinuous IOZ being observed in breakaway initiation but disappearing in post-breakaway samples, as shown in Figure 4-4 and Figure 4-5.

Cracks initiated in oxide at the fin tip corner according to observations from optical micrographs, indicating the influence of geometry on the process of oxidation. The oxide at this location is thicker than that at the fin side, indicating a two-dimensional diffusion of Fe cations and alloying elements, e.g. Cr, Mo and Si, at the fin tip corner, as analysed in Chapter 4 by Equation 4.1. Angell et al. proposed that oxide spallation is based on oxide scale thickness and stored strain [36]. As shown in Figure 4-6, the oxide at the fin tip corner grows faster than at other locations because it is influenced by oxide growth from both fin side and fin tip. Thus, oxide spallation at the fin tip corner is more likely than at other locations, leading to more stored stress and strain which can drive a crack along a plane of weakness. This plane may be in the oxide or along the oxide/metal interface. The former was observed in most breakaway initiation samples, in the oxide extending radially to the fin tip corner, while the latter may result in oxide exfoliation.

It is also found that the oxide thickness is influenced by the exposure conditions. There is a positive correlation with exposure temperature and time, but the influence of moisture is unclear. The similar oxide thicknesses of samples A-600-1510 and A-600-1520 (1200) indicate

that the influence of moisture is unclear based on the results from these two samples. A comparison between samples A-580-2542 and A-640-2526, which were exposed for a similar time but at different temperatures, shows that the oxide thickness of the former is less than the latter, indicating the positive correlation of temperature. It takes a very long time (> 80 kh) for samples exposed at 580 °C to enter breakaway initiation, while the TTB for samples exposed at 600, 620 and 640 °C is around 20 kh, 3 kh and 2 kh (in agreement with the result from this work ~1500 h) respectively according to ref [85]. The plot of oxide thickness obtained from fin side versus exposure time at 640 °C with 400 vppm moisture shows sub-parabolic kinetics before 3500 h in which TTB is larger than that determined from the plot of weight gain versus time, probably due to the non-breakaway oxidation in this location. The plot of weight gain versus time of samples exposed at 640 °C with 400 vppm moisture exhibits sub-parabolic kinetics against time at the early stage of oxidation and linear kinetics after breakaway initiation when exposed at the same temperature and moisture.

Duplex oxide was formed in non-breakaway samples or at non-breakaway locations in breakaway samples. Oxide thickness increases following sub-parabolic kinetics as shown in Figure 2-5b. The weight gain plot as a function of time shows linear kinetics for post-breakaway oxidation. Breakaway initiates during the transition from sub-parabolic to linear kinetics. The growth of magnetite and spinel occur simultaneously for the duplex oxide, inferred from the increase of both magnetite and spinel thickness which are roughly equal as shown in Table 4-4 which is in agreement with the void-induced duplex oxide formation model proposed by Rouillard et al. [39]. Voids in the oxide resulted from vacancy condensation, formed by the outward diffusion of Fe at the oxide/metal interface, and provided the space for spinel formation. This indicates that oxide grows at the gas/oxide interface via the outward diffusion of Fe across the oxide while spinel grows at the oxide/metal interface by the inward diffusion of CO_2 [112], in agreement with the investigations in ref [40] and [74]. Multi-layered oxide was formed around the breakaway initiation point. It can be observed that the magnetite stops growing and a few thin layers of magnetite form in the spinel layer, indicating that the site of oxide growth is at the oxide/metal interface by the inward diffusing of CO_2 through nano-channels and small cracks, consistent with the model proposed in ref [40]. In post-breakaway oxidation, the laminated oxide was formed, as shown by the EDS maps: Cr-rich and Cr-depleted oxide was formed alternately beneath the multi-layered oxide. It can be seen that the magnetite and multi-layered oxide stop growing while a laminated oxide has fast growth to eventually form a fan-shaped oxide, as observed from optical micrographs of the post-breakaway samples. This is consistent with the model proposed in ref [40]. Large cracks were formed in this process, which is the main diffusing method in post-breakaway oxidation.

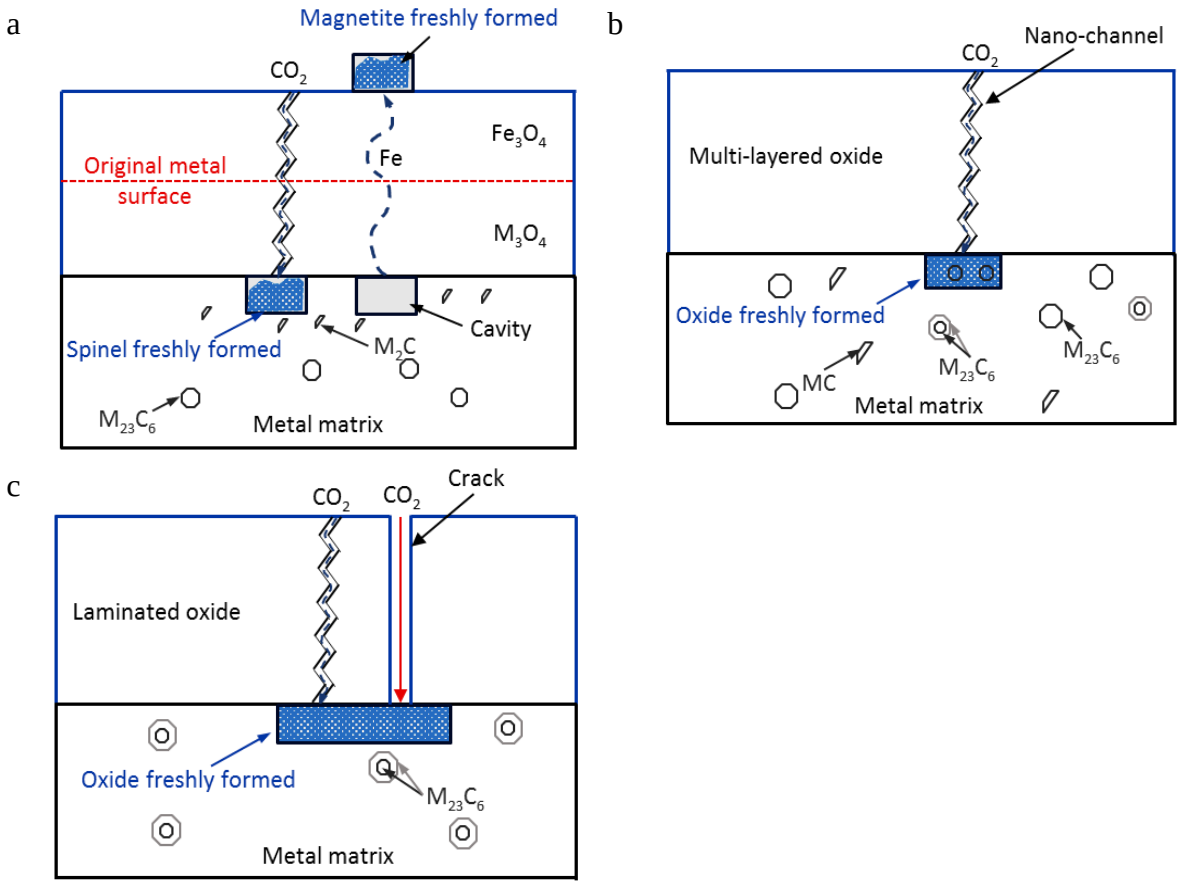

Figure 4-51: Models explaining the formation of (a) duplex oxide; (b) multi-layered oxide and (c) laminated oxide, and the carbides observed from FIB images.

It is feasible that the growth of oxide is determined by the diffusion rate of iron, and the presence of nano-channels in the oxide. The growth rate of spinel depends on the available space created by the outward diffusion of Fe ions, which diffuse along the nano-channels to cross the whole oxide scale and read the gas/oxide interface to form magnetite. A model explaining the growth of duplex oxide is shown in Figure 4-51, based on the above discussion, which demonstrates the inward flux of CO_2 and outward Fe diffusion through the nano-channels. The inward CO_2 diffusion provides oxidant for oxide formation and carbon for carburisation, as shown in Equations 4.2 and 4.3, which also explains the deposition of carbon in the oxide during this process. The outward diffusion of Fe provides spaces for spinel formation and Fe cations for magnetite formation, as illustrated by Equation 4.4. As discussed previously, fresh magnetite and spinel are formed at the gas/oxide interface and oxide/metal interface respectively. The original metal surface before exposure converts into a magnetite/spinel interface. Carbon formed from Equations 4.2 and 4.3 reacts with Fe and Cr, leading to the formation of carbides with different morphologies and compositions. The EDS map of Cr also shows a higher Cr concentration at the oxide/metal interface, consistent with the model on the formation of fresh spinel.

Raman spectra demonstrate that the IOZ is comprised of Cr_2O_3 and spinel. The presence of a small peak at 610 cm^{-1} is indicative of the presence of Cr_2O_3. The peaks at 541 and 667 cm^{-1} are evidence for the presence of spinel [203][95]. The position of the main A_{1g} mode peak from Cr_2O_3 at 554 cm^{-1} suggests a compressive stress of 3 kbar (300 MPa) based on the investigation and calibration undertaken by Birnie et al. [102]. But this indicative stress assumes that there is no relative stress within the reference sample and, more importantly, that there are no compositional effects present. A few dark spots present in the oxide are comprised of magnetite, spinel and carbon. The presence of A_{1g} mode at 668 cm^{-1}, T_{2g} at 550 cm^{-1} and E_g at 307 cm^{-1} is evidences for the existence of magnetite and/or spinel. The presence of D and G peaks at 1352 and 1589 cm^{-1} is indicative of carbon with a low-degree of order. The identification of some of the oxide types present within the oxide, however, confirms the value of scanning LRS for investigating these complex oxidation processes that occur within ferritic 9Cr-1Mo steel components.

$$CO_2 = CO + {}^1/_2\, O_2 \qquad 4.2$$

$$2CO = CO_2 + C \downarrow \qquad 4.3$$

$$4CO_2 + 3M = M_3O_4 + 4CO \qquad 4.4$$

A multi-layered oxide is formed at the fin corner of sample A-640-1495 (400 to 800 @ 245) which had entered breakaway initiation inferred from the crack present at the fin tip corner shown in Figure 4-12. The Cr concentration in multi-layered oxide is as low as 2 wt. %, which indicates the alternative formation of Cr-rich and Cr-depleted zones due to the slow mobility of Cr [37]. It is also found that the carbides consume Cr in the matrix, which may lead to the Cr depletion. Therefore, the formation of multi-layered oxide results from slow Cr mobility, consumption of Cr by carbides, or a combination of them. The conversion from metal to oxide allows volume spallation in the sample due to the differences in lattice parameter. Previous investigations describe the lattice parameter of ferrite (2.890 Å [204]), magnetite (~8.397 Å [205]) and spinel (8.350-8.410 Å [206][207]). When matching three Fe (8.670 Å) with one unit of oxide cell (8.350-8.410), the oxide will be stretched while Fe is compressed at the oxide/metal interface. Therefore, a relative tensile stress in oxide and compressive stress in metal were expected at the two sides of the oxide/metal interface, as shown in Figure 4-52. In optical micrographs, it is observed that the oxide grows separately at the fin tip centre, which is the symmetric boundary in geometry from other parts of fan-shaped oxide in post-breakaway samples [208]. The schematic of Figure 4-52 can be used to explain this phenomenon. Tensile stress in the oxide results from the growth of oxide toward two sides of the fin, leading to the quicker growth of oxide at the fin tip corner and eventually to the formation of fan-shaped oxide. However, oxide following the symmetric boundary experiences a tensile stress, resulting

in oxide growth at the fin tip centre, as observed with optical micrographs of Figure 4-4d and Figure 4-5e.

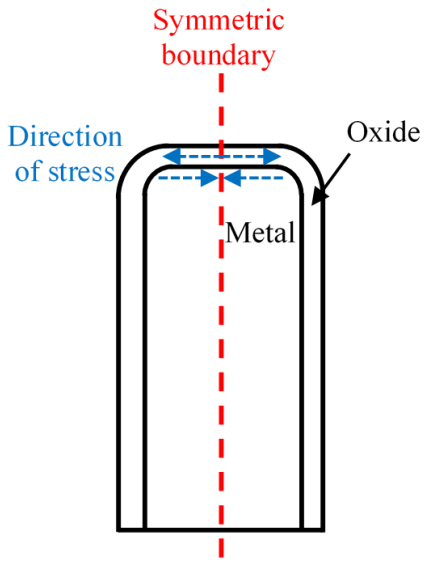

Figure 4-52: Schematic drawing of a fin illustrating the direction of stress at the two side of oxide/metal interface and the position of symmetric boundary of the fin.

Furthermore, the difference in lattice parameter of oxide and metal increases the possibility of the formation of crystal defects, e.g. dislocations, which eventually lead to the formation of cracks parallel to or at the oxide/metal interface, as observed in the optical micrographs in Figure 4-4c. In this case, the Cr depletes after oxidation is underway and then a Cr-depleted oxide layer is formed beneath the Cr-rich spinel layer. Cr-rich spinel will be formed again beneath the Cr-depleted oxide layer after Cr accumulation. This process repeats to eventually form the oxide in a multi-layered morphology, as shown in Figure 4-51b. The EDS maps of Figure 4-13 show that the spinel close to the oxide/metal interface keeps the grain boundary structure before being oxidised in the breakaway initiation sample. It appears that the oxidation follows grain boundaries, inferred from the higher Cr content along grain boundaries compared with other locations in the EDS map. The prior intergranular carbides were not completely converted into oxide, although prior intragranular carbides which cannot be observed in EDS maps were completely dissolved to provide Cr for fresh spinel formation. There is no evidence of magnetite growth in this model. Raman spectra show that the oxide close to the oxide/metal interface is comprised of spinel confirmed by the presence of a peak at 671 cm^{-1}. The single peak at 1575 cm^{-1} indicates the presence of single crystal graphite or highly ordered graphite [106][104]. The spectrum from the dark band show it to be comprised of spinel and graphite, inferred from the peaks at 676, 1352 and 1573 cm^{-1}.

The presence of cracks and fan-shaped oxide are evidence that sample A-640-3883 has entered a post breakaway oxidation regime which follows linear kinetics. The fast growth of oxide

results in the formation of fan-shaped oxide which shows a laminated morphology, as shown in Figure 4-14. A model for post-breakaway oxidation is established in Figure 4-51c. The main diffusion paths of CO_2 are cracks giving it easier access to the matrix. The metal was therefore oxidised and carburised quickly in this process resulting in the depletion of Cr. Since the oxidation is proceeding much quicker than during the formation of the duplex and multi-layered oxide, Cr-rich and Cr-depleted oxide were formed alternately to generate a laminated morphology. The EDS map of Cr from Figure 4-15 shows that Cr-rich and Cr-depleted oxide are present in the form of clots in the evaluated region, including the oxide/metal interface, where the fresh spinel is formed. There is no evidence for the growth of outer layer magnetite in this model. The types of Cr-rich and Cr-depleted oxide in the evaluated region were identified by Raman spectra. The Cr-rich oxide is comprised of spinel, confirmed by the presence of peaks at 675 cm^{-1}, while the presence of A_{1g} mode at 671 cm^{-1}, T_{2g} at 548 cm^{-1}, and E_g at 309 cm^{-1}, indicative of the presence of magnetite, and D and G peaks at 1351 and 1592 cm^{-1} respectively demonstrates that Cr-depleted oxide is mainly comprised of magnetite and a low-degree of order carbon. The carbon is distributed in most evaluated regions.

Disregarding compositional changes in the oxide, the peak position maps show relative compressive stress in the IOZ layer compared with the adjacent oxide in the non-breakaway and breakaway initiation samples. Some spots with relative compressive stress were present in the oxide scale in the post-breakaway sample.

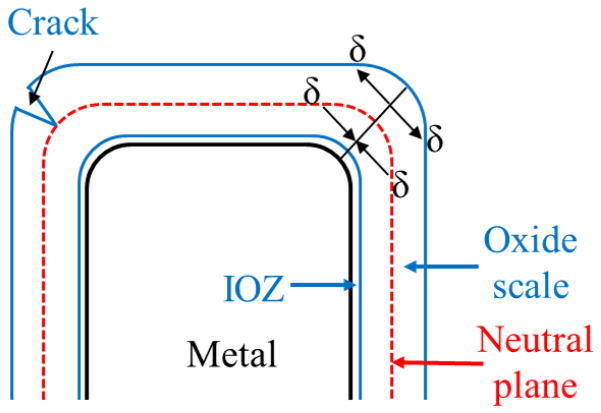

Figure 4-53: The initiation of crack at fin tip corner.

The reason for crack initiation is as shown in Figure 4-53, based on the above discussion. At the early stage of oxidation, a duplex oxide forms as well as stress due to the growth of oxide. At the outer side of the neutral plane, a tensile stress is generated while a compressive stress is generated at the inner side of the neutral plane. According to Raman results, the IOZ layer has a larger compressive stress than the oxide further away from the IOZ. Cracks then propagate through the oxide scale extending radially to the metal.

4.3.2 Carburisation

Figure 4-27 shows that coarse carbides were present in all four examined samples, additionally, fine needles were present in A-580-2542, large needles and cored coarse precipitates in A-640-1495 (400 to 800 @ 245) and cored coarse precipitates in A-640-3883. X-ray diffraction and TEM were adopted for carbide identification. The results show that the coarse precipitate is $M_{23}C_6$, fine needle M_2C, large needle MC and cored coarse precipitate $M_{23}C_6$.

In A-virgin sample, there is only one type of carbides present in the matrix: $M_{23}C_6$. The intergranular $M_{23}C_6$ is comprised of approximately 80 wt.% and a very low Fe content, while the Cr and Fe concentrations of the intragranular $M_{23}C_6$ are approximately 50 wt.% and 30 wt.%, respectively. The chromium concentration of the surrounding matrix is around 9 wt.% which is consistent with the chemical composition of 9Cr-1Mo steel.

Fine needle carbides M_2C were formed together with $M_{23}C_6$ carbides in the non-breakaway samples in the early stages of oxidation. M_2C has a hexagonal structure and lattice parameters a = 2.510 Å and c = 4.199 Å. The orientation relationship between M_2C and matrix α-Fe, which has a BCC structure and lattice constant a = 3.161 Å, is $(10.\bar{1})_{M_2C} \| (01\bar{1})_{\alpha-Fe}$ and $[01.1]_{M_2C} \| [011]_{\alpha-Fe}$. According to STEM-EDS analysis, M_2C is mainly comprised of Cr (50-90 wt. %) and Fe (less than 5 wt. %). Coarse carbide $M_{23}C_6$ is comprised of Cr and Fe, which are approximately 50 and 30 wt. % respectively. The chromium concentration of the surrounding matrix is less than 6 wt.%.

Large needle carbides MC were formed in breakaway initiation samples. These have a cubic structure (BCC) and lattice parameter a = 4.714 Å, while the surrounding α-Fe metal has a BCC structure with a = 2.673 Å. The orientation relationship between MC and matrix α-Fe is $(110)_{MC} \| (101)_{\alpha-Fe}$ and $[001]_{MC} \| [\bar{1}11]_{\alpha-Fe}$. The coarse carbide $M_{23}C_6$ was also examined in this sample and the results show that it has an FCC structure with a = 10.230 Å. For its surrounding α-Fe metal a = 2.727 Å. The relationship between coarse carbide $M_{23}C_6$ and matrix is $(11\bar{1})_{M_{23}C_6} \| (21\bar{1})_{\alpha-Fe}$ and $[011]_{M_{23}C_6} \| [011]_{\alpha-Fe}$. STEM-EDS results show that Cr and Fe concentrations of large needle MC are 40 ~ 60 wt. % and 20 ~ 40 wt. %, respectively. The coarse carbide $M_{23}C_6$ evaluated in this sample has a Cr-rich core. The Cr concentration in the core is as high as 80 wt. % (Fe as low as 10 wt. %) but reduced immediately to around 50 wt. % (Fe is around 50 wt. %) in the outer layer coarse carbide. Cr depletion occurs in the surrounding matrix (less than 5 wt. %).

In post-breakaway samples, it is found that both fine needles and large needles dissolved into the metal, providing Cr for $M_{23}C_6$ formation. Most of carbides are cored $M_{23}C_6$. The inner core and outer layer carbide were both evaluated with TEM and found to have a FCC structures. However, slight differences in lattice parameter were found. For the inner core, a = 9.86 Å and

for the outer layer $M_{23}C_6$, a = 10.07 Å. The lattice parameter for α-Fe in this case is 3.071 Å. The orientations of cored $M_{23}C_6$ and α-Fe are exactly the same, and the orientation relationship between cored coarse carbide $M_{23}C_6$ and matrix is $(200)_{M_{23}C_6} \| (0\bar{1}1)_{\alpha-Fe}$ and $[001]_{M_{23}C_6} \| [\bar{1}11]_{\alpha-Fe}$. STEM-EDS results show that Cr and Fe concentrations in the inner core $M_{23}C_6$ are both around 40 wt. %, while Cr and Fe concentrations for the outer layer $M_{23}C_6$ is around 30 and 55 wt. %, respectively. It is observed that Cr is depleted in the surrounding matrix (around 1 wt. %).

Therefore, it appears that the Cr concentration in the matrix reduces with the increase of oxidation and carburisation. In post-breakaway samples, the metal is sensitised because the Cr concentration is almost 0, indicating conversion to mild steel in breakaway samples. The Cr concentration in $M_{23}C_6$ reduces from 50 wt. % in A-virgin to 40 wt. % in post-breakaway samples. Fine needle M_2C was only present in the early stage of oxidation and mainly distributed at locations close to the oxide/metal interface and dissolved to provide Cr for other types of carbide formation, e.g. MC and $M_{23}C_6$.

It is also found that there is an abrupt change of key elements, e.g. Cr, Fe, between carbides and matrix, as well as the inner core and the outer layer carbide $M_{23}C_6$. This phenomenon indicates that $M_{23}C_6$ is a stable carbide formed in ferritic 9Cr-1Mo steels. The formation of $M_{23}C_6$ ties up free chromium in the matrix. It has been discussed that the Cr concentration of some $M_{23}C_6$ in A-virgin is as high as 80 wt. %, which is the core observed in breakaway samples. With the depletion of Cr in the matrix, $M_{23}C_6$ carbides with lower Cr concentration were formed surrounding the core and in the same orientation. The Cr concentration changes from 80 to 40 wt. % in the core and from 50 to 30 wt. % for the normal coarse carbides from A-virgin to post-breakaway sample due to the stable characteristic of $M_{23}C_6$.

The Cr concentration in the matrix is important to the corrosion resistance of 9Cr-1Mo steels, which reduces with the process of oxidation. Cr concentration in the matrix of A-virgin is around 9 wt. %, obtained from STEM-EDS analysis, and reduces to around 5 wt. % in non-breakaway sample A-580-2542 and breakaway initiation sample A-640-1495 (400 to 800 @ 245). An obvious Cr-depletion was observed in the matrix of post-breakaway sample A-640-3883, in which the Cr concentration is around 1 wt. %, indicating the parent metal now being a mild steel. The depletion of Cr indicates that the metal is very susceptible to breakaway oxidation.

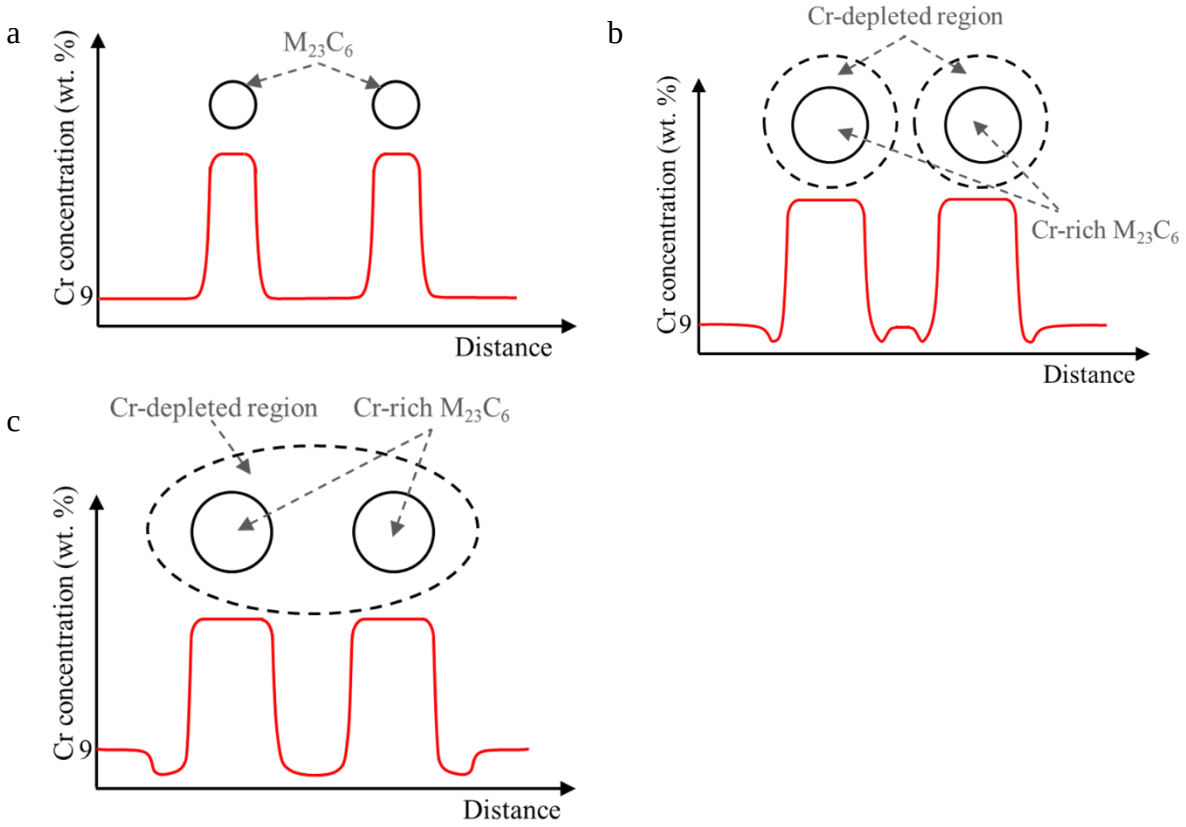

Figure 4-54: The depletion regions (black dashed line) surround the carbides (black solid line) in sample (a) no depletion; (b) beginning of depletion and (c) joining of depletion regions, as well as the corresponding Cr concentration (red solid line).

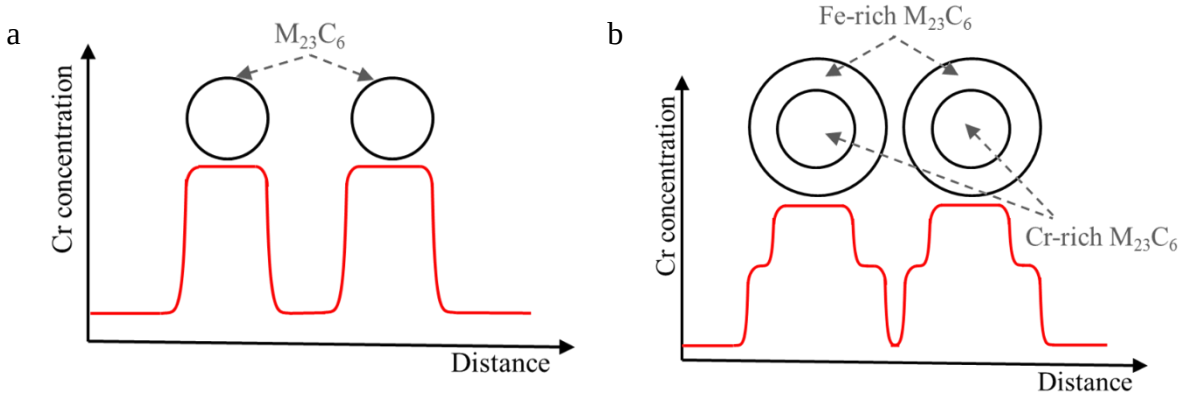

Figure 4-55: The corresponding Cr concentration (red solid line) of (a) coarse carbides $M_{23}C_6$ and surrounding matrix; (b) cored coarse carbides $M_{23}C_6$ and corresponding matrix.

Figure 4-54 shows the development of depletion regions. Figure 4-54a shows $M_{23}C_6$ carbides formed in the virgin sample which were in equilibrium, the Cr concentration in the surrounding matrix here is 9 wt. %. However, during the process of oxidation, the introduction of CO_2 breaks the equilibrium in the metal, exacerbating the growth of carbides. Thus, Cr was continuously tied up by carbides from the surrounding metal resulting in a depletion region in the surrounding area, as shown in Figure 4-54b. During the continuous carburisation process, the depletion regions join together eventually leading to Cr depletion in the whole matrix, as shown in Figure 4-54c, making the metal sensitised and breakaway initiation to occur. The Cr

concentration at breakaway initiation was observed to be 5 wt. %, as shown in Figure 4-36, which indicates that a Cr concentration of 5 wt. % in the matrix is the threshold of breakaway. The sample enters breakaway oxidation when the Cr concentration in the matrix is less than 5 wt. %.

Figure 4-55 shows the transformation from $M_{23}C_6$ to cored $M_{23}C_6$ and the corresponding Cr changes. In the virgin sample, the Cr concentration of the matrix is 9 wt. %, as discussed previously in relation to Figure 4-54a, without Cr depletion in the surrounding areas of carbides. When exposure to the CO_2-based gas, the carbides tie up the key element Cr in the matrix leading to Cr depletion (the decrease of Cr concentration) in the surrounding metal. Therefore, Fe-rich carbides form surrounding the Cr-rich carbides, as shown in Figure 4-55b. Cored carbides may form in the depletion regions shown in Figure 4-54b and c.

In the early stage of oxidation, carbon diffuses into the metal from nano-channels, following the duplex oxide model shown in Figure 4-51a at a low speed, which leads to a low carburisation rate in sample A-580-2542. Fine needles were present in the region close to oxide in this case. FIB images were processed to obtain the ratio between the area of carbides and the whole evaluated area, defined as the carbide area fraction. Area fractions were plotted against the distance to the oxide/metal interface, following the three paths shown in Figure 4-3. These plots demonstrate that area fraction decreases quickly from 19 % to 5 % within 200 μm beneath the oxide in sample A-580-2542, indicating a low rate of carburisation. A crack at the fin tip corner of sample A-640-1495 (400 to 800 @ 245) and the multi-layered oxide formed are evidence that it has entered breakaway initiation following the model shown in Figure 4-51b. The carburisation rate increases compared with the duplex model, which explains the oxidation behaviour in the early stage. Large needles are present (length > 1 μm) as well as fine needles (length < 1 μm). Cored carbides formed during carburisation of this sample, converted from coarse carbides. SEM images show that cracks were present in the post-breakaway sample A-640-3883, providing easier access for CO_2 to the matrix. Crack extension and expansion lead to direct contact between oxidant and matrix, which exacerbates the oxidation and carburisation processes. Depletion of Cr was present due to the high carburisation rate. Thus, a lot of cored carbides were formed which contained a lower Cr concentration of the outer layer carbides.

The oxidised samples A-580-2542 and A-640-3883 were analysed using FIB and HS-AFM imaging for carbide observation. HS-AFM is capable of imaging small precipitates under 10 nm in size within a region of 4.5 × 4.5 μm at a high resolution of 4.5 nm and many such images may be stitched together to cover large areas, as shown in Figure 4-43d and Figure 4-44b. Both the FIB and HS-AFM images confirm that the fine needle carbides are found only intragranularly while the coarse carbide precipitates are at grain boundaries and within grains.

HS-AFM images of sample A-640-3883 include cored carbides that show a higher hardness of the inner core than the outer layer carbide. The plots in Figure 4-46a display a high area fraction at the edge and low in the centre of the fin, demonstrating that the process of carburisation is affected by carbon diffusing from the surfaces of the fin. In addition, the plots in Figure 4-46a display a high area fraction at the edge and low in the centre of the fin demonstrating that the process of carburisation is affected by carbon diffusing from the surfaces of the fin. In addition, Figure 4-46b provides evidence of the carbide distribution from the fin tip, which is in accordance with the HS-AFM intensity map shown in Figure 4-45. The explanation of a lower area fraction at the fin edge in HS-AFM plots compared with FIB results may be differences in areas sampled, image processing or depletion of Cr in the process of oxidation. These effects will be the subject of further study. The similar trend obtained for carbide area fraction distribution from FIB and HS-AFM results and the finer spatial detail displayed by HS-AFM confirms the value of the technique for carburisation characterisation. Furthermore, HS-AFM imaging of cored carbides shows the relative hardness as of these three features: inner core > outer layer carbide > matrix. Additionally, the Vickers hardness of $Cr_{23}C_6$ is around 15 GPa [209], and of $Fe_{3.8}Cr_{19.5}C_6$ is around 22.9 GPa [210]. Based on the line profiles obtained from STEM-EDS analysis of sample A-640-3883, the weight percentage of both Fe and Cr from the inner core of the examined carbide is approximately 40 wt. %, indicating the composition to be $Fe_{12}Cr_{11}C_6$. The outer layered carbide composition can be obtained in the same way and the result is $Fe_{15.3}Cr_{7.7}C_6$ (Fe: 55 wt. % and Cr: 30 wt %). The HS-AFM result shows clearly that the hardness of $Fe_{12}Cr_{11}C_6$ is higher than that of $Fe_{15.3}Cr_{7.7}C_6$. Thus, the hardness of carbide $M_{23}C_6$ changes with the Cr content in the way as shown in Figure 4-56. Further investigation is required to establish the precise changing tendency between carbide hardness and Cr content in carbide.

The difference in carbide area fractions obtained from FIB and HS-AFM is mainly due to the different thresholding operated by different software. Since the intensity of the precipitates shown in HS-AFM images were determined by the height of carbides, the precipitates with a lower height may be neglected; area fractions obtained from FIB XeF_2 images are more reliable.

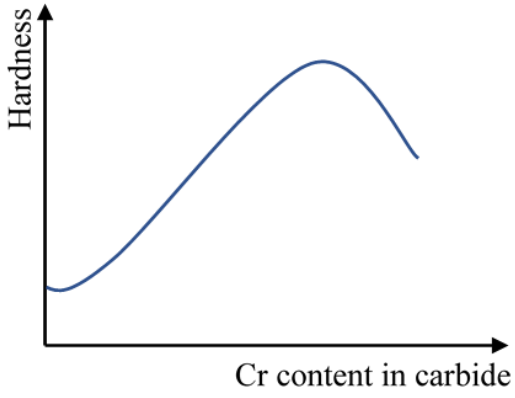

Figure 4-56: Estimated trend of hardness changes as a function of Cr content in carbide.

Figure 4-47 and Figure 4-48 show plots of carbide area fraction obtained from autoclave HRA samples. These illustrate that the area fraction has a positive correlation with exposure temperature, time and moisture. The area fraction from pre-carburised regions is in the range of area fractions obtained from the A-virgin sample. The saturation state begins from 17 % based on observation of the breakaway initiation samples. Oxidant CO_2 continues providing further carbon for carburisation. Therefore, carburisation is determined by the limit content of Cr, which is 9.2 wt. %. Assuming M compromises 50 wt. % Cr, as STEM line scans show in the coarse carbides from non-breakaway and breakaway initiation samples, the following Equation 4.5 can be used for saturated carbide area fraction calculation, assuming that all the chromium in the metal became incorporated into carbides.

$$Cr\ wt.\% \times saturated\ carbide\ area\ fraction = 9.2\ wt.\% \qquad 4.5$$

Cr wt. % represents Cr concentration in coarse carbides. This equation is based on the observation that $M_{23}C_6$ is the predominant carbide. Thus, the other types of carbides were ignored and the assumption made that there is no compositional change in carbides during the process of oxidation and carburisation. Then, the theoretical value of saturation carbide area fraction is 18.4 % by calculation, which is close to the observation from experimental results of 17 %. In some cases, the plot following path 1 is not shown due to excessive carburisation leading to the conversion from metal to oxide at this location.

In Chapter 2, we discussed modelling work on 9Cr-1Mo steel from Gong et al. [85]. Here, comparison between our experimental work and their modelling work will be discussed. In ref [85], an oxide growth model was proposed for the duplex oxide with several physical parameters, e.g. the flux balance at the gas/magnetite and spinel /alloy interfaces, which illustrated the growth direction of magnetite and spinel. It can be seen that the spinel/alloy moves toward the metal matrix, which is consistent with our models in Figure 4-51a. However, the formation of multi-layered oxide and laminated oxide was not taken into consideration. Our experimental work may provide more information for future modelling work. There are a few conditions which should also be taken into consideration in the modelling work:

1. Oxidation rate depends on the Cr level. The Cr level decreases during the process of oxidation.
2. Carburisation rate depends on oxide thickness during non-breakaway oxidation. Carbon needs to diffuse through the whole oxide scale to react with Cr and Fe cations in the metal matrix for carbide formation.
3. The influence of geometry was not taken into consideration in the modelling work. As discussed in this thesis, oxide thickness is obviously affected by the geometry. Oxide at the fin tip corner is thicker than the fin side.

4. The carbide types examined in our experimental work provide more information for modelling work akin to that in ref [85], e.g. M_2C carbides were not included in Gong's modelling work while they were detected in our experimental work.
5. The modelling work was based on the assumption of no compositional changes. However, our experimental work demonstrates that the compositions of spinel, carbides and metal change with time during oxidation and carburisation.
6. Stress and strain were not taken into consideration in the modelling work. However, our experimental work provides evidence of the presence of stress in the oxide.

Therefore, this experimental work provides further information for future modelling work and the possibility for model optimisation.

4.4 Conclusions

It can be easy to draw the conclusion that the TTB decreases significantly with increase of temperature when samples are oxidised with the same moisture. It takes more than 80 kh for samples exposed at 580 °C to reach the point of breakaway initiation, while the TTB for samples exposed at 600, 620 and 640 °C is around 20 kh, 3 kh and 2 kh, respectively. The temperature is obviously the dominant influencing parameter for oxidation. The oxide thickness exhibits sub-parabolic kinetics against exposure time before 3500 h ($y = 5.94x^{0.40}$) and linear kinetics afterwards ($y = 0.078x - 115$). In the plot of weight gain as a function of exposure time, early stage oxidation follows sub-parabolic kinetics $y = x^{0.43}$ and breakaway initiates at approximately 2000 h. It follows linear kinetics $y = 0.028x - 27$ in post-breakaway oxidation. Therefore, the TTB from the plot of oxide thickness versus time is delayed compared with that from weight gain versus time. This may be due to the influence of geometry. The oxide thickness was obtained from the non-breakaway locations. Furthermore, weight gain was affected by both oxidation and carburisation while oxide thickness was only affected by oxidation.

The three stages of oxidation form oxide in three morphologies. A duplex oxide was formed in the first stage which follows sub-parabolic kinetics in non-breakaway samples; multi-layered oxide was formed in the second stage close to the TTB in the breakaway initiation samples and laminated oxide was formed in the third stage which follows linear kinetics in samples in the post-breakaway oxidation regime. The concentration profiles illustrate that the changes in the levels of Cr and Mo are indicative of the presence of Cr and Mo-rich carbide precipitates in the metal. It is worth noting that Cr concentration is stable in spinel from duplex oxide but fluctuates significantly in the spinel layer from multi-layered and laminated oxide. The distribution of Mo follows a similar tendency with Cr, but opposite to Fe in oxide with the three morphologies duplex, multi-layered and laminated.

The composition of spinel was calculated from the EDS line scan results from the three samples. The composition of spinel in the oxide from fin side in the non-breakaway sample ranges from $Fe_{2.60}Cr_{0.40}O_4$ to $Fe_{1.91}Cr_{1.09}O_4$. The composition of spinel in the oxide from fin tip obtained from three samples ranges from $Fe_{2.73}Cr_{0.27}O_4$ to $Fe_{1.91}Cr_{1.09}O_4$ in the non-breakaway sample, from $Fe_{2.78}Cr_{0.22}O_4$ to $Fe_{1.91}Cr_{1.09}O_4$ in the breakaway initiation sample and from $Fe_{2.65}Cr_{0.35}O_4$ to $Fe_{1.86}Cr_{1.14}O_4$ in the post-breakaway sample.

The spinel was identified in three samples, in non-breakaway, breakaway initiation and post-breakaway oxidation. In the early stage of oxidation, oxide is comprised of a mixture of Cr_2O_3 and spinel in the IOZ (which has a relative compressive stress compared with adjacent oxide), spinel and deposited low-degree of order carbon in the oxide region. In the breakaway initiation sample, the oxide is comprised of spinel and crystallised carbon. The oxide evaluated the grain boundary and residual carbides. In the post-breakaway oxidation stage, the oxide is comprised of spinel, which is identified as Cr-rich oxide and magnetite as Cr-depleted oxide, as well as the deposited low-degree of order carbon.

FIB XeF_2 images show that precipitates in the matrix exhibit different morphologies. The phases present in the sample were examined using XRD. Crystal structure and lattice parameters were identified using TEM. Elemental distribution was analysed using STEM-EDS. The fine needle carbides were comprised mainly of Cr, Mo and C with an HCP structure, and the lattice parameters a and c were 2.510 Å and 4.199 Å, respectively, which is consistent with M_2C in ref [211], where they measured a = 2.85 Å and c = 4.49 Å, respectively. The coarse carbides were composed of Fe, Cr, Mo and C with an FCC structure and lattice constant of 10.230Å, which is a bit smaller than the literature lattice parameter of $M_{23}C_6$ (10.621 Å) [195], indicating the coarse carbide to be $M_{23}C_6$. Large needles were mainly comprised of Cr, Fe, Mo and C with a BCC structure and lattice parameter a of 4.714 Å, which is close to the 4.01 Å for CrC obtained from the study in [212], indicating this type of precipitate to be MC. The inner core and the outer layer carbide from cored coarse carbide were both mainly comprised of Cr, Fe, Mo and C with an FCC structure but different ratio between Cr and Fe. The former contained more Cr than the latter. Furthermore, the lattice constant of the former was 9.86 Å, which was slightly less than that of the latter, 10.07 Å. However, both of the inner core and outer layer carbide were identified to be $M_{23}C_6$ with FCC structure, growing in the same orientation. The adjacent matrix was identified as α-Fe with BCC structure, with the lattice constant ranging from 2.673 Å to 3.161 Å.

Diffraction patterns from sample A-580-2542 illustrate that the orientation relationship between M_2C and α-Fe within the examined grain in Figure 4-29a is:

$$(10.\bar{1})_{M_2C} \| (01\bar{1})_{\alpha-Fe}$$

$$[01.1]_{M_2C} \| [011]_{\alpha-Fe}$$

The orientation relationship between MC and α-Fe from sample A-640-1495 (400 to 800 @ 245) within the examined grain in Figure 4-30a is:

$$(110)_{MC} \| (101)_{\alpha-Fe}$$

$$[001]_{MC} \| [\bar{1}11]_{\alpha-Fe}$$

The orientation relationship between $M_{23}C_6$ and α-Fe from sample A-640-1495 (400 to 800 @ 245) within the examined grain in Figure 4-30d is:

$$(11\bar{1})_{M_{23}C_6} \| (21\bar{1})_{\alpha-Fe}$$

$$[011]_{M_{23}C_6} \| [011]_{\alpha-Fe}$$

The orientation relationship between cored $M_{23}C_6$ and α-Fe from sample A-640-3883 within the examined grain in Figure 4-31a is:

$$(200)_{cored\ M_{23}C_6} \| (0\bar{1}1)_{\alpha-Fe}$$

$$[001]_{cored\ M_{23}C_6} \| [\bar{1}11]_{\alpha-Fe}$$

Carbide precipitates were formed by the reaction between the deposited carbon and elements in parent metal Fe, Cr and Mo. For this non-equilibrium diffusion process, Cr would be consumed, resulting in less protection for the parent metal which would eventually lead to breakaway oxidation. STEM line scan results showed that the Cr concentration in the surrounding parent metal decreased with the increase of oxidation and carburisation, which was 9 wt. % in sample A-virgin, but depleted to different levels in the carburised samples, and even decreased to approximately 1 wt. % in sample A-640-3883, which had entered the post-breakaway oxidation regime.

The key element Cr level changes during carburisation not only in the matrix but also in the carbides formed. The Cr concentration was approximately 50 wt. % in the coarse carbide from A-virgin sample and samples had not entered the post-breakaway oxidation regime. It reduced to 40 wt.% and 25 wt.% in the core and outer layer carbide, respectively, in the cored carbide from post-breakaway samples. This reduction resulted from the quick consumption of Cr and the limitation of Cr content in the steel.

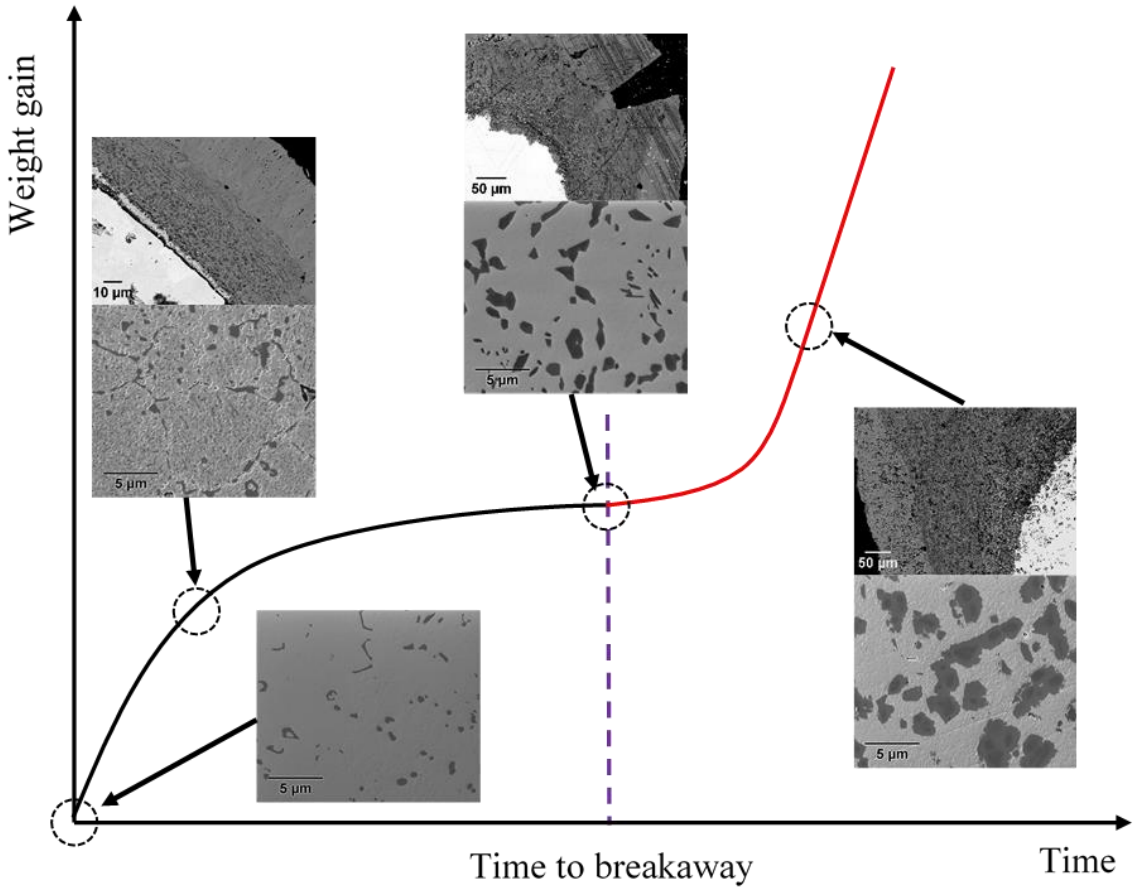

Figure 4-57: Weight gain versus exposure time accompanied with the oxide and carbides formed in each regime.

As shown in Figure 4-57, carbide precipitates with different morphologies were present at different stages of oxidation. Coarse carbides were present in all the analysed HRA samples, including A-virgin sample. In the early stage of oxidation, fine needles were present in the region close to oxide and disappeared with the increase of depth. Large needles were observed in the breakaway initiation sample, and the cored coarse carbides were present as well in this case. In the post-breakaway stage, needles were not observed, having either dissolved or converted into cored coarse carbides.

Both FIB and HS-AFM imaging confirm that the fine needle carbides are found only intragranularly while coarse carbides are both intergranular and intragranular precipitates. Images from HS-AFM indicate that the hardness of the inner core is higher than that of the surrounding outer layer carbide, illustrating that the hardness of carbides increases with the increase of Cr concentration. There is a similar tendency of the carbide area fraction plots from FIB and HS-AFM results, but more spatial details are revealed by HS-AFM, e.g. the height of the analysed features. These are evidence that HS-AFM is capable of providing spatial information for the examined samples. However, the area fractions obtained from FIB XeF_2 images are more reliable. The saturation state was present in some of the examined samples. The carbide area fraction for the saturation state from observation is consistent with that from

calculation, both of which indicate 17% as the saturated carbide area fraction for ferritic 9Cr-1Mo steels.

The oxide thicknesses of magnetite and spinel, and oxide type identification, provide more data for the future modelling work on oxidation, e.g. the modelling work from Larsson et al. on oxide thickness versus exposure time [213]. Carbide types and area fractions following different paths from samples oxidised at different temperatures and times provide more information, such as oxide types, carbide types and stress for the modelling optimisation from Larsson et al. [213] and Gong et al. [85].

Chapter 5: Comparative studies on ferritic 9Cr-1Mo steel oxidised within AGR coolant gas

The oxidation part of this chapter is mainly based on my first author paper published in "A study of breakaway oxidation of 9Cr–1Mo steel in a Hot CO_2 atmosphere using Raman spectroscopy" Mater. High Temp. 35 (2018) 50–55. © Materials at High Temperatures

In this chapter, we will discuss the process of oxidation and carburisation with experimental ferritic OMS samples that have been oxidised within HRA AGR. Optical microscopy, SEM and EDS were used for oxide morphology observation and elemental distribution analysis while scanning laser Raman spectroscopy was used for oxide identification in the same region examined with EDS. X-ray diffraction was used to identity the phases present in the evaluated samples. Carbides were observed using FIB imaging and carbide area fractions were calculated by processing FIB XeF_2 images. This investigation aims to make a comparison between ferritic HRA samples exposed to AGR coolant gas and a simulant coolant gas discussed in Chapter 4.

5.1 Oxide observation and oxidation characterisation

5.1.1 Samples used for oxidation analysis and techniques used

Experimental oxidation monitoring scheme (OMS) ferritic HRA finned samples M92M02-580-146760 and M96M01-580-146760, provided by Wood PLC, were mechanically polished for oxide observation and characterisation. The samples were exposed in electrically heated autoclaves, located within the HRA AGR containing flowing gas directed from the reactor core. The exposure conditions are shown in Table 3-2. These samples are described as sample ID-temperature-time, e.g. M92M02-580-146760 represents sample M92M02-580 °C-146760 h (Variable) because the moisture for all the OMS samples was described as variable based on the data provided by Wood PLC. The techniques used for each OMS sample are shown in Table 5-1.

Table 5-1: Techniques used for selected OMS samples.

Sample ID	***Oxidation***			***Carburisation***	
	OM	*SEM*	*Raman*	*XRD*	*FIB*
T01M26-495-171888				✓	✓
M92M02-580-146760	✓	✓	✓	✓	✓
M96M01-580 -146760	✓	✓	✓	✓	✓

5.1.2 Oxide observation

Figure 5-1 shows the optical images recorded from cross sections prepared from samples M92M02-580-146760 and M96M01-580-146760. The marked fins illustrate that both samples are in the breakaway oxidation condition. Examples of optical micrographs recorded from the fin tip corner and fin side are shown in Figure 5-2.

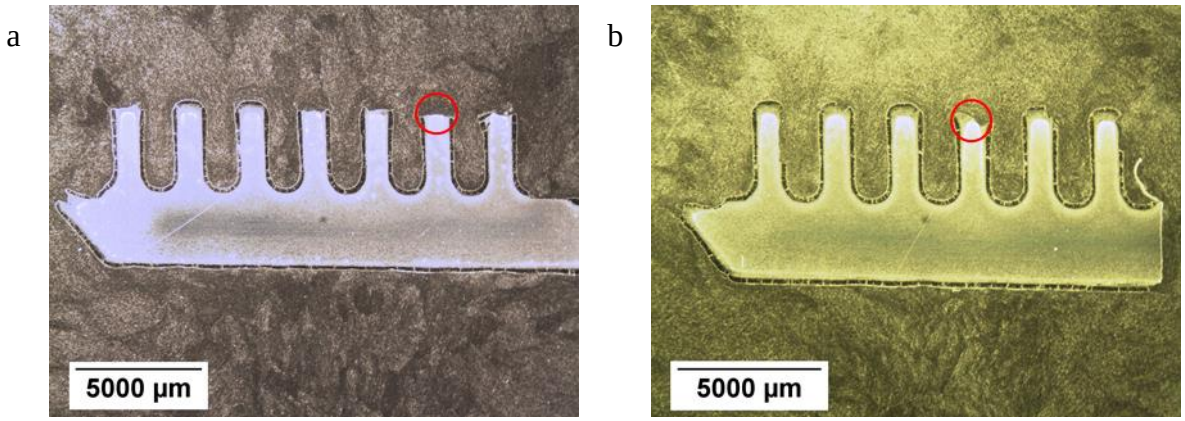

Figure 5-1: Optical images of samples (a) M92M02-580-146760 (© Materials at High temperatures) and (b) M96M01-580-146760. The fin marked by a red circle is an example of breakaway oxidation.

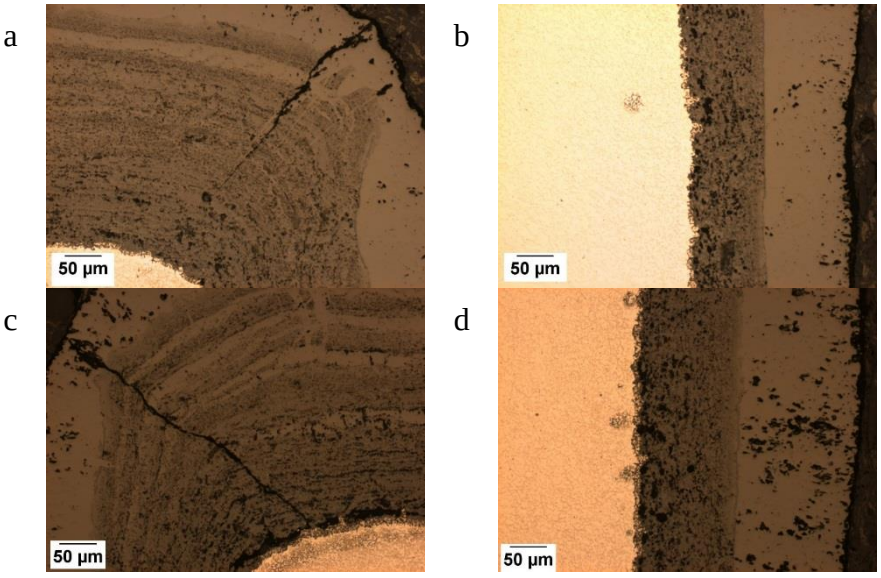

Figure 5-2: Optical micrographs of (a) fin tip in sample M92M02-580-146760 (© Materials at High temperatures); (b) fin side in sample M92M02-580-146760; (c) fin tip in sample M96M01-580-146760; (d) fin side in sample M96M01-580-146760.

It can be seen that these two OMS samples exposed to AGR coolant gas have multi-layered oxides at the fin tip corner, which are similar to samples in breakaway initiation: A-600-1520 (1200), A-640-1495 (400 to 800 @ 245) and A-640-2526 shown in Figures 4-4 and 4-5, but with thicker oxide at the examined locations, presumably resulting from the long-term exposure. Samples M92M02-580-146760 and M96M01-580-146760 are therefore breakaway initiation samples with cracks present in the oxide and extending radially to the fin tip corner. The oxide at the fin sides in these two samples has duplex structures. Similar observations were made for

the autoclave HRA samples discussed in Chapter 4. A continuous IOZ layer was observed in both OMS samples at the fin tip corner. However, M96M01-580-146760 showed a discontinuous IOZ layer while in M92M02-580-146760 showed a continuous IOZ layer at the fin side. It appears that both of the examined OMS samples were in the transition from non-breakaway to post-breakaway. This was also observed in autoclave HRA samples A-600-1520 (1200) in Figure 4-4 and A-640-1495 (400 to 800 @ 245) in Figure 4-5, which have multi-layered oxide at the fin tip corner and discontinuous IOZ layers beneath.

The average thickness of oxide scale at the fin tip corner and fin side of the two OMS samples were measured in each case as shown in Table 5-2, using the method described in Chapter 4 (Section 4.1.2) to obtain the mean value of thickness from the measurement at twelve positions.

Table 5-2: Average thickness (in μm) of magnetite, spinel, the continuous IOZ and total oxide scale.

Samples	*M92M02-580-146760*				*M96M01-580-146760*			
Oxide type	*Fe_3O_4*	*Spinel*	*IOZ*	*Total*	*Fe_3O_4*	*Spinel*	*IOZ*	*Total*
Fin tip	*/*	*/*	*/*	*449*	*/*	*/*	*10.3 ± 2.5*	*446*
Fin side	*116 ± 7*	*103 ± 6*	*/*	*219 ± 18*	*156 ± 4*	*112 ± 3*	*9.4 ± 2.1*	*286 ± 7*

The results obtained with optical micrographs indicate that the oxide scale formed at the fin tip for the two samples are similar. However, the oxide thickness at the fin tip corner is roughly twice that at the fin side for a given sample. This influence is due to the geometry at the fin tip and 2D diffusion of key elements, e.g. Cr and Fe, at the fin tip corner. Oxide at the fin tip and fin side of M92M02-580-146760 and M96M01-580-146760 is thicker than that for breakaway initiation samples A-600-1520 (1200), A-640-1495 (400 to 800 @ 245) and A-640-2526, as shown in Table 4-3. The reason for this phenomenon is the long-term exposure at low temperature which provides time for Cr diffusion. Cr has slow mobility, as discussed in ref [37]. Therefore, more Cr diffused to the oxide/metal interface during long-term low-temperature exposure to form thicker oxide before the breakaway initiation. As investigated in ref [85], the TTB at 600, 620 and 640 °C is around 20 kh, 3 kh and 2 kh, respectively, which is less than the 147 kh exposure at 580 °C for the AGR samples examined in this investigation. The plot of weight gain as a function of exposure time in Figure 4-7b in Chapter 4 also demonstrated that the TTB at 640 °C was close to 2 kh. The plot of exposure time versus temperature in Figure 5-3 shows the TTB as a function of temperature between 580 and 640 °C, providing the possibility for the estimation of TTB at other temperatures. The TTB decreases with the increase of diffusion of cations. Therefore, $TTB \propto 1/D$, where D is the diffusion coefficient (in m^2/s), which can be obtained by the Arrhenius equation, as shown in Equation 5.1:

$$D = D_0 \cdot exp\left(-\frac{E_A}{RT}\right) \qquad 5.1$$

where D_0 is the maximal diffusion coefficient (in m^2/s), E_A is the activation energy for diffusion (in J/mol), T is the absolute temperature (in K) and R is the universal gas constant which is 8.31 J/(mol·K). Putting TTB = 147 kh at 853 K, and TTB = 20 kh at 873 K into Equation 5.1, results show that D_0 and E_A are approximately 4.15×10^{34} m^2/s and 6×10^5 J/mol, respectively.

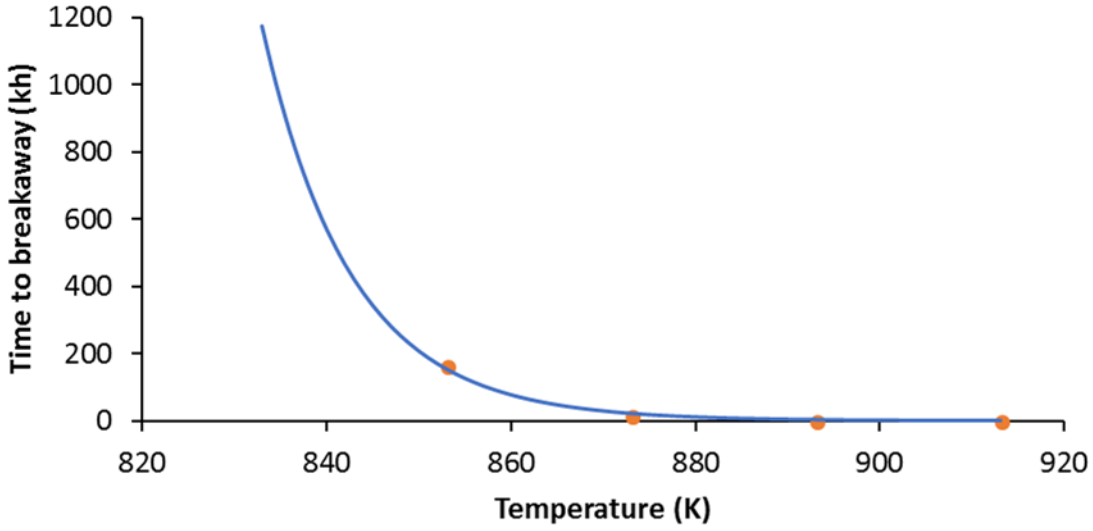

Figure 5-3: The time to breakaway (TTB) as a function of exposure temperature. The spots (orange) were fitted with a logarithm asymptotic to one function, as shown with the blue fitted curve.

5.1.3 Oxide observation and elemental distribution from SEM-EDS

Following observation of oxide with optical microscopy, SEM-EDS was used to determine the elemental distribution within the oxide, as discussed in the following context.

Figure 5-4 shows examples of the concentration profiles of the detected elements at the fin side in both M92M02-580-146760 and M96M01-580-146760. The EDS line scan has been adopted at the fin side in autoclave HRA samples in chapter 4, therefore, the oxide at the fin side was examined with the average concentration obtained from an area 20 × 10 µm in size for comparison. The profiles were made on adjacent areas in this size at 500 µm from fin tip, following path 1 marked in Figure 4-26. Oxygen was only taken into consideration in analysis of the oxide scale and the IOZ.

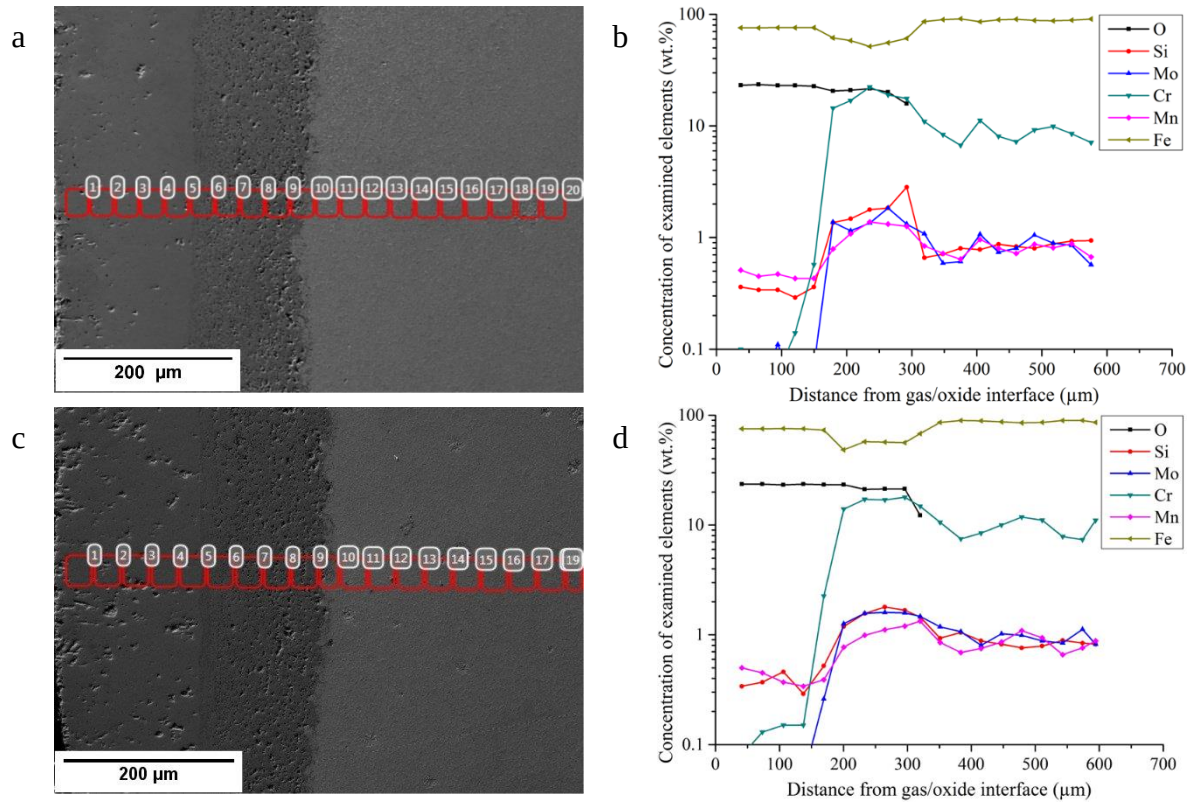

Figure 5-4: (a) SEM image of the examined area at 500 μm from the fin tip of sample M92M02-580-146760 and (b) the corresponding elemental distribution; (c) SEM image of the examined area at 500 μm from the fin tip of sample M96M01-580-146760 and (d) the corresponding elemental distribution.

The Cr and O concentration profiles displayed in Figure 5-4 show the presence of magnetite and spinel in the outer layer and inner layer of oxide respectively. It also indicates the presence of Cr and Mo-rich precipitates in the metal bulk. According to the concentration profiles shown in Figure 5-4b and d, the outer layer oxide is identified to be magnetite, Fe_3O_4 (weight percentage of Fe and O is 72.4 wt.% and 27.6 wt.%, respectively), consistent with the observation from the line scan at the fin side of sample A-580-2542, and the inner layer oxide to be spinel, $Fe_{3-x}Cr_xO_4$. The spinel exhibits a more complex composition, depending on the ratio between Fe and Cr. In sample M92M02-580-146760, the Cr level in the outer layer oxide is less than 1 wt.%, reaching approximately 14 wt.% in the inner oxide layer and 22 wt. % in the spinel. The x in the formula $Fe_{3-x}Cr_xO_4$ ranged from 0.62 to 0.97. In sample M96M01-580-146760, the Cr concentration ranged from 14 wt. % to 18 wt. %, indicating x to be in the range 0.62 to 0.79. The Cr concentrations in spinel from the two examined OMS samples are similar due to the similar exposure conditions.

The level of Mo was observed to exhibit a similar trend with Cr in both oxide and metal bulk, indicating the presence of Cr and Mo-rich precipitates in the bulk metal and and Mo exhibits a similar tendency with Cr in both oxide and bulk metal. The elemental distributions of the two examined samples are similar due to the similar exposure conditions.

Although the samples M92M02-580-146760 and M96M01-580-146760 were marked as breakaway and breakaway initiation, respectively from the data provided by EDF Energy, as shown in Table 3-2. This investigation illustrates that both of the samples were in breakaway initiation, in the transition from non-breakaway to breakaway oxidation.

5.1.4 Oxide identification using SEM-EDS and scanning laser Raman spectroscopy

For the autoclave HRA samples discussed in Chapter 4 Section 4.1.3, the spinel and IOZ in sample M92M02-580-146760 was identified with scanning laser Raman spectroscopy. An optical micrograph of a region at the fin tip corner of sample M92M02-580-146760 is shown in Figure 5-2a. As discussed previously, the morphology of the oxide on the fin corner is multi-layered, and a crack is present in the oxide, extending radially to the fin corner. The thickness of the oxide, together with the presence of multi-layering and cracking, provides evidence that the sample has entered the breakaway oxidation regime.

Scanning electron micrographs and EDS composition maps of a region at the fin tip close to the oxide/metal interface are shown in Figure 5-5. Metal, IOZ and oxide regions are marked in the SEM image of Figure 5-5a. Chromium and molybdenum are present as filamentary structures throughout the oxide and IOZ and extend into the metal, where it is associated with carbide precipitates. The Fe map shows the opposite contrast and, therefore, composition distribution. The O map shows the filamentary structures in the IOZ to contain oxygen, while some depleted regions in the oxide layer are shown to contain carbon. The outlined regions in the images indicate an area that was mapped by scanning LRS.

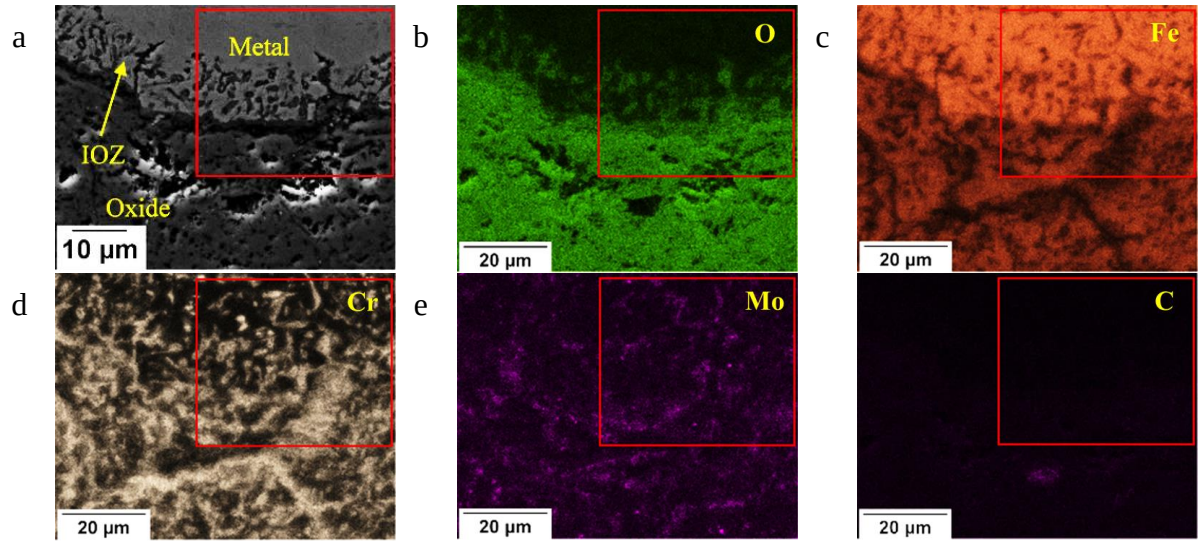

Figure 5-5: (a) Scanning electron micrograph of examined area. EDS maps of elements (b) O; (c) Fe; (d) Cr; (e) Mo and (f) C from sample M92M02-580-146760. The marked area was mapped using scanning laser Raman spectroscopy [63] (© Materials at High Temperatures).

As discussed in Chapter 2, the magnetite and spinel are formed at an oxide/gas and oxide/metal interface, respectively, in the outlined region containing oxide/metal interface. A white light

illuminated optical micrograph of sample M92M02-580-146760 obtained from the Raman instrument is shown in Figure 5-6a. The outline box shows the area mapped by Raman spectroscopy. Spectra obtained from two positions, A and B, are shown in Figure 5-6b and c, respectively. These are shown after baseline removal using Wire 4.3 software.

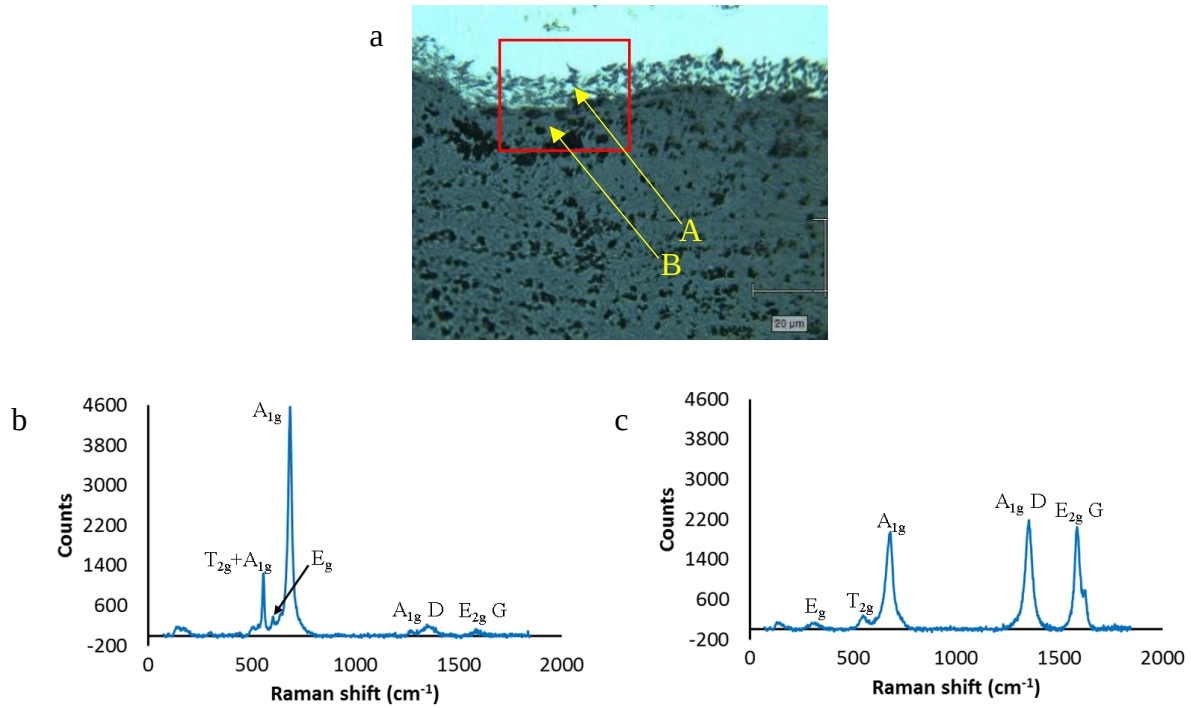

Figure 5-6: (a) White light optical micrograph of sample M92M02-580-146760 showing region mapped by Raman spectroscopy (© Materials at High Temperatures). (b) Raman spectrum from point A. (c) Raman spectrum from point B [63].

The Raman spectra for both Cr_2O_3 and $FeCr_2O_4$ contain peaks at around 553 cm^{-1}, but for the former the peak is much narrower, corresponding to the A_{1g} mode and accompanied by a smaller peak at 610 cm^{-1} which corresponds to T_{2g} mode of Cr_2O_3 [62]. This is similar to the results from sample A-580-2542 shown in Figure 4-16. For the $FeCr_2O_4$ reference spectrum shown in Figure 4-17b, the peak at 554 cm^{-1} is broad, and there is a further peak at 684 cm^{-1}. Both of these specific oxides are present within the complex oxide of the 9Cr-1Mo sample analysed here. The spectrum from position A (Figure 5-6a) contains a narrow peak at 555 cm^{-1} accompanied by a smaller peak at 610 cm^{-1} (Figure 5-6b), consistent with Cr_2O_3. At position B (Figure 5-6c), there is a broad peak at 555 cm^{-1}, with a further peak at 684 cm^{-1}, consistent with $FeCr_2O_4$. It is apparent that at many positions, the Raman spectra are mixtures of the two, presumably because of the limited spatial resolution of the technique. Two further main peaks are present in spectra observed from the oxide: (i) at 1356 cm^{-1} (D peak of graphite, A_{1g} mode) and (ii) at 1588 cm^{-1} (G peak of graphite, E_{2g} mode) [104][106] in Figure 5-6b. These are consistent with spectra from carbon in the form of graphite with a low-degree of order [214].

The spectrum from position B in Figure 5-6a contains peaks at 309, 548, and 674 cm^{-1}, indicating the presence of Fe_3O_4 [190][95] and/or spinel M_3O_4 [94]. However, the absence of a peak at around 610 cm^{-1} reveals the absence of Cr_2O_3, as shown in Figure 5-6c. Two further peaks at 1351 and 1589 cm^{-1} are corresponding to D peak (A_{1g} mode) and G peak (E_{2g} mode) from graphite with the low-degree of order [214].

Table 5-3:The Raman peak positions for each location examined in the selected experimental HRA within AGR sample M92M02-580-146760.

Sample ID and examined locations		*E_g (cm^{-1})*	*T_{2g}(spinel) /A_{1g}(Cr_2O_3) (cm^{-1})*	*E_g (cm^{-1})*	*A_{1g} (cm^{-1})*	*A_{1g} D (cm^{-1})*	*E_{2g} G (cm^{-1})*
M92M02-580-146760	*Spot A*	*/*	*555*	*603*	*684*	*1356*	*1588*
	Spot B	*309*	*548*	*/*	*674*	*1351*	*1589*

Table 5-3 shows the positions of peaks present in spots A and B and corresponding vibrational modes. The position of the A_{1g} mode peak from Cr_2O_3 at 555 and 548 cm^{-1} suggests the presence of a compressive stress of 500 MPa and 300 MPa respectively based on the investigation and calibration undertaken by Birnie et al [102]. But this indicative stress assumes that there is no relative stress within the reference sample and no compositional effects present.

A positive shift in the Raman peak position indicates a compressive stress while tensile stress produces a negative shift [194]. Assuming there are no compositional changes and thermal stress in sample M92M02-580-146760, the A_{1g} mode from spinel in the IOZ has a larger Raman shift than the oxide close to the oxide/metal interface, indicating a relative compressive stress in the IOZ and tensile stress in the oxide. To generate the cracks in the oxide in breakaway samples as shown in Figure 5-2, a tensile stress is required in the oxide compared with the matrix, consistent with the result of this investigation.

Table 5-4: D and G peak intensity, their ratio and crystallite size of graphite for each location examined in the selected experimental HRA within AGR sample M92M02-580-146760.

Sample ID	*Location*	*Intensity*		*I(D)/I(G) ratio*	*Graphite crystallite size (nm)*
		D	*G*		
M92M02-580-146760	*Spot A*	*198*	*119*	*1.66*	*3*
	Spot B	*2187*	*2050*	*1.07*	*8*

Table 5-4 shows the intensities of the graphite D and G peaks and their ratios [106]. The graphite crystallite sizes from spots A and B are 3 and 8 nm respectively. Raman intensity distribution maps of the area marked in Figure 5-5 were obtained from the 555 ($Fe_{3-x}Cr_xO_4$ and Cr_2O_3), 684 ($Fe_{3-x}Cr_xO_4$) and 1350 cm^{-1} (graphite) peaks by extracting local peak intensity values and plotting them as a function of position (Figure 5-7).

By observing the Raman spectra at each position in the maps, it can be demonstrated that the bright regions in the 555 cm^{-1} intensity map of Figure 5-7a correspond to the narrower peaks

at 555 and 610 cm^{-1} associated with Cr_2O_3, while the diffuse regions at the lower part of the image are consistent with the spectrum for chromite, $FeCr_2O_4$. The intensity map for the 684cm^{-1} peak is shown in Figure 5-7b, revealing the presence of chromite in the majority of the oxide, extending into the filamentary structures of the IOZ. The bright regions in the lower part of the 1350 cm^{-1} map of Figure 5-7c indicates the presence of graphite with a low-degree of order. It can be noted that while the peak intensity maps are consistent with the EDS element maps, the Raman spectra reveal further information about the types of oxide present within the scale.

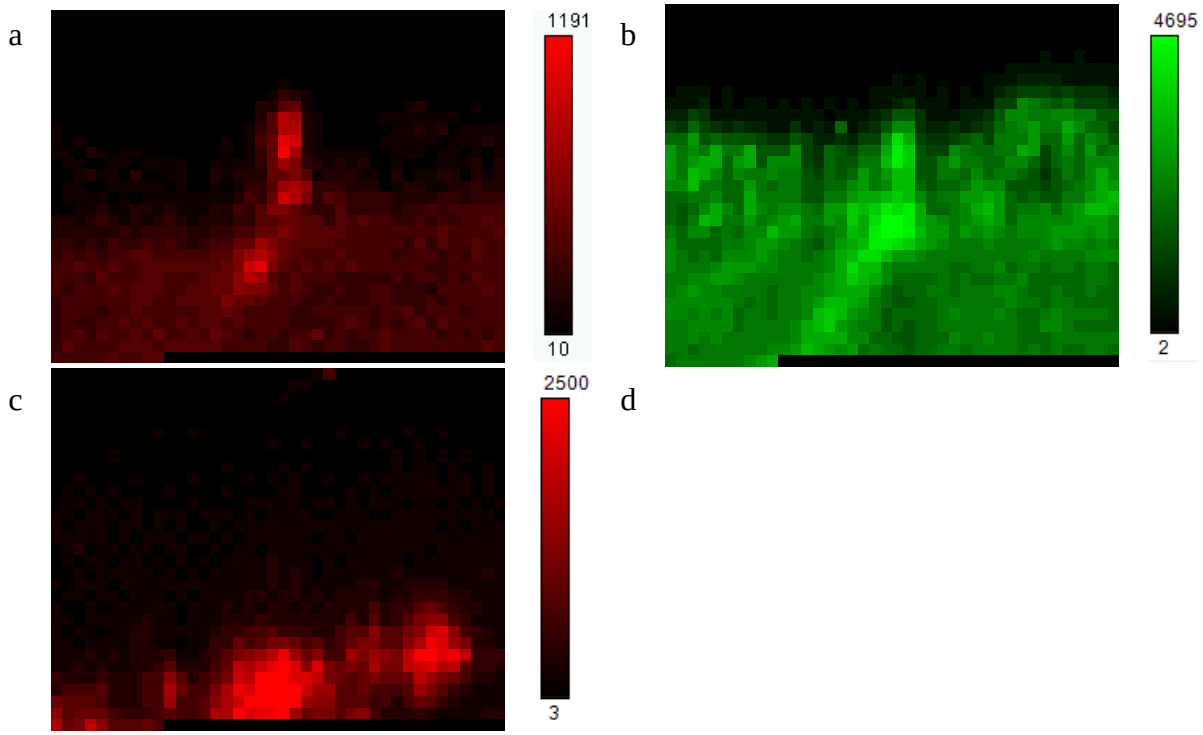

Figure 5-7: Raman peak intensity maps of sample M92M02-580-146760 for peaks at (a) 555 cm^{-1}, (b) 684 cm^{-1} and (c) 1350 cm^{-1}. The intensity scale markers in counts per pixel are shown for each map [63] (© Materials at High Temperatures).

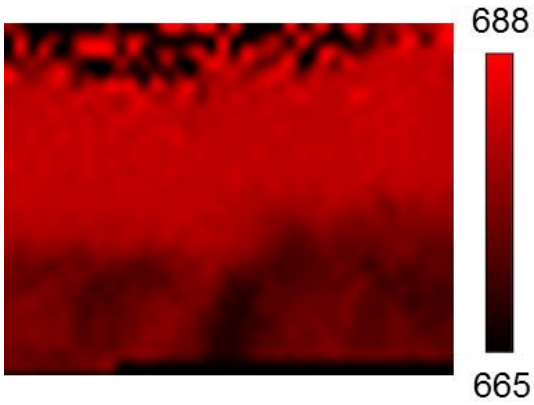

Figure 5-8: Raman peak position map at around 675 cm^{-1} from sample M92M02-580-146760.

Figure 5-8 shows a Raman peak position map in the range of 665-688 cm^{-1} in the examined region A. Higher intensity shifts were observed in the oxide close to the oxide/metal interface

and a relatively lower intensity shift at the bottom of the map. According to ref [194], a positive area shift indicates a compressive stress while tensile stress produces a negative shift. Assuming that there are no compositional changes in the examined regions, Figure 5-8 indicates a relative compressive stress in the oxide close to the oxide/metal interface compared with the oxide in the bottom region.

5.2 Carbide observation and carburisation characterisation

5.2.1 Samples used for carburisation analysis

The four experimental OMS samples were examined with FIB and XRD for carbide observation and identification, including A-virgin for comparison, T01M26-495-171888 oxidised at 495 °C, and M92M02-580-146760. Carbide area fractions were calculated by processing FIB XeF_2 images from sample M92M02-580-146760 and M96M01-580-146760 exposed at 580 °C. The two samples oxidised at 495 °C were non-breakaway while samples exposed at 580 °C were breakaway.

5.2.2 Carbide observations

A-virgin, non-breakaway sample T01M26-495-171888 and breakaway initiation sample M92M02-580-146760 were examined with FIB imaging with XeF_2 gas to reveal precipitates which have been identified as carbides in Chapter 4.

However, it should be noted that these three selected samples were from a different cast which indicating a slight difference in chemical composition as shown in Table 3-1. The Cr contents of the samples A-virgin, T01M26-495-171888 and M92M02-580-146760 were found to be 9.2, 8.9 and 9.1 wt. % respectively, while the Mo content of these three samples were 1.04, 1.00 and 0.94 wt. % respectively.

Figure 5-9 shows the four morphologies of carbides based on the FIB XeF_2 images: coarse precipitates, cored coarse precipitates, fine needle (< 1 μm) and large needle (> 1 μm) precipitates. Coarse carbides were present in all the examined samples. Figure 5-9a shows that the A-virgin sample only contains coarse precipitates and the long side of the coarse precipitates ranges from 1 to 2 μm. The fine needle precipitates (length < 1 μm) were present at the fin tip close to oxide in non-breakaway sample T01M26-495-171888, as shown in Figure 5-9b. This is similar to the observation from non-breakaway autoclave HRA samples, e.g. A-580-2542 shown in Figure 4-27b. Figure 5-9c shows that sample M92M02-580-146760 contained cored precipitates (long side > 2 μm) and large needle precipitates (length > 1 μm) as well as the coarse precipitates (long side > 2 μm) observed in all four examined samples. This is similar to the breakaway initiation sample A-640-1495 (400 to 800 @ 245) analysed in

Figure 4-27c. The coarse precipitates in M92M02-580-146760 were bigger compared with those present in the other three samples. These precipitates with will be examined with XRD in the following section.

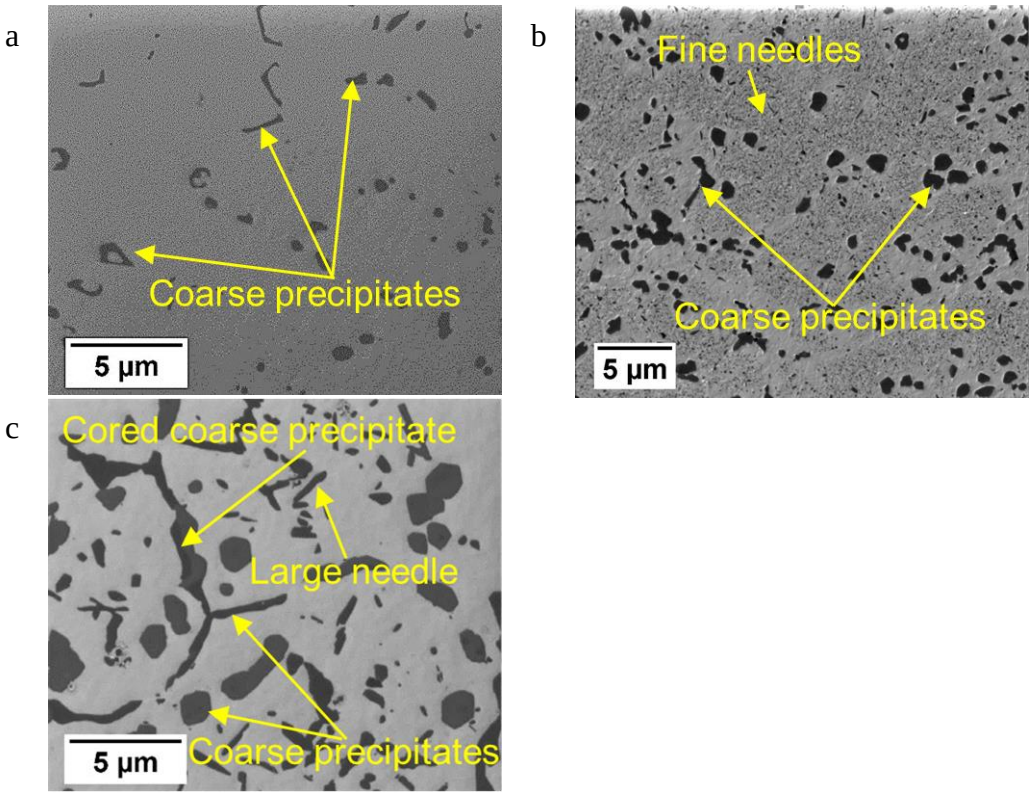

Figure 5-9: FIB XeF_2 images showing the distribution of carbide precipitates at fin centre with 500 µm from the fin tip for (a) A-virgin and (c) M92M02-580-146760; 160 µm from the fin tip for (b) T01M26-495-171888.

5.2.3 Carbide identification using XRD

The A-virgin sample was analysed using XRD in Section 4.2.2 Chapter 4. The two OMS samples, T01M26-495-171888 and M92M02-580~147000, were examined using XRD to identify the phases present and the results are shown in Figure 5-10. The mounting material was analysed separately and the diffraction peaks identified in the resulting spectra. The sizes of the examined area and parameters used were consistent with those used for the samples discussed in Section 4.2.2 Chapter 4.

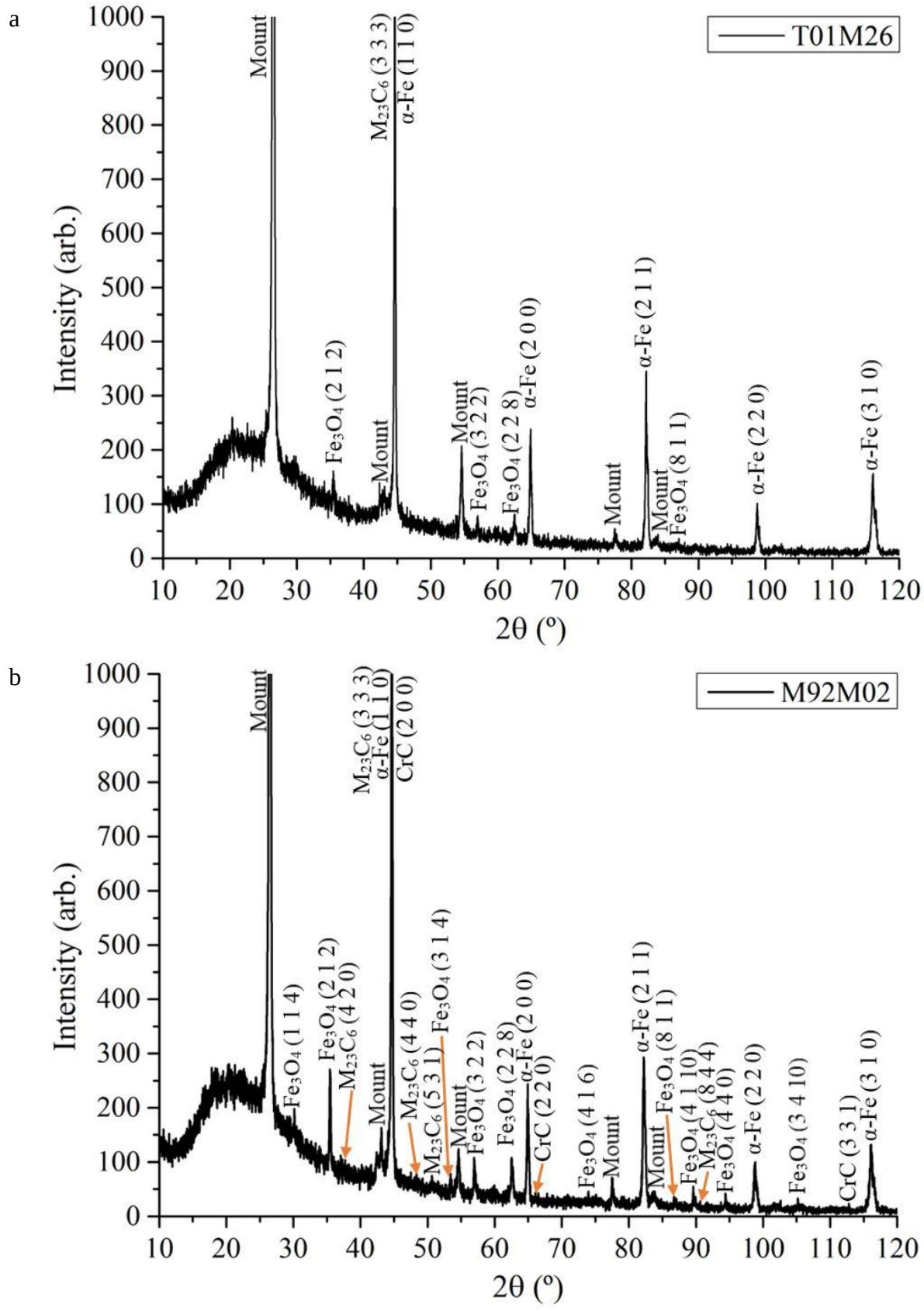

Figure 5-10: XRD results of the four examined samples (a) T01M26-495-171888 and (b) M92M02-580-146760.

Omitting peaks from the mounting material, ferrite and Fe_3O_4 were identified in all the evaluated samples, as shown in Figure 5-10. Figure 5-10a show that ferrite and oxide were

identified in sample T01M26-495-171888. More phases were identified in sample M92M02-580-146760, as shown in Figure 5-10b, including ferrite, oxide, $M_{23}C_6$, and MC.

Although these samples were not examined by TEM, considering the similar morphologies of the carbides formed in the same oxidation stage, it is very likely that the coarse carbides (either with or without cores) formed in OMS samples are $M_{23}C_6$, fine needle M_2C and large needle MC.

5.2.4 Carbide area fraction

The identified carbides were quantified by area fraction using FIB XeF_2 images. The FIB XeF_2 images were processed using image processing software ImageJ and Labview. The results from ImageJ of samples M92M02-580-146760 and M96M01-580-146760 are shown in Figure 5-11 to compare with autoclave HRA samples analysed in Chapter 4 section 4.2.4, as shown in Figure 4-46a, Figure 4-47 and Figure 4-48. The carbide area fractions from the two samples exposed at 580 °C for approximately 147 kh were similar, ranging from 18 to 26 %. The carbides from both samples have a similar area fraction at the fin side and fin centre. Comparing the carbide area fractions obtained from these two samples exposed within AGR and the HRA samples exposed in simulant coolant gas, a similarity was found between two discussed samples (ranging from 20 to 26 %) and A-640-2526 (ranging from 20 to 32 %). The carbide area fractions are summarised in Table 5-5, showing that the area fraction decreases with increasing distance from the fin tip.

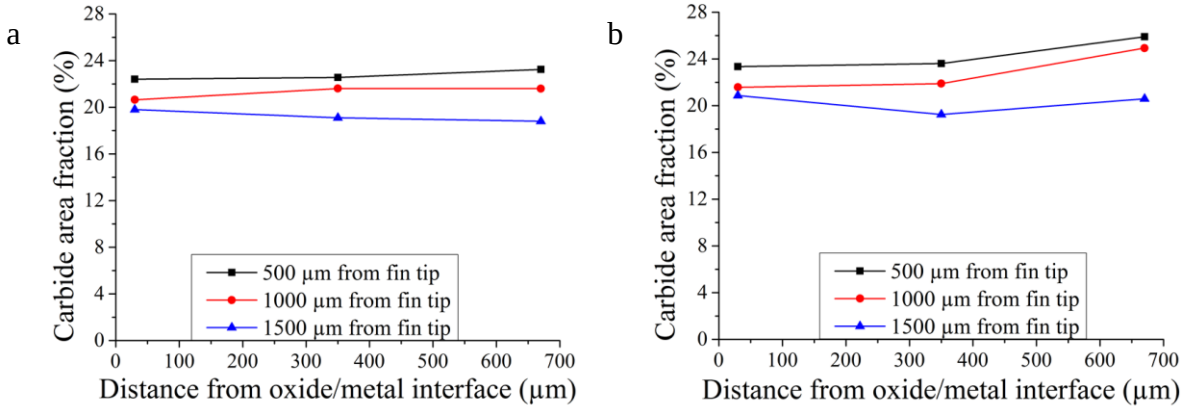

Figure 5-11: Plot of carbide area fraction as a function of distance to oxide/metal interface following three paths across the fin in Figure 4-3 from samples (a) M92M02-580-146760; (b) M96M01-580-146760.

Table 5-5: Carbide area fractions at fin side and fin centre of experimental HRA samples exposed within AGR following three paths described in Figure 4-26.

Sample ID	*Carbide area fraction at fin side (%)*			*Carbide area fraction at fin centre (%)*		
	Path 1	*Path 2*	*Path 3*	*Path 1*	*Path 2*	*Path 3*
M92M02-580-146760	*22-24*	*20-22*	*18-20*	*~23*	*~22*	*~19*
M96M01-580-146760	*23-26*	*22-25*	*20-21*	*~24*	*~22*	*~19*

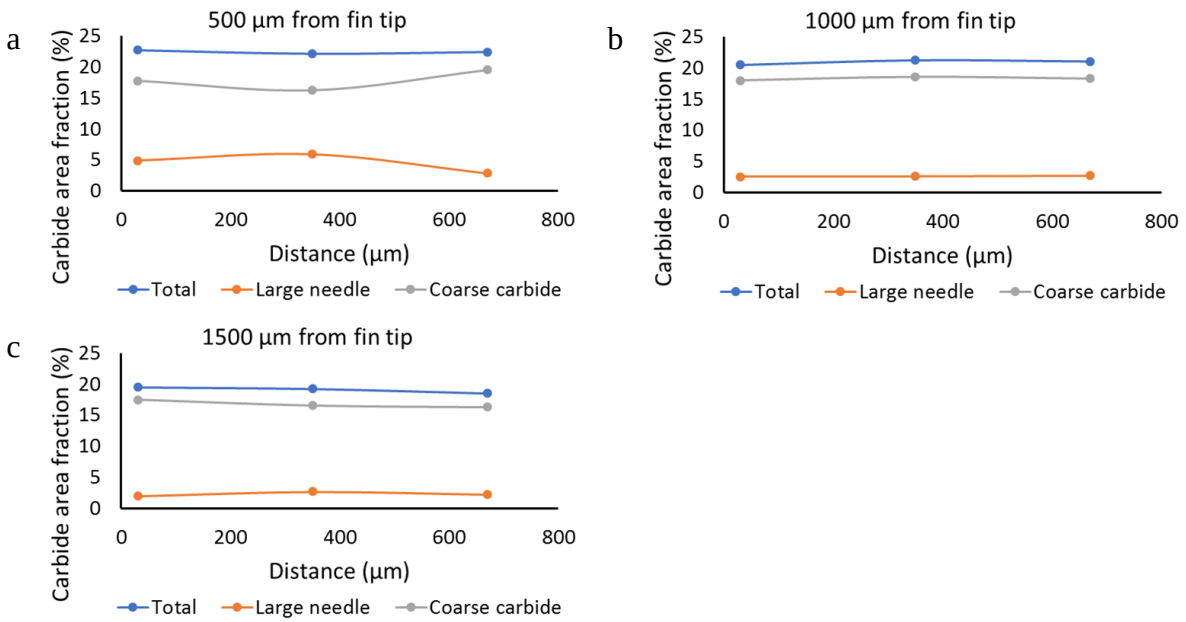

Figure 5-12: Carbide area fraction of sample M92M02-580-146760 obtained from FIB imaging following the three paths around 500, 1000 and 1500 µm from fin tip across the fin.

FIB XeF_2 images from samples M92M02-580-146760 and M96M01-580-146760 were also processed to determine the area fractions of needle and coarse carbide precipitates. The results are shown in Figure 5-12 and Figure 5-13. Following the three paths shown in Figure 4-26 analysed using FIB technology, it can be seen that the area fraction of the large needles following path 1 in sample M92M02-580-146760 (around 5 %) was higher than that from paths 2 and 3. Both were similar to those obtained from sample A-640-1495 (400 to 800 @ 245), at around 2 %. The area fractions of the large needles in sample M96M01-580-146760 following the three paths are all around 2 %. The area fractions of coarse carbides in both samples are much higher than from the needles.

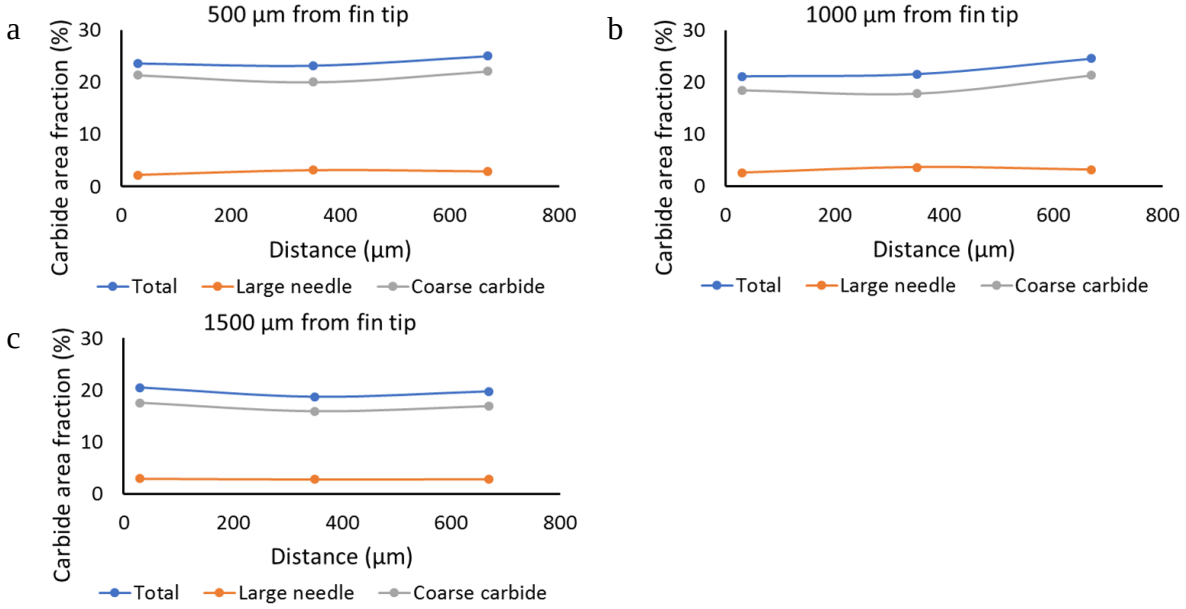

Figure 5-13: Carbide area fraction of sample M96M01-580-146760 obtained from FIB imaging following the three paths around 500, 1000 and 1500 µm from fin tip across the fin.

5.3 Discussion

5.3.1 Oxidation

The presence of cracks extending radially from oxide to the fin tip corner and multi-layered oxide are evidence that samples M92M02-580-146760 and M96M01-580-146760 are in breakaway initiation (optical micrographs in Figure 5-2). The oxide at the fin tip corner is much thicker than at the fin side which can be explained by the two-dimensional diffusion discussed in Section 4.1.2 Chapter 4 (Equation 4.1 and Figure 4-6). The IOZ from M92M02-580-146760 is discontinuous while M96M01-580-146760 contains a continuous IOZ layer. This is possibly because they were close to breakaway, at which stage the IOZ layer disappears. The thickness of magnetite and spinel are roughly the same at the fin side, consistent with observations from the autoclave HRA samples discussed in Section 4.1.2 Chapter 4.

Micrographs and elemental concentration profiles obtained from SEM-EDS showed the existence of Fe_3O_4 and spinel M_3O_4 (M represents Fe and Cr). The composition of the spinel gave a value of x in $Fe_{3-x}Cr_xO_4$ as 0.62-0.97 in the examined regions in sample M92M02-580-146760 and 0.62-0.79 in sample M96M01-580-146760. The elemental profiles illustrate a positive correlation between Mo and Cr, and a negative correlation between Cr and Fe. SEM-EDS data obtained close to the oxide/metal interface are consistent with those found previously in breakaway oxidised samples [38], indicating a spinel layer containing some deposited carbon, an IOZ layer with filamentary oxide structures and chromium-rich carbides within the metal.

Scanning laser Raman spectroscopy provided further information on the types of oxide present in sample M92M02-580-146760, confirming the presence of the spinel chromite ($FeCr_2O_4$) and also chromia (Cr_2O_3), which appeared in small areas close to the IOZ layer. The IOZ layer, therefore, comprised of chromia and spinel embedded in the matrix. The technique also identified graphite with a low-degree of order present in patches within the spinel [104]. Disregarding stress in the oxide, the oxide composition is determined by the A_{1g} mode spinel peak position of around 684 cm^{-1}. Results show that the oxide in spot A within the IOZ is comprised of $Fe_{1.08}Cr_{1.92}O_4$ while spot B within the spinel is comprised of $Fe_{2.92}Cr_{0.08}O_4$ [83].

Ignoring the influence from compositional change, there is a relative tensile stress within the spinel compared with the oxide within IOZ from the Raman peak position map in Figure 5-8. The crystallite size of graphite can be obtained from I(D)/I(G) ratio, which indicated a 3 nm crystallite size graphite at spot A within the IOZ and 8 nm at spot B within the spinel [106]. The intensity of D and G peaks at spot B is higher than of spot A, indicating the presence of more graphite at spot B.

The oxidised region evaluated in Figure 5-5 has a complex morphology and, while the onset of breakaway oxidation is clearly linked to sample geometry, it is not clear whether the cracking that often occurs within the oxide scale is the cause of breakaway by allowing ingress of gas to the oxide/metal interface, or whether breakaway is triggered by the high carbide content within the metal which gives rise to a rapidly moving oxidation front, with cracking occurring as a result of this rapid growth. Moreover, the process is potentially exacerbated by the multi-layering of spinel and magnetite. The complexity of the oxide system complicates the measurement of strain because any shift in the position of a specific Raman peak may be due to strain, a change in oxide type, the presence of an impurity element or a combination of these [94][83][215]. The position of the main peak from Cr_2O_3 for the reference sample was 553 cm^{-1}, while that obtained from the chromia within the M92M02-580-146760 sample was 555 cm^{-1} from spot A (IOZ) and 548 cm^{-1} from spot B (spinel). This preliminary work would suggest a compressive stress of 500 MPa for the former and 300 MPa for the latter, following the investigation and calibration undertaken by Birnie et al [102]. But this indicative stress assumes that there are no stresses within the reference sample and, more importantly, that there are no compositional effects present. The identification of some of the oxide types confirms the value of scanning LRS for investigating oxidation processes and identifying oxide types within the ferritic 9Cr-1Mo steel components.

5.3.2 Carburisation

X-ray diffraction was used to identify the phases present in two OMS samples: T01M26-495-171888 and M92M02-580-146760. The results demonstrate that the precipitates observed with different morphologies, including coarse precipitates, fine needles and large needles, were carbides, as for the autoclave HRA samples. Carbides beneath the oxide scale were quantified using FIB XeF_2 images to give with carbide area fraction. It was found that the carbide area fractions from the two OMS samples exposed at 580 °C (M92M02-580-146760 and M96M01-580-146760) exhibited a saturation state, indicating that the Cr was tied up in carbides during the long-term exposure. Considering the limited Cr content (approximately 9 wt. %) in the matrix, the carbide area fraction achieves an equilibrium at around 18.4 %, as calculated by Equation 4.5 in Chapter 4, where a saturation state was present.

The carbide area fraction of the fine needles following path 1 (5 %) at 500 µm from the fin tip was higher than that from paths 2 at 1000 µm and 3 at 1500 µm (2 %) in sample M92M02-580-146760. The fine needle carbide area fraction following all the three paths in sample M96M01-580-146760 was around 2 %, consistent with the result from the sample in breakaway initiation from autoclave HRA sample A-640-1495 (400 to 800 @ 245). The saturation state was present in both M92M02-580-146760 and M96M01-580-146760, and the carbide area fraction following three paths was higher than the saturated carbide area fraction

~17 % obtained from Section 4.2.4 Chapter 4, indicating the formation of cored carbide, with an outer layered carbide with lower Cr concentration than in the core.

Though coarse carbides were present in all three OMS samples and the A-virgin sample, the quantity and size increased with exposure temperature and time. Fine needle carbides were present in the OMS samples oxidised at lower temperature (495 °C) while large needles were present at higher temperature (580 °C). The disappearance of fine needles can be explained by either their dissolution in the metal or their growth into large needles. The cores formed in the coarse carbides in sample M92M02-580-146760 indicate the depletion of Cr in the matrix, leading to breakaway of the examined sample, following the mechanism discussed in Section 4.3.2 Chapter 4.

5.4 Conclusions

Based on the above discussion, the oxide thicknesses and morphologies are determined by the exposure conditions: temperature and time. The internal oxidation zone (IOZ) layer is mainly present in the non-breakaway and breakaway initiation oxidation stage. The presence of cracks extending radially from oxide to the fin tip and the presence of multi-layered oxide indicate that the two OMS samples exposed at 580 °C have entered the breakaway oxidation regime. Optical microscopy, SEM-EDS and scanning LRS have been combined for evaluation of the spinel and IOZ formed close to the oxide/metal interface and various types of oxide have been identified, indicating that the oxide is comprised of spinel ($Fe_{3-x}Cr_xO_4$), chromia (Cr_2O_3) or a combination of both. EDS results show that the x in $Fe_{3-x}Cr_xO_4$ is in the range 0.62-0.97, from average concentrations in a small region 20 × 10 μm in size, which is in the range of the line scan results from sample A-640-1495 (400 to 800 @ 245) 0.22-1.09, which is a breakaway initiation sample oxidised at higher temperature.

Meanwhile, the spinel exhibits a relative tensile stress compared with oxide in the IOZ. The distribution of Cr and Mo are similar, however opposite to that from Fe in both oxide and metal. Graphite with a low-degree of order was identified by Raman spectroscopy and peak intensity maps were used to show its location with a spatial resolution of approximately 1 μm. The graphite crystallite sizes are 3 and 8 nm at spots A and B, respectively, in sample M92M02-580-146760. The complexity of the oxide structure present complicated the measurement of strain in the material.

X-ray diffraction results demonstrated that the oxide formed is either Fe_3O_4 or M_3O_4 and that the precipitates embedded in the matrix are carbides. The presence of a saturation state in the carbide area fraction is determined by the exposure temperature and time, which also exacerbate the growth of carbides. FIB XeF_2 imaging illustrates the evolution of carbides.

Equilibrium coarse precipitates $M_{23}C_6$ were present in the virgin sample. The size of $M_{23}C_6$ increases during long-term low-temperature exposure (compared samples A-virgin and T01M26-495-171888) and there is evidence for the presence of fine needle M_2C in sample T01M26-495-171888. However, fine needles were absent while large needles were present. The large needles were then coarsened during exposure at higher temperature (580 °C), e.g. sample M92M02-580-146760, in which cored coarse carbide was present. Fine needle carbides were either dissolved in the parent metal to provide Cr for the growth of other precipitates or converted into large needles during the processes of oxidation and carburisation. The changes of carbides in OMS samples are the same as carbide evolution in autoclave HRA samples, indicating the same mechanism of carburisation for both OMS and autoclave HRA samples.

Therefore, the fundamental mechanisms of oxidation and carburisation of OMS ferritic 9Cr-1Mo steels are consistent with those of autoclave HRA 9Cr-1Mo steels examined in Chapter 4, based on the types of oxide and carbides identified and their similar morphologies.

Chapter 6: Comparison studies on martensitic 9Cr-1Mo steel exposed to a simulant AGR coolant gas

The oxidation and carburisation of experimental DNB martensitic 9Cr-1Mo steels (exposed to simulant coolant gas) will be discussed in this chapter. Unlike ferrite, which has a body-centred cubic structure, martensite has a body-centred tetragonal lattice structure. Optical microscopy and SEM-EDS were used for oxide observation and characterisation while scanning laser Raman spectroscopy (LRS) was used for oxide identification. Carbides were observed using FIB XeF_2 imaging. Carbide area fractions were measured and carbides were identified using XRD. One of the main purposes of this chapter is to make a comparison between autoclave exposure for HRA ferritic and DNB martensitic 9Cr-1Mo steel.

6.1 Oxide observation and oxidation characterisation

6.1.1 Samples used for oxidation analysis

Table 6-1 shows the experimental autoclave martensitic DNB samples used for oxide observation and identification and the corresponding techniques used for analysis. Experimental DNB samples in this chapter are marked as B-temperature-time, e.g. B-580-5000 represents sample DNB 8104-580 °C-5000 h (400 vppm). However, moistures apart from 400vppm are highlighted in brackets, e.g. B-600-3020 (1200) represents sample DNB 8666-600 °C-3020 h (1200 vppm). Two samples, B-640-245 in the early stages of oxidation and B-640-4887 in post-breakaway oxidation regime, were examined for elemental distribution (using optical microscopy and SEM-EDS) and oxide identification (using scanning laser Raman spectroscopy). Unlike the ferritic samples, the oxide from a pre-heat treatment, to which these martensitic samples were subjected, complicated the interpretation of the observations.

Table 6-1: Techniques used for all the autoclave DNB samples selected.

Sample ID	***Oxidation***			***Carburisation***	
	OM	*SEM*	*Raman*	*XRD*	*FIB*
B-Virgin	✓			✓	✓
B-580-5000	✓				✓
B-600-3020 (1200)	✓				✓
B-600-3835	✓				✓
B-620-3736	✓				✓
B-640-245	✓	✓	✓	✓	✓
B-640-4887	✓	✓	✓	✓	✓

6.1.2 Oxide observation and thickness measurement using optical microscopy

Figure 6-1 shows optical micrographs recorded at fin tip corners and fin sides for the autoclave DNB samples listed in Table 6-1. Unlike experimental autoclave HRA samples, the oxide at the fin sides of martensitic DNB samples exhibited a duplex morphology in the initiation of breakaway oxidation, disregarding the oxide formed from the pre-heat treatment, e.g. B-580-5000, B-600-3020 (1200) and B-640-245. In experimental DNB steels, it is known that a Cr-depletion layer exists beneath the oxide prior to exposure, according to the information provided from EDF Energy Ltd, which leads to a thin layer of oxide outside of the duplex oxide.

Samples B-580-5000, B-600-3020 (1200) and B-640-245 show duplex layer oxide at the fin sides, in which the thickness of the magnetite and spinel are roughly the same disregarding the thin layer of oxide formed outside in B-580-5000. The other examined DNB samples show a multi-layered oxide at the fin sides.

The oxide formed at the fin tip corner was analysed separately as follows:

1. Samples B-580-5000 and B-640-245 have duplex oxide at the fin tip corners. The presence of duplex oxide and the absence of cracks are indicative of non-breakaway oxidation of these two samples.
2. Multi-layered oxide was formed at the fin tip corner of samples B-600-3835 and B-620-3736. The presence of this morphology of oxide and cracks in the oxide extending radially to the fin tip corner are indicative of breakaway initiation in these samples.
3. A laminated fan-shaped oxide was present at the fin tip corner of samples B-600-3020 (1200) and B-640-4887. The presence of cracks allows gas to access the inner oxide and exacerbate the oxidation rate. These samples have entered the post-breakaway oxidation regime.

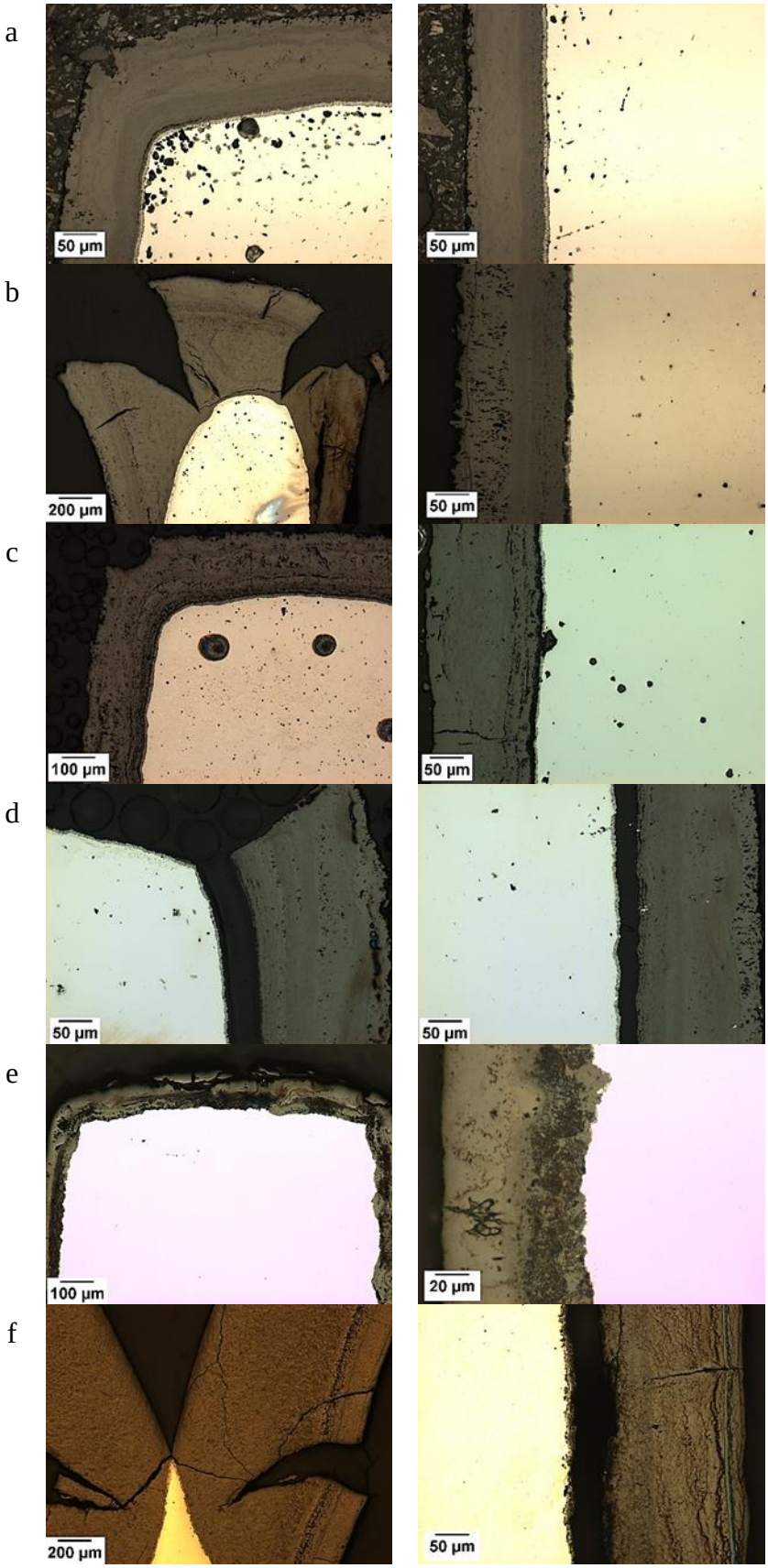

Figure 6-1: Optical micrographs at the fin tip (left) and fin side (right) of sample (a) B-580-5000; (b) B-600-3020 (1200); (c) B-600-3835; (d) B-620-3736; (e) B-640-245 and (f) B-640-4887.

The morphology of oxide formed at the fin tip corner for each sample and the corresponding oxidation regime are shown in Table 6-2. The crack present between oxide and matrix at the fin tip of sample B-620-3736 may have resulted from the mounting process. The average thickness of oxide scale at fin tip and fin side was measured in each case with the method discussed in Chapter 4. The results obtained are listed in Table 6-3. In general, the oxide thickness at the fin corner is higher than that from the fin side. A continuous IOZ layer was observed in non-breakaway (B-580-5000) and breakaway initiation (B-600-3835 and B-620-3736) samples.

Table 6-2: Oxide morphology and oxidation regime of each DNB samples.

Sample ID	*Oxide morphology at fin tip corner*	*Oxidation regime*
B-580-5000	*Duplex*	*Non-breakaway*
B-600-3020 (1200)	*Laminated fan-shaped*	*Post-breakaway*
B-600-3835	*Multi-layered*	*Non-breakaway*
B-620-3736	*Multi-layered*	*Breakaway initiation*
B-640-245	*Duplex*	*Non-breakaway*
B-640-4887	*Laminated fan-shaped*	*Post-breakaway*

Table 6-3: Average thickness (in μm) of oxide scales and the continuous IOZ layer in martensitic 9Cr-1Mo steel samples.

Samples	*B-Virgin*	*B-580-5000*	*B-600-3020 (1200)*	*B-600-3835*	*B-620-3736*	*B-640-245*	*B-640-4887*
Fin tip	*/*	*153*	*/*	*187*	*211*	*98*	*/*
Fin side	*/*	*151 ± 4*	*166 ± 5*	*160 ± 8*	*179 ± 5*	*88 ± 5*	*203 ± 8*
IOZ	*/*	*5.8 ± 0.9*	*/*	*4.5 ± 0.6*	*5.9 ± 0.9*	*/*	*/*

The discussion in Chapter 4 showed that the influence of 800 vppm moisture on the processes of oxidation and carburisation was not clear. The comparison between samples B-600-3020 (1200) and B-600-3835 shown in Figure 6-1 indicated an acceleration of oxidation with high moisture level (1200 vppm) due to the similar oxide thickness on the fin side of these two samples, despite the exposure time of B-600-3020 (1200) being about 800 h less than B-600-3835. Oxide on the fin tip of samples B-600-3020 (1200) and B-640-4887 was not measured due to the difficulty in defining the thickness of a fan-shaped oxide.

6.1.3 Oxide observation and elemental distribution from SEM-EDS

The elemental distribution of the oxide at the fin tip corner with different morphologies was determined using SEM-EDS. Samples B-640-245 and A-640-245 were exposed under the same conditions and exhibited a similar oxide thickness at the fin tip corner, as shown in Table 6-3. However, oxide at the fin side of sample B-640-245 was about 30 μm thicker than with sample A-640-245, Different production heat treatment, alloy composition and Cr-depletion may contribute to this. Therefore, an SEM-EDS line scan was used for oxide analysis at the fin tip corner of sample B-640-245 for comparison, as well as of sample B-640-4887 to compare with the laminated oxide formed in sample A-640-3883.

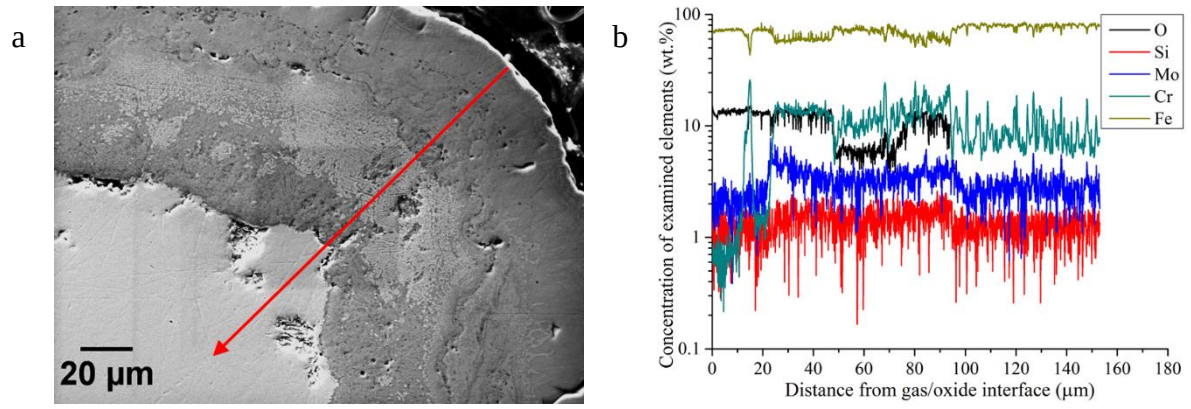

Figure 6-2: (a) SEM image on the fin tip and line scan trace; (b) concentration of elements as a function of distance from gas/oxide interface from EDS line scan from sample B-580-5000.

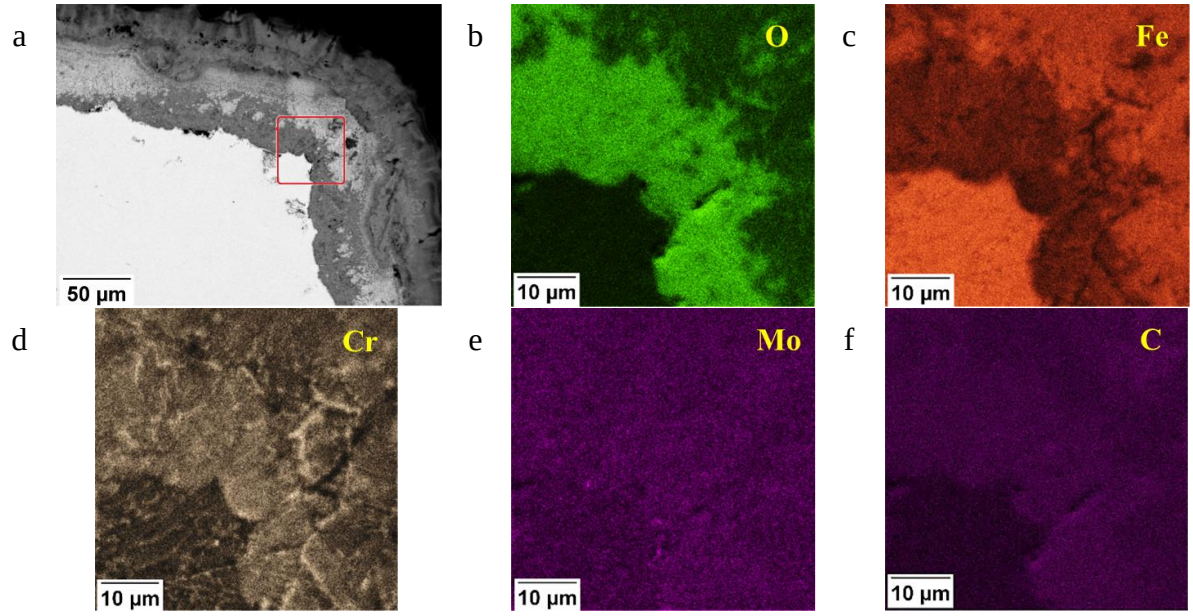

Figure 6-3: (a) SEM image on the fin tip and marked area for EDS mapping; EDS map of (b) O; (c) Fe; (d) Cr; (e) Mo; (f) C from sample B-640-245.

The oxide scale from the fin tip for the non-breakaway sample B-640-245 was examined with EDS line scanning and mapping, and the results are shown in Figure 6-2b and Figure 6-3, respectively. As discussed in Section 6.1.2, unlike the observation from ferritic HRA samples, a thin Cr-rich band was present just beneath the outermost Fe_3O_4 layer, following by a Cr-depleted layer about 10 μm thick located above the spinel layer, as shown in the Cr profile in Figure 6-2b. A 20 μm thick layer depleted in oxygen, in which Fe increased, was observed in the spinel which was not observed in HRA samples. This may result from the presence of the oxide with a higher Fe concentration, e.g. FeO, the influence from deposited carbon or a combination of them. Concentration plots of Mo in HRA samples showed a similar tendency with Cr. Locations with high levels of Cr and Mo in the matrix are indicative of the presence of carbides. The oxygen map confirmed the presence of an oxygen depletion band in the spinel layer. The Cr map (Figure 6-3d) shows that the spinel close to the oxide/metal interface keeps the structure of metal before being oxidised, in which the prior-austenite grain boundaries as

well as lath boundaries can be observed. Due to the complexity of the oxide in this sample, the spinel composition was not determined. However, the EDS map of carbon showed that there was a C,Fe-rich region in the O-depleted band, indicating that the deposited carbon led to oxygen depletion in the spinel layer.

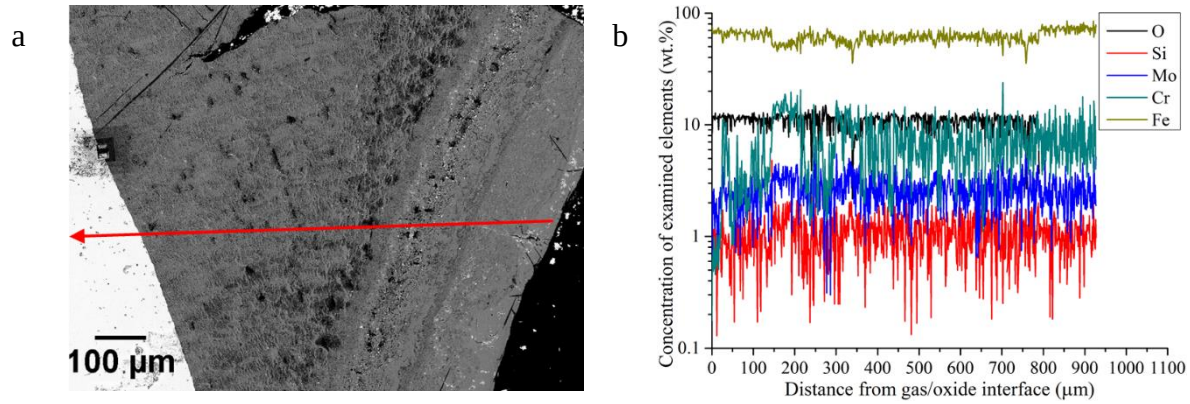

Figure 6-4: (a) SEM image on the fin tip and line scan trace; (b) concentration of elements as a function of distance from gas/oxide interface from EDS line scan from sample B-640-4887.

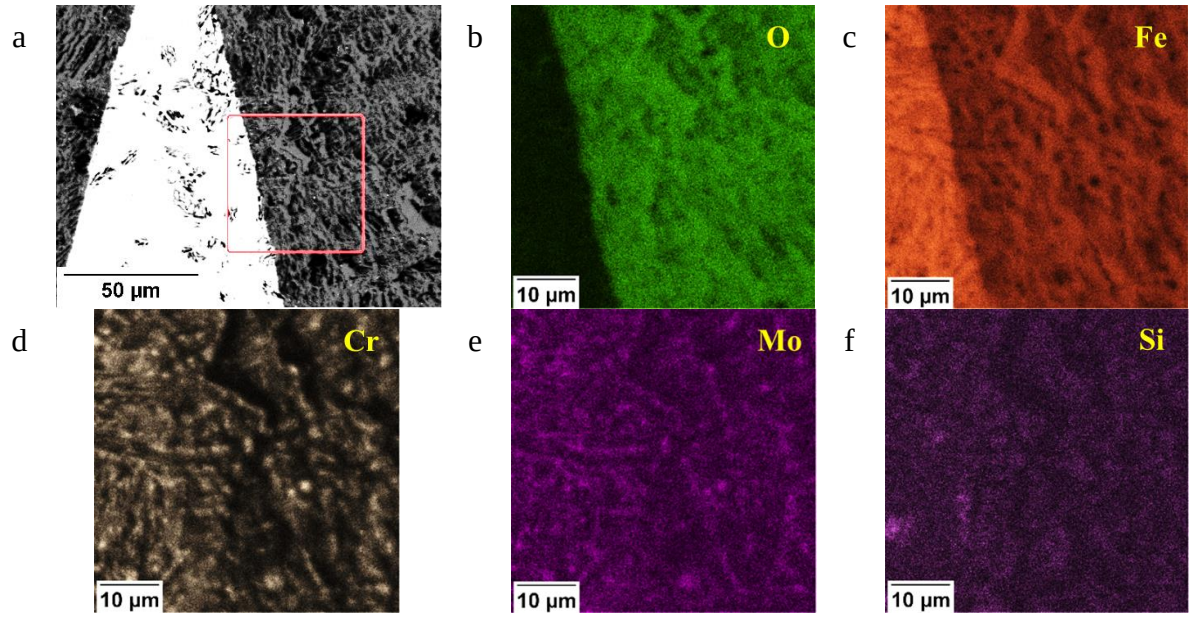

Figure 6-5: (a) SEM image on the fin tip and marked area for EDS mapping; EDS map of (b) O; (c) Fe; (d) Cr; (e) Mo; (f) Si from sample B-640-4887.

The EDS line scans and maps from the post breakaway sample B-640-4887 are shown in Figure 6-4 and Figure 6-5, respectively. The line scan result shows that a thin layer of magnetite formed at the outermost part of the examined oxide, as shown in Figure 6-4a, followed by a spinel layer beneath. A laminated oxide was inferred from the fluctuating Cr concentration. However, no Cr-rich band was observed beneath the magnetite layer in this case. The EDS map of Cr shows that the oxide close to the oxide/metal is present in a clot form comprised of Cr-rich and Cr-depleted oxide formed alternately. It is also observed from EDS maps shown in Figure 6-5 that the distribution of Mo and Si are similar to Cr but opposite to Fe. The Cr,Mo-rich

particles in the matrix correspond to carbides formed on the prior austenitic grain boundaries and lath boundaries (see section 6.2.2).

As shown in the concentration profiles in Figure 6-4b, the highest Cr level in the spinel is around 19 wt. %, which corresponds to x = 0.84 in the formula $Fe_{3-x}Cr_xO_4$. The bands with low Cr concentration correspond to Fe_3O_4, which will be further investigated with scanning laser Raman spectroscopy in the following section.

6.1.4 Oxide identification using scanning laser Raman spectroscopy

As discussed in Chapter 2, spinel is formed at the oxide/metal interface. Therefore, the oxide at this location was evaluated using scanning LRS with two samples: B-640-245 and B-640-4887. A white light image of the fin tip corner from sample B-640-245 is shown in Figure 6-6 and the evaluated region is marked as shown in Figure 6-6a. The Raman spectra of two positions A and B are shown in Figure 6-6b and c. The baseline was removed using Wire 4.3 software [106]. Two peaks present at 547 and 673 cm^{-1} in the spectrum from spot A are indicative of the presence of spinel. However, there is no evidence for the presence of deposited carbon. The spectrum from spot B contains two peaks at 557 and 671 cm^{-1} which indicates the presence of spinel. Additionally, two peaks corresponding to D and G peak from graphite are present at 1340 and 1588 cm^{-1} indicating the presence of graphite with a low-degree of order.

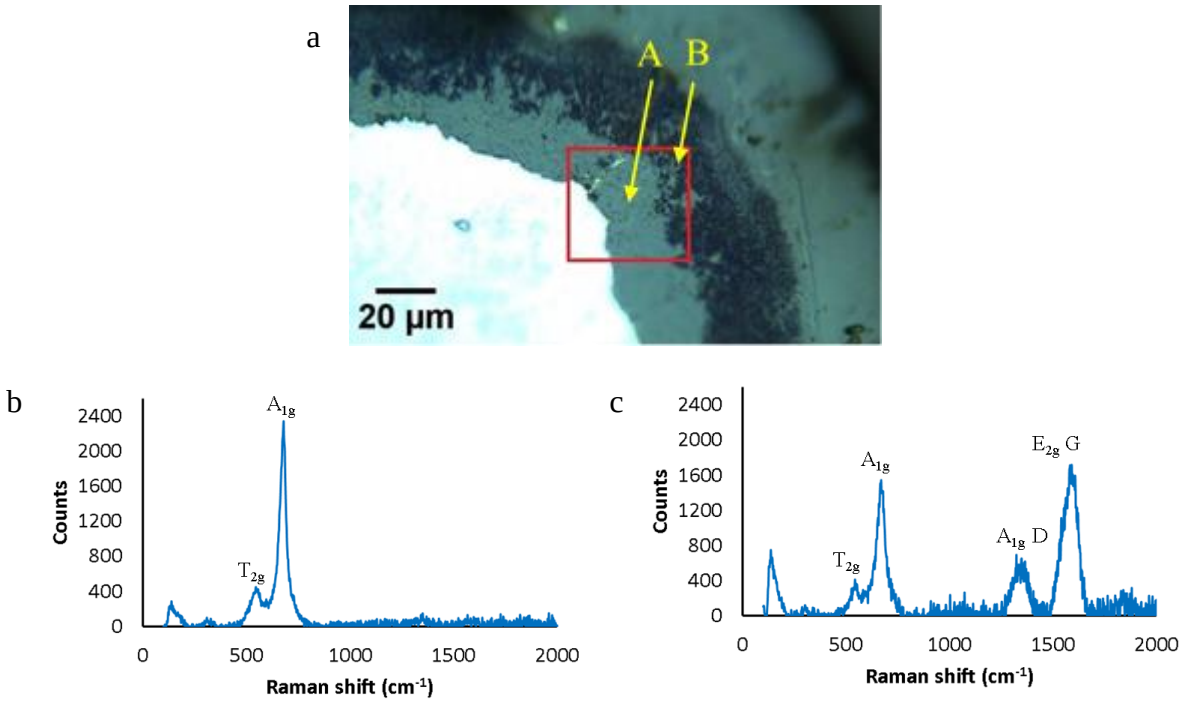

Figure 6-6: (a) White light optical micrograph of sample B-640-245 showing region mapped by Raman spectroscopy. (b) Raman spectrum from point A. (c) Raman spectrum from point B.

The intensities of the D and G peaks present in the spectrum of spot B are 921 and 1612, respectively. The crystallite size was determined via the I(D)/I(G) ratio which was 0.57, indicating a crystallite size of 7.7 nm [104][106].

Raman peak intensity maps were extracted from three peaks at 547, 670 and 1564 cm^{-1} as shown in Figure 6-7. It appears that the intensity map at 547 cm^{-1} (Figure 6-7a) has a similar distribution as to the map at 670 cm^{-1} (Figure 6-7b), both of which represent spinel. These two maps show that spinel is distributed in the whole evaluated region in the oxide. The Raman intensity map at 1564 cm^{-1} (Figure 6-7c) shows that graphite is mainly deposited in the oxide band, shown in dark in Figure 6-6a, which also corresponds to the low oxygen layer in Figure 6-2b.

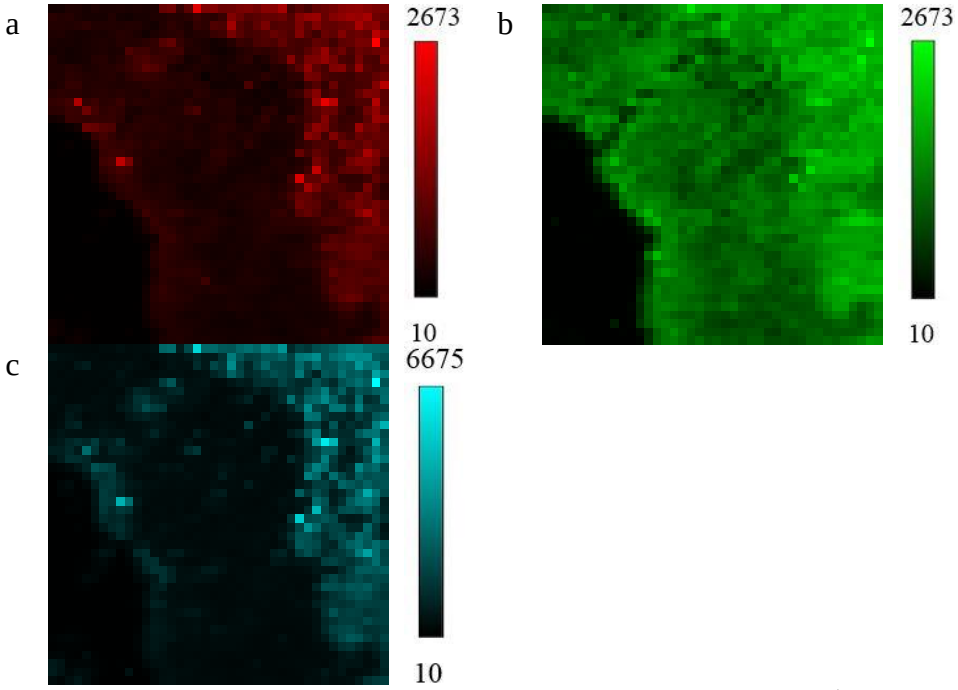

Figure 6-7: (a) Raman peak intensity map of sample B-640-245 for peaks at (a) 547 cm^{-1}; (b) 670 cm^{-1}; and (c) 1564 cm^{-1}. The intensity scale markers in counts per pixel are shown for each map.

The white light image and spectra for two positions A and B in sample B-640-4887 are shown in Figure 6-8. The spectrum from spot A shows that the oxide is mainly spinel due to the presence of a peak at 670 cm^{-1}. Two peaks which are consistent with D and G graphite are present at 1351 and 1590 cm^{-1}, indicating the presence of carbon with a low-degree of order. The presence of three peaks at 671 (A_{1g}), 540 (T_{2g}) and 307 cm^{-1} (E_g mode) in the spectrum from spot B is indicative of either magnetite or a mixture of magnetite and spinel, which corresponds to the Cr-depleted regions in the EDS map in Figure 6-5.

The D and G peaks of spot A are present at 1351 and 1590 cm^{-1}, respectively, and their intensities are 624 and 802, respectively. For spot B, the D and G peaks are present at 1350 and

1589 cm^{-1}, respectively, and their intensities are 231 and 266, respectively. The derived crystallite sizes of graphite at spots A and B are 10 and 9.1 nm, respectively.

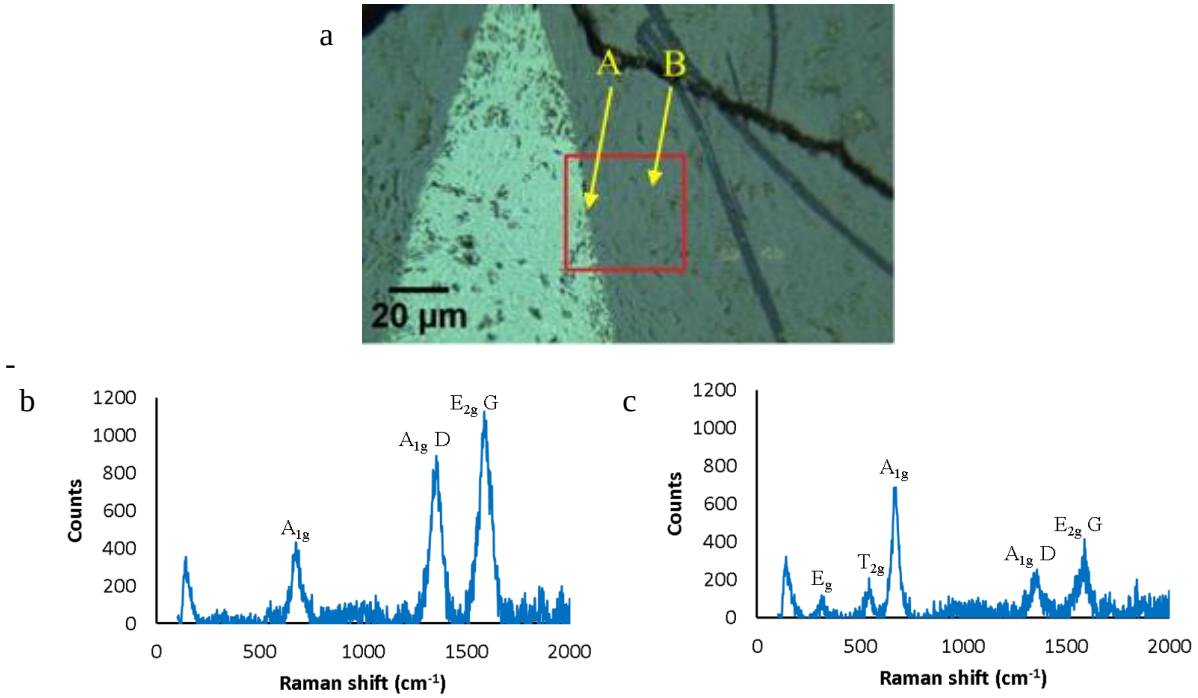

Figure 6-8: (a) White light optical micrograph of sample B-640-245 showing region mapped by Raman spectroscopy. (b) Raman spectrum from point A. (c) Raman spectrum from point B.

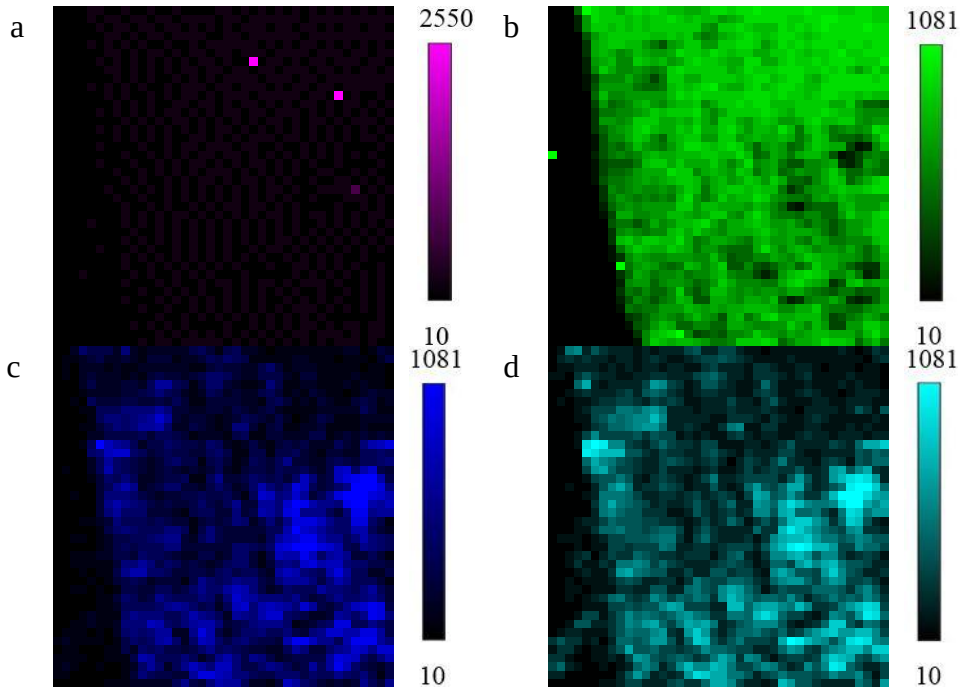

Figure 6-9: (a) Raman peak intensity map of sample B-640-4887 for peaks at (a) 306 cm^{-1}; (b) 670 cm^{-1}; and (c) 1355 cm^{-1}; and (d) 1583 cm^{-1}. The intensity scale markers in counts per pixel are shown for each map.

Raman peak intensity maps at 306, 670, 1355 and 1583 cm^{-1} are shown in Figure 6-9. The map at 306 cm^{-1} is not very clear due to the weak signal at this peak. However, a few local regions with high intensity are observed in the oxide, indicating the presence of magnetite in the spinel

layer. Graphite with a low-degree of order is distributed in the oxide, especially in those regions corresponding to the low oxygen positions.

Table 6-4 shows the Raman shift of peaks from spectra for the two locations in the two examined experimental DNB samples B-640-245 and B-640-4887. The obtained D and G peak intensities and their ratio are shown in Table 6-5.

Table 6-4: The Raman peak positions for each location examined in two selected experimental DNB samples: B-640-245 and B-640-4887.

Sample ID and examined locations		*E_g (cm^{-1})*	*T_{2g}(spinel) /A_{1g}(Cr_2O_3) (cm^{-1})*	*E_g (cm^{-1})*	*A_{1g} (spinel) (cm^{-1})*	*A_{1g} D (graphite) (cm^{-1})*	*E_{2g} G (cm^{-1})*
B-640-245	*Spot A*	*/*	*547*	*/*	*673*	*/*	*/*
	Spot B	*/*	*557*	*/*	*671*	*1340*	*1588*
B-640-4887	*Spot A*	*/*	*/*	*/*	*670*	*1351*	*1590*
	Spot B	*307*	*540*	*/*	*671*	*1350*	*1589*

Table 6-5: The D and G peak intensity, their ratio and crystallite size of graphite for each location examined in two selected experimental DNB samples: B-640-245 and B-640-4887.

Sample ID	*Location*	*Intensity*		*I(D)/I(G) ratio*	*Graphite crystallite size (nm)*
		D	*G*		
B-640-245	*Spot A*	*/*	*/*	*/*	*/*
	Spot B	*921*	*1612*	*0.57*	*7.7*
B-640-4887	*Spot A*	*624*	*802*	*0.78*	*10*
	Spot B	*231*	*266*	*0.87*	*9.1*

According to Wolf [194], a positive Raman peak shift indicates a compressive stress while tensile stress produces a negative shift. However, the peak position with A_{1g} (spinel) mode at approximately 680 cm^{-1} changes from spot A to B, caused by the change in composition, stress or a combination of both.

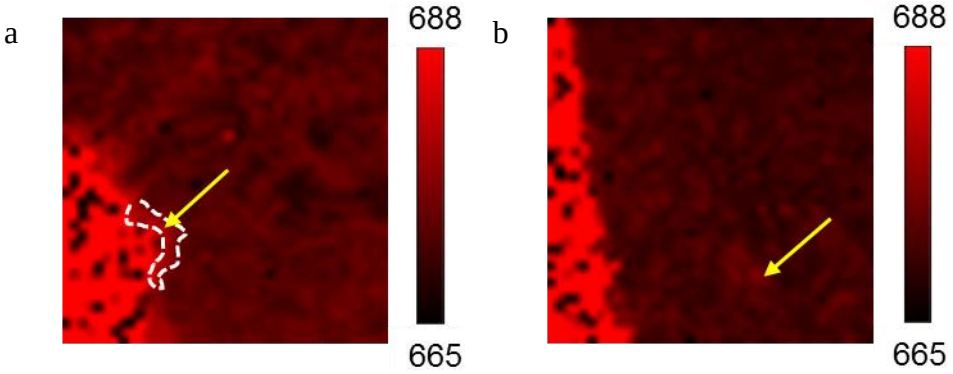

Figure 6-10: Raman peak position map at around 675 cm^{-1} from sample (a) B-640-245 and (b) B-640-4887.

Figure 6-10 shows a Raman peak position map in the range of 665-688 cm^{-1} in the examined regions from two samples: B-640-245 and B-640-4887. A higher Raman shift was observed in the oxide close to the oxide/metal interface compared with other locations in the oxide scale in sample B-640-245, as shown in Figure 6-10a, which indicates a relative compressive stress in the oxide close to the interface [194]. In some regions of oxide in sample B-640-4887, the

Raman shift is higher than other regions in the oxide scale, as shown in Figure 6-10b, indicating a relative compressive stress in these regions.

6.2 Carbide observation and carburisation characterisation

6.2.1 Samples used for carburisation analysis

Samples B-virgin, B-640-245 and B-640-4887 were analysed using FIB for carbide observation and XRD for carbide identification. The FIB XeF_2 images were processed with ImageJ software to obtain the carbide area fraction, defined as the ratio between the total area of carbide and the whole examined region. The carbide area fractions were measured from all the samples listed in Table 6-1.

6.2.2 Carbide observation and area fraction calculation

The three evaluated DNB samples, B-virgin, B-640-245 and B-640-4887, were analysed using the FIB XeF_2 imaging technique and the results are given in Figure 6-11, which shows clearly that the precipitates embedded in the matrix were mainly formed along the prior austenitic grain boundaries and lath boundaries.

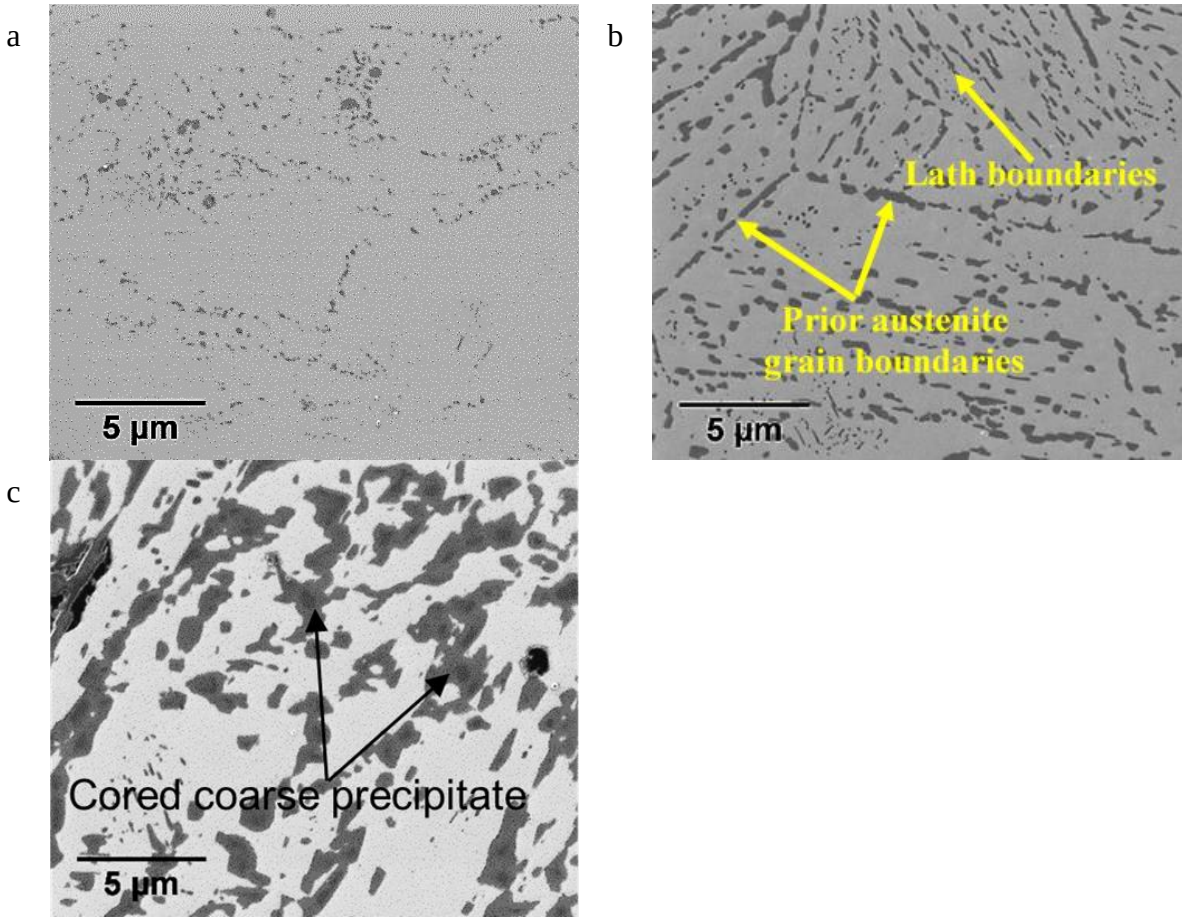

Figure 6-11: FIB XeF_2 images close to oxide at the fin sides about 500 µm from the fin tips in samples (a) B-virgin; (b) B-640-245 and (c) B-640-4887.

Coarse precipitates were observed in all three examined samples. Needle-like precipitates were also observed in the matrix, mainly distributed along lath boundaries and between laths as shown in Figure 6-11b and c, and it is difficult to distinguish them from each other. Cored coarse precipitates were observed in the breakaway sample B-640-4887 and showed different contrast between the inner core and the outer layer precipitate, as in Figure 6-11c. These precipitates can be identified with XRD, as well as other phases present in the matrix.

6.2.3 Carbide identification using XRD

The results from XRD shows phases present in the samples analysed. The results are shown in Figure 6-12. The only phase detected in B-virgin is α-Fe, which is also the main phase in 9Cr-1Mo steels. This phase was also detected in the other two samples, B-640-245 and B-640-4887. Omitting peaks from α-Fe, a peak from $M_{23}C_6$ was detected overlapping with the peak from α-Fe (110) in sample B-640-245. However, no peaks were present from oxide, probably due to its thin layer nature. In the XRD spectrum from sample B-640-4887, $M_{23}C_6$ was detected, together with oxide (Fe_3O_4 and M_3O_4). Luo [216] studied martensite with XRD and found that the peaks of planes (200) and (211) were present at 64 ° and 84 °, respectively. However, the peaks in this investigation were present at about 65 ° and 82 °, which correspond to the (200) and (211) planes of ferrite, respectively.

a

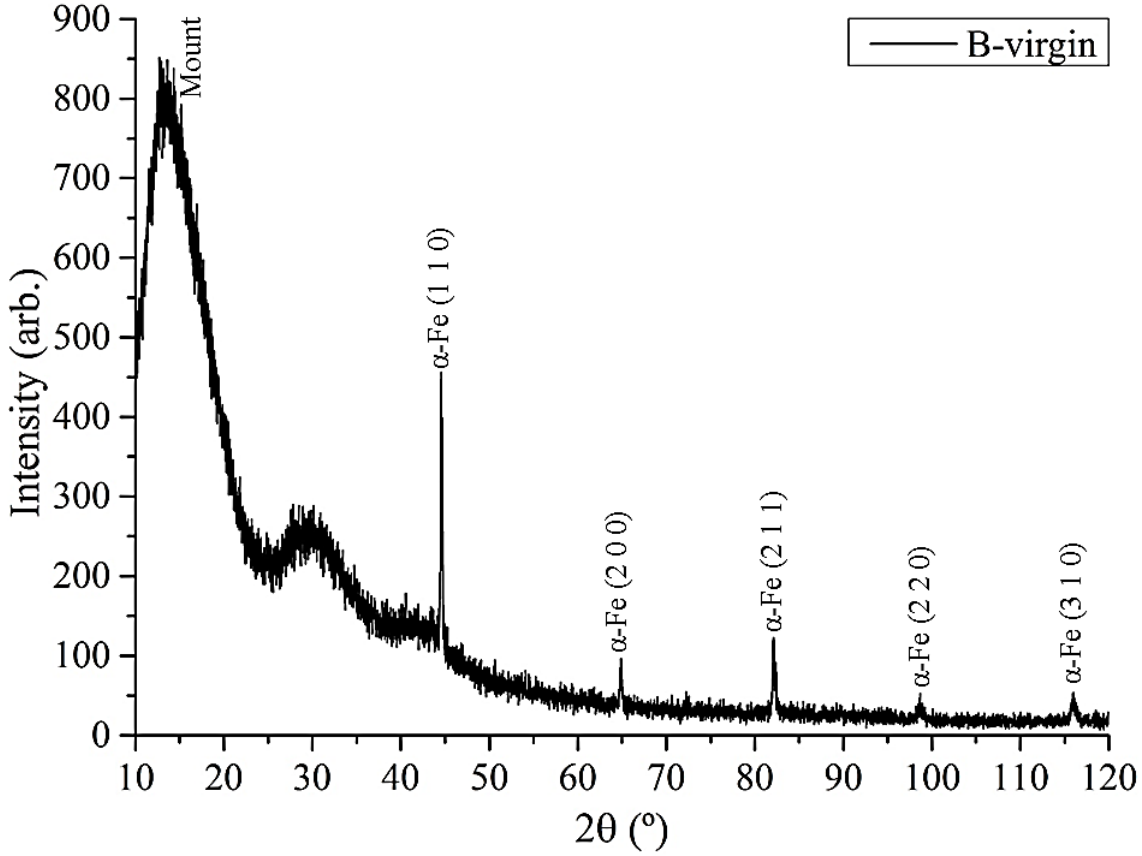
B-virgin
Mount
α-Fe (1 1 0)
α-Fe (2 0 0)
α-Fe (2 1 1)
α-Fe (2 2 0)
α-Fe (3 1 0)
Intensity (arb.)
2θ (º)

b

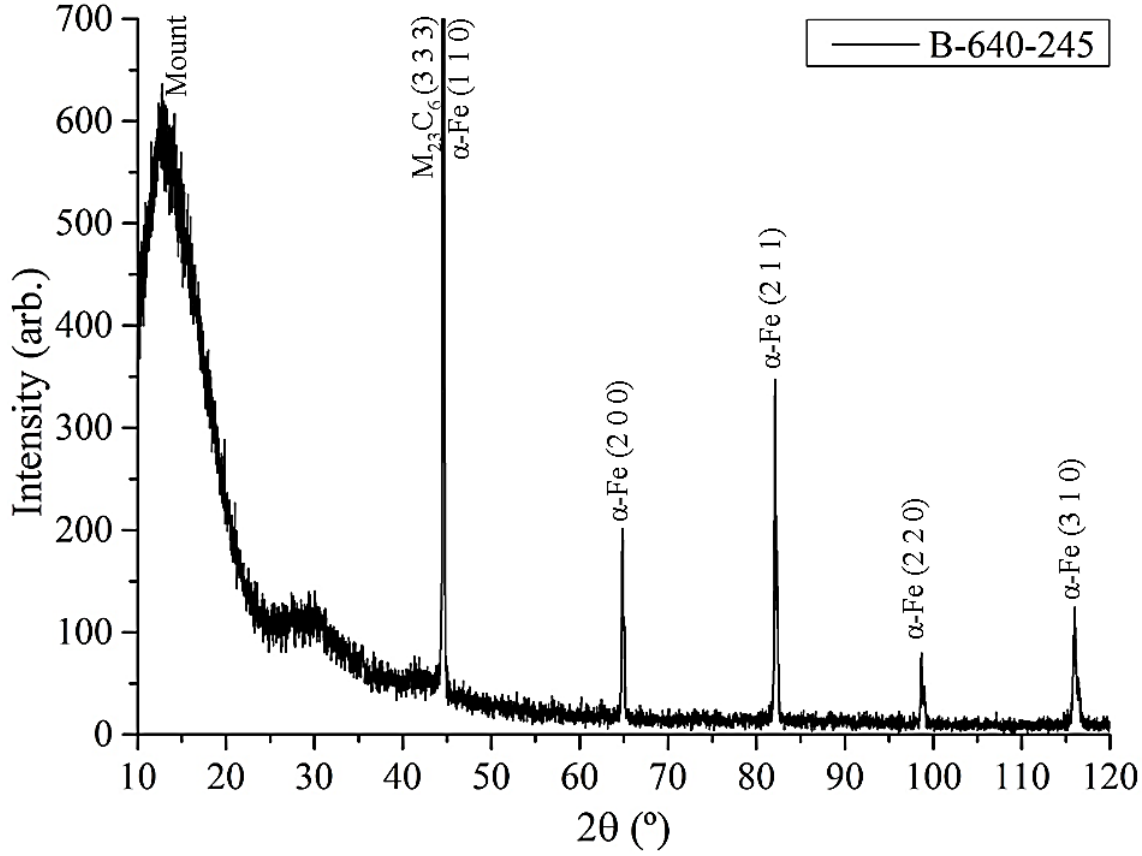
B-640-245
Mount
M23C6 (3 3 3)
α-Fe (1 1 0)
α-Fe (2 0 0)
α-Fe (2 1 1)
α-Fe (2 2 0)
α-Fe (3 1 0)
Intensity (arb.)
2θ (º)

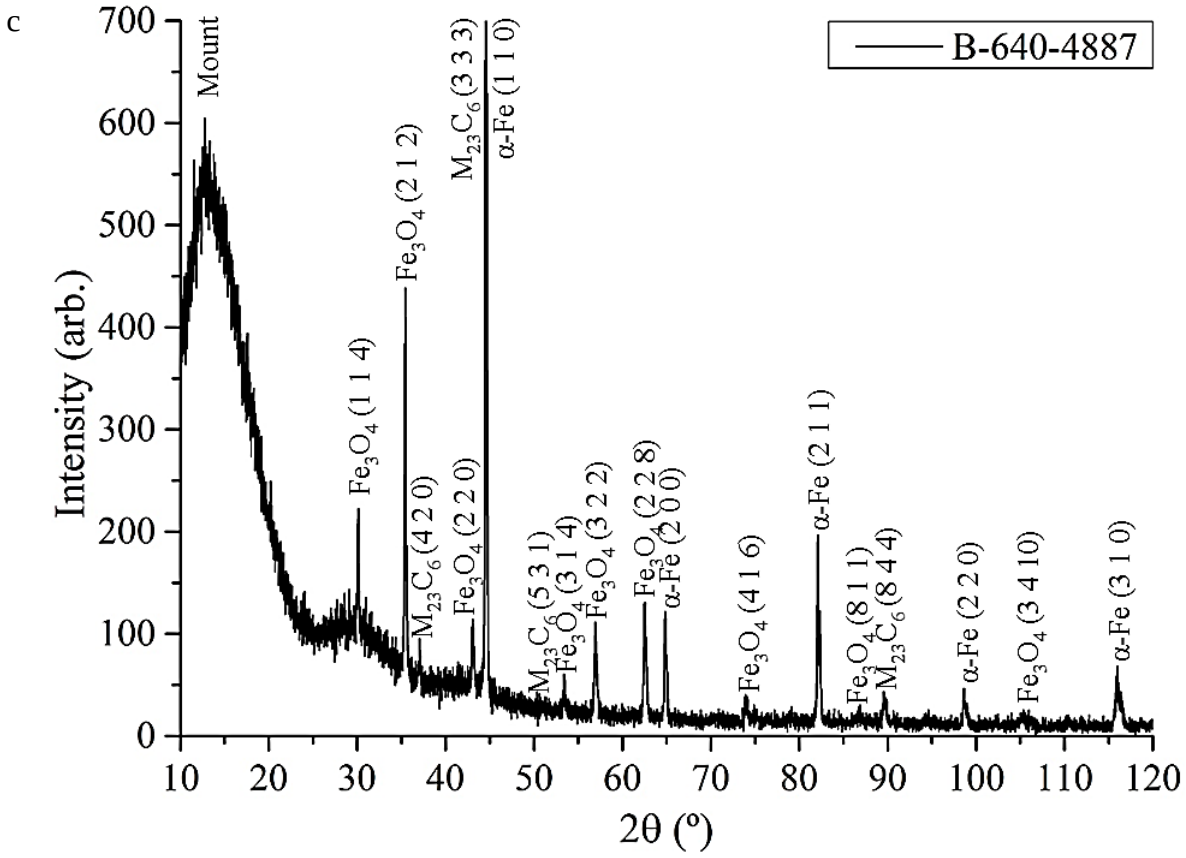

Figure 6-12: XRD results of the three examined samples (a) B-virgin; (b) B-640-245; (c) B-640-4887.

The reason for the unexpected absence of peaks from martensite may be that the martensite converted into ferrite during the pre-heat treatment and exposure to the simulant coolant gas. Therefore, the observed microstructure of samples from DNB can be summarised as ferrite with lath boundaries in the grains.

From XRD analysis, $M_{23}C_6$ is the predominant carbide. Therefore, most carbides formed along prior-austenitic grain boundaries and lath boundaries are $M_{23}C_6$ in the breakaway sample B-640-4887.

6.2.4 Carbide area fraction calculation

Carbides identified using XRD have been quantified by carbide area fraction. Plots of carbide area fraction versus distance from oxide/metal interface following the three paths of FIB imaging (Figure 4-26) are shown in Figure 6-13.

The area fractions from B-virgin sample range from 3.5 to 6.5 %, which is the lowest carbide area fraction that can be obtained from an un-carburised region in exposed DNB samples. A saturation state in which there is a similar area fraction at the fin side and fin centre was present in the samples exposed at high temperature and/or with long time. It appears that the saturation

area fraction was ~19 % see Figure 6-13. Sample B-580-5000 exhibits lower area fractions than B-600-3835, especially at the fin centre, due to the lower temperature.

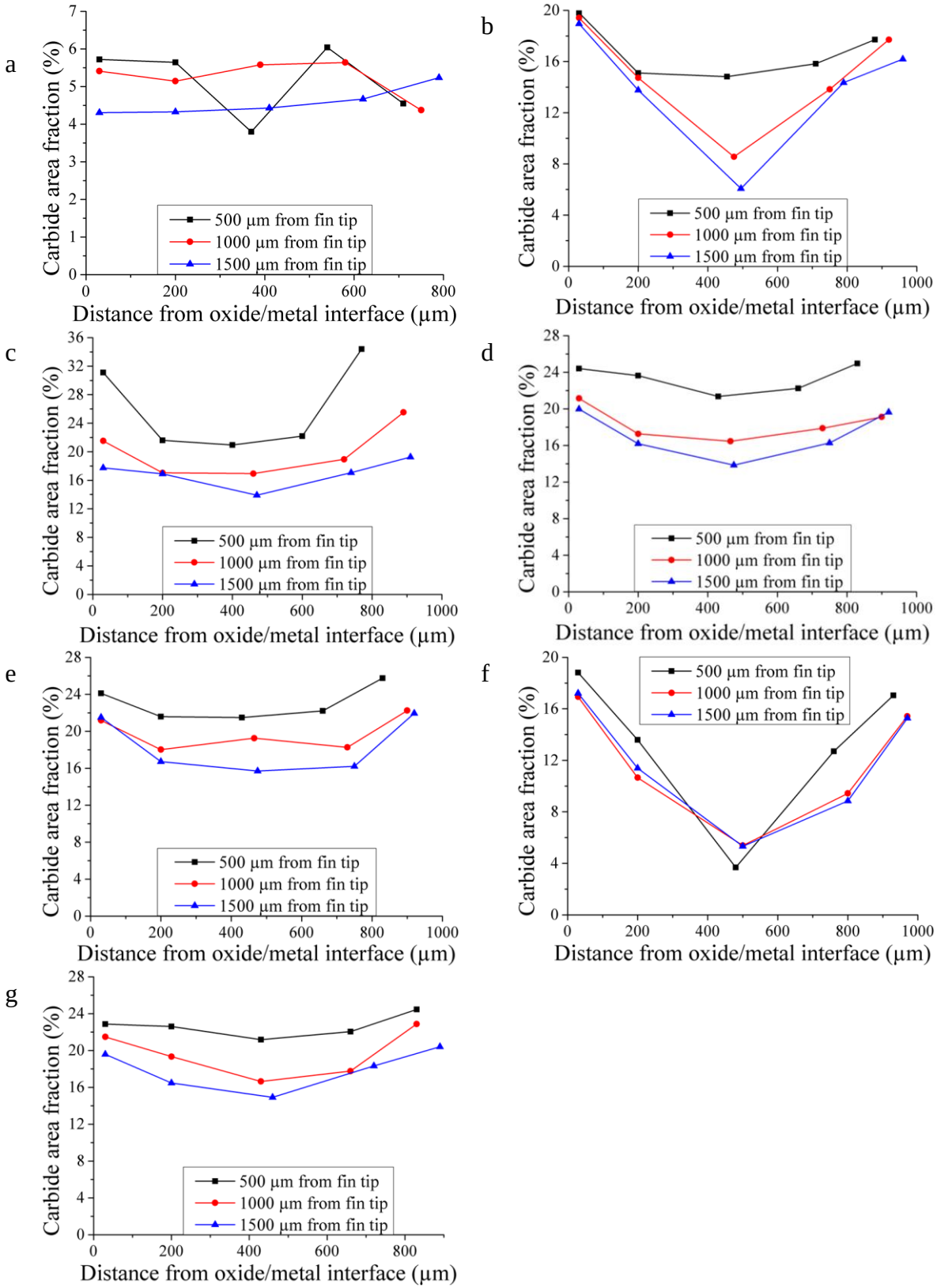

Figure 6-13: Carbide area fraction vs distance following three paths from sample (a) B-virgin; (b) B-580-5000; (c) B-600-3020 (1200); (d) B-600-3835; (e) B-620-3736; (f) B-640-245; and (g) B-640-4887.

The plots in Figure 6-13 show that the area fraction at the fin side following path 1 in sample B-600-3020 (1200) is higher than that from B-600-3835 exposed with 400 vppm moisture. This indicates that high moisture accelerates the process of carburisation. Ehlers' et al. [217] found that higher water content enhanced the oxidation rate, which means that the higher water content reduces the TTB as well as the time for crack formation, which provides the access for CO_2 to the inner oxide and metal, thereby exacerbating the diffusion of carbon (produced by the Boudouard reaction) to the bulk metal. This indicates that the higher water content exacerbates the process of carburisation.

The carbide area fractions at the fin side following path 1, as shown in Figure 4-26, from samples B-640-245 (Figure 6-13f) and A-640-245 (Figure 4-48a) ranged from 16 to 19 % and 13 to 15 %, respectively. A higher area fraction was obtained in the martensitic steel, indicating easier penetration of CO_2 into the matrix than with the ferritic steel. However, it may be also caused by the higher Cr concentration in the ferritic steel (9.2 wt. %) than the martensitic steel (8.6 wt. %), as shown in Table 3-1.

6.3 Discussion

6.3.1 Oxidation

Optical micrographs show that duplex oxide was formed in the early stage of oxidation for these martensitic microstructure steel samples, apart from the oxide formed during pre-heat treatment at the fin side, as shown in Figure 6-1a b and e. However, multi-layered oxide was formed at the fin side of other samples shown in Figure 6-1. The oxide morphologies at the fin tip corner followed models of duplex, multi-layered and laminated oxide growth as discussed in Chapter 4: (1) The non-breakaway samples B-580-5000 and B-640-245, which are in the early stage of oxidation, showed a duplex oxide at this location; (2) samples B-600-3835 and B-620-3736 have entered breakaway initiation, inferred from the presence of cracks extending radially toward the fin corner, together with the multi-layered oxide; (3) oxide at the fin corner of samples B-600-3020 (1200) and B-640-4887, which had entered the post breakaway regime, exhibited a laminated morphology. These confirm the feasibility of the three models of oxide formation established with respect to the process of oxidation shown in Figure 4-52. Although the morphologies of oxide from martensitic 9Cr-1Mo DNB samples are more complicated than from HRA samples, the oxidation of martensitic steels should follow the same mechanisms as for ferritic steels from HRA as shown in Figure 4-51, due to the similar oxide types and morphologies, apart from those oxides formed during pre-heat treatment. The continuous IOZ observed in non-breakaway and breakaway initiation samples is consistent with the results from Chapter 4, which is also evidence that HRA and DNB samples follow the same mechanisms of oxidation.

Optical micrographs show that B-600-3020 (1200) has entered the post-breakaway regime while B-600-3835 is in breakaway initiation. This suggests that a very high moisture level, 1200 vppm, exacerbates breakaway oxidation, which was not found from the HRA samples exposed to CO_2-based gas with a moisture level of 1200 vppm.

The two samples, B-640-245 subject to non-breakaway oxidation and B-640-4887 in the post-breakaway oxidation regime, were analysed with EDS line scan and mapping. The results show that sample B-640-245 which is in the early stage of oxidation has a complicated oxide. A thin layer of magnetite followed by a very thin Cr-rich band was formed possibly during pre-heat treatment. Then another thin layer of magnetite followed by spinel was formed during exposure to CO_2 simulant coolant gas. The EDS map of Cr shows that prior-austenitic grain boundary and lath boundaries can be clearly observed in the spinel formed close to the oxide/metal interface. The Cr-rich locations in the matrix correspond to the carbides. According to the concentration profiles of sample B-640-4887, a multi-layered oxide was formed beneath a thin layer of magnetite, followed by a laminated oxide in which Cr-rich and Cr-depleted spinel were formed alternately due to the fast-growing oxide during breakaway oxidation. EDS maps show that the distribution of Mo and Si was similar to Cr but opposite to Fe.

Scanning LRS was adopted to identify the type of spinel in the samples. The Raman peaks at 673 and 547 cm^{-1} were assigned to A_{1g} and T_{2g} symmetries respectively in spinel [94]. Cr_2O_3 was not detected in the non-breakaway DNB sample, probably due to the lack of an IOZ layer at the fin tip corner in sample B-640-245. There was no evidence of deposited carbon at spot A, about 10 µm from the oxide/metal interface. The Raman spectrum from spot B showed that the oxide in this location is comprised of magnetite, which is inferred from the peak at 671 cm^{-1} in A_{1g} mode [94][83], as well as deposited carbon with low-degree of order in the form of graphite. The crystallite size of graphite in spot B determined by I(D)/I(G) was 7.7 nm [104][106].The oxide was mainly comprised of spinel, based on Figure 6-7b. According to the peak intensity map at 1564 cm^{-1}, the deposited carbon (graphite) is mainly distributed in the dark band in the white light image.

The Raman spectrum from spot A in the post-breakaway sample B-640-4887 comprised Cr-rich oxide, and has been identified as spinel due to the presence of the peak at 670 cm^{-1} corresponding to A_{1g} symmetry [94] although the exact composition is difficult to confirm due to the influence of stress. The material at spot B is identified as magnetite due to the presence of peaks at 306, 543 and 670 cm^{-1}, corresponding to A_{1g}, T_{2g} and E_g symmetries, respectively [95]. The Boudouard reaction occurs when CO_2 diffuses into the oxide, leading to the formation of deposited carbon. Therefore, low-degree order carbon in the form of graphite was present in

both spots A and B. The crystallite size of graphite is 10 nm in spot A and 9.1 nm in spot B, as determined by I(D)/I(G) [104][106].

6.3.2 Carburisation

Precipitates embedded in the matrix were observed and identified using FIB and XRD. Coarse precipitates were present in all the examined samples from DNB including the virgin sample. Needle-shaped precipitates were present in the non-breakaway sample B-640-245 while both needles and cored coarse precipitates were present in the post-breakaway sample B-640-4887. The coarse precipitates were formed along both prior-austenite grain boundaries and lath boundaries. However, it was difficult to distinguish the needle-shaped precipitates along lath boundaries and in the regions between boundaries. To identify these precipitates, XRD was used to reveal the phases present. The coarse precipitates were expected to be $M_{23}C_6$, which is the predominant carbide in martensitic 9Cr1Mo steels [218][219]. The needle shaped carbides were expected to be either M_2C, MC or $M_{23}C_6$ according to the results of the ferritic 9Cr-1Mo steel in Chapter 4. However, M_2C and MC carbides were not detected in the XRD analysis. Therefore, the needle-shaped precipitates are thought to be $M_{23}C_6$ carbides formed along lath boundaries. There was no peak detected from carbide precipitates in sample B-virgin, probably due to the small size and low quantity of carbides. Considering the unlimited ingress of CO_2 and, hence, carbon provided from the Boudouard reaction, the lack of Cr is the main reason for the formation of cored precipitates during the process of carburisation. The formation of carbides tied up Cr in the matrix, leading to the reduction of Cr concentration. A saturation state was present in the plot of carbide area fraction as a function of distance to the oxide/metal interface. The reduction of Cr resulted in insufficient Cr for the formation of Cr-rich $M_{23}C_6$. Therefore, Fe-rich $M_{23}C_6$ formed surrounding the Cr-rich $M_{23}C_6$, resulting in the formation of the cored carbides.

The carbide area fractions from the B-virgin sample were in the range of 3.5-6.5 %, which is consistent with the lowest value obtained from the fin centre of samples B-580-5000 and B-640-245. This represents the pre-carburised zone at the fin centre of these two samples. The carbide data illustrate that the area fraction increases with the increase of exposure temperature, time and moisture. A saturation state is present when the carbide area fraction at the fin centre achieves approximately 17 % and keeps increasing during breakaway oxidation due to the formation of cored carbides, based on the observation from experimental results. As shown in Table 3-1, the Cr concentration of the DNB virgin sample is 8.6 wt. %, which can be used in the Equation 6.1 to calculate the value of the saturation state. Assuming that the Cr content (Cr wt. %) of carbides in B-virgin is the same as that in A-virgin, which is approximately 50 wt. %, the theoretical saturation area fraction is about 17.2 %, by Equation 6.1, which is

close to the experimental result of 17 %, as observed from the plots of carbide area fraction shown in Figure 6-13. The Cr content in B-virgin is about 8.6 wt. %, as shown in Table 3-1.

$$Cr\ wt.\% \times saturation\ carbide\ area\ fraction = 8.6\ wt.\% \qquad 6.1$$

6.4 Conclusions

There is a consensus that exposure temperature and time exacerbate the processes of oxidation and carburisation. However, the influence of 800 vppm moisture was not clear, as discussed in Chapter 4. 1200 vppm moisture was found to accelerate the processes of oxidation and carburisation of martensitic material in this chapter. Disregarding the outer layer oxide formed in pre-heat treatment, the process of oxidation of DNB samples follows the same mechanism and models discussed in Figure 4-51. The oxide is identified as spinel from the non-breakaway sample and retains the microstructure from the metal being oxidised. The oxide from samples in post-breakaway is comprised of Cr-rich and Cr-depleted oxide, identified as spinel and magnetite respectively. Therefore, the fast-growing oxide resulting from breakaway is comprised of spinel and magnetite in a laminated morphology. The distribution of Mo and Si is found to correlate with Cr but to be opposite to Fe in both non-breakaway and post-breakaway stages. Furthermore, the deposited graphite is present in the duplex oxide from non-breakaway samples as well as the laminated oxide from post-breakaway samples.

The exposure temperature, time and moisture are also found to have positive correlation with carburisation. The area fractions increase with the increase of these three factors. The carbide area saturation state is present at about 19 %. Assuming the Cr concentration of the coarse carbides from DNB is also 50 wt. %, the saturation area fraction can be obtained following Equation 4.5, with the result being 17.2 %, which is close to the experimental observation. The comparison of area fraction between DNB and HRA samples exposed in the same condition suggests that the ferritic microstructure is more protective than the martensitic microstructure. The coarse carbides identified as $M_{23}C_6$ grow larger with the increase of carburisation. Cored carbides are formed in breakaway samples due to the limited Cr concentration in the steels.

Based on the investigation in this chapter, the fundamental mechanisms of oxidation and carburisation of martensitic 9Cr-1Mo steels are consistent with those of HRA ferritic 9Cr-1Mo steels examined in Chapters 4 and 5, in terms of the morphologies and types of oxide (spinel) and carbides identified ($M_{23}C_6$).

Chapter 7: Discussion

The aim of this chapter is to consider the mechanisms of oxidation and carburisation of 9Cr-1Mo steels and explore the initiation of breakaway based on the results empirically obtained from Chapters 4, 5 and 6. Comparative experiments were performed on experimental ferritic 9Cr-1Mo samples oxidised in an autoclave with a simulant AGR coolant gas and within the AGR environment, as discussed in Chapters 4 and 5, respectively. Another comparison was made between experimental ferritic HRA 9Cr-1Mo samples and martensitic DNB samples, which were both exposed in an autoclave with a simulant AGR gas in Chapters 4 and 6, respectively. We will discuss: (1) the mechanism for multi-layered oxide formation; (2) the influence of other factors; (3) the identification of different types of oxide and carbides formed in different stages of oxidation and carburisation.

7.1 Mechanisms of oxidation and carburisation

Three morphologies of oxide formed during oxidation can be seen observed in Figure 4-51, illustrating oxide growth in non-breakaway, breakaway initiation and post-breakaway stages, as well as the carbides formed in each stage during exposure to a hot CO_2-based gas. The Boudouard reaction provides both the oxidant for the process of oxidation and the carbon for the process of carburisation. The morphology of the oxide changes from duplex in the early stage, which follows sub-parabolic kinetics, to multi-layered in breakaway initiation samples, and eventually to laminated oxide in the post-breakaway samples, which follow linear kinetics in their plots of weight gain versus exposure time. The oxide thickness at the fin side of experimental HRA samples exposed within the simulant AGR environment at 640 °C was plotted against exposure time in Figure 4-7b. It follows sub-parabolic kinetics in non-breakaway oxidation and linear kinetics in post-breakaway oxidation, with a transition period for breakaway initiation oxidation.

A comparison of experimental ferritic steels, as shown in Figure 4-5b and Figure 5-2a, illustrates that thicker and more layers of oxide were formed in the sample exposed at low temperature for a longer time. Figure 7-1 shows a schematic illustrating the evolution of oxide from the start of oxidation to multi-layered formation, together with the variation of local Cr concentration. It is proposed that multi-layered oxide is formed by the following five processes:

1. A block of steel is initially surrounded by CO_2-based gas. There is no oxide present at this stage, as shown in Figure 7-1a. However, equilibrium coarse $M_{23}C_6$ carbides produced by the pre-heat treatment were observed in the virgin sample.

2. At the early stage of non-breakaway oxidation, a thin layer of Cr-rich oxide, e.g. spinel, is formed in a CO_2-based coolant gas, as shown in Figure 7-1b. Newcomb et al. [73] and Stobbs et. al. [74] studied the oxidation of Fe-Cr steels and found that this thin layer of Cr-rich oxide was present before the formation of duplex oxide. It leads to an Fe-rich (Cr-depleted) region beneath, producing a gradient of Fe between the metal and gas/oxide interface. The Fe therefore diffuses outward through the Cr-rich oxide, forming Kirkendall voids at the oxide/metal interface [220].
3. The Fe-rich oxide Fe_3O_4 is formed at the gas/metal interface by the reaction between Fe cations and CO_2. Spinel is formed at the oxide/metal interface due to its lower mobility of Cr than Fe [221]. The fresh spinel is formed at cavities generated by the accumulation of Kirkendall voids formed by the outward diffusing of Fe, as shown in Figure 4-51a. This is the so-called Kirkendall diffusion effect in which voids are formed due to the difference in diffusion rates between the two metal (Fe and Cr) cations [222]. A duplex oxide is formed in this process as shown in Figure 7-1c. The original metal surface becomes the magnetite/spinel interface at this stage (non-breakaway oxidation), in which the oxide layer growth follows sub-parabolic kinetics, as shown in Figure 4-7a. A continuous IOZ layer can be observed beneath the duplex oxide in Figures 4-4a, b and Figure 4-5a, with a combined oxide thickness as given in Table 4-4. A Cr-depleted region is formed beneath the IOZ layer due to the consumption of Cr in the formation of spinel as well as carbides in the bulk metal. CO_2 gas diffuses in during the process of oxidation and the carbon is produced by the Boudouard reaction, as described by Equation 2.3 which subsequently reacts with Fe and alloying elements, e.g. Cr, to form carbide precipitates. Fine needle M_2C and coarse carbide $M_{23}C_6$ are formed with the carbon diffusing in the grains while only coarse carbide $M_{23}C_6$ is formed along the grain boundaries (see Figure 4-27 and Figure 4-43). The formation of these carbides ties up Cr in the bulk metal leading to a decrease of Cr available, by comparing the Cr level in the matrix as shown in Figure 4-32, Figure 4-34, Figure 4-36 and Figure 4-39. The Cr content in the matrix below the Cr-depleted region is thereby reduced to < 9 wt. % (see Figure 4-34) due to the growth of duplex oxide and the formation of carbides. The graphite deposited in the oxide is also produced by the Boudouard reaction (see Equation 2.3).
4. When Cr reduces to below a certain level, a new duplex oxide layer, including magnetite and spinel, is formed beneath the previous duplex oxide. The new pair of oxide layers is formed at the oxide/metal interface. The time for the beginning of the four-layered oxide formation (the end of duplex oxide) is defined here as time to breakaway (TTB). Breakaway initiation is a transition period between non-breakaway and post-breakaway with the formation of multi-layered oxide. Magnetite is formed in the Cr-depleted region while spinel is formed in the bulk metal beneath this region, as shown in Figure 7-1d. It is worth noting that a spinel layer is always present at the oxide/metal interface rather than magnetite, indicating that new layers are formed in pairs. The oxide growth still follows sub-parabolic kinetics. A discontinuous IOZ layer is present in this stage of oxidation, as shown in Figure 4-4c and Figures 4-5b, c. Fresh spinel is formed at the IOZ/metal interface. The Cr concentration in the bulk metal is further reduced compared with that beneath

duplex oxide. A Cr depleted region is also formed during the formation of this second two-layer oxide but thinner than that beneath the duplex oxide.

5. This process repeats to form a six-layer, eight-layer and multi-layer oxide until the Cr concentration reduces to 5 wt. % (see Figure 4-36) in the ferrite matrix below the Cr-depleted region, at which point breakaway occurs, as shown in Figure 7-1e, and after which the growth of oxide follows linear kinetics. Multi-layered oxide for samples oxidised at 580, 600, 620 and 640 °C are formed at approximately 147, 20, 3 and 2 kh respectively. More cored carbide precipitates are formed beneath the multi-layered oxide. The size of the large needles increases while their quantity is reduced at the TTB. The IOZ disappears at this stage of oxidation due to the fast growth of oxide, which gives insufficient time for IOZ formation. Cored carbides $M_{23}C_6$ are observed, leading to Cr reduction in the bulk metal, as well as large needles MC. The carbides convert into spinel and metal converts into magnetite, as shown in Figure 4-13d and Figure 4-15d, during the transition from sub-parabolic kinetics to linear kinetics after TTB, as well as the stage following linear kinetics.

Martensitic 9Cr-1Mo steel samples follow the same mechanism for the multi-layered oxide formation in general. There may be some difference in the time for layer formation and the thickness of layers due to the different microstructure between ferrite and martensite.

It is interesting to note that the layer pairs become thinner and thinner as the oxidation process progresses. Take M92M02-580-146760 for example. Figure 5-2a shows that the thickness of the oxide layer pairs decrease from the outermost magnetite layer to the inner oxide layer. This observation indicates that new pairs of oxide are formed faster but the thickness becomes thinner, thereby the time for the new duplex oxide formation becomes shorter than the previous ones during the process of multi-layered oxide formation. It is seen that the Cr concentration in the matrix from virgin experimental steel (9 wt. %, as shown in Figure 4-32) reduces in the steel with multi-layered oxide formed at TTB (5 wt. %, as shown in Figure 4-36). It is assumed that a new pair of layers formed when the Cr concentration in the Cr-depleted region reached 5 wt. %, which is considered as the critical Cr concentration for the new pair of oxide formation. The time decreases for the Cr concentration in the depleted region to reduce to 5 wt. %, which leads to the thickness decreasing for the new pair of oxides. Therefore, when the Cr concentration reduces to less than 5 wt. %, post-breakaway oxidation occurs and there is a different mechanism of oxide formation.

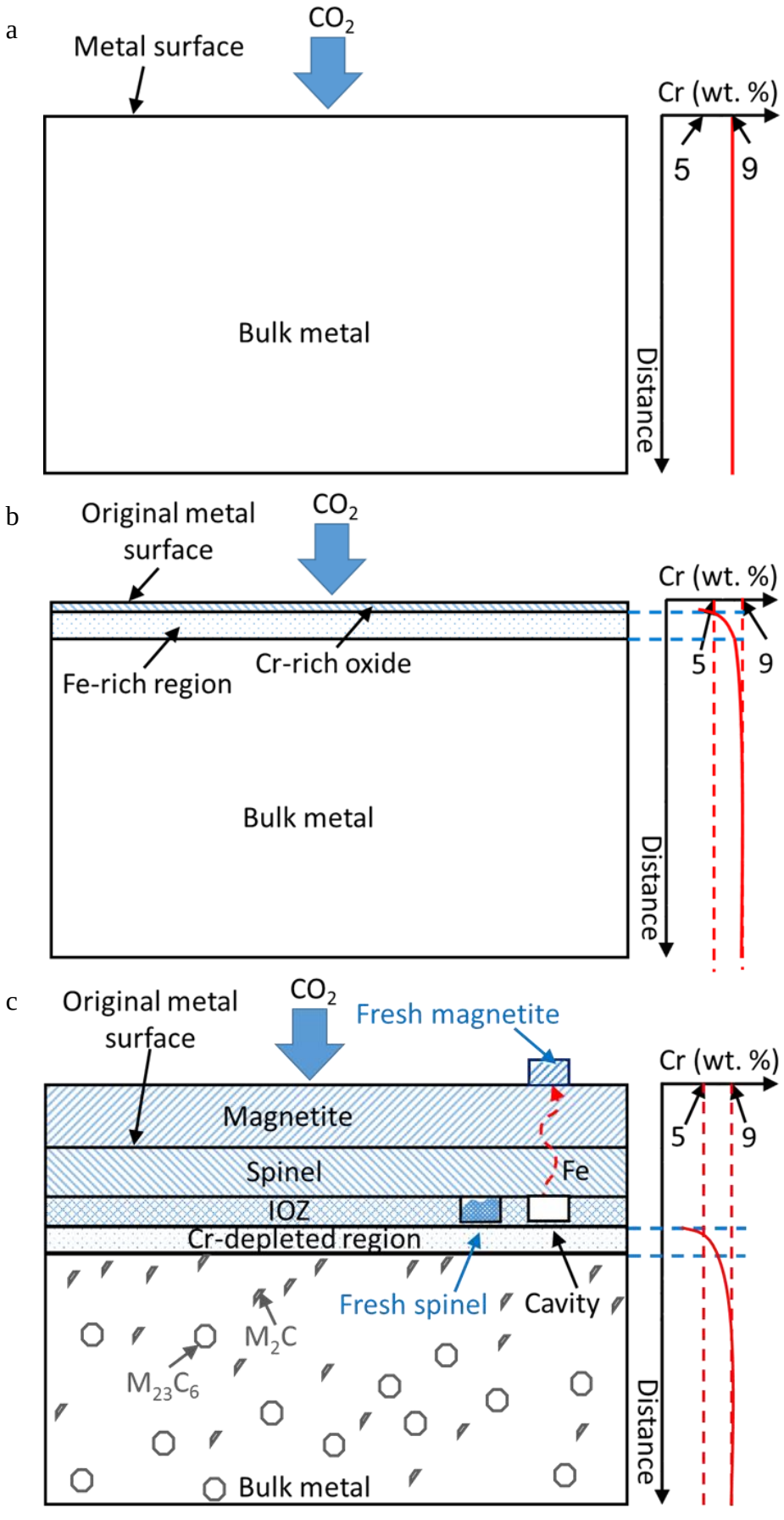
a
Metal surface
CO_2
Bulk metal
Cr (wt. %)
5
9
Distance
b
Original metal surface
CO_2
Fe-rich region
Cr-rich oxide
Bulk metal
Cr (wt. %)
5
9
Distance
c
Original metal surface
CO_2
Fresh magnetite
Magnetite
Spinel
Fe
IOZ
Cr-depleted region
Fresh spinel
Cavity
M_2C
$M_{23}C_6$
Bulk metal
Cr (wt. %)
5
9
Distance

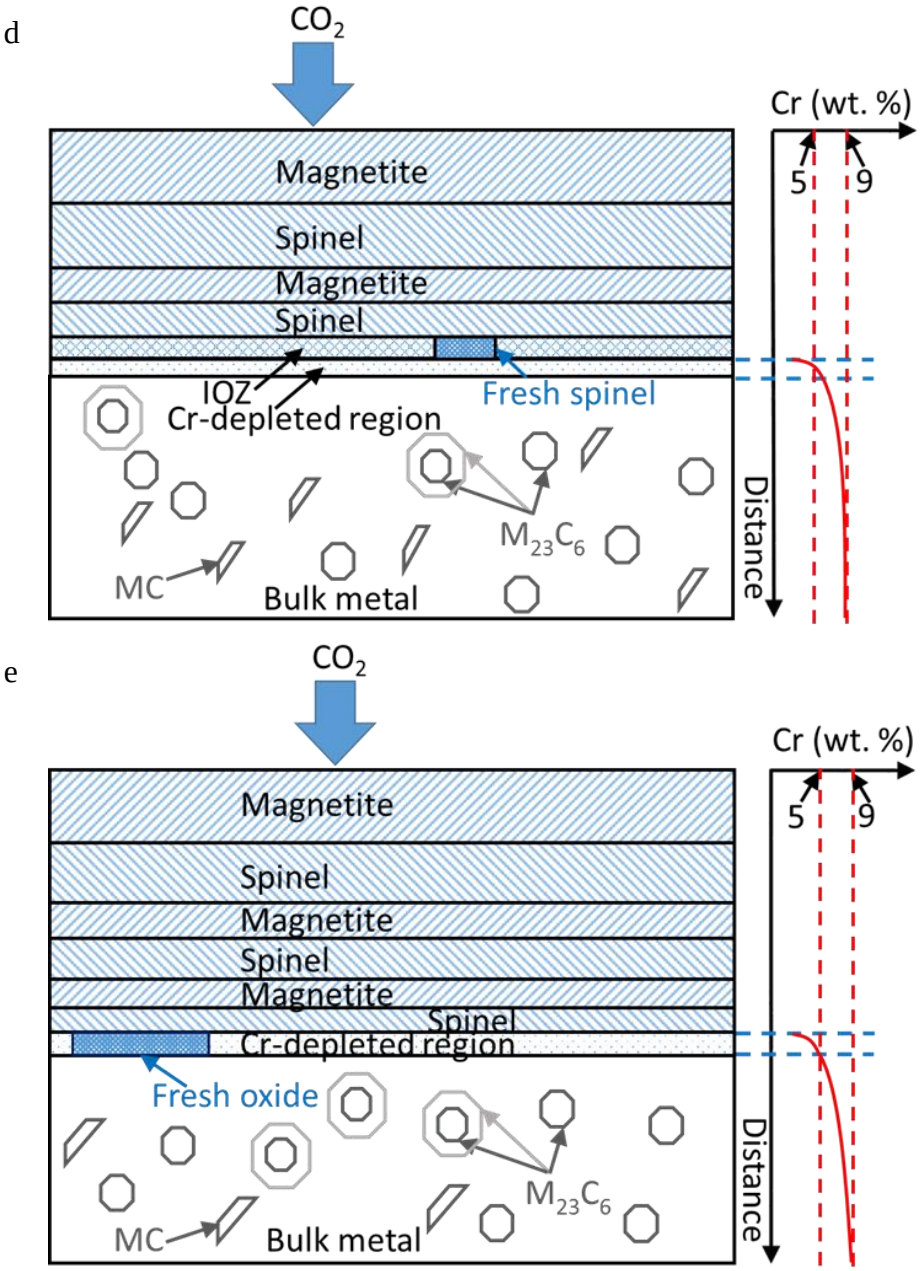

Figure 7-1: Schematic drawings illustrating the formation of multi-layered oxide and the Cr concentration in the location beneath the oxide: (a) no oxidation occurs; (b) the formation of a thin layer of spinel; (c) the formation of duplex oxide; (d) the formation of four-layered oxide and (e) the formation of multi-layered oxide.

Concentration profiles from EDS line scans and maps showing the distribution of elements illustrate that the outer layer oxide is mainly comprised of Fe_3O_4 and the inner layer $Fe_{3-x}Cr_xO_4$ in ferritic and martensitic 9Cr-1Mo samples.

The peak positions from each Raman spectrum obtained from experimental HRA (Table 4-5), OMS HRA (Table 5-3) and DNB (Table 6-4) samples suggest that the IOZ is comprised of spinel and chromia embedded within the matrix. The oxide close to the oxide/metal interface is mainly comprised of spinel and graphite with a low-degree of order (nanocrystalline graphite) before post-breakaway oxidation. Highly ordered graphite was only observed in the ferritic

steel exposed at a higher temperature (640 °C) in the breakaway initiation stage, which is probably caused by the Boudouard reaction proceeding at a certain speed. The oxide close to the oxide/metal interface from post-breakaway samples was mainly comprised of spinel and magnetite, as well as graphite with a low-degree of order. The Raman peak position maps indicate a relative compressive stress in the IOZ and tensile stress of the oxide in the spinel layer in the non-breakaway and breakaway initiation samples. The stress situation is unpredictable in the post-breakaway samples. The oxide composition in the examined samples obtained from EDS analysis (see Section 4.1.3 in Chapter 4, Section 5.1.3 in Chapter 5 and Section 6.1.3 in Chapter 6) and scanning laser Raman spectroscopy (see Section 4.1.4 in Chapter 4, Section 5.1.4 in Chapter 5 and Section 6.1.4 in Chapter 6) are given in Table 7-1.

Due to the complex situation present during the process of oxidation, it is impossible to obtain the oxide composition in sample B-640-245 from the EDS line scan results (see Section 6.1.3 in Chapter 6). However, the oxide in sample A-640-3883 contains more Cr than B-640-4887, according to Table 7-1, and both are in post-breakaway oxidation. This may be due to the higher Cr content in 9Cr-1Mo steels from reactor A (9.2 wt. %) than from reactor B (8.6 wt. %) as shown in Table 3-1.

Table 7-1: The value of x in the formula $Fe_{3-x}Cr_xO_4$ for the spinel examined with both EDS and Raman in the examined experimental HRA, OMS and DNB samples.

A-580-2542	*EDS*	*Raman*	
		Spot A	*Spot B*
	0.27-1.09	*0.4 or 0.17*	*0*
A-640-1495 (400 to 800 @ 245)	*EDS*	*Raman*	
		Spot A	*Spot B*
	0.22-1.09	*0*	*0.16, 1.04 or 1.44*
A-640-3883	*EDS*	*Raman*	
		Spot A	*Spot B*
	0.35-1.14	*0.12, 1.12 or 1.44*	*0*
M92M02-580-146760	*EDS*	*Raman*	
		Spot A	*Spot B*
	0.62-0.97	*1.92*	*0.08*
B-640-245	*EDS*	*Raman*	
		Spot A	*Spot B*
	/	*0.08*	*0*
B-640-4887	*EDS*	*Raman*	
		Spot A	*Spot B*
	≤0.84	*0*	*0*

The Raman peak position maps in Figure 4-25, Figure 5-8 and Figure 6-10 suggest a relative compressive stress in the IOZ during non-breakaway and breakaway initiation oxidation. However, the regions with compressive stress are unpredictable in post-breakaway oxide.

Results from TEM diffraction pattern analysis show that the orientation relationships between the carbides of different types and their parent metal are as follows:

M_2C	$(10.\bar{1})_{M_2C} \| (01\bar{1})_{\alpha-Fe}$ $[01.1]_{M_2C} \| [011]_{\alpha-Fe}$
MC	$(110)_{MC} \| (101)_{\alpha-Fe}$ $[001]_{MC} \| [\bar{1}11]_{\alpha-Fe}$
$M_{23}C_6$	$(11\bar{1})_{M_{23}C_6} \| (21\bar{1})_{\alpha-Fe}$ $[011]_{M_{23}C_6} \| [011]_{\alpha-Fe}$
Cored $M_{23}C_6$	$(200)_{cored\ M_{23}C_6} \| (0\bar{1}1)_{\alpha-Fe}$ $[001]_{cored\ M_{23}C_6} \| [\bar{1}11]_{\alpha-Fe}$

The relationship between coarse carbides and matrix is different from that between cored coarse carbides and matrix. Since the results are based on a measurement of only one carbide in the sample, this difference may not be representative. However, if the relationships work on all the coarse carbides and cored coarse carbides with respect to their matrix, this difference indicates a changing of the orientation between carbides and matrix in the post-breakaway oxidation stage. Strain may be formed due to the rapid oxidation rate, which leads to less coherency between the carbides and matrix. Another possible reason for this difference is that one grain could grow large and take the space of a neighbouring grain which is in a different orientation. However, the carbides forming in the neighbouring grain keeping the original orientation, leading to a different orientation relationship between these carbides and the coarsened grain, as shown in Figure 7-2.

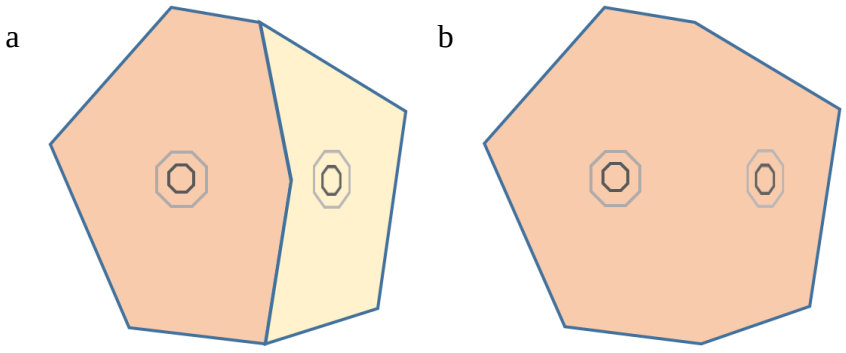

Figure 7-2: The schematic drawings of the grain growth: (a) two grains with the carbides formed in each in different orientations; (b) the growth of one grain leads to the disappearance of the other grain while the carbides keep the original orientations.

The Cr EDS maps of breakaway initiation and post-breakaway oxidation samples from both ferritic and martensitic steels show filamentary structures, indicating that Cr-rich oxide is very likely to be formed by the oxidation of carbides (see Figure 4-13, Figure 4-15, Figure 5-5 and Figure 6-5). A structure of grain boundaries was observed in the oxide from the EDS map of Cr, confirming the conversion of carbides to Cr-rich oxide (spinel) during the process of

oxidation. Figure 4-15 shows EDS maps of post-breakaway sample A-640-3883. The distribution of Cr shows a residual core from a cored coarse carbide, which is supporting evidence for this conversion. According to the analysis in Section 4.2.3 in Chapter 4, the Cr concentration in the matrix in sample A-640-3883 is approximately 1 wt. %, which converted into magnetite during the rapid oxidation process. As discussed in Section 4.1.2 in Chapter 4 and Section 5.1.2 in Chapter 5, breakaway oxidation has initiated in these two samples and similar carbide area fractions were obtained from them, as shown in Figure 4-48b and Figure 5-11a respectively. This suggests that breakaway is triggered when the carbides reach a certain volume fraction and, therefore, the matrix Cr level reaches a critical value, rather than when the oxide reaches a certain thickness.

Carbides with different morphologies were present in the samples entering different oxidation stages. As proposed in the above discussion, the process of oxidation is linked to the process of carburisation, which occurs at the same time. In the early stages of oxidation, the fast-growth and most of the period of steady growth, fine needles M_2C were present in non-breakaway ferritic 9Cr-1Mo samples. Large needles of MC were mainly present in the period close to TTB. It is proposed that this type of carbide dissolves into the metal or gradually converts into $M_{23}C_6$ in the next period following linear kinetics in which cored coarse carbides are formed. The Cr concentration in the inner core was higher than the outer layer of the cored coarse carbides, which were formed due to the depletion of Cr in the matrix. The metal was no longer protective in this period. Thus, both processes of oxidation and carburisation were exacerbated. The Cr and Fe concentration in the carbide with different morphologies and Cr concentration in the surrounding matrix are important for the analysis of oxidation and carburisation and are summarised in Table 7-2. This shows that the Cr concentration in the coarse carbide decreases from the early stage to the stage following linear kinetics while the Fe concentration follows the opposite trend. The Cr concentration in the surrounding matrix is important to the properties of the steel. It is approximately 9 wt. % in A-virgin, which subsequently reduces to almost 1 wt. % in post-breakaway samples.

Table 7-2: Concentration of Cr and Fe in the carbide precipitates and Cr concentration in the surrounding ferrite matrix obtained from experimental samples A-virgin, A-580-2542, A-640-1495 (400 to 800 @ 245) and A-640-3883.

Key Elements	*Small needles (M_2C)*	*Large needles (MC)*	*Coarse carbides ($M_{23}C_6$)*	*Cored coarse carbides ($M_{23}C_6$)*	
				Inner core	*Outer layer*
Cr in carbides (wt. %)	*50-90*	*40-60*	*50*	*40-80*	*30-50*
Fe in carbides (wt. %)	*<5*	*20-40*	*30*	*15-40*	*50-55*
Cr in surrounding matrix (wt. %)	*~5*	*~2*	*1 (post-breakaway)-9 (virgin)*	*~1*	

7.2 Other factors

7.2.1 Environment

The oxide growth was affected by the exposure conditions. The process of oxidation is accelerated by the higher temperature and time obeying Arrhennius kinetics (see Equation 5.1). Moisture, however, also exacerbates the process of oxidation. With sample A-600-17065 (1200), for example, Figure 4-4d shows a laminated oxide, which was formed at the fin tip corner, indicating that the sample has entered post-breakaway oxidation. However, the TTB (breakaway initiation oxidation) of samples exposed at 600 °C was approximately 20 kh with a moisture level of 400 vppm. This phenomenon suggests acceleration of oxidation at a moisture level 1200 vppm.

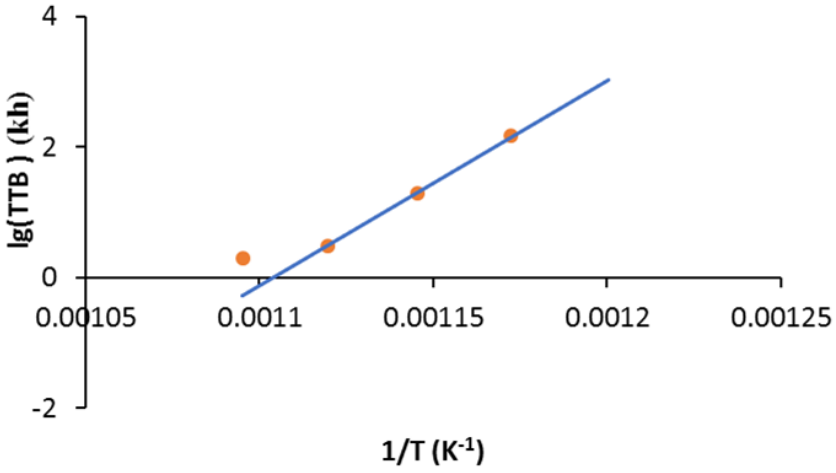

Figure 7-3: The plot of lg(TTB) against (1/T), where TTB represents time to breakaway (kh) and T represents temperature (in K).

Considering experimental samples exposed within the AGR environment had just entered breakaway, we can assume that the TTB of samples exposed at 580 °C with 400 vppm moisture is around 147 kh. As proposed by Gong et al., the TTB of samples exposed with 400 vppm moisture at 600, 620 and 640 °C was 20, 3 and 2 kh, respectively [85]. The trend of TTB versus temperature in the range of 580-640 °C can be obtained, as shown in Figure 5-3, which provides the possibility to obtain the estimated TTB at the working temperature within the reactor. Figure 7-3 shows a plot of lg(TTB) as a function of (1/T), in which the value of E_A/R can be obtained from the slope of the plot to be approximately 7×10^4 and E_A is about 600 kJ/mol. The activation energy for oxygen diffusion in BCC and FCC metal are 105-145 and 180-220 kJ/mol, respectively [61]. The higher activation energy indicates a slower oxidation process. Therefore, the higher activation energy in this work suggests a slower process for multi-layered oxide formation. Moreover, the oxidant in this investigation is CO_2 rather than O_2, which also increases the activation energy. The intercept is $-\lg D_0$ and D_0 is about 4.15 ×

10^{34} (m^2/s). The TTB at 560 °C can be estimated from the plot to be approximately 1173 kh (about 134 years).

It is also found that the oxide thickness increases sub-parabolically with time when exposed at the same temperature. Oxide morphologies from the experimental DNB samples are more complicated than those of the experimental HRA samples due to Cr-depletion of the DNB specimen surface prior to exposure. Due to the oxide from pre-heat treatments, the actual situation is more complex due to the interaction processes and moving boundaries during the process of oxidation.

Multi-layered and laminated oxides were formed at the fin tip corner, as shown in Figure 4-4 and Figure 4-5. The oxide in all the examined experimental HRA samples was obviously thicker at the fin tip corner than at the fin side, indicating the influence of geometry and 2D diffusion at the fin tip corner, as shown in Figure 4-6. The key alloying elements, e.g. Fe, Cr and Mo, diffuse from both horizontal and vertical directions for the growth of oxide at the fin tip corner, while at the fin side it is mainly affected by diffusion from one direction. Therefore, the onset of breakaway oxidation will tend to occur at corners. Cracks were also formed at the fin tip corners, allowing ingress of CO_2-based gas to the matrix for further oxidation, exacerbating the oxide growth and eventually leading to breakaway oxidation.

Compared with the bulk metal, breakaway oxidation is always present on the fins in the finned samples. It is ascribed to the smaller thickness of the fins. Furthermore, the oxidation and carburisation occur from both left and right sides of each fin. Therefore, the saturation state was present on the fins of samples rather than the bulk metal which always has plenty of 9 wt. % Cr left at a deeper level.

7.2.2 Moisture

The oxides from B-600-3020 (1200) and B-600-3835, as shown in Figures 6-1b and c, respectively demonstrate that a moisture content of 1200 vppm reduces the TTB. Cracks were present at the fin tip corners in both experimental HRA and DNB samples in breakaway initiation and post-breakaway oxidation, extending radially to the fin tip corner. The cracks in the breakaway initiation samples stopped before reaching the metal while the cracks extend to the metal in post-breakaway samples. The presence of cracks is indicative of the occurrence of breakaway, which appears to be a result of the high temperature, long exposure time, high moisture or a combination of them. Therefore, it can be inferred that the initiation of cracks in the oxide which extends almost to the metal is one of the signs of onset breakaway oxidation.

Three morphologies of oxide were observed at the fin tip corner in the investigation of experimental ferritic and martensitic 9Cr-1Mo steel: duplex, multi-layered and laminated.

Disregarding the oxide formed due to rust or pre-heat treatment in the experimental DNB samples, the oxide from non-breakaway samples in the early stage of oxidation shows a duplex morphology, often with a continuous IOZ layer formed beneath the oxide, as shown in the optical micrographs in Figure 6-1. The oxide from samples in the stage close to breakaway exhibits a multi-layered structure. Laminated oxide, which was often in the form of a fan shape, was present in the post-breakaway oxidation samples. Samples with duplex oxide were exposed at low temperature, short exposure time or a combination of these. The oxide thickness increases with the increase of temperature, time and moisture. However, temperature had the most significant influence on the oxide growth, followed by exposure time. Only a very high moisture level (1200 vppm) was observed to have an effect on the oxidation process. An IOZ layer was present beneath the oxides with duplex morphology and it was sometimes present in the samples with multi-layered oxide. The thickness of IOZ decreased with increase of temperature and time, and at very high moisture levels. In general, a continuous IOZ layer was present in non-breakaway samples and in some breakaway initiation samples, while discontinuous IOZ was present in some breakaway initiation samples but disappeared in most post-breakaway samples.

7.2.3 Geometry

The oxide in all the examined experimental HRA samples was obviously thicker at the fin tip corner than at the fin side, indicating the influence of geometry and the 2D diffusion at the fin tip corner. The key alloying elements, e.g. Cr, Mo, diffuse from both horizontal and vertical directions for the growth of oxide at the fin tip corner while at the fin side it is mainly affected by diffusion from one direction. Therefore, the onset of breakaway oxidation will tend to occur at corners.

7.2.4 Residual stress and strain

The results from Raman peak position maps indicate that there is compressive stress in the IOZ and tensile stress in the neighbouring oxide of non-breakaway and breakaway initiation oxidation (see Figure 4-25). The existence of stress and strain is indicative of the possibility of crack initiation parallel to the oxide/metal interface, as shown in Figure 4-4c and Figure 4-5g. The tensile stress outside of the neutral plane in oxide at the fin tip corner leads to the initiation of cracks, as shown in Figure 4-52. Cracks initiated in the multi-layered oxide extend radially from the fin tip corner and become large, driving post-breakaway oxidation which follows linear kinetics as shown in the plot of weight gain vs exposure time in Figure 2-8b. Cracks allow ingress of CO_2-based gas to the matrix for further oxidation, exacerbating the oxide growth and eventually leading to breakaway oxidation. The presence of multi-layered oxide was one of the signs of breakaway oxidation. The initiation and extension of these cracks

exacerbates the oxidation rate and reduces the TTB. Therefore, multi-layered oxide is formed earlier in the samples with strain in their oxides.

7.2.5 Composition of the gas

Carbide area fractions obtained across the examined fins following three paths at 500, 1000 and 1500 μm from the fin tip are shown in Figure 4-46, Figure 4-47, and Figure 4-48. It can be seen that there are similar area fractions from samples A-600-1510, A-600-1520 (1200), A-640-245, which were oxidised at different temperatures, indicating the effect of temperature in the process of carburisation. A longer exposure time is required for samples oxidised at lower temperature to achieve a similar area fraction with those at higher temperature. The carbide area fraction results of samples A-600-1510 and A-600-1520 (1200) illustrate that a 1200 vppm moisture content accelerates the process of carburisation in experimental HRA samples. We see lower carbide area fractions of the former sample than the latter, following the path at 500μm from the fin tip, in Figure 4-47. The plot in Figure 4-47d shows the carbide area fractions of sample A-600-17065 (1200), providing evidence that this sample has entered post-breakaway oxidation. This demonstrates that the moisture level of 1200 vppm exacerbates the processes of both oxidation and carburisation in ferritic steels. A comparison between samples B-600-3020 (1200) and B-600-3835 also suggests the exacerbating influence of moisture level at 1200 vppm in martensitic steels. The carbide area fraction is high at the fin side and low in the fin centre from samples in which oxide exhibits a duplex morphology. However, the carbide area fraction at the fin side of ferritic samples, e.g. A-640-245, was distributed by both coarse carbide $M_{23}C_6$ and fine needle carbide M_2C, while it is mainly present as $M_{23}C_6$ in martensitic steels, as suggested by the XRD results as shown in Figure 6-12. A saturation state is used to describe the highest carbide area fraction that can be achieved without the formation of cored carbides. As obtained from Equations 4.5 and 6.1, the theoretical saturation states in samples from reactor A and B are 18.4 % and 17.2 %, respectively. A saturation state of approximately 17 % was observed in both experimental HRA and DNB samples which have multi-layered oxide. The area fractions are further increased in the post-breakaway samples which show a laminated morphology in the oxide.

7.3 Triggers of breakaway

The comparison of oxide thickness and carbide area fraction between A-640-1495 (400 to 800 @ 245) and M92M02-580-146760 shows that these two breakaway initiation samples exhibit similar carbide area fractions (around 20 %) across the fin at 500 μm from the fin tip but different oxide thicknesses at the fin tip corner. This suggests that breakaway oxidation is triggered by carburisation rather than oxidation. Combined with the results obtained in Section 4.2.3 in Chapter 4 and Table 7-2, the possible triggers of breakaway are as follows:

1. Breakaway oxidation may occur when a saturation state of carbide area fraction is present at around 18 %.
2. Breakaway oxidation may occur when the Cr concentration in the matrix close to oxide is less than 5 wt. %, leading to the formation of cored carbides.
3. Breakaway oxidation may occur when the Cr concentration in the core of the cored coarse carbides is less than 50 wt. %.

Chapter 8: Conclusions

In this work, experimental finned 9Cr-1Mo steel tubes used as components in AGR were examined to study their oxidation and carburisation when exposed to the real or simulant AGR environment composed of CO_2 with minor additions. Previous workers studied the protective and less protective oxide formation and carbide precipitates formed under certain circumstances. Here, the evolution of oxides and carbide precipitates formed at various temperatures and times was investigated to understand the mechanisms of oxidation and carburisation systematically. Some affecting factors, including exposure environment, sample geometry, moisture content of the CO_2 gas, strain within the oxide and microstructure, were considered.

In chapter 3, two techniques, FIB XeF_2 imaging and HS-AFM, were used to study carbide precipitate distributions. FIB XeF_2 imaging highlights carbide precipitates due to the different work function between carbides and the matrix metal. XeF_2 gas reduces the work function of metal, but has less effect on carbides, leading to an obvious contrast between them. HS-AFM images carbide precipitates from the difference in height between precipitates and matrix metal. A strict polishing procedure produces an extremely high quality surface for the high-resolution HS-AFM imaging. The results of these two techniques are in general agreement. However, slight differences were observed due to the different thresholds of the image processing software. FIB XeF_2 imaging is more reliable in carbide area fraction calculation, while HS-AFM provides more extensive spatial distribution detail due to its higher resolution.

In chapter 4, the optical micrographs illustrate that cracks tend to be present in the oxide at the fin tip corners and edges extending radially into the matrix. The oxide thickness at the fin tip corner increases faster than at a planar surface, and this can be explained by 2D diffusion. The oxide thickness and the quantity and size of the carbide precipitates formed in the matrix increase with increase in the exposure temperature, time and moisture level (1200 vppm). A continuous IOZ layer is present in non-breakaway samples and its thickness reduces with the increase of temperature, time and moisture, resulting in a discontinuous IOZ layer where breakaway initiates in samples and the absence of IOZ in most samples in post-breakaway oxidation.

In the early stages of oxidation, which follow sub-parabolic kinetics, a duplex oxide was developed and fine needles and coarse carbide precipitates were formed in the matrix beneath the oxide scale. In the stage close to the time to breakaway (TTB), a multi-layered oxide was

formed accompanied by the presence of cracks in the oxide at the fin tip corner, with these extending radially to the metal at the fin tip corners, Large needles and coarse carbides were present in the matrix at this stage of oxidation. In the post-breakaway oxidation stage, which follows linear kinetics, a laminated oxide, often in a fan shape, was formed, and most coarse carbide precipitates were formed with a Cr-rich inner core surrounded by an outer layer less rich in Cr. The needle carbides were dissolved in the matrix to provide Cr for the formation of (cored) coarse carbides in the post-breakaway oxidation. The spinel of duplex oxide was formed by the oxidation of metal beneath the oxide where there is Cr accumulation. However, the spinel in multi-layered and laminated oxide was mainly formed from the oxidation of carbides while the depleted matrix converted into magnetite during oxidation. Graphite in the oxide was formed via the Boudouard reaction.

Raman spectra and peak position maps show that the duplex oxide was comprised of $Fe_{3-x}Cr_xO_4$ and deposited carbon in the form of graphite, accompanied by the occasional presence of Fe_3O_4 in the spinel layer. The IOZ layer is comprised of Cr_2O_3 and $Fe_{3-x}Cr_xO_4$ embedded in the matrix and, in some cases, with graphite. The multi-layered oxide is comprised of $Fe_{3-x}Cr_xO_4$ and deposited graphite, but thin layers of deposited carbon also formed in the spinel layer. The magnetite Fe_3O_4 was present occasionally in this type of oxide. The fast-growing laminated oxide is different from the previous two, and it is comprised of Cr-rich and Cr-depleted oxide. The Cr-rich oxide is $Fe_{3-x}Cr_xO_4$ and graphite while the Cr-depleted oxide consists of Fe_3O_4 or a combination of Fe_3O_4, $Fe_{3-x}Cr_xO_4$ and graphite. Results from scanning laser Raman spectroscopy show that the IOZ layer exhibits a compressive stress relative to the oxide scale close to the oxide/metal interface. This indicates that the oxide has a relative tensile stress compared with the metal close to the oxide/metal interface.

Carbide precipitates formed in the early stages of oxidation are fine needles and coarse carbides, which were identified as M_2C and $M_{23}C_6$ respectively. Large needles were identified as MC. Both inner core and surrounding carbides in cored coarse carbides were identified as $M_{23}C_6$ in the same orientation.

Both FIB and HS-AFM images confirm that the fine needle carbides are intragranular while the coarse carbide precipitates are both intergranular and intragranular. The height images from HS-AFM indicate that the hardness of the inner core is greater than that of the surrounding outer layer carbide, illustrating that the hardness of carbides increases with the increase of Cr concentration. There is a similar trend to the carbide area (volume) fraction plots obtained from FIB and HS-AFM results, but more spatial details are reveal by HS-AFM, e.g. the height of the analysed features. This is evidence that HS-AFM is capable of providing spatial information for the examined samples. However, the area fractions obtained from FIB XeF_2 images are more reliable. A saturation state was reached in some of the examined samples. The carbide

area fraction for the saturation state from observation is consistent with that from calculation; both indicate 17% as the saturated carbide area fraction for ferritic 9Cr-1Mo steels.

In chapter 5, the TTB at different temperatures of the ferritic 9Cr-1Mo was obtained: 147, 20, 3, 2 kh at 580, 600, 620 and 640 °C respectively. The plot of TTB as a function of temperature can be fitted by 1/D, where D represents the diffusion coefficient which can be obtained by an Arrhenius equation. The TTB decreased with the increase of diffusion of key elements as well as exposure temperature by the equation $\frac{1}{TTB} = D_0 \cdot exp\left(-\frac{E_A}{RT}\right)$. The experimental 9Cr-1Mo steels exposed to a real coolant gas at AGR follow the same mechanisms of oxidation and carburisation to those samples exposed to a simulant coolant gas, based on observation of the same or similar types and morphologies of the oxide and carbides formed between these steels.

In chapter 6, it was seen that the analysed martensitic steels follow a similar mechanism of oxidation to that observed from the ferritic 9Cr-1Mo steel. Oxides of the same type with only slight differences in composition were formed at the location of the IOZ and close to the oxide/metal interface. However, the observed difference in the TTB and oxidation rate is due to the different microstructures. Although the dominant carbides in both ferritic and martensitic steels are $M_{23}C_6$, there is no observation of the presence of M_2C and MC carbides in martensitic steels.

In chapter 7, the mechanisms of oxidation and carburisation during the transition from protective to post-breakaway oxidation were discussed. Five schematic stages illustrate the multi-layered oxide formation. Breakaway oxidation was enhanced at fin tip corners. The oxide at these locations grows faster than at the planar surfaces due to the 2D diffusion of key elements, Fe and Cr. It is also found that the higher moisture level (1200 vppm) exacerbates the process of oxidation. Breakaway oxidation is triggered by the Cr composition of ferritic matrix rather than the oxide thickness. Possible factors leading to breakaway oxidation are as follows:

1. Breakaway oxidation occurs when a saturation state carbide area fraction is present at around 18 %.
2. Breakaway oxidation occurs when the Cr concentration in the matrix close to oxide is less than 5 wt. %, which is associated to the formation of cored carbides.
3. Breakaway oxidation occurs when the Cr concentration in the core of the cored coarse carbides is less than 50 wt. %.

Chapter 9: Future work

The experimental finned 9Cr-1Mo steel tube samples exposed in a CO_2 rich atmosphere have been investigated in this thesis to determine factors influencing oxide growth and breakaway oxidation, as well as the mechanisms of oxidation and carburisation. It is important to have a further understanding of the factors that influence the mechanisms during the processes of oxidation and carburisation of 9Cr-1Mo steel when exposed to a hot CO_2 gas containing minor additions. Hence it is proposed that the following should be addressed:

- Samples with different geometries, e.g. sharp corner, round, etc., should be studied after exposure to a CO_2-based gas. However, since breakaway oxidation has been observed to occur at fin tip corners, the influence of curvature and sharpness of the surface should be investigated to establish the role of geometry on oxidation.
- Samples with the same shape but oxidised in CO_2 gases with different amounts of moisture, e.g. 900, 1000 and 1100 vppm can be studied to obtain the critical moisture content to have an obvious influence of the processes of oxidation and carburisation. It is known that a moisture level of 1200 vppm accelerates oxidation while 800 vppm has little influence. Therefore, the moisture level between 800 and 1200 vppm should be investigated to find the critical moisture level which starts to accelerate oxidation. Then, the moisture in AGRs could be controlled to be below this critical level.
- Binary Fe-Cr steels with different Cr content, e.g. 1, 2, 4, 6, 8, 10 and 12 wt. %, should be studied to obtain the critical Cr concentration in the matrix that triggers breakaway oxidation. It is found that breakaway occurs when the Cr level reaches approximately 5 wt. % in the matrix in 9Cr-1Mo steels. Therefore, steels with different Cr content should be studied to observe if breakaway oxidation occurs at the very beginning of oxidation process where the Cr content is less than 5 wt. %. Steels with Cr content greater than 12 wt. % are defined as stainless steel. Therefore, it is unnecessary to investigate steels with Cr content more than this level.
- Samples removed from a plain tube can be bent and then oxidised in a CO_2-based gas to investigate the influence of tensile and compressive stress and strain on the process of oxidation and carburisation. Strain was observed in the oxide and IOZ during the process of oxidation. It would be interesting to study the influence of both tensile and compressive stress on the oxide growth.
- The microstructure of the steel (ferrite and martensite) and the formation of multi-layered oxide should be taken into account in future modelling work.
- The work function of matrix metal and carbide precipitates of different types and composition should be evaluated using a NanoESCA II photoemission electron microscope (PEEM). It has an ultimate lateral resolution of 13 nm and is able to analyse the precipitates at the nanoscale. This may help to explain the contrast observed for different carbide precipitates when using XeF_2 gas during FIB imaging.

References:

[1] G.B. Gibbs, L.A. Popple, Oxidation of Structural Steels in CO_2 Cooled Reactors, Nucl. Energy. 21 (1982) 51–55.

[2] S.M. Goldberg, R. Rosner, Nuclear Reactors: Generation to Generation, the American Academy of Arts and Sciences, 2011.

[3] T. Abram, S. Ion, Generation-IV Nuclear Power: A Review of the State of the Science, Energy Policy. 36 (2008) 4323–4330.

[4] G.L. Olson, R.K. McCardell, D.B. Illum, Fuel Summary Report: Shippingport Light Water Breeder Reactor, Idaho Falls, ID, 1999. doi:10.2172/5765.

[5] B. Barré, The Nuclear Reactors from a « Natural History » Perspective, 2005. http://localhost/library/public/enews/ebulletinautumn2004/issue-6-print.htm (accessed June 21, 2017).

[6] C.E. Dickerman, E.S. Sowa, D. Okrent, J. Monaweck, L.B. Miller, Studies of Fast Reactor Fuel Element Behavior under Transient Heating to Failure. I. Initial Experiments on Metallic Samples in the Absence of Coolant, 1961. doi:10.2172/4823898.

[7] G.F. Kessinger, M.C. Thompson, Chop-Leach Dissolution of Commercial Reactor Fuel, AIP Conf. Proc. 673 (2003).

[8] G. Locatelli, M. Mancini, N. Todeschini, Generation IV Nuclear Reactors: Current Status and Future Prospects, Energy Policy. 61 (2013) 1503–1520.

[9] M.N.H. Comsan, Status of Nuclear Power Reactor Development, in: 6th Conf. Nucl. Part. Phys., Luxor, Egypt, 2007: pp. 79–89.

[10] J. Gilleland, C. Ahlfeld, D. Dadiomov, R. Hyde, Y. Ishikawa, D. McAlees, J. McWhirter, N. Myhrvold, J. Nuckolls, A. Odedra, K. Weaver, C. Whitmer, L. Wood, G. Zimmerman, Novel Reactor Designs to Burn Non-fissile Fuels, in: Proc. 2008 Int. Congr. Adv. Nucl. Power Plants, American Nuclear Society, Anaheim, Califonia, 2008: pp. 3378–2284.

[11] D.K.L. Tsang, B.J. Marsden, S.L. Fok, G. Hall, Graphite Thermal Expansion Relationship for Different Temperature Ranges, Carbon N. Y. 43 (2005) 2902–2906.

[12] K.A. Parkhill, N.F. Pidgeon, K.L. Henwood, P. Simmons, D. Venables, From the Familiar to the Extraordinary: Local Residents' Perceptions of Risk When Living with Nuclear Power in the UK, Trans. Inst. Br. Geogr. 35 (2010) 39–58.

[13] T.L. Schulz, Westinghouse AP1000 Advanced Passive Plant, Nucl. Eng. Des. 236 (2006) 1547–1557.

[14] T. Jamasb, W.J. Nuttall, M.G. Pollitt, Future Electricity Technologies and Systems, 1st ed., Cambridge University Press, 2006.

[15] G. Rothwell, A Real Options Approach to Evaluating New Nuclear Power Plants, Energy J. 27 (2006) 37–53.

[16] M. Fischer, The Severe Accident Mitigation Concept and the Design Measures for Core Melt Retention of the European Pressurized Reactor (EPR), Nucl. Eng. Des. 230 (2004) 169–180.

[17] D.F. Torgerson, B.A. Shalaby, S. Pang, CANDU Technology for Generation III+ and IV Reactors, Nucl. Eng. Des. 236 (2006) 1565–1572.

[18] R.A. Matzie, A. Worrall, The AP1000 Reactor- the Nuclear Renaissance Option, Nucl. Energy. 43 (2004) 33–45.

[19] D. Hinds, C. Maslak, Next-Generation Nuclear Energy: The ESBWR, Nucl. News. (2006) 35–40.

[20] D. Mun, J. Hwang, S. Han, H. Seki, J. Yang, Sharing Product Data of Nuclear Power Plants across Their Lifecycles by Utilizing a Neutral Model, Ann. Nucl. Energy. 35 (2008) 175–186.

[21] V. V. Bezlepkin, M.A. Zatevakhin, O.P. Krektunov, Y. V. Krylov, O. V. Maslennikova, S.E. Semashko, R.A. Sharapov, V.K. Efimov, Y.A. Migrov, Computational and Experimental Validation of a Passive Heat Removal System for NPP Containment with VVER-1200, At. Energy. 115 (2014) 215–223.

[22] K. Kamei, K. Kataoka, K. Imasaki, Enhancement of Plant Availability by Outage Shortening in European Advanced Boiling Water Reactor (EU-ABWR), in: 2013 21st Int. Conf. Nucl. Eng., Chengdu, 2013: pp. 1–9.

[23] T.K. Kim, GEN-IV Reactors, in: Tsoulfanidis N. Nucl. Energy, Springer New York, New York, NY, 2013: pp. 175–201.

[24] K.L. Murty, I. Charit, Structural Materials for Gen-IV Nuclear Reactors: Challenges and Opportunities, J. Nucl. Mater. 383 (2008) 189–195.

[25] W. Hoffelner, Materials for the Very High Temperature Reactor (VHTR): A Versatile Nuclear Power Station for Combined Cycle Electricity and Heat Production, Chem. Mater. Nucl. Power Prod. 59 (2005) 977–982.

[26] J. Serp, M. Allibert, O. Benes, S. Delpech, O. Feynberg, V. Ghetta, D. Heuer, D. Holcomb, V. Ignatiev, J.L. Kloosterman, L. Luzzi, E. Merle-Lucotte, J. Uhlir, R. Yoshioka, D. Zhimin, The Molten Salt Reactor (MSR) in Generation IV: Overview and Perspectives, Prog. Nucl. Energy. 77 (2014) 308–319.

[27] S. Baindur, Materials Challenges for the Supercritical Water-Cooled Reactor (SCWR), Bull. Can. Nucl. Soc. 29 (2008) 32–38.

[28] R. Rosner, S. Goldberg, J. Hezir, Small Modular Reactors - Key to Future Nuclear Power, 2011. https://www.energy.gov/sites/prod/files/2015/12/f27/ECON-SMRKeytoNuclearPowerDec2011.pdf (accessed September 21, 2017).

[29] Z. Liu, J. Fan, Technology Readiness Assessment of Small Modular Reactor (SMR)

designs, Prog. Nucl. Energy. 70 (2014) 20–28.

[30] J. Vujić, R.M. Bergmann, R. Škoda, M. Miletić, Small Modular Reactors: Simpler, Safer, Cheaper?, Energy. 45 (2012) 288–295.

[31] E. Nonbel, Description of the Advanced Gas Cooled Type of Reactor (AGR), Rise National Laboratory Roskilde, Denmark, 1996.

[32] P.C. Rowlands, A. Whittaker, A. Hoaksey, J.C.P. Garrett, The Oxidation Performance of Magnox and Advanced Gas-cooled Reactor Steels in High Pressure CO_2, Nucl. Energy. 25 (1986) 267–275.

[33] I. Pioro, P. Kirillov, Current Status of Electricity Generation at Thermal Power Plants, in: A. Mendez-Vilas (Ed.), Mater. Process. Energy Commun. Curr. Res. Technol. Dev., Formatex Research Center, 2013: pp. 796–805.

[34] J.W. Taylor, AGR Boiler Materials Selection Considerations, in: Gas-Cooled React. Today, British Nuclear Energy Society, Bristol, 1982: p. 328.

[35] A.I. Martinez Ubeda, Effect of Composition Variation and Service Environment on the Long Term Ageing of Type 316H Austenitic Stainless Steels, University of Bristol, 2017.

[36] M.G. Angell, S.. Lister, A. Rudge, The Effect of Steam Pressure on the Oxidation Behaviour of Annealed 9Cr-1Mo Boiler Tubing Material, in: 15th Int. Conf. Prop. Water Steam, Berlin, 2008: pp. 1–9.

[37] Q. Shi, J. Liu, W. Wang, W. Yan, Y. Shan, K. Yang, High Temperature Oxidation Behavior of SIMP Steel, Oxid. Met. 83 (2015) 521–532.

[38] A.S. Khanna, P. Rodriguez, J.B. Gnanamoorthy, Oxidation Kinetics, Breakaway Oxidation, and Inversion Phenomenon in 9Cr-1Mo Steels, Oxid. Met. 26 (1986) 171–200.

[39] F. Rouillard, G. Moine, M. Tabarant, J.C. Ruiz, Corrosion of 9Cr Steel in CO_2 at Intermediate Temperature II: Mechanism of Carburization, Oxid. Met. 77 (2012) 57–70.

[40] J. Robertson, The Mechanism of Carbon Deposition During the Breakaway Oxidation of Steels in Carbon Dioxide, Catal. Today. 7 (1990) 267–276.

[41] R.L. Klueh, Ferritic/Martensitic Steels for Advanced Nuclear Reactors, Trans. Indian Inst. Met. 62 (2009) 81–87.

[42] A. Karmakar, M. Ghosh, D. Chakrabarti, Cold-rolling and Inter-critical Annealing of Low-carbon Steel: Effect of Initial Microstructure and Heating-rate, Mater. Sci. Eng. A. 564 (2013) 389–399.

[43] J. Chipman, Thermodynamics and Phase Diagram of the Fe-C System, Metall. Mater. Trans. B. 3 (1972) 55–64.

[44] M.N. Mungole, G. Sahoo, S. Bhargava, R. Balasubramaniam, Recrystalised Grain Morphology in 9Cr1Mo Ferritic Steel, Mater. Sci. Eng. A. 476 (2008) 140–145.

[45] J. Blach, L. Falat, P. Ševc, Fracture Characteristics of Thermally Exposed 9Cr–1Mo Steel after Tensile and Impact Testing at Room Temperature, Eng. Fail. Anal. 16 (2009) 1397–1403.

[46] P.J. Ennis, A. Czyrska-Filemonowicz, Recent Advances in Creep-resistant Steels for Power Plant Applications, Sadhana. 28 (2003) 709–730.

[47] S. Hollner, B. Fournier, J. Le Pendu, T. Cozzika, I. Tournié, J.C. Brachet, A. Pineau, High-temperature Mechanical Properties Improvement on Modified 9Cr-1Mo Martensitic Steel through Thermomechanical Treatments, J. Nucl. Mater. 405 (2010) 101–108.

[48] W.-G. Kim, S.-N. Yin, G.-H. Koo, Generation of Isochronous Stress-strain Curves with a Nonlinear Least Square Fitting Method for Modified 9Cr-1Mo Steel, Met. Mater. Int. 15 (2009) 727–732.

[49] W.B. Jones, C.R. Hills, D.H. Polonis, Microstructural Evolution of Modified 9Cr-1Mo Steel, Metall. Trans. A. 22 (1991) 1049–1058.

[50] V. Thomas Paul, S. Saroja, M. Vijayalakshmi, Microstructural Stability of Modified 9Cr–1Mo Steel during Long Term Exposures at Elevated Temperatures, J. Nucl. Mater. 378 (2008) 273–281.

[51] F. Abe, S. Nakazawa, H. Araki, T. Noda, The Role of Microstructural Instability on Creep Behavior of a Martensitic 9Cr-2W Steel, Metall. Trans. A. 23 (1992) 469–477.

[52] A. Czyrska-Filemonowicz, A. Zielińska-Lipiec, P.J. Ennis, Modified 9% Cr Steels for Advanced Power Generation: Microstructure and Properties, J. Achiev. Mater. Manuf. Eng. 19 (2006) 43–48.

[53] K. Hashimoto, K. Asami, M. Naka, T. Masumoto, The Role of Alloying Elements in Improving the Corrosion Resistance of Amorphous Iron Base Alloys, Corros. Sci. 19 (1979) 857–867.

[54] H.E. Townsend, Effects of Alloying Elements on the Corrosion of Steel in Industrial Atmospheres, Corros. Sci. 57 (2001) 497–501.

[55] R. Hales, A.F. Smith, J.C. Killeen, The Role of Phase Stability and Metal Lattice Diffusion in the High Temperature Oxidation of Stainless Steels, in: Proc. Br. Nucl. Energy Soc. Int. Conf. Read. Univ., British Nuclear Energy Society, 1974: pp. 311–319.

[56] S. Sroda, D. Baxter, M. Arponen, The Influence of Alloying Elements on the Corrosion Behaviour of Ferritic Steels in Simulated Combustion Atmospheres, Mater. Corros. 56 (2005) 791–795.

[57] R.L. Klueh, E.E. Bloom, The Development of Ferritic Steels for Fast Induced-radioactivity Decay for Fusion Reactor Applications, Nucl. Eng. Des. Fusion. 2 (1985) 383–389.

[58] E.J. Pavlina, J.A. Roubidoux, Hot-rolled Steel with Very High Strength and Method for Production, US 2018/0251871 A1, 2018.

[59] M.P. Ryan, D.E. Williams, R.J. Chater, B.M. Hutton, D.S. McPhail, Why Stainless Steel Corrodes, Nature. 415 (2002) 770–774.

[60] R.K.S. Raman, J.B. Gnanamoorthy, S.K. Roy, Synergistic Influence of Alloy Grain Size and Si Content on the Oxidation Behavior of 9Cr−1Mo Steel, Oxid. Met. 42 (1993) 335–355.

[61] P. Kofstad, High Temperature Corrosion, Elsevier Applied Science Publishers Ltd., London - New York, 1988.

[62] X. Zhong, X. Wu, E.H. Han, The Characteristic of Oxide Scales on T91 Tube after Long-term Service in an Ultra-supercritical Coal Power Plant, J. Supercrit. Fluids. 72 (2012) 68–77.

[63] C. Liu, P.J. Heard, S.J. Greenwell, P.E.J. Flewitt, A Study of Breakaway Oxidation of 9Cr–1Mo Steel in a Hot CO_2 Atmosphere Using Raman Spectroscopy, Mater. High Temp. 35 (2018) 50–55.

[64] D.J. Young, High Temperature Oxidation and Corrosion of Metals, Elsevier, 2008.

[65] T. Olszewski, Oxidation Mechanisms of Materials for Heat Exchanging Components in CO_2/H_2O-containing Gases Relevant to Oxy-fuel Environments, Forschungszentrum Jülich, 2012.

[66] R. Viswanathan, J. Sarver, J.M. Tanzosh, Boiler Materials for Ultra-Supercritical Coal Power Plants—Steamside Oxidation, J. Mater. Eng. Perform. 15 (2006) 255–274.

[67] F. Rouillard, T. Furukawa, Corrosion of 9-12Cr Ferritic–Martensitic Steels in High-Temperature CO_2, Corros. Sci. 105 (2016) 120–132.

[68] F. Rouillard, G. Moine, L. Martinelli, J.C. Ruiz, Corrosion of 9Cr Steel in CO_2 at Intermediate Temperature I: Mechanism of Void-Induced Duplex Oxide Formation, Oxid. Met. 77 (2012) 27–55.

[69] L. Martinelli, F. Balbaud-Célérier, A. Terlain, S. Delpech, G. Santarini, J. Favergeon, G. Moulin, M. Tabarant, G. Picard, Oxidation Mechanism of a Fe–9Cr–1Mo Steel by Liquid Pb–Bi Eutectic Alloy (Part I), Corros. Sci. 50 (2008) 2523–2536.

[70] K.A. Hay, F.G. Hicks, D.R. Holmes, The Transport Properties and Defect Structure of the Oxide $(Fe, Cr)_2O_3$ formed on Fe-Cr alloys, Mater. Corros. Und Korrosion. 21 (1970) 917–924.

[71] M.I. Manning, P.C. Rowlands, Method of Preparing TEM Foils from Thick Oxides and Metal/Oxide Interfaces, Br. Corros. J. 15 (1980) 184–189.

[72] G.C. Wood, D.P. Whittle, On the Mechanism of Oxidation of Iron-16.4% Chromium at High Temperature, Corros. Sci. 4 (1964) 263–292.

[73] S.B. Newcomb, W.M. Stobbs, E. Metcalfe, A Microstructural Study of the Oxidation of Fe-Ni-Cr Alloys I. Protective Oxide Growth, Philos. Trans. R. Soc. A Math. Phys. Eng. Sci. 319 (1986) 191–218.

[74] W.M. Stobbs, S.B. Newcomb, E. Metcalfe, A Microstructural Study of the Oxidation of Fe-Ni-Cr Alloys II. "Non-Protective" Oxide Growth, Source Philos. Trans. R. Soc. London. Ser. A, Math. Phys. Sci. Phil. Trans. R. Soc. Lond. A. 319 (1986) 219–247.

[75] S.B. Newcomb, W.M. Stobbs, The Characterization of Interfacial Structures in the Oxidation of Fe and FeNiCr Alloys by Edge-on Tansmission Electron Microscopy, J. Microsc. 140 (1985) 209–220.

[76] J. Żurek, E. Wessel, L. Niewolak, F. Schmitz, T.U. Kern, L. Singheiser, W.J. Quadakkers, Anomalous Temperature Dependence of Oxidation Kinetics during Steam Oxidation of Ferritic Steels in the Temperature Range 550–650 °C, Corros. Sci. 46 (2004) 2301–2317.

[77] G.B. Gibbs, R. Hales, The Influence of Metal Lattice Vacancies on the Oxidation of High Temperature Materials, Corros. Sci. 17 (1977) 487–507.

[78] G.B. Gibbs, A Model for Mild Steel Oxidation in CO_2, Oxid. Met. 7 (1973) 173–184.

[79] A. Atkinson, D.W. Smart, Transport of Nickel and Oxygen during the Oxidation of Nickel and Dilute Nickel/Chromium Alloy, J. Electrochem. Soc. 135 (1988) 2886.

[80] L. Martinelli, C. Desgranges, F. Rouillard, K. Ginestar, M. Tabarant, K. Rousseau, Comparative Oxidation Behaviour of Fe-9Cr Steel in CO_2 and H_2O at 550 °C: Detailed Analysis of the Inner Oxide Layer, Corros. Sci. 100 (2015) 253–266.

[81] L. Martinelli, F. Balbaud-Célérier, A. Terlain, S. Bosonnet, G. Picard, G. Santarini, Oxidation Mechanism of an Fe–9Cr–1Mo steel by Liquid Pb–Bi Eutectic Alloy at 470 °C (Part II), Corros. Sci. 50 (2008) 2537–2548.

[82] G. Muller, G. Schumacher, F. Zimmermann, Investigation on Oxygen Controlled Liquid Lead Corrosion of Surface Treated Steels, J. Nucl. Mater. 278 (2000) 85–95.

[83] T. Gheno, D. Monceau, D.J. Young, Mechanism of Breakaway Oxidation of Fe–Cr and Fe–Cr–Ni Alloys in Dry and Wet Carbon Dioxide, Corros. Sci. 64 (2012) 222–233.

[84] T. Gheno, D. Monceau, D.J. Young, Kinetics of Breakaway Oxidation of Fe–Cr and Fe–Cr–Ni Alloys in Dry and Wet Carbon Dioxide, Corros. Sci. 77 (2013) 246–256.

[85] Y. Gong, D.J. Young, P. Kontis, Y.L. Chiu, H. Larsson, A. Shin, J.M. Pearson, M.P. Moody, R.C. Reed, On the Breakaway Oxidation of Fe9Cr1Mo Steel in High Pressure CO_2, Acta Mater. 130 (2017) 361–374.

[86] J.R. Davis, ASM Specialty Handbook: Heat-resistant Materials, ASM International, 1997.

[87] W.J. Quadakkers, P.J. Ennis, J. Zurek, M. Michalik, Steam Oxidation of Ferritic Steels – Laboratory Test Kinetic Data, Mater. High Temp. 22 (2005) 47–60.

[88] W.J. Quadakkers, J. Żurek, Oxidation in Steam and Steam/Hydrogen Environments, in: Shreir's Corros., Elsevier, 2010: pp. 407–456.

[89] A. Rahmel, J. Tobolski, Influence of Water Vapor and Carbon Dioxide on the Oxidation

of Iron in Oxygen at High Temperatures, Corros. Sci. 5 (1965) 333–346.

[90] E. Essuman, G.H. Meier, J. Żurek, M. Hänsel, L. Singheiser, W.J. Quadakkers, Enhanced Internal Oxidation as Trigger for Breakaway Oxidation of Fe–Cr Alloys in Gases Containing Water Vapor, Scr. Mater. 57 (2007) 845–848.

[91] E. Essuman, G.H. Meier, J. Żurek, M. Hänsel, W.J. Quadakkers, The Effect of Water Vapor on Selective Oxidation of Fe–Cr Alloys, Oxid. Met. 69 (2008) 143–162.

[92] C.S. Giggins, F.S. Pettit, Corrosion of Metals and Alloys in Mixed Gas Environments at Elevated Temperatures, Oxid. Met. 14 (1980) 363–413.

[93] G.H. Meier, W.C. Coons, R.A. Perkins, Corrosion of Iron-, Nickel-, and Cobalt-base Alloys in Atmospheres Containing Carbon and Oxygen, Kluwer Academic Publishers-Plenum Publishers, 1982.

[94] K.F. McCarty, D.R. Boehme, A Raman Study of the Systems $Fe_{3-x}Cr_xO_4$ and $Fe_{2-x}Cr_xO_3$, J. Solid State Chem. 79 (1989) 19–27.

[95] O.N. Shebanova, P. Lazor, Raman Spectroscopic Study of Magnetite ($FeFe_2O_4$): a New Assignment for the Vibrational Spectrum, J. Solid State Chem. 174 (2003) 424–430.

[96] J.L. Verble, Temperature-dependent Light-scattering Studies of the Verwey Transition and Electronic Disorder in Magnetite, Phys. Rev. B. 9 (1974).

[97] L.V. Gasparov, D.B. Tanner, D.B. Romero, H. Berger, G. Margaritondo, L. Forró, Infrared and Raman Studies of the Verwey Transition in Magnetite, Phys. Rev. B. 62 (2000) 7939–7944.

[98] J. Dünnwald, A. Otto, An Investigation of Phase Transitions in Rust Layers using Raman Spectroscopy, Corros. Sci. 29 (1989) 1167–1176.

[99] D.L.A. de Faria, S. Venâncio Silva, M.T. de Oliveira, Raman Microspectroscopy of Some Iron Oxides and Oxyhydroxides, J. Raman Spectrosc. 28 (1997) 873–878.

[100] I.R. Beattie, T.R. Gilson, The Single-crystal Raman Spectra of Nearly Opaque Materials. Iron(III) Oxide and Chromium(III) Oxide, J. Chem. Soc. A. (1970) 980–986.

[101] M.J. Massey, U. Baier, R. Merlin, W.H. Weber, Effects of Pressure and Isotopic Substitution on the Raman Spectrum of α-Fe_2O_3: Identification of Two-magnon Scattering, Phys. Rev. B. 41 (1990) 7822–7827.

[102] J. Birnie, C. Craggs, D.J. Gardiner, P.R. Graves, Ex Situ and in Situ Determination of Stress Distributions in Chromium Oxide Films by Raman Microscopy, Corros. Sci. 33 (1992) 1–12.

[103] J. Zuo, C. Xu, B. Hou, C. Wang, Y. Xie, Y. Qian, Raman Spectra of Nanophase Cr_2O_3, J. Raman Spectrosc. 27 (1996) 921–923.

[104] A.C. Ferrari, J. Robertson, Interpretation of Raman Spectra of Disordered and Amorphous Carbon, Phys. Rev. B. 61 (2000) 14095–14107.

[105] A.C. Ferrari, Determination of Bonding in Diamond-like Carbon by Raman Spectroscopy, Diam. Relat. Mater. 11 (2002) 1053–1061.

[106] F. Tuinstra, J.L. Koenig, Raman Spectrum of Graphite, J. Chem. Phys. 53 (1970) 1126–1130.

[107] P.J. Heard, L. Payne, M.R. Wootton, P.E.J. Flewitt, Evaluation of Surface Deposits on the Channel Wall of Trepanned Reactor Core Graphite Samples, J. Nucl. Mater. 445 (2014) 91–97.

[108] L.G. Birta, G. Arbez, Modelling and Simulation, Springer London, London, 2013.

[109] F. Rouillard, L. Martinelli, Corrosion of 9Cr Steel in CO_2 at Intermediate Temperature III: Modelling and Simulation of Void-induced Duplex Oxide Growth, Oxid. Met. 77 (2012) 71–83.

[110] H.E. Evans, J.R. Nicholls, S.R.J. Saunders, The Influence of Diffusion-Related Mechanisms in Limiting Oxide-Scale Failure, Solid State Phenom. 41 (1995) 137–156.

[111] H.K.D.H. Bhadeshia, T. DebRoy, J.A. Johnson, H.B. Smartt, J.M. Vitek, Design of Creep-resistant Steel Welds, in: Trends Weld. Res., ASM International, Ohio, 1999: pp. 795–804.

[112] S.B. Newcomb, W.M. Stobbs, The Initiation of Breakaway Oxidation of Fe-9Cr-1Mo in a High Pressure CO_2 Atmosphere, Oxid. Met. 26 (1986) 431–466.

[113] S. Spigarelli, E. Cerri, P. Bianchi, E. Evangelista, Interpretation of Creep Behaviour of a 9Cr–Mo–Nb–V–N (T91) Steel Using Threshold Stress Concept, Mater. Sci. Technol. 15 (1999) 1433–1440.

[114] T. Gheno, D. Monceau, J. Zhang, D.J. Young, Carburisation of Ferritic Fe–Cr Alloys by Low Carbon Activity Gases, Corros. Sci. 53 (2011) 2767–2777.

[115] C. Keller, M.M. Margulies, Z. Hadjem-Hamouche, I. Guillot, Influence of the Temperature on the Tensile Behaviour of a Modified 9Cr-1Mo T91 Martensitic Steel, Mater. Sci. Eng. A. 527 (2010) 6758–6764.

[116] J.Y. Maetz, T. Douillard, S. Cazottes, C. Verdu, X. Kléber, $M_{23}C_6$ Carbides and Cr_2N Nitrides in Aged Duplex Stainless Steel: A SEM, TEM and FIB Tomography Investigation, Micron. 84 (2016) 43–53.

[117] H.L. Yakel, Atom Distributions in Tau-carbide Phases: Fe and Cr distributions in $(Cr_{23-x}Fe_x)C_6$ with x = 0, 0.74, 1.70, 4.13 and 7.36, Acta Crystallogr. Sect. B Struct. Sci. 43 (1987) 230–238.

[118] K.M. Lee, H.S. Cho, D.C. Choi, Effect of Isothermal Treatment of SAF 2205 Duplex Stainless Steel on Migration of δ/γ Interface Boundary and Growth of Austenite, J. Alloys Compd. 285 (1999) 156–161.

[119] A.F. Padilha, P.R. Rios, Decomposition of Austenite in Austenitic Stainless Steels, ISIJ Int. 42 (2002) 325–327.

[120] C.M. Fang, M.A. van Huis, H.W. Zandbergen, Structure and Stability of Fe_2C Phases from Density-functional Theory Calculations, Scr. Mater. 63 (2010) 418–421.

[121] M. Dirand, L. Afqir, Identification Structurale Precise des Carbures Precipites dans Les Aciers Faiblement Allies aux Divers Stades du Revenu, Mecanismes de Precipitation, Acta Metall. 31 (1983) 1089–1107.

[122] Z.Q. Lv, S.H. Sun, P. Jiang, B.Z. Wang, W.T. Fu, First-principles Study on the Structural Stability, Electronic and Magnetic Properties of Fe_2C, Comput. Mater. Sci. 42 (2008) 692–697.

[123] R. Sinclair, T. Itoh, R. Chin, In Situ TEM Studies of Metal-carbon Reactions, Microsc. Microanal. 8 (2002) 288–304.

[124] L.V. Zaslavskaya, N.V. Ivanova, N.F. Lashko, Separation of Alloyed Chromium Carbides of the Cr_2C (Metastable) and $Cr_{23}C_6$ or Cr_7C_3 Types Isolated from Steels and Alloys, in: Chem. Prop. Anal. Refract. Compd., Springer US, Boston, MA, 1972: pp. 68–71.

[125] A. Runiewicz, W. Dudzinski, A. Fischer, Microstructure of Laser Hardened Martensitic High Nitrogen Steel Subsurfaces, Pract. Metallogr. 43 (2006) 364–372.

[126] Y.Z. Shen, S.H. Kim, H.D. Cho, C.H. Han, W.S. Ryu, Precipitate Phases of a Ferritic/Martensitic 9% Cr Steel for Nuclear Power Reactors, Nucl. Eng. Des. 239 (2009) 648–654.

[127] A.J. Ramirez, J.C. Lippold, S.D. Brandi, The Relationship between Chromium Nitride and Secondary Austenite Precipitation in Duplex Stainless Steels, Metall. Mater. Trans. A. 34 (2003) 1575–1597.

[128] T.-H. Lee, H.-Y. Ha, B. Hwang, S.-J. Kim, Isothermal Decomposition of Ferrite in a High-nitrogen, Nickel-free Duplex Stainless Steel, Metall. Mater. Trans. A. 43 (2012) 822–832.

[129] Y.K. Luan, N.N. Song, Y.L. Bai, X.H. Kang, D.Z. Li, A Segregative MC Carbide in Centrifugal Casting High Speed Steel Roll, Adv. Mater. Res. 154–155 (2006) 269–272.

[130] Y.Z. Shen, S.H. Kim, C.H. Han, H.D. Cho, W.S. Ryu, C.B. Lee, Vanadium Nitride Precipitate Phase in a 9% Chromium Steel for Nuclear Power Plant Applications, J. Nucl. Mater. 374 (2008) 403–412.

[131] B. Sundman, B. Jansson, J.-O. Andersson, The Thermo-Calc Databank System, Calphad. 9 (1985) 153–190.

[132] T. Turpin, J. Dulcy, M. Gantois, Carbon Diffusion and Phase Transformations during Gas Carburizing of High-alloyed Stainless Steels: Experimental Study and Theoretical Modeling, Metall. Mater. Trans. A. 36 (2005) 2751–2760.

[133] J.-O. Andersson, T. Helander, L. Höglund, P. Shi, B. Sundman, Thermo-Calc & DICTRA, Computational Tools for Materials Science, Calphad. 26 (2002) 273–312.

[134] B.S. Motagi, R. Bhosle, Effect of Heat Treatment on Microstructure and Mechanical

Properties of Medium Carbon Steel, Int. J. Eng. Res. Dev. 2 (2012) 2278–67.

[135] A. Shin, M. Chevalier, E. Laney, J. Pearson, Oxidation Behaviour of Steels in Advanced Gas Cooled Reactors, Mater. High Temp. 35 (2018) 30–38.

[136] A.D. Warren, A.I. Martinez-Ubeda, O.D. Payton, L. Picco, T.B. Scott, Preparation of Stainless Steel Surfaces for Scanning Probe Microscopy, Micros. Today. 24 (2016) 52–55.

[137] R. Haynes, Optical Microscopy of Materials, Blackie & Son Ltd, 1984.

[138] D.J. Gardiner, P.R. Graves, Practical Raman Spectroscopy, Springer Berlin Heidelberg, Berlin, Heidelberg, 1989.

[139] M. Hanesch, Raman Spectroscopy of Iron Oxides and (Oxy)hydroxides at Low Laser Power and Possible Applications in Environmental Magnetic Studies, Geophys. J. Int. 177 (2009) 941–948.

[140] H.B. Qi, Y.N. Yan, F. Lin, W. He, R.J. Zhang, Direct Metal Part Forming of 316L Stainless Steel Powder by Electron Beam Selective Melting, Proc. Inst. Mech. Eng. Part B J. Eng. Manuf. 220 (2006) 1845–1853.

[141] H. Richter, Z.P. Wang, L. Ley, The One Phonon Raman Spectrum in Microcrystalline Silicon, Solid State Commun. 39 (1981) 625–629.

[142] E. Smith, G. Dent, Modern Raman Rpectroscopy a Practical Approach, Wiley, 2005.

[143] F.W.L. Esmonde-White, M.D. Morris, Raman Imaging and Raman Mapping, in: Emerg. Raman Appl. Tech. Biomed. Pharm. Fields, Springer, Berlin, Heidelberg, 2009: pp. 97–110.

[144] A. Srisrual, S. Coindeau, A. Galerie, J.P. Petit, Y. Wouters, Identification by Photoelectrochemistry of Oxide Phases Grown during the Initial Stages of Thermal Oxidation of AISI 441 Ferritic Stainless Steel in Air or in Water Vapour, Corros. Sci. 51 (2009) 562–568.

[145] N. Karimi, F. Riffard, F. Rabaste, S. Perrier, R. Cueff, C. Issartel, H. Buscail, Characterization of the Oxides Formed at 1000 °C on the AISI 304 Stainless Steel by X-ray Diffraction and Infrared Spectroscopy, Appl. Surf. Sci. 254 (2008) 2292–2299.

[146] Y. Wouters, A. Galerie, J.-P. Petit, Photoelectrochemical Study of Oxides Thermally Grown on Titanium in Oxygen or Water Vapor Atmospheres, J. Electrochem. Soc. 154 (2007) C587–C592.

[147] A. Galerie, S. Henry, Y. Wouters, M. Mermoux, J.P. Petit, L. Antoni, Mechanisms of Chromia Scale Failure during the Course of 15–18Cr Ferritic Stainless Steel Oxidation in Water Vapour, Mater. High Temp. 22 (2005) 105–112.

[148] J. Mougin, T. Le Bihan, G. Lucazeau, High-pressure Study of Cr_2O_3 Obtained by High-temperature Oxidation by X-ray Diffraction and Raman Spectroscopy, J. Phys. Chem. Solids. 62 (2001) 553–563.

[149] D. Stokes, Principles and Practice of Variable Pressure/Environmental Scanning Electron Microscopy (VP-ESEM), Wiley, 2008.

[150] J.I. Goldstein, D.E. Newbury, J.R. Michael, N.W.M. Ritchie, J.H.J. Scott, D.C. Joy, Scanning Electron Microscopy and X-ray Microanalysis, 3rd ed., Springer New York, New York, 2018.

[151] J.I. Goldstein, D.E. Newbury, P. Echlin, D.C. Joy, A.D. Romig, C.E. Lyman, C. Fiori, E. Lifshin, Scanning Electron Microscopy and X-Ray Microanalysis : A Text for Biologists, Materials Scientists, and Geologists, 2nd ed., Springer US, 1992.

[152] D.B. Williams, C. Barry Carter, Transmission Electron Microscopy: A Textbook for Materials Science, Springer, New York, 2009.

[153] An Introduction to Electron Microscopy Booklet, (2015). https://www.fei.com/documents/introduction-to-microscopy-document/ (accessed October 29, 2017).

[154] P.E.J. Flewitt, R.K. Wild, Physical Methods for Materials Characterisation, 3rd ed., CRC Press, Taylor & Francis Group, Boca Raton, London, New York, 2017.

[155] Philips EM430 Electron Microscope, (n.d.). https://www.slapsale.com/philips-em430-electron-microscope-37500 (accessed February 9, 2018).

[156] A. Muller, J. Grazul, Optimizing the Environment for Sub-0.2 nm Scanning Transmission Electron Microscopy, Microscopy. 50 (2001) 219–226.

[157] N.D. Browning, E.M. James, K. Kishida, I. Arslan, J.P. Buban, J.A. Zaborac, S.J. Pennycook, Y. Xin, G. Duscher, Scanning Transmission Electron Microscopy: an Experimental Tool for Atomic Scale Interface Science, Rev. Adv. Mater. Sci. 1 (2000) 1–26.

[158] S. Khanal, Advanced Electron Microscopy Characterization of Multimetallic Nanoparticles, University of Pittsburgh, 2014.

[159] D. Shindo, T. Oikawa, Energy Dispersive X-ray Spectroscopy, in: Anal. Electron Microsc. Mater. Sci., Springer Japan, Tokyo, 2002: pp. 81–102.

[160] C.E. Lyman, J.I. Goldstein, A.D. Romig, P. Echlin, D.C. Joy, D.E. Newbury, D.B. Williams, J.T. Armstrong, C.E. Fiori, E. Lifshin, K.-R. Peters, Light Element Microanalysis, in: Scanning Electron Microsc. X-Ray Microanal. Anal. Electron Microsc., Springer US, Boston, MA, 1990: pp. 117–121.

[161] Charles G., Barkla M.A. D.Sc., XXXIX. The Spectra of the Fluorescent Röntgen Radiations, London, Edinburgh, Dublin Philos. Mag. J. Sci. 22 (1911) 396–412.

[162] E.P. Bertin, Principles and Practice of X-Ray Spectrometric Analysis, Springer US, 1975.

[163] P. Doig, D. Lonsdale, P.E.J. Flewitt, The Spatial Resolution of X-ray Microanalysis in the Scanning Transmission Electron Microscope, Philos. Mag. A. 41 (1980) 761–775.

[164] G.F. Bastin, H.J.M. Heijligers, F.J.J. van Loo, The Performance of the Modified Φ(ϱz) Approach as Compared to the Love and Scott, Ruste and Standard ZAF Correction Procedures in Quantitative Electron Probe Microanalysis, Scanning. 6 (1984) 58–68.

[165] S.J.B. Reed, Characteristic Fluorescence Corrections in Electron-probe Microanalysis, Br. J. Appl. Phys. 16 (1965) 913–926.

[166] C.A. Volkert, A.M. Minor, Focused Ion Beam Microscopy and Micromachining, MRS Bull. 32 (2007) 389–399.

[167] S. Reyntjens, R. Puers, A Review of Focused Ion Beam Applications in Microsystem Technology, J. Micromechanics Microengineering. 11 (2001) 287–300.

[168] Z.M. Wang, FIB Nanostructures, Springer, 2013.

[169] R. Smoluchowski, Anisotropy of the Electronic Work Function of Metals, Phys. Rev. 60 (1941) 661–674.

[170] H.B. Michaelson, The Work Function of the Elements and Its Periodicity, J. Appl. Phys. 48 (1977) 4729–4733.

[171] V. Guillaumin, P. Schmutz, G.S. Frankel, Characterization of Corrosion Interfaces by the Scanning Kelvin Probe Force Microscopy Technique, J. Electrochem. Soc. 148 (2001) B163.

[172] R. Fujii, M.Y. Liao, H. Tsuji, J. Ishikawa, Work Function Measurement of Transition Metal Nitride and Carbide Thin Films, Vacuum. 80 (2006) 832–835.

[173] V.G.M. Sivel, J. Van Den Brand, W.R. Wang, H. Mohdadi, F.D. Tichelaar, P.F.A. Alkemade, H.W. Zandbergen, Application of the Dual-beam FIB/SEM to Metals Research, J. Microsc. 214 (2004) 237–245.

[174] P.J. Eaton, P. West, Atomic Force Microscopy, Oxford University Press, 2010.

[175] O.D. Payton, L. Picco, D. Robert, A. Raman, M.E. Homer, A.R. Champneys, M.J. Miles, High-speed Atomic Force Microscopy in Slow Motion—Understanding Cantilever Behaviour at High Scan Velocities, Nanotechnology. 23 (2012) 205704.

[176] H.H. Nassif, M. Gindy, J. Davis, Comparison of Laser Doppler Vibrometer with Contact Sensors for Monitoring Bridge Deflection and Vibration, NDT E Int. 38 (2005) 213–218.

[177] P.L. Cullen, K.M. Cox, M.K. Bin Subhan, L. Picco, O.D. Payton, D.J. Buckley, T.S. Miller, S.A. Hodge, N.T. Skipper, V. Tileli, C.A. Howard, Ionic Solutions of Two-dimensional Materials, Nat. Chem. 9 (2017) 244–249.

[178] W.H. Bragg, W.L. Bragg, The Reflection of X-rays by Crystals, Proc. R. Soc. London. Ser. A, Contain. Pap. a Math. Phys. Character. 88 (1913) 428–438.

[179] H.P. Myers, Introductory Solid State Physics, Taylor & Francis, 1997.

[180] J.P. McEvoy, O. Zarate, Introducing Quantum Theory, Totem Books, New York, 2014.

[181] B.E. Warren, X-ray Diffraction, Dover Publications, New York, 1990.

[182] C. Suryanarayana, M.G. Norton, X-Ray Diffraction : A Practical Approach, Springer, 1998.

[183] Instrument X-ray Optics: Reflection Geometry, (n.d.). http://pd.chem.ucl.ac.uk/pdnn/inst1/optics1.htm (accessed January 16, 2018).

[184] S.-D. Tsai, D. Mahulikar, H.L. Marcus, I.C. Noyan, J.B. Cohen, Residual Stress Measurements on Al-graphite Composites Using X-ray Diffraction, Mater. Sci. Eng. 47 (1981) 145–149.

[185] B.D. Cullity, Elements of X Ray Diffraction, Addison-Wesley Publishing Company, Inc., Massachusetts, 1956.

[186] R.E. Green, K.J. Kozaczek, C.O. Ruud, Nondestructive Characterization of Materials VI, Springer US, 1994.

[187] J. Crank, The Mathematics of Diffusion, Clarendon Press, 1975.

[188] C. Zoppou, J.H. Knight, Analytical Solution of a Spatially Variable Coefficient Advection–diffusion Equation in up to Three Dimensions, Appl. Math. Model. 23 (1999) 667–685.

[189] F.H. Stott, G.C. Wood, Internal Oxidation, Mater. Sci. Technol. 4 (1988) 1072–1078.

[190] Chromite R110059 - RRUFF Database [DB/OL], (n.d.). http://rruff.info/chem=Cr,O,Fe/display=default/R110059 (accessed April 28, 2017).

[191] Graphite R050503 - RRUFF Database [DB/OL], (n.d.). http://rruff.info/graphite/chem=C/display=default/R050503 (accessed March 15, 2018).

[192] Graphite R120025 - RRUFF Database [DB/OL], (n.d.). http://rruff.info/graphite/chem=C/display=default/R120025 (accessed March 15, 2018).

[193] Fe_3O_4 R060191 - RRUFF Database [DB/OL], (n.d.). http://rruff.info/chem=Fe,O/display=default/R060191 (accessed December 19, 2017).

[194] I. De Wolf, Stress Measurements in Si Microelectronics Devices Using Raman Spectroscopy, J. Raman Spectrosc. 30 (1999) 877–883.

[195] K.W. Andrews, D.J. Dyson, S.R. Keown, Interpretation of Electron Diffraction Patterns, 2nd ed., Springer US, Boston, MA, 1967.

[196] J.C. Slater, Atomic Radii in Crystals, J. Chem. Phys. 41 (1964) 3199–3204.

[197] Periodic Table of Elements: Sorted by Atomic Radius, (n.d.). https://environmentalchemistry.com/yogi/periodic/atomicradius.html (accessed April 9, 2018).

[198] Nglos324 - Chromium, (n.d.). https://www.princeton.edu/~maelabs/mae324/glos324/chromium.htm (accessed March

17, 2018).

[199] Nglos324 - Iron, (n.d.). https://www.princeton.edu/~maelabs/mae324/glos324/iron.htm (accessed March 17, 2018).

[200] Metallic, Covalent and Ionic Radii(r), (n.d.). http://www.wiredchemist.com/chemistry/data/metallic-radii (accessed April 10, 2018).

[201] J.A. Bearden, A.F. Burr, Reevaluation of X-ray Atomic Energy Levels, Rev. Mod. Phys. 39 (1967) 125–142.

[202] O.D. Payton, L. Picco, T.B. Scott, High-speed Atomic Force Microscopy for Materials Science, Int. Mater. Rev. 61 (2016) 473–494.

[203] C.P. Constable, J. Yarwood, P. Hovsepian, L.A. Donohue, D.B. Lewis, W.D. Münz, Structural Determination of Wear Debris Generated from Sliding Wear Tests on Ceramic Coatings using Raman Microscopy, J. Vac. Sci. Technol. A Vacuum, Surfaces, Film. 18 (2000) 1681–1689.

[204] M. Onink, C.M. Brakman, F.D. Tichelaar, E.J. Mittemeijer, S. van der Zwaag, J.H. Root, N.B. Konyer, The Lattice Parameters of Austenite and Ferrite in Fe-C Alloys as Functions of Carbon Concentration and Temperature, Scr. Metall. Mater. 29 (1993) 1011–1016.

[205] G.F. Goya, T.S. Berquó, F.C. Fonseca, M.P. Morales, Static and Dynamic Magnetic Properties of Spherical Magnetite Nanoparticles, J. Appl. Phys. 94 (2003) 3520–3528.

[206] M.H. Francombe, Lattice Changes in Spinel-type Iron Chromites, J. Phys. Chem. Solids. 3 (1957) 37–43.

[207] H.J. Yearian, J.M. Kortright, R.H. Langenheim, Lattice Parameters of the $FeFe_{(2-x)}Cr_xO_4$ Spinel System, J. Chem. Phys. 22 (1954) 1196–1198.

[208] P. Chellapandi, S.C. Chetal, Influence of Mis-match of Weld and Base Material Creep Properties on Elevated Temperature Design of Pressure Vessels and Piping, Nucl. Eng. Des. 195 (2000) 189–196.

[209] K. Hirota, K. Mitani, M. Yoshinaka, O. Yamaguchi, Simultaneous Synthesis and Consolidation of Chromium Carbides (Cr_3C_2, Cr_7C_3 and $Cr_{23}C_6$) by Pulsed Electric-current Pressure Sintering, Mater. Sci. Eng. A. 399 (2005) 154–160.

[210] C.M. Lin, C.M. Chang, J.H. Chen, W. Wu, Hardness, Toughness and Cracking Systems of Primary $(Cr,Fe)_{23}C_6$ and $(Cr,Fe)_7C_3$ Carbides in High-carbon Cr-based Alloys by Indentation, Mater. Sci. Eng. A. 527 (2010) 5038–5043.

[211] L.M. Berger, S. Saaro, T. Naumann, M. Kašparova, F. Zahálka, Influence of Feedstock Powder Characteristics and Spray Processes on Microstructure and Properties of WC-$(W,Cr)_2C$-Ni Hardmetal Coatings, Surf. Coatings Technol. 205 (2010) 1080–1087.

[212] D.J. Singh, B.M. Klein, Electronic Structure, Lattice Stability, and Superconductivity of CrC, Phys. Rev. B. 46 (1992) 14969–14974.

[213] H. Larsson, T. Jonsson, R. Naraghi, Y. Gong, R.C. Reed, J. Ågren, Oxidation of Iron at 600 °C-Experiments and Simulations, Mater. Corros. 68 (2017) 133–142.

[214] M.A. Pimenta, G. Dresselhaus, M.S. Dresselhaus, L.G. Cançado, A. Jorio, R. Saito, Studying Disorder in Graphite-based Systems by Raman Spectroscopy, Phys. Chem. Chem. Phys. 9 (2007) 1276–1290.

[215] K. Natesan, Z. Zeng, D.L. Rink, Materials Performance of Structural Alloys in CO_2 and in CO_2-Steam Environments, in: Proc. 22nd Annu. Conf. Foss. Energy Mater., Pittsburgh, 2008.

[216] Q. Luo, A New XRD Method to Quantify Plate and Lath Martensites of Hardened Medium-carbon Steel, J. Mater. Eng. Perform. 25 (2016) 2170–2179.

[217] J. Ehlers, D.J. Young, E.J. Smaardijk, A.K. Tyagi, H.J. Penkalla, L. Singheiser, W.J. Quadakkers, Enhanced Oxidation of the 9%Cr Steel P91 in Water Vapour Containing Environments, Corros. Sci. 48 (2006) 3428–3454.

[218] A. Danon, C. Servant, A. Alamo, J.. Brachet, Heterogeneous Austenite Grain Growth in 9Cr Martensitic Steels: Influence of the Heating Rate and the Austenitization Temperature, Mater. Sci. Eng. A. 348 (2003) 122–132.

[219] M. Taneike, K. Sawada, F. Abe, Effect of Carbon Concentration on Precipitation Behavior of $M_{23}C_6$ Carbides and MX Carbonitrides in Martensitic 9Cr steel during Heat Treatment, Metall. Mater. Trans. A. 35 (2004) 1255–1262.

[220] G.C. Wood, J.A. Richardson, M.G. Hobby, J. Boustead, The Identification of Thin Healing Layers at the Base of Oxide Scales on Fe-Cr Base Alloys, Corros. Sci. 9 (1969) 659–671.

[221] S. Saroja, M. Vijayalakshmi, V.S. Raghunathan, Effect of Prolonged Exposures of 9Cr-1Mo-0.07C Steel to Elevated Temperatures, Mater. Trans. JIM. 34 (1993) 901–906.

[222] J.R. Manning, Diffusion and the Kirkendall Shift in Binary Alloys, Acta Metall. 15 (1967) 817–826.